Advances in Polymer Science 241

Axel H.E. Müller
Oleg Borisov *Editors*

Self Organized Nanostructures of Amphiphilic Block Copolymers I

Springer

241

Advances in Polymer Science

Advances in Polymer Science

Recently Published and Forthcoming Volumes

Self Organized Nanostructures of Amphiphilic Block Copolymers II
Volume Editors: Müller, A.H.E., Borisov, O.
Vol. 242, 2011

Self Organized Nanostructures of Amphiphilic Block Copolymers I
Volume Editors: Müller, A.H.E., Borisov, O.
Vol. 241, 2011

Bioactive Surfaces
Volume Editors: Börner, H.G., Lutz, J.-F.
Vol. 240, 2011

Advanced Rubber Composites
Volume Editor: Heinrich, G.
Vol. 239, 2011

Polymer Thermodynamics
Volume Editors: Enders, S., Wolf, B.A.
Vol. 238, 2011

Enzymatic Polymerisation
Volume Editors: Palmans, A.R.A., Heise, A.
Vol. 237, 2010

High Solid Dispersion
Volume Editor: Cloitre, M.
Vol. 236, 2010

Silicon Polymers
Volume Editor: Muzafarov, A.
Vol. 235, 2011

Chemical Design of Responsive Microgels
Volume Editors: Pich, A., Richtering, W.
Vol. 234, 2010

Hybrid Latex Particles – Preparation with Emulsion
Volume Editors: van Herk, A.M., Landfester, K.
Vol. 233, 2010

Biopolymers
Volume Editors: Abe, A., Dušek, K., Kobayashi, S.
Vol. 232, 2010

Polymer Materials
Volume Editors: Lee, K.-S., Kobayashi, S.
Vol. 231, 2010

Polymer Characterization
Volume Editors: Dušek, K., Joanny, J.-F.
Vol. 230, 2010

Modern Techniques for Nano- and Microreactors/-reactions
Volume Editor: Caruso, F.
Vol. 229, 2010

Complex Macromolecular Systems II
Volume Editors: Müller, A.H.E., Schmidt, H.-W.
Vol. 228, 2010

Complex Macromolecular Systems I
Volume Editors: Müller, A.H.E., Schmidt, H.-W.
Vol. 227, 2010

Shape-Memory Polymers
Volume Editor: Lendlein, A.
Vol. 226, 2010

Polymer Libraries
Volume Editors: Meier, M.A.R., Webster, D.C.
Vol. 225, 2010

Polymer Membranes/Biomembranes
Volume Editors: Meier, W.P., Knoll, W.
Vol. 224, 2010

Organic Electronics
Volume Editors: Meller, G., Grasser, T.
Vol. 223, 2010

Inclusion Polymers
Volume Editor: Wenz, G.
Vol. 222, 2009

Advanced Computer Simulation Approaches for Soft Matter Sciences III
Volume Editors: Holm, C., Kremer, K.
Vol. 221, 2009

Self-Assembled Nanomaterials II
Nanotubes
Volume Editor: Shimizu, T.
Vol. 220, 2008

Self-Assembled Nanomaterials I
Nanofibers
Volume Editor: Shimizu, T.
Vol. 219, 2008

Self Organized Nanostructures of Amphiphilic Block Copolymers I

Volume Editors: Axel H.E. Müller
Oleg Borisov

With contributions by

M. Ballauff · O.V. Borisov · M. Charlaganov
M.A. Cohen Stuart · M. Hof · J. Humpolíčková
A. de Keizer · P. Košovan · J. Kuldová
F.A.M. Leermakers · Z. Limpouchová · P. Matějíček
A.H.E. Müller · D.V. Pergushov · K. Procházka · R. Šachl
M. Štěpánek· M. Uchman· F. Uhlík· I.K. Voets
A.B. Zezin· E.B. Zhulina

Springer

Editors
Prof. Axel H.E. Müller
Makromolekulare Chemie II
and Bayreuther Zentrum für Kolloide
und Grenzflächen
Universität Bayreuth
95440 Bayreuth
Germany
axel.mueller@uni-bayreuth.de

Dr. Oleg Borisov
Institut Pluridisciplinaire de Recherche sur
l'Environnement et les Matériaux
UMR 5254 CNRS/UPPA
64053 Pau
France
oleg.borisov@univ-pau.fr

ISSN 0065-3195 e-ISSN 1436-5030
ISBN 978-3-642-22485-0 e-ISBN 978-3-642-22486-7
DOI 10.1007/978-3-642-22486-7
Springer Heidelberg Dordrecht London New York

Library of Congress Control Number: 2011934436

Cover design: WMXDesign GmbH, Heidelberg

Printed on acid-free paper

Springer is part of Springer Science+Business Media (www.springer.com)

Volume Editors

Prof. Axel H.E. Müller
Makromolekulare Chemie II
and Bayreuther Zentrum für Kolloide
und Grenzflächen
Universität Bayreuth
95440 Bayreuth
Germany
axel.mueller@uni-bayreuth.de

Dr. Oleg Borisov
Institut Pluridisciplinaire de Recherche sur
l'Environnement et les Matériaux
UMR 5254 CNRS/UPPA
64053 Pau
France
oleg.borisov@univ-pau.fr

Editorial Board

Advances in Polymer Sciences
Also Available Electronically

Advances in Polymer Sciences is included in Springer's eBook package *Chemistry and Materials Science*. If a library does not opt for the whole package, the book series may be bought on a subscription basis. Also, all back volumes are available electronically.

For all customers who have a standing order to the print version of *Advances in Polymer Sciences*, we offer free access to the electronic volumes of the Series published in the current year via SpringerLink.

If you do not have access, you can still view the table of contents of each volume and the abstract of each article by going to the SpringerLink homepage, clicking on "Browse by Online Libraries", then "Chemical Sciences", and finally choose *Advances in Polymer Science*.

You will find information about the

- Editorial Board
- Aims and Scope
- Instructions for Authors
- Sample Contribution

at springer.com using the search function by typing in *Advances in Polymer Sciences*.

Color figures are published in full color in the electronic version on SpringerLink.

Aims and Scope

The series *Advances in Polymer Science* presents critical reviews of the present and future trends in polymer and biopolymer science including chemistry, physical chemistry, physics and material science. It is addressed to all scientists at universities and in industry who wish to keep abreast of advances in the topics covered.

Review articles for the topical volumes are invited by the volume editors. As a rule, single contributions are also specially commissioned. The editors and publishers will, however, always be pleased to receive suggestions and supplementary information. Papers are accepted for *Advances in Polymer Science* in English.

In references *Advances in Polymer Sciences* is abbreviated as *Adv Polym Sci* and is cited as a journal.

Special volumes are edited by well known guest editors who invite reputed authors for the review articles in their volumes.

Impact Factor in 2010: 6.723; Section “Polymer Science”: Rank 3 of 79

Preface

The spontaneous assembly of amphiphilic molecules in an aqueous environment represents a generic mechanism of self-organization on the supramolecular level exemplified by nature. In the living cell, the process of hierarchical assembly of bio(macro)molecules propagates from the nano- to the mesoscopic level and beyond, giving rise to highly organized structures, each perfectly adjusted for performing specific functions. This self-organization across multiple length scales occurs as an outcome of a delicate balance between a number of attractive and repulsive interactions: electrostatic, hydrophobic, hydrogen bonding, metal coordination, etc., each with its characteristic strength and range.

Recent advances in polymer chemistry, in particular, in controlled radical polymerization, have enabled the synthesis of complex macromolecular architectures with controlled topology, which comprise chemically different (functional) blocks of controlled length in well-defined positions. Block co- and terpolymers, molecular and colloidal polymer brushes, and star-like polymers present just a few typical examples. Furthermore, miktoarm stars, core-shell stars and molecular brushes, etc. exemplify structures where chemical and topological complexity are combined in one macromolecule.

Significant progress has been made in terms of understanding the self-assembly of amphiphilic diblock copolymers in selective solvents. In aqueous solutions, the assembly is typically driven by hydrophobic attraction between associating blocks and gives rise to diverse nanostructures (micelles, vesicles) and mesophases. Theory has established relationships between the macromolecular architectures of ionic/hydrophobic diblock copolymers and the equilibrium morphologies of the self-assembled aggregates. Unusual responsive properties of micelles with pH-sensitive coronas were predicted on the basis of the concept of coupling between ionization of the polyelectrolyte block and the aggregation state of the copolymer molecule and they have been recently observed in experiments. A multitude of experimental techniques, including radiation scattering, fluorescence spectroscopy, electron and atomic force microscopy, etc., have been used for structural and dynamic characterization of the block-copolymer self-assembly in solution and at liquid–solid and liquid–air interfaces.

Self-assembled structures of amphiphilic copolymers have been extensively explored in biomedicine as vectors for targeted delivery of drugs and biological molecules (enzymes, nucleic acids), in biomaterials engineering (antifouling surfaces), biosensors, etc. Further applications include food industry and agrochemistry, uptake and pre-concentration of toxic organic compounds and heavy metal ions in water treatment, molecular templates for nano-electronic devices. Many water-based industrial formulations include polymeric amphiphiles that aggregate and co-assemble with other macromolecules, nanoparticles and surfactants to form nano-aggregates, and different types of mesophases and structures at interfaces. An important requirement for the biomedical applications are pronounced stimuli-responsive properties of the polymeric nano-structures, that is ability of a triggered response to smoothly varied external conditions (e.g., tiny variations in temperature or pH) or recognition of weak specific stimuli (e.g., trace concentrations of biologically active or toxic compounds).

The electrostatic attraction between oppositely charged ionic macromolecules and (bio)nanocolloids is an appealing alternative mechanism for building up functional nano-assemblies in aqueous media. The association of linear polyelectrolytes in solutions or at charged interfaces leads to interpolyelectrolyte complexes or polyelectrolyte multilayers. The strength of attractive electrostatic interactions can be easily tuned by the pH or ionic strength of the solution. Hence, electrostatically assembled structures exhibit pronounced stimuli-responsive features. The enormous diversity of possible combinations of co-assembling components, including oppositely charged ionic polymers, nucleic acids and proteins, metal/ligand complexes, and inorganic nano-particles, opens a fascinating perspective of the possibility to use this mechanism to design novel functional materials based on supramolecular and supracolloidal assemblies.

Furthermore, such advanced applications as (bio)nanoreactors or molecular templates require progressing beyond the most elementary forms of self-organization and generic types of copolymer nanostructures. We need to explore routes of self- and co-assembly of macromolecules into non-centrosymmetric multi-compartment supramolecular nano-assemblies. For example, construction of nanoreactors for enzymatic (cascade) reactions requires immobilization of multiple proteins in close proximity to each other in well-segregated (protective) environments. Such enzyme cascades are very promising in biotechnological applications. The development of pathways for fabrication of well-defined multi-domain nano-structures via the spontaneous assembly of elementary macromolecular building blocks represents one of the future challenges in supra-macromolecular chemistry.

Co-assembly of amphiphilic and bis-hydrophilic block copolymers with oppositely charged polyelectrolyte blocks gives rise to sophisticated nanostructures with compartmentalized core or corona domains. The combination of nano-sized compartments that differ in polarity and composition within one colloidally stable polymeric nanostructure is promising in the development of novel, highly effective, multifunctional polymeric reagents for wastewater treatment (e.g., an one-stage removal of organic impurities and heavy metal ions from aqueous environment) as well as smart nano-containers capable of incorporation of various physiologically active

compounds, e.g., proteins and nucleic acids. Co-assembly of two ionic-neutral block copolymers can lead to surface-compartmentalized polymer-based Janus nanoparticles ("Janus micelles") with two chemically different "faces" exposed to the surrounding environment. Janus micelles with coronas solvated in a common good solvent (e.g., water), but laterally segregated, are promising as they can selectively incorporate different enzymes or metal nano-particles possessing catalytic activity in segregated compartments, thus offering opportunities for (bio)catalytic cascades. Janus micelles are intrinsically highly surface active; their use may cut down the use of conventional surfactants with concomitant environmental impact.

Biomedical applications strongly require nanostructures based on the assembly of amphiphilic macromolecules comprising functional blocks of biological origin (peptides, oligo- or polynucleotides, polysaccharides) or their synthetic analogs. A novel class of biohybrid copolymers comprising a synthetic block conjugated to a polypeptide or polynucleotide block has attracted considerable attention. Their self-assembly gives rise to diverse ordered structures in aqueous media and at solid–liquid interfaces. The ability of biopolymer blocks to take part in specific interactions (e.g., ligand–receptor, DNA hybridization, etc.) with target molecules opens up a fascinating perspective for the design of novel generations of label-free diagnostic systems, or of smart vector systems that can deliver drugs or biologically active molecules on the basis of self-assembled bio-hybrid structures.

Based on these considerations, the European Union funded a Marie Curie Research Training Network "Self-Organized Nanostructures of Amphiphilic Copolymers (POLYAMPHI)." This network, consisting of 14 research teams from 7 European countries, worked successfully from 2004 to 2008. Some of the results obtained in these collaborations are presented in these two volumes, supplemented by chapters dealing with additional aspects of the topic. Thus, we present a comprehensive overview of the state of the art in experimental research and theory of self-organization via self- and co-assembly of amphiphilic or hydrophilic ionic (macro)molecules in aqueous solutions and at interfaces.

Pau and Bayreuth
Summer 2011

Oleg Borisov
Axel Müller

Contents

Adv Polym Sci (2011) 241: 1–55
DOI:10.1007/12_2010_104

Published online: 23 November 2010

Conformations and Solution Properties of Star-Branched Polyelectrolytes

Oleg V. Borisov, Ekaterina B. Zhulina, Frans A.M. Leermakers, Matthias Ballauff, and Axel H.E. Müller

Abstract Aqueous solutions of star-like polyelectrolytes (PEs) exhibit distinctive features that originate from the topological complexity of branched macromolecules. In a salt-free solution of branched PEs, mobile counterions preferentially localize in the intramolecular volume of branched macroions. Counterion localization manifests itself in a dramatic reduction of the osmotic coefficient in solutions of branched polyions as compared with those of linear PEs. The intramolecular osmotic pressure, created by entrapped counterions, imposes stretched conformations of branches and this leads to dramatic intramolecular conformational transitions upon variations in environmental conditions. In this chapter, we overview the theory of conformations and stimuli-induced conformational transitions in star-like PEs in aqueous solutions and compare these to the data from experiments and Monte Carlo and molecular dynamics simulations.

O.V. Borisov (✉)
Institut Pluridisciplinaire de Recherche sur, l'Environnement et les Matériaux,
UMR 5254 CNRS/UPPA, 064053 Pau, France
e-mail: oleg.borisov@univ-pau.fr
and
Institute of Macromolecular Compounds of the Russian Academy of Sciences, 199004
St. Petersburg, Russia

E.B. Zhulina
Institute of Macromolecular Compounds of the Russian Academy of Sciences, 199004
St. Petersburg, Russia

F.A.M. Leermakers
Laboratory of Physical Chemistry and Colloid Science, Wageningen University, 6703
Wageningen, The Netherlands

M. Ballauff
Humboldt Universität and Helmholtz-Zentrum Berlin für Materialien und Energie GmbH Berlin,
Germany

A.H.E. Müller
Makromolekulare Chimie II and Bayreuther Zentrum für Kolloide und Grenzflächen,
Universität Bayreuth, 95440 Bayreuth, Germany

Keywords Branched polyelectrolytes · Ionic fractals · Charge renormalization · Intra-molecular conformational transitions

Contents

1 Introduction

Ionic polymers constitute an important class of water-soluble macromolecules [1]. Synthetic polyelectrolytes (PEs) and polyampholytes have been in the focus of attention for many years. Most biomacromolecules (proteins, nucleic acids and polysaccharides) carry ionizable groups and are therefore included in this class of polymers. Ionic macromolecules have an ability to significantly change their conformations as a response to variations in the environmental conditions. This makes them interesting candidates for technological applications that range from nanomedicine and food production to paper making and oil recovery.

Highly intriguing and truly unique properties of PE solutions arise from an interplay between long-ranged electrostatic interactions and the chemical connectivity of ionic monomers in these polymer chains. Even though the basic understanding of properties of linear PEs has advanced during the past decade (see, for example, reviews [2, 3] and references therein), the corresponding insights for more complex macro- and supramolecular PE assemblies are less developed. Examples of such assemblies include colloidal PE brushes [4], ionic dendrimers [5], charged microgels [6], randomly [7] or regularly branched PEs [8, 9], and aggregates of amphiphilic ionic block copolymers [10].

Self-assembled nanostructures of biopolymers play an important role in nature. For example, extracellular branched polysaccharides decorate bacterial surfaces and therewith mediate cell adhesion [11], aggrecans (protein–polysaccharide complexes) control mechanical stresses in synovial joints [12], whereas neurofilaments (neuron-specific protein assemblies) support the elongated cell shape and participate in the maintenance of the axonal caliber [13]. It is believed that these biological functions rest on the ability of bioassemblies to provide adequate responses to variations in the local environment. Therefore, a better understanding of the physical mechanisms that govern conformational rearrangements in (bio)nanostructures, is of key importance, not only for colloid and material sciences, but also for cell biology.

The molecular organization of biopolymers is often much more complex than that of polymers synthesized in a chemical laboratory. Work is underway to systematically close this gap. Recent progress in controlled radical polymerization has made it possible to synthesize increasingly complex ionic macromolecules with controlled dimensions and topology. As a result, well-defined ionic block copolymers [10], colloidal [4] and molecular [8] PE brushes, and star-like PEs [9] have become available. In addition to emerging applications, such nanostructures constitute excellent model systems.

Star-shaped macromolecules exemplify generic features that result from the branched topology [14, 15]. Started by pioneering work of Stockmayer and Zimm [16], conformations of nonionic star-branched macromolecules were amply studied theoretically [16–20]. The fact that conformations of nonionic star-shaped polymers in dilute and semidilute solutions are determined by the repulsive short-range binary (in good solvent conditions) or ternary (in theta-solvent conditions) interactions between monomers has been demonstrated by more recent scaling models of Daoud and Cotton [21] and of Zhulina and Birhstein [22–24]. The equilibrium size of a star-like polymer (or simply star polymer) is determined by the conformations of its branches. These are controlled by the balance between intramolecular repulsive interactions, which induce stretching at the expense of conformational entropy losses.

Compared to short-ranged excluded-volume interactions, long-ranged intramolecular electrostatic repulsion has a much bigger impact on the conformations of the arms in ionic polymer stars. The Coulomb interactions in a PE solution are, however, always partially screened by small mobile counterions that are invariably present to ensure the electroneutrality of the system. The importance of nonlinear screening effects and of the counterion localization in solutions of strongly charged linear polyions, was first understood in terms of the Manning condensation [25].

In a dilute salt-free solution of branched PEs, the distribution of counterions is strongly inhomogeneous [26–35]. Similarly to strongly charged colloidal particles [36], branched PEs (stars, dendrimers, hyperbranched PEs, molecular and colloidal PE brushes) can maintain a high local electrostatic potential. The latter might be so strong that the attraction of mobile counterions to such macroion competes with their translational entropy. As a result, ions remain preferentially localized in the vicinity of macroions. In contrast to a classical solid colloidal particle, a branched PE macromolecule has a relatively low internal volume fraction of the monomer units and, therefore, these molecules can accommodate a huge fraction of its counterions in their volume. The escape of counterions into the bulk solution is discouraged by the strong Coulombic attraction to these highly branched (and thereby heavily charged) macromolecules. Because the internalized counterions retain some translational freedom, they generate an osmotic pressure. As a response to this pressure, a branched ionic macromolecule can stretch its arms, providing more space for the counterions. The equilibrium structure is thus the result of the balance between a restoring force in stretched arms and an osmotic one.

The concept of counterion localization in colloidal PE brushes and star-like PEs was first formulated on the basis of scaling arguments [26, 27], and later supported by a Poisson–Boltzmann-type analysis [27, 29, 37]. It has been further understood that the counterion localization and the osmotic swelling are generic properties of branched macroions, and that the onset of counterion localization occurs at a certain characteristic degree of branching for each particular polyion topology [31–33]. Unambiguous evidence of a clearly inhomogeneous distribution of counterions in solutions of star polyions, was provided by Monte Carlo [38] and molecular dynamics simulations [39–42]. A convincing experimental proof of the counterion localization, was given by osmotic pressure measurements in dilute salt-free solutions of PE star polymers [43] and colloidal PE brushes [44, 45].

Due to the counterion localization, conformations of branched macroions that comprise strongly dissociating groups (charge is quenched) are almost insensitive to the addition of salt, up to relatively high salt concentrations. The ability of a branched polyion to maintain a virtually constant ionic strength in its interior is of special interest for potential applications, where a controlled (buffered) microenvironment is essential (e.g., colloidal bionanoreactors, smart nanocontainers for biologically active molecules, etc.).

In quenched PE stars, the degree of dissociation is hardly affected by the proton concentration inside the macroion volume. In contrast to this, in a weakly dissociating (charge is annealing) branched macroion, the degree of ionization is affected by the local intramolecular proton concentration, which may differ from that in the bulk. The change in charge density in the PE star has a corresponding effect on the charge compensation by the counterions. Annealing PE stars, therefore, have peculiar responsive properties, e.g., they exhibit a non-monotonic variation of their size as a function of the ionic strength in the solution [28, 30].

Experimental studies of solutions of PE star polymers are rare, because the synthesis of macromolecules with a controlled number and length of branches still presents a significant challenge. A few recent studies report on various properties

of solutions of star-branched PEs, in which the number of arms was systematically varied [43, 46–51]. A number of studies on the pH and salt response, has been performed on star-like micelles with a PE corona and a kinetically frozen hydrophobic core [52–63]. These micelles mimic many-armed PE stars, although the number of arms (equal to the micelle aggregation number) is poorly controlled.

The objective of this chapter is to present an overview of the existing theories on conformations of star-branched PEs and to compare these to experimental data and the results of computer simulations. Some emphasis is made on the effect of counterion localization and its consequences for the conformations of branched PEs.

We start with a brief reminder on the scaling theory of nonionic star-branched polymers (Sect. 2), and proceed with the scaling model of a PE star polymer in a salt-free dilute solution (Sect. 3). We then discuss the physical basis of counterion localization and its manifestation in branched PEs of different topologies (Sect. 4).)

A quantitative analysis of counterion localization in a salt-free solution of star-like PEs is carried out on the basis of an exact numerical solution of the corresponding Poisson–Boltzmann (PB) problem (Sect. 5). Here, the conformational degrees of freedom of the flexible branches are accounted for within the Scheutjens–Fleer self-consistent field (SF-SCF) framework. The latter is used to prove and to quantify the applicability of the concept of colloidal charge renormalization to PE stars, that exemplify "soft" charged colloidal objects. The predictions of analytical and numerical SCF–PB theories are complemented by results of Monte Carlo (MC) and molecular dynamics (MD) simulations. The available experimental data on solution properties of PE star polymers are discussed in the light of theoretical predictions (Sect. 6).

Finally, an analytical theory of conformations of highly branched PE stars is discussed (Sect. 7). The predictions are critically compared to numerical SCF–PB results. Here we focus on the responsive properties of strongly and weakly dissociating PE star polymers, e.g., their ability to change their conformations in response to a varied ionic strength and pH in solution. Inferior solvent quality triggers conformational transitions in PE star polymers (Sect. 8). Relevant theoretical insights are reviewed and compared to MD simulation results.

2 Solutions of Neutral Star Polymers: Reminder on the Scaling Theory

We start with a brief review of the theory for conformational and solution properties of neutral (uncharged) star-branched polymers.

Consider a star polymer, composed of p linear arms, each arm with a length of N monomers. As shown in Fig. 1, a star comprises a central "core" domain onto which the linear arms are grafted by one of their ends. The effect of a finite core size on the star characteristics is negligible, as long as the dimensions of extended arms exceed, by far, that of the core. The arms of the star are assumed to be intrinsically flexible, so that the Kuhn length is on the order of monomer size a.

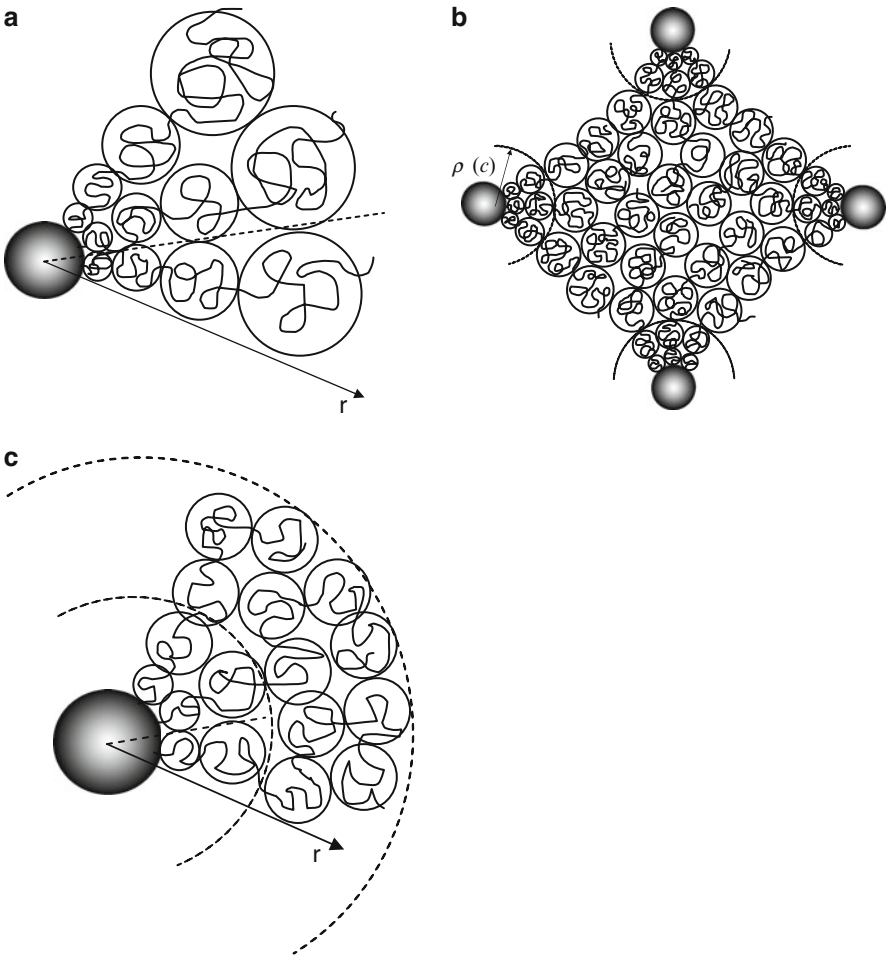

Fig. 1 Blob model for nonionic polymer stars: a single star under good or theta-solvent conditions (**a**), semidilute star solution (**b**), single polymer star partially collapsed in poor solvent (**c**). r distance from the center of the star

In the classical theory of Stockmayer and Zimm [16], a star polymer consists of p ideal (Gaussian) non-interacting branches, linked together in the center of the molecule. This model can be used to evaluate the decrease in the size of a star polymer (e.g., in its radius of gyration), as compared with that of a linear macromolecule with the same degree of polymerization pN. The theory further developed by Benoit presents an estimate for the form factor, explaining the scattering of radiation by a dilute solution of (ideal) star polymers [17, 18]. Because interarm interactions are neglected in this model (i.e., the arms are treated as independently fluctuating ideal coils), the overall size of the star is systematically underestimated.

Short-range interactions (van der Waals attraction and hard-core repulsion) between monomers can be accounted for using a virial expansion. As long as the volume fraction of monomers in a star polymer is significantly below unity, only pairwise monomer–monomer interactions, with second virial coefficient $\upsilon \sim a^3(1-2\chi(T))$, or ternary interactions, with third virial coefficient $w \sim a^6$, are relevant. The former depends on the Flory–Huggins parameter χ and is positive under good solvent ($\chi < 1/2$) and negative under poor solvent conditions ($\chi > 1/2$). In a good solvent, binary interactions are dominated by the repulsive part of the monomer–monomer interaction potential (hard-core repulsion), whereas in a poor solvent, binary interactions are attractive (due to the van der Waals forces). A special case $\upsilon = 0$ (vanishing net binary interactions) corresponds to theta-solvent conditions, where weak attraction between monomers is exactly compensated by their excluded volume.

Subsequent theoretical studies [19, 20] have incorporated short-range monomer–monomer interactions using the mean field approximation, but systematically underestimated conformational entropy losses in the stretched arms. These theories thus overestimate the star size.

The first theories that implemented a proper balance of intramolecular interactions and conformational elasticity of the branches were developed by Daoud and Cotton [21] and by Zhulina and Birshtein [22–24]. These theories use scaling concepts (the blob model), originally developed by de Gennes and Alexander to describe the structure of semidilute polymer solutions [64] and planar polymer brushes [65, 66]. Here, the monomer–monomer interactions were incorporated on the level of binary or ternary contacts (corresponding to good and theta-solvent conditions, respectively), and both dilute and semidilute solutions of star polymers were considered. Depending on the solvent quality and the intrinsic stiffness of the arms, the branches of a star could be locally swollen, or exhibit Gaussian statistics [22–24].

2.1 Star Polymer Conformation in a Dilute Solution

According to the blob model, a flexible neutral star polymer can be envisioned as an array of concentric shells of closely packed blobs. For a visualization of the blobs, see Fig. 1a. The chain ends are assumed to be localized at the edge (i.e., within the outermost blobs), and each chain contributes one blob to each shell. The chain segment inside a blob remains unperturbed by the interactions with other branches and, therefore, exhibits Gaussian or excluded-volume statistics under theta- or good solvent conditions, respectively. For transparency, we consider first athermal, $\upsilon \cong a^3$, and theta-solvent, $\upsilon = 0$, conditions. The blob size at distance r from the star center is equal to the average interchain separation $\cong r/p^{1/2}$, which coincides with the local correlation length, $\xi(r)$. The latter is related to the local polymer concentration, $c_p(r)$, by the same scaling law as in a semidilute polymer solution, $\xi(r) \cong a[c_p(r)a^3]^{-\nu/(3\nu-1)}$, where ν is the Flory exponent ($\nu \approx 3/5$ and

$\nu = 1/2$ under good and theta-solvent conditions, respectively). Hence, the blob picture enables one to derive the power law for the radial decay in polymer density:

$$c_{\mathrm{p}}(r) \cong (p^{1/2}a/r)^{(3\nu-1)/\nu}a^{-3} \tag{1}$$

Here and below, the sign "$\cong$" implies that a numerical coefficient on the order of unity, is omitted.

The radial decay in polymer density corresponds to a radial decrease in local stretching of the arms, $\mathrm{d}r/\mathrm{d}n \cong p/[r^2 c_{\mathrm{p}}(r)] \cong a(p^{-1/2}r/a)^{(\nu-1)/\nu}$. At the same time, the local stretching of the branches controls the elastic tension and, thereby, the size of the elastic blob [67], $\xi_{\mathrm{elastic}} \cong a(a\mathrm{d}n/\mathrm{d}r)^{\nu/(1-\nu)}$. Within the blob picture, $\xi_{\mathrm{elastic}}(r) \cong \xi(r)$. Hence, the radial increase in the size of the concentrational blob, $\xi(r)$, also ensures the decrease in local tension in the arms of the star, $\xi_{\mathrm{elastic}}^{-1} \cong p^{1/2}/r$.

Making use of the normalization condition for the density profile:

$$4\pi \int_0^R c_{\mathrm{p}}(r) r^2 \mathrm{d}r = pN \tag{2}$$

one obtains a scaling expression for the overall size R of a star polymer:

$$R \cong aN^{\nu}p^{(1-\nu)/2} \tag{3}$$

As follows from (3), the star size, R, depends on the degree of polymerization, N, of the individual arms, with the same power law as that for a linear polymer chain, $R \sim N^{\nu}$. However, the repulsion between the branches of the star leads to the extension of its branches in the radial direction, as compared with the dimensions of an individual linear chain with the same degree of polymerization N. This cooperative effect of interbranch repulsion is described by the factor $p^{(1-\nu)/2}$ in (3). Because of the relatively high monomer concentration in the intramolecular volume of the star, the extension of its arms occurs even under theta-solvent conditions. In contrast to a linear polymer, the repulsion due to ternary monomer–monomer contacts inside the star ensures the stretching of its branches with respect to the Gaussian dimension. Remarkably, if the solvent is marginal good, the corona of a star with sufficiently long arms consists of two regions. In the central (theta) region, the chain segments within the blobs retain Gaussian statistics, and the density profile decays here as $c_{\mathrm{p}}(r) \cong p^{1/2}(wa^{-6})^{-1/4}a^{-2}r^{-1}$. Closer to the star periphery, the blobs become sufficiently large and swollen the density profile acquires a shape that is typical for a good solvent, $c_{\mathrm{p}}(r) \cong p^{2/3}\upsilon^{-1/3}a^{-2/3}r^{-4/3}$. The boundary between these regions, r_θ, is determined by the condition $\xi(r_\theta)\upsilon a^{-4} \cong 1$, i.e., $r_\theta \cong p^{1/2}\upsilon^{-1}a^4$. On the scale of the star as a whole, the crossover from the theta-regime to the good solvent regime can be estimated from the condition of swelling of the outermost coronal blob, $\xi(R)\upsilon a^{-4} \geq 1$, and implies $N\upsilon^2 p^{-1/2}a^{-6} \geq 1$. The overall star size R is then given by:

$$R \cong \begin{cases} aN^{3/5}(\upsilon/a^3)^{1/5}p^{1/5}, & \text{good solvent} \\ aN^{1/2}(w/a^6)^{1/8}p^{1/4}, & \text{theta-solvent} \end{cases} \tag{4}$$

The scaling arguments presented above capture the essential features of a neutral star polymer both in good and theta-solvent conditions: there is a power law decay of the radial monomer density and there are scaling dependencies for the overall star size R on number of branches p and the degree of polymerization N. These scaling predictions were tested by MD and MC simulations [68–72] and experimentally [73–79]. Although certain discrepancies were detected (see, e.g., the discussion in [72]), a simple blob model remains an important theoretical tool for interpreting experimental data on nonionic star macromolecules. A similar blob Ansatz, however, cannot be directly applied to the case when long-ranged electrostatic interactions come into play.

2.2 *Effects of Concentration and Interactions Between Polymer Stars*

Interactions between star polymers in dilute solutions were considered by Witten and Pincus [80, 81] using a scaling approach. According to the scaling model, the intermolecular repulsion between two star polymers arises at distance $d \leq 2R$ between their centers, due to the overlap of the coronae. The interactions are described by a "soft" binary repulsive potential $U_{\text{star}}(d)/k_{\text{B}}T \cong p^{1/2}\ln(2R/d)$ in both good and theta-solvents. The corresponding second virial coefficient of interaction between two nonionic stars scales as $\cong R^3$. A more complex analytical expression for the interaction potential interpolating between the logarithmic behavior at $d \leq 2R$ and the Yukawa form at $d \geq 2R$ has been suggested in [82] to fit the experimental data on scattering from star polymer solutions. The structure factor of a dilute solution of star polymers can be approximated by that of a solution of soft spheres [82, 83].

There are relatively few experimental studies on the interactions between star polymers. Therefore, to date, MD simulations have mostly been used to validate theoretical models. A comprehensive comparison between theoretical and experimental results has recently been reviewed by Jusufi and Likos [84].

Beyond the overlap concentration threshold, $c \geq c^* \cong pN/R^3$, star polymers form a semidilute solution. Because of the fact that the arms in a star are stretched, the scaling theory [24] predicts that the properties of semidilute solutions of star polymers are distinctively different from those of linear polymers. When the polymer concentration $c \geq c^*$, a semidilute solution is envisioned as a system of closely packed and virtually non-interpenetrating (segregated) polymer stars. A further increase in polymer concentration leads to a progressive contraction of the coronae of the individual stars. This contraction results in an increase in the conformational entropy of the partially stretched star arms.

The blob picture of a semidilute solution of polymer stars is schematically presented in Fig. 1b. The peripheral (contracted) regions of the star coronae are envisioned as a "sea of blobs" of constant size, which corresponds to a constant polymer concentration in this region. In contrast to this, within radius $\rho(c) \leq R$, the structure of the corona of individual stars is preserved (a system of growing

in radial direction blobs). Remarkably, the segments of star branches in the sea of blobs remain stretched up to relatively high polymer concentrations [24]. The local stretching of the arms decreases monotonously with increasing distance r from the center of the star. The interpenetration of the stars occurs at the periphery of the coronae, where the terminal segments of the arms in the sea of blobs lose stretching with respect to the Gaussian dimensions. An increase in the concentration, c, leads to the decrease in both $\rho(c)$ and overall star size R and, progressively, there is an increase of the interpenetration.

The conformational structure of stars in a semidilute solution regime is mirrored by the corresponding thermodynamic consequences. There is, e.g., a discontinuity in the osmotic compressibility near c^* [81]. The intensity of scattered radiation (normalized by the polymer concentration) exhibits a pronounced correlation peak, as a function of the scattering vector, in both dilute and semidilute regimes close to the overlap concentration c^*. The evolution of the correlation peak in these scattering curves has a remarkable dependence on the polymer concentration: its magnitude increases below, and decreases above c^*. The latter is due to the increasing interpenetration of the coronae and the decreasing size of the unperturbed central region of the stars [86, 87]. The theory of scattering from semidilute solutions of star polymers was developed in [85–87].

Only at a sufficiently high polymer concentration, when the dimensions of the arms approach those of individual linear chains in a semidilute solution at the same concentration, do the star coronae become fully interpenetrated and the correlation peak in the scattering curves disappears. In this concentration regime, the thermodynamic properties of the solution of branched macromolecules become similar to those of linear chains.

3 Cell Model of the Salt-Free Solution of Polyelectrolyte Stars

We will now focus on star polymers that carry charges, and introduce a cell model for a dilute solution of such macromolecules. To this end, we consider a PE star that occupies the central region of a spherical cell of radius $D \geq R$, as shown in Fig. 2. The cell comprises at least the corresponding number of mobile monovalent counterions that compensate the charge of the PE star, and additional salt may be included. Typically, the ion concentrations are different in the intrastar volume, $0 \leq r \leq R$, and in the exterior part of the cell, $R \leq r \leq D$. We will first focus on the case that no salt is added to the cell, and thus only counterions participate in the partial screening of long-ranged electrostatic interactions. A fraction α of the monomers in a PE star is electrically charged (ionized). If the Bjerrum length $l_B = e^2/\epsilon k_B T$ is on the order of monomer size a, the condition of weak charging, $\alpha \leq 1$, implies that a local stiffening of the arms due to the intraarm Coulomb repulsion can be neglected [2, 88, 89]. The "bare" charge of the star-branched polyion is $Qe = p\alpha Ne$, where e is the elementary charge.

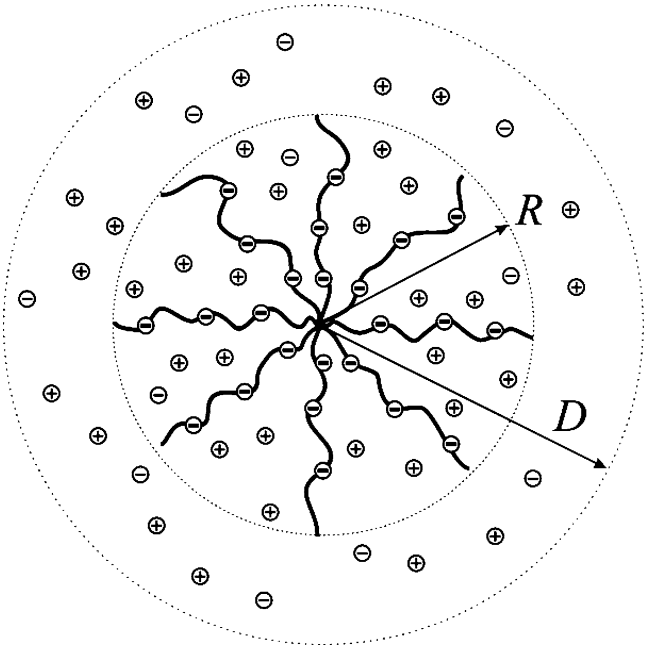

Fig. 2 Anionic star PE with eight arms having a radius R in 1:1 electrolyte solution (as indicated by the small spheres that carry a *plus* or a *minus* sign) in a spherical electroneutral Wigner–Seitz cell with radius D

We will distinguish between strongly and weakly ionizable PEs. In the former case, the fraction $\alpha \leq 1$ of "permanently" ionized monomers is quenched and determined by the chemical sequence in the arms. Environmental conditions, such as the pH and the local ionic strength, have a negligible effect on the charge of these quenched PEs. Partially sulfonated poly(styrene) (PSS) or partially quaternized poly(4-vinylpyridine) (PVP) are typical examples of a quenched polyanion and a polycation, respectively.

In the case of weakly ionizable PEs, the fraction of charged monomer units, α, is controlled by an ionization equilibrium and is affected by the local proton concentration and ionic strength. Weak polyacids such as poly(acrylic acid) (PAA) and poly(methacrylic acid) (PMAA), or polybases such as PVP and poly(dimethylaminoethyl methacrylate)(PDMAEMA) are typical examples of these pH-sensitive or "annealing" PEs.

Each monomer of a weak polyacid can be ionized via the dissociation of a hydrogen ion, H^+. The degree of dissociation of such acidic monomer, $\alpha(\mathbf{r})$, depends on the local concentration of hydrogen ions, $c_{\mathrm{H}^+}(\mathbf{r})$, via the mass action law:

$$\frac{\alpha(\mathbf{r})}{1-\alpha(\mathbf{r})} = \frac{K_{\mathrm{a}}}{c_{\mathrm{H}^+}(\mathbf{r})} \tag{5}$$

where K_a is the acidic ionization constant for an isolated monomer. For a polybase, the ionization occurs through the protonation of the monomers, and the generalization of the theory for this case is straightforward.

Remarkably, for branched PEs, which are characterized by a high intramolecular concentration of ionized monomers and, consequently, by a high intramolecular electrostatic potential, the value of the pH (here defined as minus the logarithm of the local proton concentration) in the intramolecular volume may differ significantly from that in the surrounding solution. Moreover, because of the connectivity of the charged monomers in the branches of the star, the local (excess) electrostatic potential created by neighboring monomers along a given arm is even larger than the average intramolecular one. The chemical connectivity of charges can be accounted for via an effective dissociation constant of a monomer, $K_a^{\text{eff}} \leq K_a$. However, in our subsequent discussion, we disregard these effects in the branches and only allow for radial gradients in the (average) intramolecular electrostatic potential, i.e., we will assume that $c_{H^+}(\mathbf{r}) = c_{H^+}(r)$ and $\alpha(\mathbf{r}) = \alpha(r)$.

3.1 Box-Like Cell Model of a Polyelectrolyte Star

The box-like cell model of a PE star can be considered as a generalization of a classical mean-field Flory approach, which was first suggested to describe the swelling of a polymer chain in a good solvent [90]. The Flory approach estimates the equilibrium dimensions of a macromolecule, as a function of its parameters, by balancing the free energy of intramolecular (repulsive) interactions with the conformational entropy loss of a swollen chain. Within the box-like approximation, the star is characterized by the radius of its corona, R (end-to-end distance of the arms), or by the average intramolecular concentration of its monomers:

$$c = \frac{3}{4\pi}\frac{pN}{R^3} \tag{6}$$

where radial gradients in polymer density, degree of ionization of the arms, and distributions of small ions are disregarded.

The free energy of the star is:

$$F = F_{\text{conf}} + F_{\text{ev}} + F_{\text{Coulomb}} + F_{\text{ions}} \tag{7}$$

Provided that the arms remain stretched with respect to their Gaussian size, $R \geq aN^{1/2}$, the conformational free energy of p uniformly stretched Gaussian chains (arms) is:

$$F_{\text{conf}}/k_BT = p\frac{3R^2}{2Na^2} = p\frac{3}{2Na^2}\left(\frac{3Np}{4\pi c}\right)^{2/3} \tag{8}$$

The free energy of non-electrostatic interactions is, within the virial expansion, given by:

$$F_{\text{ev}}/k_BT = pN\left(\upsilon c + wc^2\right) \tag{9}$$

In the absence of charges, or at a low degree of ionization of the arms, the star conformation is controlled by a balance between two first terms in (7) (i.e., the short-range interarm repulsions and the conformational entropy of stretched arms). As a result, the star size is given by (4). That is, the power law dependencies, obtained on the basis of the blob model, are recovered. The physical reasons why there is a match of the star size as obtained by the scaling and in the mean field approximations are discussed in details in [23].

3.2 Polyelectrolyte Star Conformation in a Dilute Salt-Free Solution

The box-like model allows for a straightforward analysis of the counterion localization, which is essential for understanding the specific properties of salt-free solutions of branched PEs. In the case of a PE star, the first two terms in the free energy in (7) are complemented by a contribution due to Coulomb interactions between all the charges (charged monomers and mobile ions) in the cell, F_{Coulomb}, and by the translational entropy of all mobile ions, F_{ions}. Following the line of arguments of [27, 29], we first focus on the case when no salt is added, and the cell contains only mobile (monovalent) counterions, which compensate the net charge of the star polyion. We assume that $Q^* \leq Q$ counterions are localized in the outer volume of the cell, $R \leq r \leq D$, whereas the remaining $(Q - Q^*)$ counterions are retained inside the star volume $(0 \leq r \leq R)$. In the framework of the box-like model, the counterion concentration is assumed to have constant (but different) values inside and outside the star: $c_{\text{ions}}^{(\text{in})} = 3(Q - Q^*)/4\pi R^3$ and $c_{\text{ions}}^{(\text{out})} = 3Q^*/4\pi(D^3 - R^3)$, respectively. The entropic term in the free energy is, therefore, given by:

$$F_{\text{ions}}/k_{\text{B}}T = (Q - Q^*)\ln c_{\text{ions}}^{(\text{in})} + Q^* \ln c_{\text{ions}}^{(\text{out})} \tag{10}$$

and the Coulomb interaction term is given by:

$$F_{\text{Coulomb}}/k_{\text{B}}T = l_{\text{B}}\frac{Q^*}{R}\vartheta(R/D) \tag{11}$$

where $l_{\text{B}} = e^2/\epsilon k_{\text{B}}T$ is the Bjerrum length and $\vartheta(x)$ is a rational function of x, whose form is specified in [27, 29]. At the limit, when the cell size far exceeds the star size, $x = R/D \to 0$, $\vartheta(x) \to 3/5$. The minimization of the free energy, (7), (8), (9), (10), and (11), results in equilibrium values of the star size, R, and that of the uncompensated charge, Q^*. The latter is of special interest and can be found from the equation:

$$Q^* = \frac{R}{l_{\text{B}}}\frac{1}{2\vartheta(R/D)}\ln\left[\left(\frac{Q}{Q^*} - 1\right)\left(\frac{D^3}{R^3} - 1\right)\right] \tag{12}$$

It follows from the analysis of (12) that, in the limit of dilute solutions $D \gg R$, the distribution of counterions is governed by the parameter $l_B Q/R$, which is proportional to the dimensionless excess electrostatic potential (in units $k_B T/e$) created by the bare charge, $Q^* \approx Q$ of the star. When $Q l_B/R \ll 1$, the Coulomb attraction of counterions to the star polyion is weak compared to the thermal energy $k_B T$, and the counterions are distributed fairly uniformly in the solution. The uniform distribution optimizes the translational entropy for the ions. As a result, in the limit of dilute solutions, $D \gg R$, the fraction of counterions found in the intramolecular volume of the star is negligible, $Q^* \approx Q$, and the charged monomers in the branches interact via unscreened Coulomb repulsion. Balancing the Coulomb energy, (11), with the conformational penalty for the extension of the branches, (8), and neglecting the contributions due to non-electrostatic monomer–monomer interactions, (9), one obtains:

$$R \cong aN(\alpha^2 l_B/a)^{1/3} p^{1/3} \tag{13}$$

According to (13), the arms of the star are stretched proportionally to their degree of polymerization N, similarly to linear PEs in a dilute salt-free solution [91, 92]. The additional factor, $p^{1/3} \geq 1$, reflects the interarm Coulomb repulsion. A comparison to (4) shows that long-ranged interbranch Coulomb repulsion has a much stronger effect on the size of a PE star than the short-range interbranch repulsion that is found in a neutral star.

As follows from (13), the ratio $Q l_B/R$ increases upon an increase in the number of arms p, because the star size $R \sim p^{1/3}$ grows less fast than the bare charge $Q \sim p$. The excess electrostatic potential becomes on the order of $k_B T/e$ at $p \cong \alpha^{-1/2}(l_B/a)^{-1}$. Increasing the number of arms above this value causes the excess electrostatic potential to become sufficiently strong that it will retain the majority of counterions within the intramolecular volume. Indeed, as follows from (12), when $Q l_B/R \gg 1$, the number of counterions released from the intrastar volume (and, correspondingly, the uncompensated charge Q^* of the star), scales as $Q^* \cong R/l_B$, and increases only logarithmically with Q. When $Q \gg Q^* \cong R/l_B$, one can neglect F_{Coulomb} and the second term in (10), and find the size of the star by balancing the translational entropy of $Q - Q^* \approx Q$ counterions, which are confined inside the intrastar volume, with the conformational entropy of the stretched arms. This leads to the expression:

$$R \cong aN\alpha^{1/2} \tag{14}$$

which can also be interpreted as a result of balancing the osmotic pressure of the confined counterions with the elastic (entropic) force that arises from stretching the arms. A striking feature of (14) is the absence of a power law dependence of the star size R on the number of arms p. In the limit of dilute solutions, $D \gg R$, an equation for the star size, which interpolates between the $Q l_B/R \ll 1$ and $Q l_B/R \gg 1$ limits (i.e., takes into account the contributions of both the Coulomb repulsions and the osmotic pressure of counterions), is given by:

$$R \cong a(N/p)^{1/3}[Q^{*2} l_B/5a + R(Q - Q^*)a^{-1}]^{1/3} \tag{15}$$

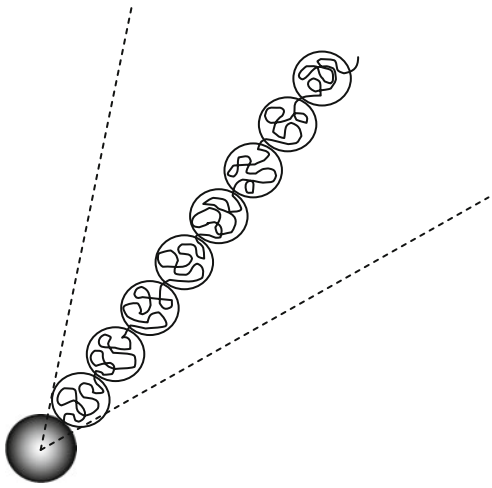

Fig. 3 Blob model of a PE star in salt-free solution

Remarkably, in a salt-free solution of the PE stars, the star size is found to be proportional to N, i.e., $R \sim N$, for both considered regimes. As a result, each arm can be envisioned as a string of elastic blobs of constant (independent of r) size [27], $\xi_{\text{elastic}} \cong a(\alpha^2 l_B/a)^{-1/3}$ and $\xi_{\text{elastic}} \cong a\alpha^{-1/2}$, in the regimes of unconfined and confined counterions, respectively. Hence, in contrast to the blob picture of a neutral star, the blobs in a PE star are not close-packed in a salt-free solution (see Fig. 3 for a schematic drawing).

3.3 Charge Renormalization Concept

The idea of counterion confinement (charge renormalization), is of central importance in understanding the properties of salt-free solutions of branched PEs. The concept was first formulated for a dilute salt-free solution of spherical charged colloidal particles by Alexander et al. [36]. It is illustrative to repeat the arguments briefly. Let us consider a dilute salt-free solution of charged colloidal particles with radius R_c and (positive) charge eQ. Counterions are distributed non-uniformly in the solution, with the highest concentration near the surface of the particles. If one applies a cell model, in which each particle is placed at the center of a regular Wigner–Seitz cell (approximated as a sphere), the osmotic pressure in the solution is determined by the counterion concentration at the cell boundary. The distribution of the electrostatic potential and that of the counterions within the cell (in the range $R_c \leq r \leq D$, where r is the radial distance from the center of the particle and D is the cell radius), are determined by the PB equation:

$$\frac{1}{r}\frac{\partial^2 r\psi(r)}{\partial r^2} = 4\pi l_B n_0 \exp(\psi(r)) \tag{16}$$

where $n(r) = n_0 \exp(\psi(r))$ is the local number density of (negatively charged) counterions, $\psi(r) \equiv e\Psi(r)/k_B T$ is the dimensionless electrostatic potential, and n_0 is a constant that depends on the calibration of the electrostatic potential. If we set $\psi(D) = 0$, then n_0 is the concentration of counterions at the cell edge, $r = D$. Equation (16) has to be complemented by two boundary conditions:

$$\left(\frac{\partial \psi(r)}{\partial r}\right)_D = 0 \qquad \left(\frac{\partial \psi(r)}{\partial r}\right)_{R_c} = -\frac{l_B Q}{R_c^2} \tag{17}$$

where the former reflects the electroneutrality of the cell as a whole.

If the value of the electrostatic potential at the particle surface is low, $\psi(R_c) \approx l_B Q/R_c \ll 1$, the electrostatic potential at $r \geq R_c$ is even lower and the linearized form of the PB equation, often referred to as the Debye Hückel (DH) approximation:

$$\frac{1}{r}\frac{\partial^2 r\psi(r)}{\partial r^2} = \kappa^2(1 + \psi(r)) \tag{18}$$

can be safely applied in the whole cell volume, $R_c \leq r \leq D$. Equation (18), together with the boundary conditions (17), correctly describe the electrostatic potential $\psi(r)$ and the number density of counterions $n(r) = \frac{\kappa^2(1+\psi(r))}{4\pi l_B}$ in the whole cell. Here $\kappa^2 = 4\pi l_B n(D)$ and the value of κ has to be found from the boundary conditions (and the calibration of the potential, $\psi(D) = 0$), together with the solution of (18). In the dilute regime, $D \gg R_c$, one finds that $\kappa^2 \approx 2l_B Q/D^3$. The counterion concentration at $r = D$, which determines the osmotic pressure in the solution, equals $n(D) = \kappa^2/4\pi l_B$. Hence, $n(D) \approx Q/2\pi D^3$, and the counterions are distributed fairly uniformly throughout the cell (the concentration of counterions near the edge of the cell is close to the average concentration). This is what one also expects from the Boltzmann law, $n(r) = n(D)\exp(\psi(r))$, with a low value of the reduced potential ($\psi(r) \leq 1$) throughout the cell.

If the particle is strongly charged, so that it creates a large surface potential $\psi(R_c) = l_B Q/R_c \gg 1$, the DH approximation cannot be used in the proximity of the surface. However, the DH approximation can still be safely applied far away from the particle surface (close to the cell boundary $r = D$, where the potential is reduced to values $\psi(r) \leq 1$). At this point, we come to the concept of charge renormalization: when $l_B Q/R_c \gg 1$ and the electrostatic potential at the surface of the charged particle is high, $\psi(R_c) \gg 1$, a certain number of counterions become localized ("condensed") in the vicinity of the surface and this reduces the apparent surface potential down to a level $\psi \sim 1$. The last condition determines the number of uncondensed (osmotically active) counterions as $Q^* \sim R_c/l_B$. In the range $r \gg R_c$, where the potential is sufficiently reduced, one can again apply the DH approximation and describe the radial distribution of uncondensed counterions using the DH equation presented above, wherein the actual charge of the particle Q is replaced by a renormalized charge $Q^* \sim R_c/l_B$. Similarly to the case for weakly charged particles, the osmotically active counterions are distributed fairly uniformly in the range $R_c \ll r \leq D$, so that their concentration at $r = D$ and the osmotic pressure

coincide (with the accuracy of a numerical factor on the order of unity) with their average concentration in the cell $\sim Q^*/D^3$. We note that, even though one can never unambiguously distinguish between condensed and uncondensed counterions, the value of Q^* has a clear physical meaning (as it appears in the DH solution), which properly matches the exact (PB) distribution of the potential (and of the counterion density) in the peripheral and intermediate regions of the cell.

In contrast to a solid charged colloid, a branched polyion can accommodate a large number of counterions in its interior volume. The analogy between the charge renormalization in a solution of hard-core colloids and the counterion localization in a star-like PE or a colloidal PE brush was first pointed out by Pincus [26]. Because counterions retain translational degrees of freedom in the intramolecular volume of a polyion, they exert an osmotic pressure to the volume of the corona. Hence, the polyion swells due to the "entrapped" counterions. The uncompensated charge within the star corona with radius R equals the number of released (osmotically active) counterions and is given by $Q^* \sim R/l_B$. The electrostatic potential drops to a value $\psi(R) \cong 1$ at the edge of the corona, and the distribution of counterions in the exterior space, $R \leq r \leq D$, is fairly uniform.

3.4 *Effects of Concentration and Interactions in Star Polyelectrolyte Solutions*

The cell model enables one to describe the effects of polymer concentration, which manifest themselves in a salt-free solution of PEs, even in the dilute regime. Here, the solution is modeled as an array of spherical Wigner–Seitz cells, each comprising one branched polyion with its counterions. The radius D of each cell equals half the average distance between polyions in the solution. As has been demonstrated in [29], PE stars exhibit a pronounced contraction upon an increase in polymer concentration (a decrease in D) in dilute solutions, $D \geq R$. This effect is caused by the progressive re-partitioning of counterions from the inter- to the intramolecular space. An increase in polymer concentration makes the counterion distribution more uniform, leading thereby to a decrease in the uncompensated charge of the star Q^* and a corresponding decrease of the electrostatic potential ψ at the edge of the star.

A decrease in the size, R, of a PE star as a function of polymer concentration is most pronounced for polyions with a relatively small number of branches p. As discussed above, in this case the counterions are distributed most uniformly between intra- and intermolecular space. Therefore, an increase in the average concentration of counterions in the solution leads to a proportional increase in their concentration in the intramolecular volume of these branched polyions. In contrast to this, stars that have many arms have a modest response to an increase in the PE concentration. This is because at any (arbitrarily small) solution concentration, only a small fraction of the counterions is found in the intermolecular space. This behavior of PE stars should be contrasted with that of neutral star polymers. In the latter case, screening of the intramolecular excluded-volume repulsion, and the contraction of

star-branched polymers upon the increase in star concentration, occurs only in the semidilute regime, i.e., when the average polymer concentration in the solution exceeds the intramolecular concentration in an isolated star [24].

The repulsive forces acting between the PE stars in salt-free solutions are of long-range character. Analogous to the crystalline ordering of charged colloids [36], PE stars might organize in a three-dimensional periodic lattice. This long-ranged ordering is governed by the Coulomb repulsion between star polyions. The magnitude of this repulsion is controlled by the effective (uncompensated) charge Q^* of the star. The formation of a periodic supramolecular structure is only expected in a certain range of PE concentrations. The lower concentration limit is specified by the condition that the energy of Coulomb repulsion between neighboring polyions becomes on the order of k_BT. An upper concentration limit arises due to the enhanced screening of interstar Coulomb repulsion upon an increase in the solution concentration [27].

Probing forces between PE stars in a solution is a challenging experimental problem. However, advances in the technique of optical tweezers now allow direct measurement of repulsive forces between brushes of DNA [94, 95] and synthetic PE chains [96, 97] grafted onto colloidal particles of submicrometer size.

The MD simulation study of the interaction between PE stars in a salt-free solution has been performed in [39]. The simulation results were fitted using a simplified analytical equation for repulsive force, which arises due to the decrease in translational entropy of counterions entrapped in overlapping star coronae. In this model, the repulsion starts at distances between star centers smaller than $2R$, where R is the unperturbed size of an individual star. A similar approach has been applied in [40] to describe repulsion between colloidal PE brushes.

The repulsive force between colloidal PE brushes in a salt-free solution can be calculated within the PB–Derjaguin approximation (Zhulina and Borisov, unpublished data) without pre-assumptions about the spatial distribution of counterions. This can be done on the basis of an exact solution of the PB problem for a planar PE brush in a salt-free solution [98]. Application of the Derjaguin approximation implies that size of the particle, $R_c + H$ (where H is the thickness of corona of colloidal PE brush) exceeds by far the characteristic thickness of ionic atmosphere. Then, the total force $\mathcal{F}$ acting between spherical PE brushes is given by:

$$\mathcal{F}(d) = 2\pi(R_c + d)\int_d^\infty \Pi(D)dD \tag{19}$$

Here, $2d$ is the smallest distance between the surfaces of spherical core particles, whereas $\Pi(D)$ is the disjoining pressure between two planar PE brushes (with the same grafting density, degree of ionization, and degree of polymerization of grafted PEs) at separation $2D$ between the grafting surfaces. Note that the latter expression is applicable in the range of interparticle separations $2d \ll 2(R_c + H)$. The disjoining pressure, $\Pi(D)$, as well as the brush thickness, $H(D)$, were calculated in [98].

Analysis shows that the force versus separation profile, calculated from (19), exhibits a different shape depending on the surface charge density due to grafted

polyions. If the surface of the particle is decorated by the "osmotic" PE brush, i.e., $H(d=\infty) \gg \Lambda$, where $\Lambda = s/2\pi l_B \alpha N$ and s is the grafting area per chain, then the majority of counterions are localized inside the brush and:

$$\frac{\mathcal{F}}{k_B T R} \approx \begin{cases} \pi^2/4 l_B d, & H(d=\infty) \ll d \ll R_c \\ (\Lambda l_B)^{-1} \ln\left[H(d=\infty)/d\right] , & d \ll H(d=\infty) \end{cases} \tag{20}$$

In the opposite case of a relatively sparse PE brush, $H(d=\infty) \ll \Lambda$, the thickness of ionic atmosphere is $\cong \Lambda$, and most of counterions are retained in the proximity of the particle outside the brush. Under these conditions, the force–distance profile is given by:

$$\frac{\mathcal{F}}{k_B T R} \approx \begin{cases} \pi^2/4 l_B d, & \Lambda \ll d \ll R_c \\ (\Lambda l_B)^{-1} \ln\left(\Lambda/d\right) , & d \ll \Lambda \end{cases} \tag{21}$$

Comparison of (20) and (21) shows that at large separations, the force $\mathcal{F}$ decays as $\sim 1/d$, irrespective of the charge density created on the particle surface by the PE brush. In the case of a sparse PE brush with fairly uniform distribution of counterions within the layer of thickness $\cong \Lambda$, the crossover to logarithmic force decay occurs smoothly at $d \cong \Lambda$. By contrast, in the case of the osmotic brush with strongly inhomogenous distribution of counterions (most of them trapped inside the brush), the repulsive force $\mathcal{F}$ sharply increases at $d \cong H(\infty)$, i.e., when the coronas of colloidal PE brushes approach close contact.

We emphasize that the Derjaguin approximation leads to a qualitatively different physical picture for interacting colloidal PE brushes compared to that in [40]. According to [40], the repulsion between spherical colloids decorated by PE brushes starts when the opposing brushes "touch" each other, i.e., at distance $2d = 2H$ between colloid surfaces, where $H = H(d=\infty)$ is the thickness of the unperturbed PE brush. According to the PB–Derjaguin approximation, the interaction between counterion atmospheres perturbs the chain conformations in PE brushes prior to their overlap. The grafted chains in the gap between core particles locally contract, and the PE brush becomes asymmetric upon the approach of colloids. That is, the brush thickness $H(d)$ is minimal at the smallest distance, $2d$, between surfaces of core particles, and gradually increases up to $H(d=\infty)$ outside the gap between colloids. In contrast to the model in [40], PE colloidal brushes remain separated by a layer of water, containing mobile ions, for a range of distances $2d < 2H(\infty)$, until the thermal fluctuations of terminal arm segments close the gap between PE brushes.

It is expected that a similar physical picture also holds for interacting PE stars. At distances between core domains $2d \geq 2R$, the star coronae would start to contract due to the overlap of ionic atmospheres. As a result, the stars would become asymmetric and remain separated by a water layer in a range of distances $2d < 2R$. The long-range interactions due to the overlap of ionic atmospheres are essential for PE stars with a moderate number of arms (typical for experimental systems), and at low ionic strength in the solution [27].

4 Localization of Counterions in Salt-Free Solutions of Branched Polyelectrolytes: Effect of the Polyion Topology

The localization of counterions in the intramolecular volume is a common feature manifested in dilute salt-free solutions of branched polyions of different topologies, including dendritic (star-burst), randomly (hyper)branched PEs, PE molecular brushes, etc. The physical reason for this phenomena is the same as outlined for PE stars: a strongly charged, branched, macroion creates a high electrostatic potential, which attracts counterions and retains them in the intramolecular volume, in spite of a significant loss in the translational entropy. The effect is most pronounced in a dilute solution, where the concentration of counterions in the bulk is extremely low.

Remarkably, linear PEs of arbitrary large N cannot induce a similar effect. This is because both the charge, αNe, and the size, $R \cong aN(\alpha^2 l_B/a)^{1/3}$, of a stretched polyion in a dilute salt-free solution, scale proportionally to N [91, 92], so that their ratio remains $\sim \alpha^{1/3} \leq 1$. Note that we do not discuss here the effect of Manning condensation, which occurs when the distance between two neighboring charges along the chain is smaller than l_B. A detailed discussion of this case can be found in [93].

A theoretical analysis of the effect of counterion localization in a dilute solution of weakly charged branched polyions of different topologies [31–33] and ionic microgels [34, 35], was performed on the basis of a cell model, similar to that used here for a star-like PE. The elastic term in the free energy that accounts for the conformational entropy of a uniformly swollen branched macromolecule, has to be specified depending on the polyion topology. The shape of the cell might also be modified. For example, in the case of a molecular PE brush, a cylindrical instead of spherical cell should be used.

Similarly to the case of a quenched star-like PE, two regimes of ion distribution were distinguished. A fairly uniform distribution of "free" counterions is found at low degree of branching, whereas a strong localization of counterions in the intramolecular volume is expected for a high degree of branching of the polyion. In the latter case only a minor fraction of the counterions is released to the exterior volume of the cell.

We recall that for a star-like PE, the transition from the regime of a barely charged polyion, to the osmotic regime, occurs at a characteristic number of branches, $p \cong \alpha^{-1/2}(l_B/a)^{-1}$. The latter depends on the combination of the parameters $\alpha(l_B/a)^2$, and is independent of the length N of an arm. Below we briefly summarize the results obtained for branched polyions of different topologies.

4.1 Ionic Dendrimers (Star-Burst Polyelectrolytes)

The conformations of charged (regular) star-burst polymers (flexible ionic dendrimers), were analyzed theoretically in [33]. Referring to Fig. 4a, relevant architectural parameters for a star-burst polymer are the number of generations,

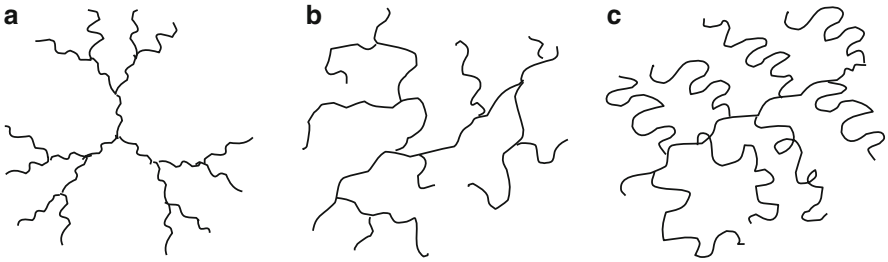

Fig. 4 Branched polyions of different topologies: star-burst (**a**), randomly branched or hyper-branched (**b**), molecular brush (**c**)

g, and the length of a spacer, n. If each branching point has a functionality 2, then the total degree of polymerization is $N = 3n(2^g - 1)$, where $g = 1, 2, \ldots$. In a uniformly swollen dendrimer, all the spacers are extended in the radial direction. The conformational free energy of a dendrimer, with a distance R between the center of the molecule and the ends of the last generation spacers, is given by [33]:

$$F_{\text{conf}}/k_{\text{B}}T \cong \frac{2R^2(g)}{na^2}\left(1 - \frac{4}{3}g^{-2}\right)^{-1} \tag{22}$$

where a force balance condition was used in each branching point. Substituting this equation into the free energy of the cell model, (7), leads to the following expression for the size of ionic dendrimer:

$$R_{\text{dendr}} \cong \begin{cases} aN^{2/3}(\alpha^2 l_{\text{B}}/a)^{1/3}n^{1/3}, & N/n \ll (\alpha(l_{\text{B}}/a)^2)^{-1} \\ aN^{1/2}\alpha^{1/2}n^{1/2}, & N/n \gg (\alpha(l_{\text{B}}/a)^2)^{-1} \end{cases} \tag{23}$$

Hence, counterion localization occurs when the number of generations in the star-burst polymer, $g \approx \log_2(N/n)$, reaches some characteristic value, which is controlled by the same combination of the parameters, $\alpha^{-1}(l_{\text{B}}/a)^{-2}$, as for a PE star. Note that this combination is independent of the spacer length, n.

4.2 Randomly Branched Polyelectrolytes and Charged Fractals

A randomly branched PE was modeled in [31, 32], as a branched tree (without loops) formed by N bi- and trifunctional monomers, cf. Fig. 4b. The average number of trifunctional monomers (branching points) is $\sim N/n$, so that the average number of monomers in a spacer, connecting two neighboring branching points, is n. The condition of $N/n \gg 1$ corresponds to the limit of strong branching, whereas at low branching probability, $N/n \cong 1$, the linear chain behavior is recovered. Here we insist that the average spacer contains a large number of monomers, $n \gg 1$. The opposite limit of $n \cong 1$ corresponds to a hyper-branched polymer. The conformational

entropy losses due to the uniform swelling of a randomly branched polymer, up to the size R, can be accounted for as [99, 100]:

$$F_{\text{conf}}/k_{\text{B}}T \cong \frac{R^2}{(Nn)^{1/2}a^2} \tag{24}$$

where $R_{\text{ideal}} \cong a(Nn)^{1/4}$ is the unperturbed, Gaussian, size of an ideal, randomly branched polymer [101]. Balancing the entropic elastic force with the intramolecular Coulomb repulsions and/or the osmotic pressure of counterions leads to:

$$R_{\text{random}} \cong \begin{cases} aN^{5/6}(\alpha^2 l_{\text{B}}/a)^{1/3}n^{1/6}, & N/n \ll (\alpha(l_{\text{B}}/a)^2)^{-2} \\ aN^{3/4}\alpha^{1/2}n^{1/4}, & N/n \gg (\alpha(l_{\text{B}}/a)^2)^{-2} \end{cases} \tag{25}$$

An interesting feature of (25) is the fractal dimension, specifying how the mass $\sim N$ of a randomly branched PE depends on its size R. For small clusters that release many counterions into the bulk solution, $d_{\text{f}} = 6/5$, whereas for large (osmotic) clusters, $d_{\text{f}} = 4/3$. Again, the counterion localization threshold is set by the increase in the electrostatic potential, $\cong l_{\text{B}}Q/R$ which grows upon an increase in N as $\sim N^{1/6}$ in the regime of free counterions (small clusters). Another remarkable feature of (25) is, that the counterion condensation threshold occurs when the number of branching points N/n reaches the characteristic value $\cong \alpha^{-2}(l_{\text{B}}/a)^{-4}$, which again is independent of the spacer length n.

These results have been generalized further in [31], for charged polymeric fractals with arbitrary connectivity characterized by spectral dimension, d_{s}, (the latter relates the longest path in the fractal, $R_{\max} \cong aN^{1/d_{\text{s}}}$, to its mass $\sim N$) and arbitrary fractal dimension d_{f} (in the absence of ionic charges) in d-dimensional space. For ideal (Gaussian) fractals $d_{\text{f}} = 2d_{\text{s}}/(2-d_{\text{s}})$. For charged fractals:

$$R_{\text{fractal}} \cong \begin{cases} aN^{\frac{2d_{\text{f}}-d_{\text{s}}}{d_{\text{s}}d_{\text{f}}+(d-2)(d_{\text{f}}-d_{\text{s}})}}(\alpha^2 l_{\text{B}}/a)^{\frac{d_{\text{f}}-d_{\text{s}}}{d_{\text{s}}d_{\text{f}}+(d-2)(d_{\text{f}}-d_{\text{s}})}}, & N \ll N^* \\ aN^{1/d_{\text{s}}}\alpha^{\frac{d_{\text{f}}-d_{\text{s}}}{d_{\text{s}}d_{\text{f}}}}, & N \gg N^* \end{cases} \tag{26}$$

Here, the threshold value for the number of monomers, corresponding to the onset of charge renormalization, is specified as:

$$N^* \cong \alpha^{\frac{d_{\text{s}}d_{\text{f}}-(d-2)(d_{\text{f}}-d_{\text{s}})}{d_{\text{f}}(d-2-d_{\text{s}})}}(l_{\text{B}}/a)^{\frac{d_{\text{s}}}{(d-2-d_{\text{s}})}} \tag{27}$$

As follows from (26) charge renormalization effects occur only when $d < d_{\text{s}} + 2$.

4.3 Polyelectrolyte Cylindrical (Molecular) Brushes

Molecular brushes are polymers composed of a long main chain (backbone), onto which side chains (grafts) are attached at regular intervals. See Fig. 4c for a graphic illustration. The graft-copolymers are classified as molecular brushes, provided the

number of monomer units in a graft, n, exceeds that in a spacer (the segment of the backbone between two neighboring grafts), m. A steric or electrostatic repulsion between the grafts (referred to as crowding), leads to their extension in the radial direction. The crowding of grafts induces an axial tension in the backbone, which, in turn, also gets stretched. Locally, the molecular brush acquires a cylindrical symmetry on a length scale that is characterized by an apparent (or induced) persistence length [102–107]. The latter is comparable to, or exceeds, the brush thickness, which is controlled by the radial extension of the side chains, R.

The box-like model considers a molecular PE brush with the backbone extended along the axis of an (infinitely long) cylindrical cell of radius D, wherein the end segments of the grafts are localized at a distance $R \ll D$ from the axis of the cell. The cell contains counterions who compensate the net charge of the brush. This model enables one to analyze the local conformational properties and the distribution of the counterions in a dilute salt-free solution of molecular PE brushes. The Coulomb interactions (calculated per graft) can be presented as:

$$F_{\text{Coulomb}}/k_{\text{B}}T = -l_{\text{B}}q^{*}\ln(R/a)\varphi(R/D) \tag{28}$$

where q^{*} is the number of counterions, per unit length along the cell axis, that is released from the brush, and $\varphi(x)$ is a rational function of x. The conformational free energy (per graft) includes the contributions from both a spacer, extended up to length h, and a graft, extended up to length R:

$$F_{\text{conf}}/k_{\text{B}}T = \frac{3}{2a^{2}}\left(\frac{R^{2}}{n}+\frac{h^{2}}{m}\right) \tag{29}$$

The Gaussian elasticity of the grafts and spacers could be modified to account for the local swelling effects [102]. Finally, the translational entropy of the counterions is accounted for as:

$$F_{\text{ions}}/k_{\text{B}}T = h(q-q^{*})\ln c_{\text{ions}}^{(\text{in})} + hq^{*}\ln c_{\text{ions}}^{(\text{out})} \tag{30}$$

where $q \approx \alpha n/h$. The minimization of this free energy with respect to R, h and q^{*}, provides the thickness of a molecular PE brush:

$$R \cong \begin{cases} an^{7/6}(\alpha^{2}l_{\text{B}}/a)^{1/3}m^{-1/6}, & n/m \ll (\alpha(l_{\text{B}}/a)^{2})^{-1} \\ an\alpha^{1/2}, & n/m \gg (\alpha(l_{\text{B}}/a)^{2})^{-1} \end{cases} \tag{31}$$

The characteristic branching parameter (grafting density), $n/m \cong \alpha^{-1}(l_{\text{B}}/a)^{-2}$, specifies the onset of counterion localization inside the molecular brush. Note that in the osmotic regime, the spacers get fully extended, $h \sim m$. It is therefore not surprising, that the counterion localization in a cylindrical molecular brush coincides (in scaling terms) with the Manning condensation threshold [25] for a charged cylinder, $ql_{\text{B}} \cong 1$.

Molecular brushes composed of biopolymers, are typically more complex than their synthetic analogs. They may comprise different types of biomacromolecules, and involve self-assembly mechanisms. For example, in aggrecanes [108] and

mucins [109], polysaccharide side chains are densely grafted ($m \cong 1$) to an unfolded core protein with intergraft distance $h \cong am$. In cylindrical assemblies of neuronal proteins (neurofilaments, or NFs), a rigid core comprises numerous coiled-coil domains of constituent proteins. The flexible side arms of three different lengths (referred to as projections) emanate from the core at a distance $h = 2 - 3$ nm between the grafts, and form a corona with thickness $R \simeq 40$ nm [110]. The large persistence length $\simeq 450$ nm [110] insures local cylindrical symmetry and the nematic ordering of NFs in hydrogels [111, 112]. Variations in the environmental conditions (pH, solution salinity, etc.) affect the conformations of protein projections, but do not change intergraft distance h. The brushes (coronae) of heavily charged ($\alpha \simeq 0.1 - 0.2$) projections prevent close approach of neurofilaments, presumably due to the electrostatic repulsions between the grafts [113].

Box-like model highlights generic PE features of a neurofilament brush [114]. It specifies the onset of osmotic regime, and rationalizes the increase in brush thickness, R, upon progressive protein phosphorylation (an increase in α). An advanced SF-SCF numerical modeling highlights the respective roles of different NF proteins in coronal organization and the conformational re-arrangements triggered by the phosphorylation [115–119]. It demonstrates an approximately parabolic profile for the electrostatic potential $\psi(r)$ in the NF brush proximal region, occupied by the shortest projections. A parabolic shape of $\psi(r)$ was theoretically predicted for a planar PE brush [98], and is also found to be a reasonable approximation for a cylindrical PE brush [114].

5 Localization of Counterions in a Salt-Free Solution of Polyelectrolyte Stars: Numerical Results

Theoretical predictions concerning the localization of counterions in salt-free solutions of star-branched PEs have provoked a number of studies on this effect using different numerical simulation techniques. Although MD [40–42] and MC [38] simulations have given a qualitative proof of a clearly inhomogeneous distribution of the counterions (whose concentration differs between the interior and exterior of the star), the numerical SCF modeling has allowed a more systematic and quantitative study of the effect of macroion branching on the degree of counterion localization. The latter technique was used to explore the transition from the charged star regime to the osmotic regime, and to quantify the fraction of released (osmotically active) counterions as a function of number of branches in a star polymer.

5.1 Molecular Dynamics and Monte Carlo Simulations

MC [38] and MD simulations [39–42] provided an unambiguous proof of the preferential localization of counterions in the intramolecular volume of a star polymer.

Furthermore, in the case of a sufficiently high linear charge density in the branches ($\alpha \cong 1$), the simulations indicated a strong correlation in the angular distribution of the counterions and the position of an arm. That is, a certain fraction of the counterions that are entrapped inside a star polymer have restricted translational freedom and can be envisioned as "condensed" on the branches. This effect is analogous to the classical Manning condensation of counterions on a strongly charged linear PE [25]. A typical snapshot of the PE star with its counterions is shown in a paper of Jusufi et al. (see figure 2b of [84]), wherein three possible states of the counterions can be visually distinguished: (a) condensed around the arms, (b) possessing translational freedom but localized in the intrastar volume, and (c) released into the solution.

Mean field theories that implement a spherically symmetric distributions of counterions assume that the (effective) charge density on the star branches is below the Manning condensation threshold. In this limit, one can neglect the angular correlations between the positions of the arms of the star and those of its counterions.

5.2 Self-Consistent Field Poisson–Boltzmann Theory

A quantitative analysis of counterion localization in a salt-free solution of star-like PEs is described in [29, 37]. Radial distributions for both the electrostatic potential and the density of counterions were obtained by a numerical solution of the corresponding PB problem within a cell model. The conformational degrees of freedom of the branches of a central star were accounted for within the SF-SCF method [120]. Due to the computational efficiency, the SF-SCF framework allows for a systematic study of a many-armed star with sufficiently long arms in a large cell. The range of the parameters that could be covered by the SF-SCF method exceeds that of contemporary MD and MC simulations.

The PB equation was solved at low concentrations of 1:1 electrolyte using the discretization scheme in a spherical coordinate system with a PE star in the center. The characteristic length of a lattice site is set equal to the monomer length, which is fixed to $a = 0.5\,\text{nm}$ (close to the Bjerrum length $l_B \approx 0.7\,\text{nm}$ in water). The corresponding conversion factor for the volume fraction of salt, φ_s, to the corresponding molar concentration obeys $c_s \approx 12.9\varphi_s\,\text{M}$. All lengths are normalized with the length a of a lattice site. The default value of $N = 200$ was taken for the arm length. The number of arms per star p was varied in the range 20–50. The first segment of each arm was restricted to be near the center of the coordinate system. PE stars with a fixed (quenched) fraction of charged monomers $0.2 \leq \alpha \leq 1.0$ were considered. Because the monomer size a is slightly smaller than l_B, the effect of Manning condensation becomes relevant for $\alpha \approx 1$. It can, however, be safely neglected at lower values of the fractional charge α. The outer radius of the cell D was taken as large enough to minimize finite cell size effects. All nearest-neighbor interactions, except for the excluded volume effects, were neglected (athermal solvent conditions). Further details of the SF-SCF method can be found in [37].

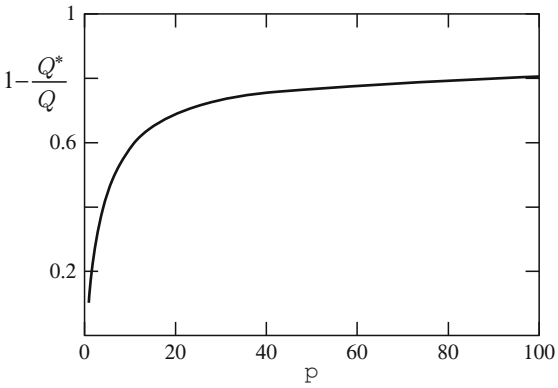

Fig. 5 Fraction of counterions localized inside the star (at $r < R$) as a function of the number of branches, p, under theta-solvent conditions; $N = 200$, $\alpha = 0.2$, $D = 150$, volume fraction of salt in the bulk solution $\varphi_s^b = 10^{-7}$; Q total bare charge of the star, Q^* uncompensated charge

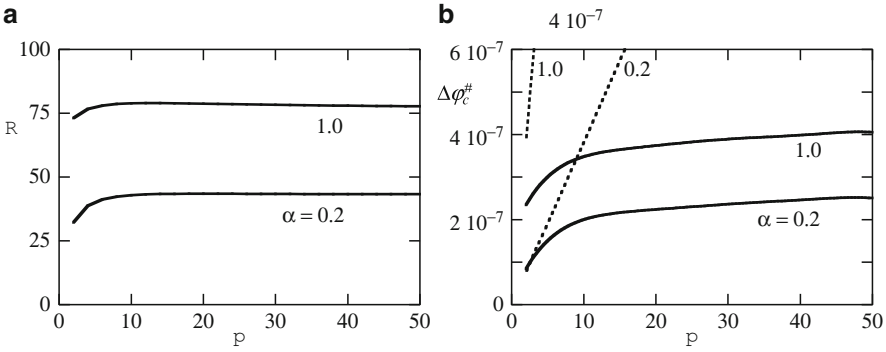

Fig. 6 (**a**) The first moment of the radial end-point distribution, R, as a function of the number of arms p in the PE stars; $N = 100$, $D = 500$, and α as indicated. (**b**) The corresponding excess density (volume fraction) of ions at the system boundary. The *dotted lines* are the expected results when all counterions of the PE star are distributed homogeneously in the system

In Fig. 5, the average fraction of counterions, $1 - Q^*/Q$, that are localized inside the star (i.e., at $r \leq R$, where the star size R is introduced as a first moment of the radial distribution of arm terminal segments) is presented as a function of the number of branches, p.

In Fig. 6, the star size R and the excess concentration of counterions at the outer cell boundary, $r = D$, are presented as a function of the number of arms, p, for different values of α (shown by solid lines). Dotted lines in Fig. 6b, indicate the corresponding expectations for uniform distribution of the cell counterions. An increase in the number of arms in each star implies an increase in the number of charged monomers $Q = p\alpha N$, and in the corresponding number of mobile counterions in the cell. Figures 6 and 7 clearly demonstrate a transition from a "barely charged" to an "osmotic" star behavior upon the increase in p. At a relatively small number of arms, the star size and the concentration of counterions at the outer cell boundary grow as a function of p. The latter is approximately proportional to p and is close to the average counterion concentration in the cell. This proves that ions

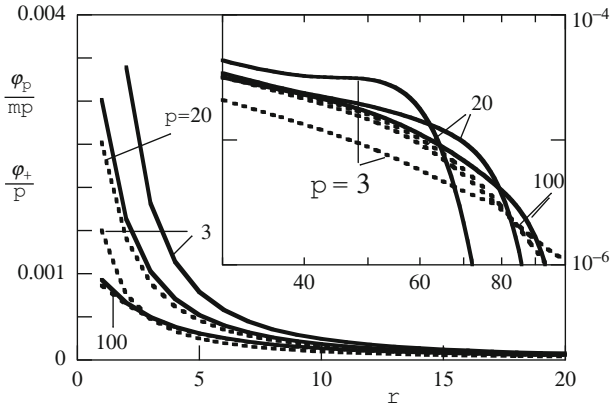

Fig. 7 Radial volume fraction profile, normalized per arm and by the distance between charges $m = \alpha^{-1}$, i.e., $\varphi_p(r)/pm$ (*solid lines*), and the radial counterion density profile, normalized by the number of arms, i.e. φ_+/p (*dotted lines*), for stars with different numbers of branches p as indicated, under theta-solvent conditions; $N = 200$, $\alpha = 0.2$, $D = 150$, $\varphi_s^b = 10^{-7}$. *Inset*: the same curves in log–log coordinates

are distributed fairly uniformly between interior and exterior volumes of a star with a small number of branches. By contrast, the size of a many-armed star becomes almost independent of p (in line with the expectation in the osmotic regime). Here, the concentration of osmotically active counterions grows weakly as a function of p, and is much smaller than the average concentration of counterions in the cell. (The latter grows proportionally to p, as shown by the dotted lines in Fig. 6b).

In Fig. 7, the radial density profiles of charged monomers and of counterions (normalized for one branch) are shown for stars with different numbers of arms, p (in a salt-free system). For small p, the distribution of counterions is fairly uniform, whereas that for the stars with a large number of arms both distributions almost coincide.

Based on the SF-SCF results, we may give a quantitative estimate for the characteristic number of branches at which a PE star enters the osmotic regime. As follows from Fig. 7, for the experimentally relevant range of $\alpha \leq 1$, this number is of the order of unity. That is, a star polymer with ~ 10 arms efficiently retains its counterions and is reliably found in the osmotic regime.

6 Localization of Counterions in a Salt-Free Solution of Star-Like Polyelectrolytes: Experimental Results

The effect of counterion confinement in star-branched polyions manifests itself most directly in osmotic pressure measurements. The osmotic pressure is a colligative property of the solution and is determined by the (number) density of mobile particles. In a dilute salt-free PE solution, the osmotic pressure is controlled by the number density of osmotically active counterions, because their number is much

larger than the number of polyions. The degree of confinement of counterions is quantified by the osmotic coefficient ϕ, which is the ratio of the measured osmotic pressure to the net average concentration of counterions in the solution.

As discussed in Sect. 3.3, the distribution of the counterions outside the corona of the PE star is fairly uniform. Therefore, the osmotic coefficient ϕ approximately equals the ratio Q^*/Q.

The osmotic coefficient ϕ has been measured both in solutions of strongly dissociating poly[2-(methacryloyloxy)ethyl]-trimethylammonium iodide (PMETAI) [48], and weakly dissociating PAA [43] star polymers.

Figure 8a presents the osmotic coefficients measured in solutions of PMETAI and PAA stars with 18 and 21 arms, respectively, as a function of the polymer

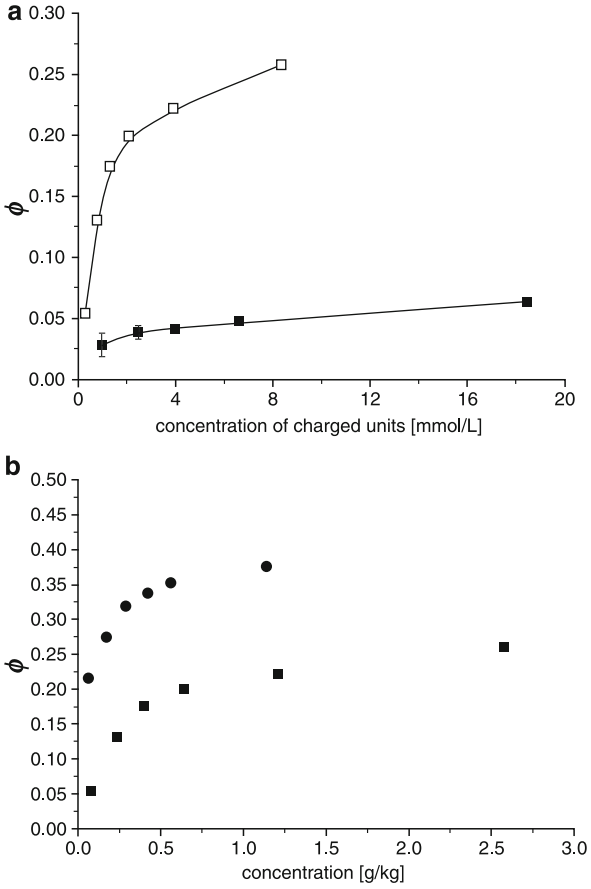

Fig. 8 Osmotic coefficients in solutions of (**a**) PMETAI stars with 18 arms, each comprising 170 monomer units (*closed squares*) and PAA stars with 21 arms, each comprising 100 monomer units, degree of neutralization $\alpha = 0.24$ (*open squares*), and (**b**) PAA stars with 8 (*circles*) and 21 (*squares*) arms, each arm comprises 100 monomer units, degree of neutralization $\alpha = 0.25$, as a function of polymer concentration

concentration. The experimental curves demonstrate a weak increase in the osmotic coefficient as a function of polymer concentration. However, in both cases, the osmotic coefficient is significantly lower than unity and its magnitude is close to that obtained in [37] on the basis of SF-SCF calculations. This unambiguously proves the reduced osmotic activity of counterions. This reduction can be rationalized by their confinement in the intramolecular volume.

Clearly, for pH-sensitive PAA stars, the osmotic coefficient depends on the degree of ionization α, which is controlled by the pH in the solution. Under these conditions, the lower charge of a PAA star as compared with that of a fully ionized ($\alpha \cong 1$) PMETAI star, leads to a lower degree of localization of counterions and, thereby, to a larger value of the osmotic coefficient ϕ.

In Fig. 8b, we show the osmotic coefficients for PAA stars that differ with respect to the numbers of arms at the given degree of neutralization. In accordance with theoretical predictions, the osmotic coefficient ϕ decreases (i.e., the degree of localization of counterions increases) upon an increase in the number of arms, p, in the star. Note that in the case of star polymers with relatively small number of arms, the osmotic coefficient is significantly larger (by two orders of magnitude) than that measured previously in the solutions of colloidal PE brushes [44, 45].

7 Effects of Ionic Strength and pH on the Polyelectrolyte Star Conformation

From the summary of the theoretical results presented above, it follows that the intramolecular volume of a star-branched PE, with a sufficiently large number of arms, is essentially electroneutral. That is, the bare charge of a star polymer is neutralized by mobile counterions. These counterions are predominantly retained inside the macroion volume, even if the star is immersed in a dilute salt-free solution. Moreover, if the "intrinsic" Debye length associated with the intramolecular concentration of entrapped counterions, $r_D^{(in)} \cong (l_B p \alpha N/R^3)^{-1/2}$, is used as an upper estimate for the intramolecular electrostatic screening length, one finds that in the osmotic PE star, $p \gg \alpha^{-1/2}(l_B/a)^{-1}$, the electrostatic interactions are screened at distances much smaller than the star size R.

Therefore, a detailed analysis of the conformations of many-armed star-like PEs may take place within the so-called local electroneutrality approximation (LEA). The latter also allows for an equilibrium of the ionization of the macroion, hence also covering the pH-responsive (annealing) star-like PEs.

As long as monovalent salt ions are added to the solution, the total ion concentration:

$$\Phi_{ion} \equiv \sum_j c_{bj} \tag{32}$$

determines the ionic strength, and the Debye screening length in the bulk of the solution is:

$$r_D = (4\pi l_B \Phi_{ion})^{-1/2} \tag{33}$$

(The summation in (32) is performed over all ion species, including H^+ and OH^- ions).

The effect of salt on the conformations of a many-arm (osmotic) PE star becomes important when the salt-controlled bulk Debye screening length, given by (33), becomes smaller than the intrinsic screening length, $r_D^{(in)}$, in a salt-free osmotic PE star. This is also true, equivalently, when the concentration of added salt exceeds the intramolecular concentration of counterions in the osmotic star. Clearly, the local electroneutrality in this case is ensured, and the LEA is applicable for analysis of the PE star conformations on a length scale larger than r_D.

The opposite limiting case of a PE star with a small number $p \ll \alpha^{-1/2}(l_B/a)^{-1}$ of arms in a salt-free solution was considered in [121]. In the latter case, the counterions can be disregarded and the Poisson equation allowed for an exact numerical solution for the polymer density profile, which confirmed the uniform stretching of the arms in the interior region of the star. The LEA may be applied for analysis of conformations of stars with a small number of arms in salt-added solution, provided the bulk Debye length r_D is smaller than the overall size of the star [28].

7.1 The Mean-Spherical Equal Arm Stretching Approximation: General Formalism

To analyze the effects of ionic strength and pH of the solution on the conformations of PE stars, we switch from the "canonical" cell model (where the number of ions was fixed) to the "partially open" ensemble. In the latter model, (a) one central star polymer occupies a spherical volume within radius R, and (b) the chemical potentials of all mobile ions are set equal to those in the bulk of the solution (infinite reservoir).

The concentrations c_{bj} (or, equivalently, the chemical potentials) of all the mobile ions are assumed to be constant in bulk solution. Therefore, the relevant free energy of the corona is the Gibbs free energy.

If all the star branches are assumed to be equally stretched (i.e., all the ends of the arms are localized at the edge of the star), the free energy of a star polymer can be presented as:

$$F = p\frac{3k_BT}{2a^2}\int_0^R \left(\frac{dr}{dn}\right) dr + 4\pi \int_0^R f_{int}\{c_p(r)\} r^2 dr \tag{34}$$

Here, the first term accounts for the conformational entropy losses in non-uniformly extended branches that exhibit the Gaussian elasticity [122], whereas the second term is the interaction contribution to the free energy. The local chain extension (dr/dn) at distance r from the center is related to the local concentration of monomers, $c_p(r)$, as:

$$c_p(r) = \frac{p}{4\pi r^2}\frac{dn}{dr} \tag{35}$$

Then, the free energy, (34), can be presented as:

$$F = 4\pi \int_0^R f\{c_p(r), r\} r^2 dr \tag{36}$$

where:

$$f\{c_p(r), r\} = \frac{3k_B T p^2}{32\pi^2 a^2 r^4 c_p(r)} + f_{int}\{c_p(r)\} \tag{37}$$

is the total density of the free energy in a star polymer.

The term $f_{int}\{c_p(r)\}$ accounts for the short-ranged (excluded volume) interactions between monomers $f_{ev}\{c_p(r)\}$ and for the ionic contribution $f_{ion}\{c_p(r)\}$:

$$f_{int}\{c_p(r)\} = f_{ev}\{c_p(r)\} + f_{ion}\{c_p(r)\} \tag{38}$$

where:

$$f_{ev}\{c_p(r)\}/k_B T = \upsilon c_p^2(r) + w c_p^3(r) + \ldots \tag{39}$$

The expressions for the ionic contribution to the free energy density, $f_{ion}\{c_p(r)\}$, are derived within the LEA in the Appendix, both for quenched and annealing PE coronas.

The polymer density profile, $c_p(r)$, and the radius of the star, R, are determined from the minimization of the free energy, (36), while taking the conservation of the number of monomer units, (2) into account as a constraint. This leads to:

$$\frac{\delta}{\delta c_p(r)} f\{c_p(r), r\} = \lambda \tag{40}$$

Here λ is a Lagrange multiplier that is coupled to the constraint that the total number of the monomer units, (2) is conserved. The constant λ coincides with the exchange chemical potential of the monomer, which is constant throughout the star. The equilibrium value of R is obtained by a minimization of the free energy with respect to R, which is equivalent to the condition that the differential osmotic pressure vanishes at the edge of the corona $r = R$:

$$\Delta\Pi(r = D) \equiv \left(c_p(r) \frac{\delta}{\delta c_p(r)} f\{c_p(r), r\} - f\{c_p(r), r\} \right)_{r=R} = 0 \tag{41}$$

In a simplified model, which generalizes the Daoud–Cotton approach [21], the condition of a local balance between the elastic tension in the extended branches and the excess osmotic pressure due to (repulsive) monomer–monomer interactions:

$$c_p(r) \frac{\delta}{\delta c_p(r)} f\{c_p(r), r\} - f\{c_p(r), r\} = 0 \tag{42}$$

is implemented at all distances r from the center of the polyion. This "quasi-planar" approach generalizes the blob model that was described in Sect. 2. Clearly, the normalization condition for the polymer density profile (2) also has to be satisfied.

When (42) is used in the derivation of the polymer density profile, the profile appears independent of the degree of polymerization N of the arms. The degree of polymerization N only determines the cut-off distance for the profile via the normalization condition, (2). This implies that the local conformations of the arms at any distance $r < R$ are independent of N. In particular, the elastic tension in the chains at any distance $r < R$ does not depend on the overall degree of polymerization of the chains.

Alternatively, implementing (40) and (41) leads to a quite different picture for the star structure. Here, the elastic tension in the arms is determined by the local monomer–monomer repulsion only at the edge of the corona, $r = R$. At $r < R$ the arms are stretched more strongly, due to an excess pulling force exerted by the terminal parts of the arms. Therefore, the polymer density profile $c_p(r,N,R)$ and the chemical potential $\lambda(N,R)$ depend explicitly on N (or the star size R) [123].

7.2 Density Profiles

Closed analytical expressions for the polymer density profiles $c_p(r)$ can be obtained only in certain limiting cases (asymptotic regimes), when the free energy density can be presented as a power law function of the polymer concentration, $f_{int}\{c_p(r)\} \sim c_p^{\gamma}(r)$. The density profiles have the simplest form when they are presented in reduced variables, r/R and $c_p(r)/c_p(R)$.

A simplified quasi-planar approach predicts a power law decay of the density profile for any value of γ and at any distance r:

$$c_p(r)/c_p(R) \approx (R/r)^{\frac{4}{\gamma+1}} \tag{43}$$

A more accurate theory predicts a different functional form for the density profile that depends on the value of γ. The polymer concentration, $c_p(r)$, can be approximated by a power law function only in the central region of the corona.

For a neutral star, $\gamma = 2$ or 3 in a good or a theta-solvent, respectively. The same exponent, $\gamma = 2$, is found for a PE star in a concentrated salt solution, see (60). The latter is not surprising, because at a high salt concentration, the electrostatic repulsion between charged monomers is partially screened and the monomer–monomer interactions are described via binary short-range repulsion.

By simultaneously solving (40) and (41), one gets for the polymer density profile:

$$c_p(r)/c_p(R) \approx \left(\frac{\gamma-1}{2\gamma}\right)^{\frac{1}{\gamma+1}} (R/r)^{\frac{4}{\gamma+1}} \tag{44}$$

Hence, the power law dependencies $c_p(r) \sim r^{-4/3}$ and $c_p(r) \sim r^{-1}$, derived above for neutral star polymers under good and theta-solvent conditions, are recovered, but the numerical prefactor is smaller than in quasi-planar model, (43).

In the case of a quenched PE star in a low salt solution (osmotic regime), $\gamma = 1$ and:

$$c_p(r)/c_p(R) \approx (R/r)^2 \{2\ln[c_p(r)/c_p(R)]\}^{-1/2} \tag{45}$$

We, therefore, find a logarithmic correction to the polymer density profile predicted earlier, $c_p(r) \sim r^{-2}$, which corresponds to a uniform radial stretching of the arms.

Finally, the density profile found for an annealing PE star in the low salt regime, $\gamma = 1/2$, is:

$$c_p(r)/c_p(R) \approx (R/r)^2/3^{1/2} \tag{46}$$

Here, the density profile decays as $c_p(r) \sim r^{-2}$, which corresponds to a uniform stretching of the arms in interior region of an annealing PE star. Note that this result differs from that obtained in a simplified quasi-planar model ($c_p(r) \sim r^{-8/3}$). The latter predicts an increase in the local stretching of the arms as a function of distance r from the star center. Remarkably, in spite of the difference in the polymer density distributions specified by the two models, the overall size R of the star macromolecule obeys the same power law dependence [123]. One can therefore use either of the two approaches, or even a box-like cell model, to get the power law dependencies for the star size R.

We emphasize that in both models discussed here, the free ends of the branches are fixed at the external boundary of the corona. Relaxation of this constraint is possible in the numerical SCF model of Scheutjens and Fleer. It is therefore instructive to compare the predictions of the analytical theory to the more accurate results obtained by means of the numerical SF-SCF computations.

In Figs. 9 and 10a, the polymer volume fraction profiles are presented in double logarithmic (log–log) coordinates for both quenched and annealing stars with

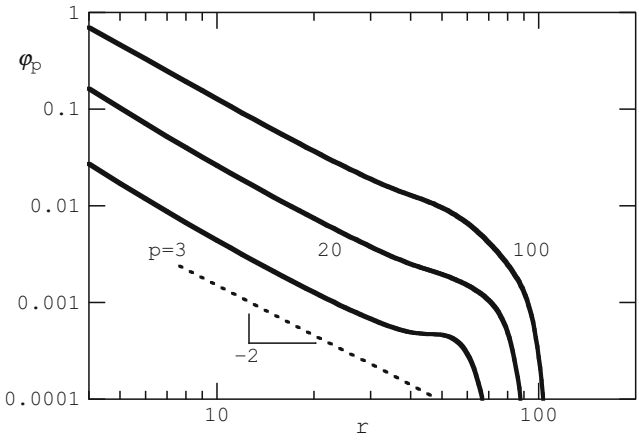

Fig. 9 Radial volume fraction profile $\varphi_p(r)$ (in log–log coordinates) for quenched PE stars with different numbers of branches p; theta-solvent conditions; $N = 200$, $\alpha = 0.2$, $D = 150$, $\varphi_s^b = 10^{-7}$. The *dotted line* indicates the slope -2, corresponding to a uniform extension of the branches

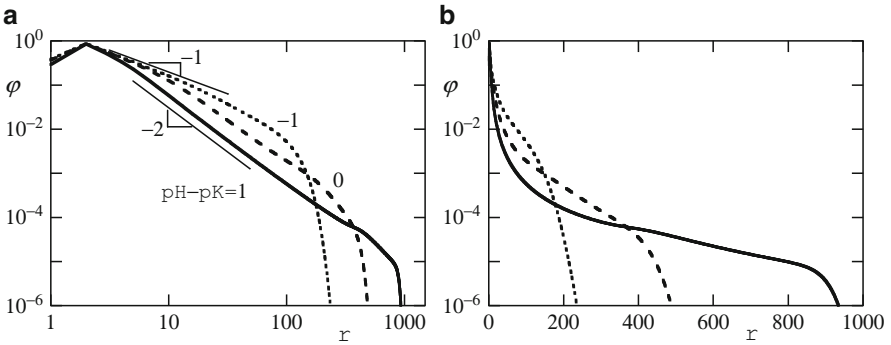

Fig. 10 Radial polymer volume fraction profiles $\varphi_{\mathrm{p}}(r)$ for three values of the difference between pH and pK_{a}: -1, 0 and 1 under theta-conditions; $N = 4000$ $p = 20$, $\varphi_{\mathrm{s}}^{b} = 10^{-7}$. (**a**) Double logarithmic (log–log) coordinates; the slopes -2 and -1 are indicated. (**b**) Semilogarithmic coordinates

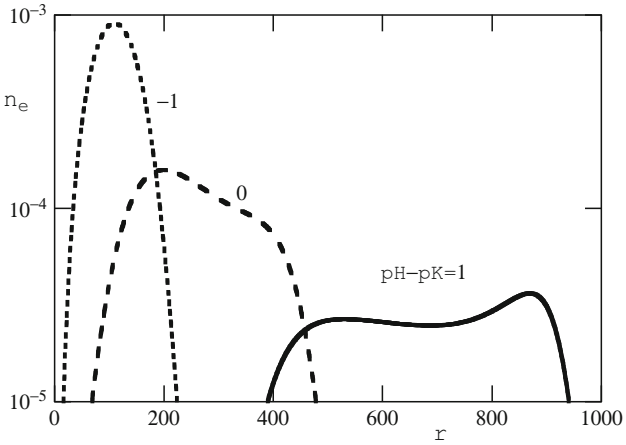

Fig. 11 Radial distribution of end segments $n_e(r)$ for three values of the difference between pH and pK_{a}: -1, 0 and 1 under theta-conditions; $N = 4000$ $p = 20$, $\varphi_{\mathrm{s}}^{b} = 10^{-7}$; semilogarithmic coordinates

different numbers of arms, p, respectively. A power law decay with slope -2 is clearly seen in central regions of both quenched and annealing PE stars. This corresponds to a uniform stretching of the arms. In Fig. 10b, the volume fraction profiles for annealing PE stars are presented in semilogarithmic coordinates. These prove that there is an exponential decay of the polymer density in the peripheral region of the star corona.

In Fig. 11, the radial distribution of the end segments in an annealing PE star, with different number p of arms, is shown for a range of pH values. A "dead zone", i.e., a region close to the center of the star where free ends are depleted, is visible. The end-point distribution is clearly bimodal for $pH \geq pK_{\mathrm{a}}$, when the star corona

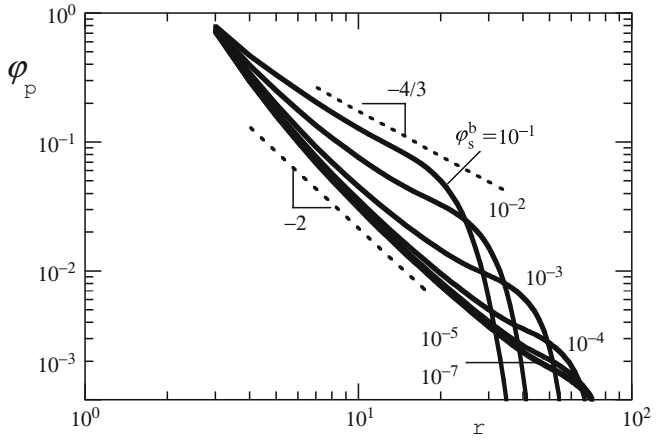

Fig. 12 Radial volume fraction profile of polymer segments $\varphi_p(r)$ in log–log coordinates, of a quenched PE star with $p = 20$ branches under theta-conditions; $N = 200$, $\alpha = 0.2$, $D = 300$, for various ionic strength conditions (φ_s^b) as indicated. *The dotted line* with the slope -2 corresponding to a uniform extension of the branches

is moderately ionized. Obviously, the two peaks in the distribution of chain ends correspond to two populations of the arms: the stronger ionized ones constitute the distal maximum in the distribution, whereas the weaker ionized ones are less stretched and contribute to the proximal maximum.

In Fig. 12, similar segment density profiles are presented for quenched PE stars with a given number of arms, $p = 20$, and for several salt concentrations, in log–log coordinates. Clearly, in the central region a power law regime is recovered. At low salt concentration, the slope -2 corresponds to the uniform stretching of the arms. Upon an increase in salt concentration, this slope is progressively changed to $-4/3$, corresponding to the salt-dominated regime.

The results of the SF-SCF calculations indicate that fluctuations in the extension of individual branches lead to a wide peripheral distribution of the free ends. Similarly to a neutral star polymer [124], the corona of a PE star consists of two regions. In the internal region, the arms are stretched fairly equally, and the decay of the polymer density is described by a power law function. This is in good agreement with findings of the analytical theory, which uses the assumption of equal stretching of the arms. At the periphery of a star polymer, the curvature effects are less important. Here, the corona can be structurally mimicked by a quasi-planar PE brush [98]: the free ends are distributed throughout the peripheral region with a well-pronounced maximum. For a quenched PE star polymer, the self-consistent electrostatic potential can be approximated by a parabolic function, whereas the number density profile of monomers has either a Gaussian (in a salt-free case) or a parabolic (in a salt-added case) shape, followed by an exponential decay at the tail of the distribution. The latter arises due to the fluctuations of non-stretched terminal segments of the arms.

7.3 Star Size and Degree of Ionization

In the context of the LEA, the size R of a PE star can be obtained by integrating the polymer density profile, $c_p(r)$, according to (2). In the limiting cases, when the density profiles are described by a power law function of distance from the star center, (44)–(46), the exact numerical pre-factors in the scaling expressions can be specified for the star size. Remarkably, if the simplified quasi-planar approach is applied, the star size is systematically underestimated. As mentioned above, this is due to a neglected additional pulling force exerted on the central regions of the star by the terminal segments of its arms. The difference between the results obtained by the two different approaches is marginal in the case of nonionic star polymers, whose conformations are governed by short-ranged repulsive intramolecular interactions, or for PE stars at high salt concentration. However, it becomes significant for PE stars at low salt concentrations, particularly for weakly dissociating (pH-sensitive) PE stars.

Quenched Polyelectrolyte Star

For the dimensions of a quenched PE star in a salt-free osmotic regime, one recovers the scaling dependence, (14), obtained earlier on the basis of a box-like model.

An increase in concentration Φ_{ion} of added salt ions, leads to the penetration of salt ions into the star interior and a decrease in the differential osmotic pressure. When the concentration of added ions sufficiently exceeds the average concentration of counterions in the osmotic star, the polyion is found in the so-called salt-dominated regime. Here, the differential osmotic pressure of ions is equivalent to that created by binary monomer–monomer interactions with an effective second viral coefficient $\upsilon_{eff} = \alpha^2/2\Phi_{ion}$. As a result, one recovers the same scaling dependence for the size of a PE star as that found for neutral star polymer under good solvent conditions, (4), with replacement $\upsilon \rightarrow \upsilon_{eff}$:

$$R \cong aN^{3/5}p^{1/5}(\alpha^2/a^3\Phi_{ion})^{1/5} \tag{47}$$

We, therefore, find that the PE star size, R, in the salt-dominated regime decreases as $\Phi_{ion}^{-1/5}$, upon an increase in salt concentration. Note that the same scaling dependence is obtained when the electrostatic repulsions between the charged monomers are accounted for through the screened Coulomb binary interaction potential, $u(r)/k_BT = l_Br^{-1}\exp(-r/r_D)$. A further increase in Φ_{ion} leads to an additional decrease in υ_{eff}. When υ_{eff} becomes on the order of the bare virial coefficient υ, the star size R approaches that of a neutral star, (4). Therefore, the size R of a quenched PE star demonstrates a plateau at low salt concentrations (in the osmotic regime), decreases in the salt-dominated regime as $R \sim \Phi_{ion}^{-1/5}$, and approaches a second plateau at high salt concentrations (in the quasi-neutral regime), as schematically illustrated in Fig. 13.

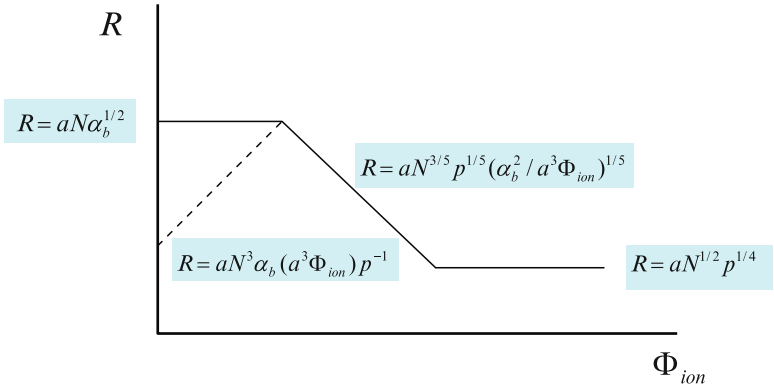

Fig. 13 Evolution of the size (radius R) of quenched and annealing PE stars as a function of salt concentration Φ_{ion}. See text for details

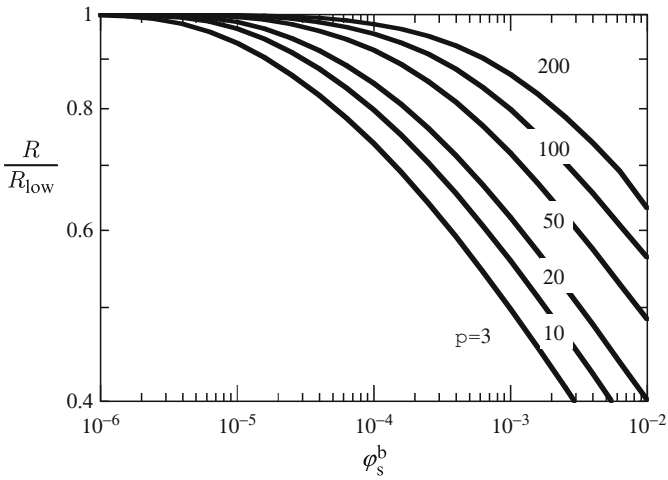

Fig. 14 Quenched PE star size R as a function of the volume fraction of salt in the bulk φ_s^b (in log–log coordinates) for stars with different number of branches p as indicated, under theta-conditions; $N = 200$, $\alpha = 0.2$, $D = 150$. The size is normalized with respect to the limiting value at low ionic strength conditions R_{low}

In Fig. 14, the overall size of a quenched PE star is plotted as a function of salt concentration for different values of p (in log–log coordinates). In accordance with the analytical predictions, the plateau at low salt is followed by a decrease in the star size with a slope of -0.2.

The salt-controlled behavior of PE coronae of kinetically frozen star-like micelles was examined experimentally [52, 58]. A good correspondence between the theoretical $(-1/5)$ and the observed (-0.18 in [52], and -0.2 in [58]) values of the exponent was found.

A more refined scaling model, developed recently in [93], introduces the concept of a screening length $r_B < r_D$ to specify the PE star behavior in the salt-dominated regime. According to [125], r_B governs the screening of the electrostatic interactions in a semidilute PE solution with added salt. A smaller value of $r_B = r_D \alpha^{1/6}$, with respect to the salt-controlled Debye length, r_D, is due to a more effective screening by charged polymer segments than by single ions. However, such modification leads to a rather moderate revision compared to the osmotic model described above. In particular, it predicts the appearance of a very narrow subregime, wherein $R \sim \Phi_{ion}^{-1/2}$. This dependence is expected in the middle of the salt-dominated regime (wherein $R \sim \Phi_{ion}^{-1/5}$), but up to now it has not been detected experimentally.

Annealing Star Polyelectrolyte

In contrast to the monotonous decrease in R expected for quenched PE stars upon an increase in salt concentration, an annealing PE star polymer demonstrates more sophisticated behavior. As discussed above, the ionization equilibrium in a strongly branched polyion is coupled to the local concentration of hydrogen ions in its interior (local pH) according to the mass action law (5). The local pH (computed using the local proton concentration) in an anionic star is always lower than the "buffered" pH in the solution, and the degree of ionization α of a monomer in a polyion interior is, therefore, lower than that in the bulk of the solution. Therefore, the degree of ionization of the star branches could be tuned by variations either in the ionic strength or in the pH of the solution. As a result, an annealing PE star might demonstrate a non-monotonous variation of its dimensions as a function of salt concentration Φ_{ion}.

The LEA gives, for the average degree of ionization α of a highly branched PE star:

$$\alpha \cong \begin{cases} \alpha_b^2 a^6 N^4 p^{-2} \Phi_{ion}^2, & \alpha_b c_p / \Phi_{ion} \gg 1 \\ \alpha_b, & \alpha_b c_p / \Phi_{ion} \ll 1 \end{cases} \tag{48}$$

where α_b is the degree of ionization of a monomer in the bulk solution at given pH. Hence, at low salt concentration Φ_{ion}, the average degree of ionization of monomers in a star polymer is a decreasing function of the number of arms, p, and increases upon an increase in Φ_{ion}, asymptotically approaching (from below) the value of α_b.

In Fig. 15, the average degree of ionization versus the bulk pH is plotted for weak polyacid stars with different numbers of arms. A progressive shift of the curves towards larger pH values upon an increase in p is clearly noticeable. Correspondingly, at low salt concentrations, the size $R \cong aN\alpha^{1/2}$ of an annealing PE star is given by:

$$R \cong a^4 N^3 p^{-1} \alpha_b \Phi_{ion}, \qquad \alpha_b c_p / \Phi_{ion} \gg 1 \tag{49}$$

The theory, therefore, predicts a linear increase in the size of an annealing PE star polymer at relatively low salt concentration (in the osmotic regime), as shown by the dashed line in Fig. 13. When salt is added, salt ions substitute protons in the interior of the polyion and thereby increase the local pH. As a result, the ionization of the branches increases, and the PE star swells upon an initial increase in Φ_{ion}.

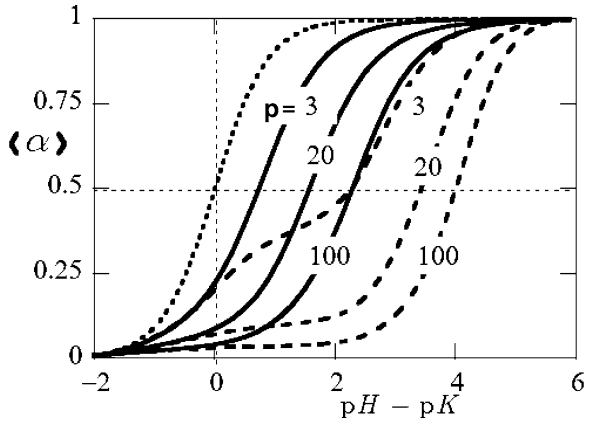

Fig. 15 Average fraction of dissociated groups $\langle\alpha\rangle$ as a function of the difference between pH of the solution and the pK_a value of the weak acidic groups. The number of branches (p) is indicated; theta-conditions and $N = 200$ The ionic strength is $\varphi_s^b = 10^{-5}$ ($c_s = 10^{-4}$ M) (*solid lines*) and $\varphi_s^b = 10^{-7}$ ($c_s = 10^{-6}$ M) (*dashed lines*)

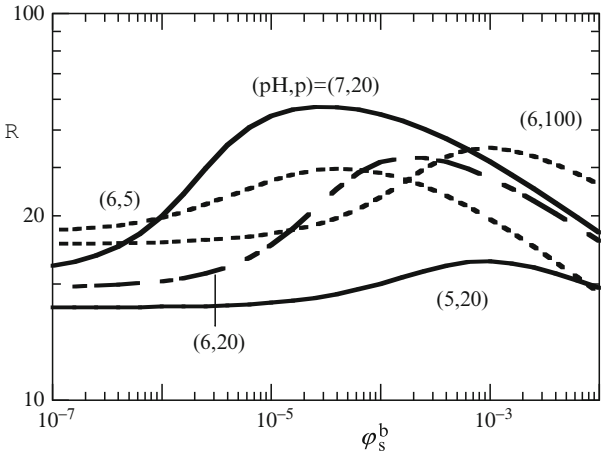

Fig. 16 Size of an annealing PE star R as a function of the ionic strength for $N = 200$, $D = 500$, $m = 5$, p$K_a = 6$ under theta-conditions. The pH is 6 or 7, and the number of branches p is 5, 20, or 100 as indicated

When the local (interior) pH approaches the bulk pH, $\alpha \cong \alpha_b$ and the size of a swollen polyion reaches its maximum, $R \cong aN\alpha_b^{1/2}$. After this point, the behavior of quenched and annealing PE star polymers becomes similar: both decrease their size R upon a further increase in Φ_{ion} as $R \sim \Phi_{ion}^{-1/5}$, following (47), and approach the quasi-neutral plateau at high salt conditions (as schematically shown in Fig. 13).

In Fig. 16, the average size R of an annealing PE star (specified as the first moment of the end segment distribution) is plotted as a function of the salt concentration, $\Phi_{ion} \sim \varphi_s^b$, for different values of the bulk pH. A maximum is observed for $pH \leq pK_a$.

At low salt concentration, however, the degree of ionization α of an annealing PE star might become so low that a star macroion releases a noticeable fraction of its counterions into the surrounding solution. As a result, the increase in local pH promotes ionization of the branches. The released counterions become more strongly attracted to the macroion and eventually condense back into its interior. Therefore, under low salt conditions, an annealing branched macroion stays at the threshold of ion release, $Q = \alpha pN \cong R/l_B$. The ion localization condition, $\alpha pN \cong R/l_B$, together with the intrastar osmotic balance condition, $R \cong a\alpha^{1/2}N$, set the scaling dependence for the star size in this so-called annealing charged regime [28]:

$$R \cong \frac{a^2 N}{l_B p} \tag{50}$$

The crossover between (49) and (50) specifies the boundary between the annealing osmotic and the annealing charged regimes as $a^2 l_B \alpha_b N^2 \Phi_{ion} \approx a^2 l_B K_a N^2 \Phi_{ion}/c_{bH+} \simeq 1$.

Remarkably, in both annealing charged and annealing osmotic regimes, (49) and (50) predict a decrease in the star size as a function of the number of branches p. The reason for this is a decrease in the average degree of ionization of the arms upon an increase in the intramolecular density of the monomers. However, the strong dependence, $R \sim p^{-1}$, predicted by (49) and (50) is hardly observable in real or numerical experiments because of a corresponding increase of the non-electrostatic (excluded-volume) intramolecular repulsion.

Various scaling regimes of quenched and annealing PE star polymers are summarized in the diagram of states given in Fig. 17. For an annealing star, in addition to the annealing osmotic and annealing charged regimes (where the star size R is given by (49) and (50), respectively), one finds the regime of a charged star (13), the salt-dominated regime (47), and the regime of a neutral star (3). The latter is specified in Fig. 17 for theta-solvent conditions, $\upsilon = 0$. Remarkably, in the charged annealing regime, the size R of a star polymer does not exhibit a power law dependence on Φ_{ion}. This might explain why, in contrast to planar brushes, the spherically curved weak PE colloidal brushes do not demonstrate a distinct increase in R upon an increase in Φ_{ion} [45]. Note that, in a planar geometry, the scaling theory predicts a salt-induced increase in brush thickness, $H \sim \Phi_{ion}^{1/3}$, for both the annealing osmotic and the annealing charged regimes [126]. Whereas the general theoretical trends predicted for the annealing planar and quasi-planar brushes were confirmed in a number of experimental studies [45, 127–133], a comprehensive test of annealing star-like spherical brushes remains a challenging problem. The width of the osmotic annealing regime is rather limited (see diagram in Fig. 17), and a proper choice of the relevant parameters (p, N, and pH) is of crucial importance for detecting the $R \sim \Phi_{ion}$ dependence, (49).

The coupling between the ionization of an annealing polyion and its conformation is expected for other branched macroions as well. Recently, this effect was unambiguously demonstrated for thermoresponsive spherical star-like micelles of diblock copolymers with a polybasic (PDMAEMA) corona [134]. Due to the

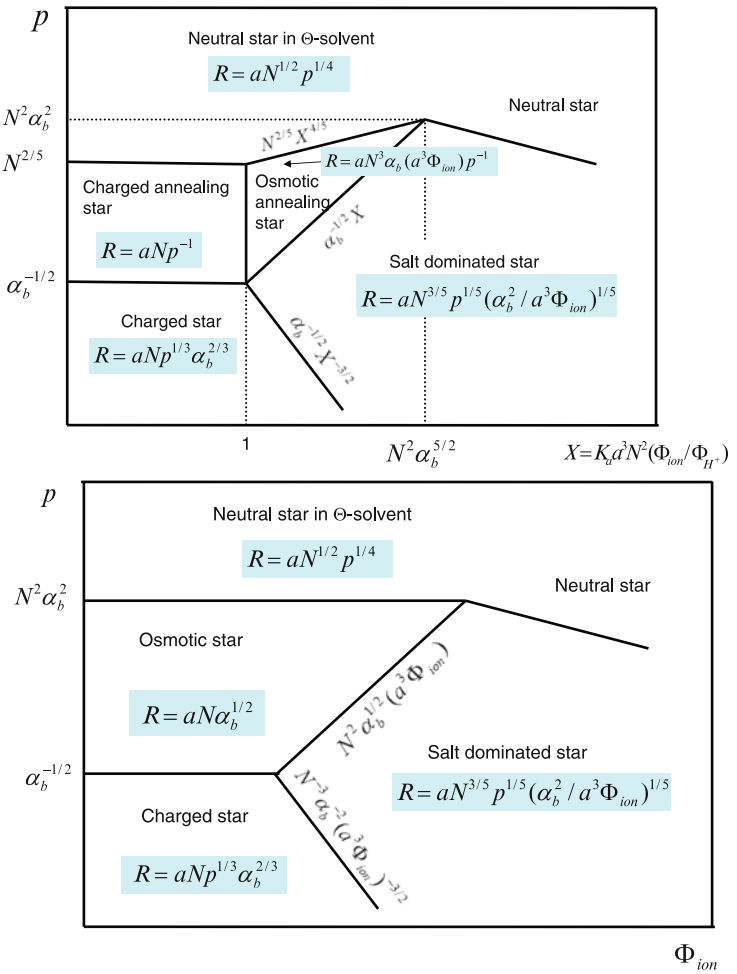

Fig. 17 Diagram of states of annealing (**a**) and quenched (**b**) PE stars. The ratio l_B/a is set to unity. See text for details

connection between the conformations of coronal chains and the ionization of their segments, variations in the temperature and pH could cause large micelles with a quasi-neutral corona to reversibly abruptly rearrange into small micelles with a highly charged corona.

7.4 Annealing Star Polyelectrolytes: Titration Curves

To experimentally monitor the ionization of weak PE stars, one can measure the variation of the pH in the solution of PE stars upon adding strong acid or strong base.

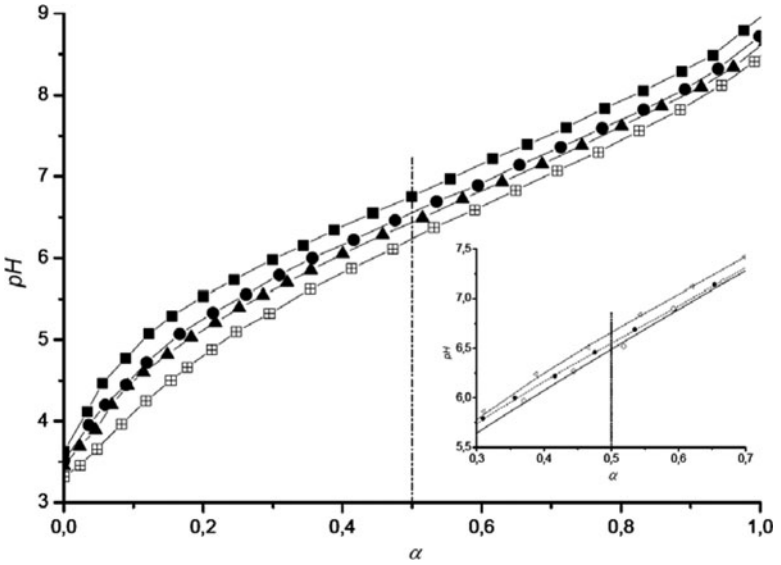

Fig. 18 Potentiometric titration curves for PAA stars: $(PAA_{100})_{21}$ (*closed squares*), $(PAA_{100})_8$ (*closed circles*), $(PAA_{100})_5$ (*closed triangles*), and linear PAA_{100} (*open squares*). *Inset* is the cutout of $(PAA_{75})_8$ (*open triangles*), $(PAA_{160})_8$ (*open diamonds*), and $(PAA_{100})_8$ (*closed circles*) [43]. Reprinted by permission of Wiley-VCH

The degree of neutralization of the PE macroion can be calculated from the added amount of acid or base in relation to the detected pH. The apparent pK_a (or pK_b) values can be found from the pH that corresponds to the degree of neutralization of $\alpha = 0.5$.

A solution of PAA stars was titrated by adding a concentrated NaOH solution, giving a titration curve [43]. Figure 18 shows the obtained result for pH as a function of the degree of neutralization, $\alpha = [Na^+]/[COOH]$, where [COOH] is the total concentration of carboxyl and carboxylate groups of the stars and $[Na^+]$ is equal to the amount of added NaOH. It is clearly seen that the titration curves are systematically shifted toward larger pH values when the number of arms (at constant arm length) is increased. This result is in accordance with (48). Thus, the apparent pK_a increases as a function of the number or arms, as predicted by theory: the larger the number of arms, the higher the excess electrostatic potential inside the star and the smaller is the degree of ionization of the arms.

7.5 Effect of Counterion Valency

As discussed in the previous section, the addition of monovalent salt to a solution of PE stars leads to a screening of the intramolecular Coulomb repulsion and a subsequent decrease of the differential osmotic pressure. For quenched PE stars, this results in a monotonic decrease in the star size, most pronounced in the

salt-dominated regime. For pH-sensitive PE stars, the promotion of ionization due to replacement of H^+ (or OH^-) counterions by salt ions dominates under low salt conditions and, as a result, the star swells upon an addition of salt (cf. osmotic annealing regime in Fig. 17). This swelling is followed by a decrease in the star size, R, at higher salt concentrations (salt-dominated regime in Fig. 17). Both trends are strongly affected by the valency of the counterions.

The effect of counterion valency on the swelling behavior of planar and colloidal PE brushes was theoretically studied in [135–137]. In the case of a counterion with a valency of Z ($Z = 1$, 2 and 3 for, e.g., Na^+, Ca^{2+} and Al^{3+} ions, respectively), the Donnan equilibrium is formulated as:

$$c_{Z+}/c_{bZ+} = (c_{j^+}/c_{bj^+})^Z = (c_{bj^-}/c_{j^-})^Z = \exp(-Ze\Delta\Psi/k_BT) \tag{51}$$

where c_{Z+} and c_{bZ+} are the concentrations of the Z-valent ions inside and outside the star, and $c_{j^\pm}$ and $c_{bj^\pm}$ are the concentrations of monovalent ions (including H^+ and OH^- ions) inside the star volume and in the bulk of the solution, respectively. In experiments, the ratio $c_{bZ}/Z\sum_{j^+} c_{bj^+} \equiv \zeta$ and the total concentration of monovalent salt co-ions, $\sum_{j^-} c_{bj^-} \equiv \Phi_s/2$, are often used as control parameters.

By combining (51) with the local electroneutrality condition, $\sum_{j^-} c_{j^-} + \alpha c_p = \sum_{j^+} c_{j^+} + Zc_{Z+}$, one finds an equation for the excess (Donnan) potential inside the star and for the differential osmotic pressure. This differential osmotic pressure has to be balanced with the elastic force of entropic origin that is linked to the extension of the branches to give the equilibrium size of the star polymer.

It can be shown that the addition of trace amounts of Z-ions to the solution leads to a rapid substitution of monovalent counterion in the star corona by Z-ions. This is due to their stronger attraction to the oppositely charged PE star polymer. Since a smaller number of Z-ions is needed to ensure the electroneutrality of the star interior, an increase in ζ (i.e., in relative amount of Z-ions in the bulk of the solution) leads to a rapid decrease in the osmotic pressure inside the corona and, consequently, to a de-swelling of the PE star. This effect, of replacing monovalent counterions by multivalent ones is most pronounced at low salt concentrations (in the osmotic regime), where:

$$R \cong aN\left(\frac{\alpha}{Z}\right)^{1/2} \tag{52}$$

and, thus, $R_{Z=1}/R_Z \cong Z^{1/2}$. By contrast, in the salt-dominated regime, the differential osmotic pressure and the star size, R, are controlled by the ionic strength in the solution via r_D. That is, $R \cong aN^{3/5}p^{1/5}\upsilon_{eff}^{1/5}$, where:

$$\upsilon_{eff} = 2\pi\alpha^2 l_B r_D^2 = \frac{\alpha^2}{\Phi_s}\cdot\frac{1+Z^2\zeta}{2+Z^2\zeta+Z^3\zeta} \tag{53}$$

Thus, the replacement of monovalent counterions by multivalent ones (at constant and high bulk concentration of monovalent salt co-ions), results in a contraction of the star macroion by a factor of $R_{Z=1}/R_Z \cong Z^{1/5}$.

The effect of multivalent counterions has been studied experimentally for colloidal PE brushes in [137]. Remarkably, the magnitude of the observed collapse described in [137] exceeds the decrease in R predicted on the basis of osmotic balance arguments (52). A similar trend was also found for planar PE brushes in the presence of multivalent ions [132, 138]. At least two additional effects might be responsible for this behavior. Firstly, a correlational attraction in the star corona, due to Z-ions, may serve as a co-driving force of the star collapse. Secondly, multivalent counterions might bind specifically (adsorb) to the star branches, thereby reducing their effective charge density. Under these conditions, the Donnan equilibrium should be supplemented by a Langmuir-like balance [139] between the counterions that are adsorbed onto the branches and the mobile ones in the star interior. Finally, one has to keep in mind that the replacement of monovalent counterions by multivalent ones reduces the maximal charge density on the arms corresponding to the Manning condensation threshold.

For an annealing star polyion, the degree of ionization, α, becomes a function of the counterion valence, Z, and of the Z-ion bulk concentration, c_{bZ}, due to a progressive substitution of the monovalent counterion (H^+ for a polyacid) by Z-ions and the corresponding increase in local pH inside the star. Implementation of the Donnan rule (51), together with the mass action law (5) and the osmotic balance (52), provides a scaling dependence for the star size:

$$R \cong a\alpha_{\mathrm{b}}^{Z/(2Z-1)} N^{(2Z+1)/(2Z-1)} \left(\frac{Zc_{bZ}}{p}\right)^{1/(2Z-1)} \tag{54}$$

where the exponents depend on the counterion valency, $Z \geq 1$. Remarkably, under low salt conditions the substitution of monovalent counterions by multivalent ones leads to a weaker swelling of the star corona (as a function of the added salt concentration). In the salt-dominated regime, multivalent counterions provide a stronger screening of the electrostatic interactions (smaller value of the Debye length, r_{D}) for both quenched and annealing polyions.

8 Collapse of a Polyelectrolyte Star in Poor Solvent

Triggered by a decrease in the solvent strength, isolated nonionic star polymers suffer a collapse transition. The theory of the collapse transition has been developed in [140, 141]. This theory predicts a progressive deswelling (collapse) of the star polymer as a function of decreasing solvent strength. The onset of the collapse transition, which corresponds, e.g., to a vanishing second virial coefficient of interactions between the stars in solution, is shifted with respect of the theta-point for linear polymers, $\upsilon = 0$, towards poorer solvent strength conditions, $\upsilon \leq 0$. In the framework of the blob model, the onset of the collapse of a star polymer as a whole corresponds to the collapse of the outermost coronal blobs. A further decrease in the solvent strength results in the formation of a region of virtually constant

concentration at the periphery of the star, see Fig. 1c. This concentration is determined by the local balance of binary attractive and ternary repulsive interactions. In a more dense central region, the stretching of the arms is controlled by ternary monomer–monomer interactions. Upon progressive decrease in solvent strength, the boundary between the collapsed and the theta-region shifts progressively towards the center of the star. The star acquires a conformation of a spherical globule with a uniform density of its monomers.

These theoretical predictions are in good agreement with experiments [142] on the collapse transition in dilute solutions of organosoluble star polymers, i.e., poly(styrene) stars in cyclohexane. In these experiments, the temperature was varied around the theta-point (ca. 34.5°C). Lowering the temperature corresponds to an inferior solvent strength of cyclohexane.

In water, the solubility of most of synthetic PEs (e.g. PMAA or polysulfonic acid) depends strongly on the presence of ionized groups. In other words, the monomers of most synthetic PEs are often intrinsically hydrophobic [143].

In contrast to organosoluble polymers, for most known water-based nonionic polymers, the quality of water as a solvent decreases upon an increase in temperature. This is known as LCST (lower critical solution temperature) behavior [144]. Experimental observations of LCST behavior (thermoinduced collapse) of neutral stars or spherical polymer brushes in water are rare [145, 146], and do not yet provide systematic relationships between the LCST and the degree of branching.

Furthermore, polymers such as PDMAEMA combine a weak polybase character with thermoresponsive properties: at high pH and low temperatures PDMAEMA is not ionized, but, nevertheless, is soluble in water. An increase in temperature, however, leads to an increase in the hydrophobicity of the monomers and, at $T \geq$ LCST, the unionized polymers collapse, lose solubility, and precipitate from aqueous solution [47].

In poor solvents, the conformations of charged macromolecules are controlled by the competition between short-ranged attractive monomer–monomer interactions and long-ranged electrostatic repulsions between ionized monomers. The first theory of the collapse transition in a single linear (quenched) PE chain was proposed by Khokhlov [147], who predicted a gradual collapse of a PE chain upon a decrease in the solvent strength. According to this theory, a partially collapsed PE chain acquires the conformation of a longitudinally uniform cylindrical ("cigar-like") globule. The collapse transition in a weak (pH-sensitive) PE chain was considered by Raphael and Joanny [148], who predicted an abrupt transition from a stretched to a collapsed globular state, because of the coupling between the conformations and the ionization of a weak PE chain. That is, a lower degree of ionization of the monomers is expected in the collapsed globular conformation.

The theory of Khokhlov [147] was revised by Dobrynin, Rubinstein and Obukhov [149], who demonstrated that a partially collapsed quenched PE chain acquires a "pearl-necklace" conformation, consisting of collapsed globular beads connected by stretched bridges. The pearl-necklace structure appears due to interplay of short-range monomer-monomer attraction with long range repulsion and is a manifestation of the Rayleigh instability constrained by the chain connectivity [158, 159].

The size of each globular bead is controlled by a balance between the excess interfacial free energy of a bead and the intrabead Coulombic repulsion. The length of the bridges (strings of thermal blobs) adjusts the Coulomb force of the interbead repulsion to a critical force at which the mechanical unfolding of a polymer globule occurs [152]. MC and MD simulations unambiguously indicated the formation of such a intramolecular pearl-necklaces structure in strongly dissociating PE chains, where the local collapse is due to short-range monomer–monomer attraction [153, 154].

The nonlinear branched topology is expected to introduce novel specific features in the collapse transition of individual charged macromolecules, due to the interplay between intra- and interbranch Coulomb repulsion. Conformations of intrinsically hydrophobic star-branched PE have been studied experimentally in the past decade [50, 51]. Recently synthesized PDMAEMA stars responsive to both pH and temperature [47, 48] are expected to undergo an intramolecular collapse transition as a response to the increase in temperature. The latter provokes a decrease in the solubility of the monomers in the star arms.

The theory of the collapse transition in star-like PEs was developed by Borisov et al. [155] and Ross and Pincus [156] on the basis of a box-like model, which assumes a fairly uniform concentration of the monomers within the star (see Sect. 5). This analysis suggested that, in contrast to a neutral polymer star, which collapses gradually upon a decrease in the solvent strength [141], the collapse of a PE star has a first-order nature and involves coexistence of the collapsed and swollen states.

In a salt-free solution, the onset of collapse transition in a PE star corresponds to the collapse of individual electrostatic blobs in the uniformly stretched arms of the star. An increase in the number of star branches, p, enhances interbranch Coulomb repulsions, and, thereby, decreases the electrostatic blob size. Therefore, the collapse transition is shifted towards poorer solvent conditions upon an increase in p.

The picture of the collapse transition in quenched PE star has been revised by Misra et al. [157], who proposed that microphase coexistence, between a collapsed core domain and a swollen corona may occur inside an individual PE star. An essential Ansatz of all the mean field theories developed in [155–157] is the preassumption that the PE star retains its spherically symmetrical configuration in a partially collapsed state. The collapse transition is described in terms of the evolution of radial density distribution as a function of the solvent quality.

In contrast to this, the scaling theory of the PE star collapse developed in [27] suggested that, instead of the formation of a collapsed core, a decrease in the solvent strength may provoke the formation of bundles by the sticking of individual branches to each other. The bundle formation reduces the excess interfacial free energy of the collapsed domains, without a significant penalty in terms of the intramolecular Coulomb repulsion. More recently, the formation of bundles was theoretically predicted in colloidal PE brushes [42].

An intriguing question is, however, whether the pearl necklace, or some other types of multidomain intramolecular structures of low symmetry, may correspond to the equilibrium conformation of a partially collapsed star-branched PE. This problem has been recently addressed by Kosovan et al. [158] by means of MD simulations.

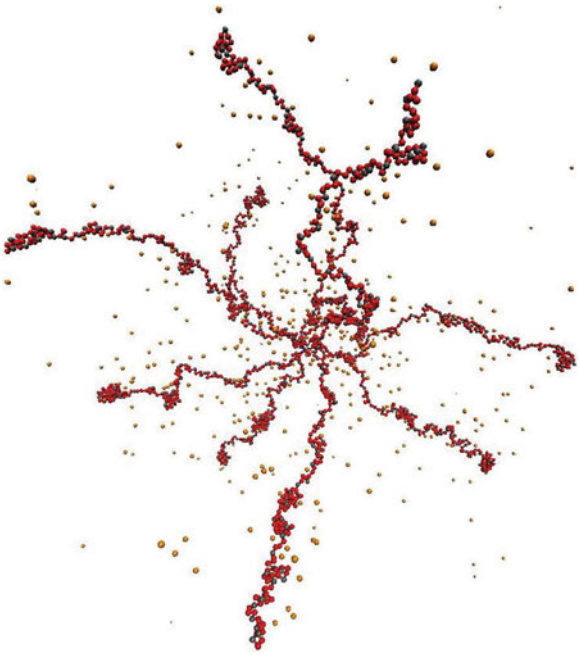

Fig. 19 MD simulation snapshot of a PE star in poor solvent; $p = 10$, $N = 200$, $\alpha = 0.25$

The simulations proved that a progressive decrease in the solvent quality induces a series of conformational transitions, giving rise to intramolecular multidomain structures of different morphologies. The pearl-necklace structures in separate branches are found at moderately poor solvent conditions. This structural motive persists for stars with a relatively small number of arms, also in the intermediate range of solvent quality. With inferior solvent strengths, the simulations provide evidence of sticking of individual branches/necklaces into bundles. The bundling is more pronounced in the central region of many-armed stars, whereas at the periphery of the star the bundles split into single-chain necklaces, Fig. 19. At sufficiently poor solvent strength, multiple intramolecular structures of different morphologies are observed in the simulations, i.e., the system is strongly frustrated. It is anticipated that this behavior is an inherent property of branched PEs, where the repulsive electrostatic interactions that operate on a large length scale compete with short-ranged attractions under the constraints of monomer connectivity in branched topologies.

9 Conclusions

We have presented an overview of theories that describe the conformations and solution properties of star-branched PEs. Whereas the principal qualitative results can be obtained on the basis of a simplified box-like cell model, systematic

treatments of the corresponding PB problem were achieved by employing the SF-SCF approach. The latter gives access to the partition function of stars in the self-consistent electrical field created by the charged arms in the presence of mobile counterions. Additional insights into counterion distributions in PE stars in both radial and angular directions are provided by MC and MD simulations.

The theoretical analysis proves that the majority of the counterions are localized inside the star, provided that the number of arms is large. The arm length has no significant influence on the degree of counterion localization. The PB analysis shows that the dimensionless electrostatic potential at the edge of the star corona drops almost to unity. Consequently, the counterions outside the corona are distributed fairly uniformly. The effective (renormalized) charge of the star, which determines the counterion concentration at the boundary of the Wigner–Seitz cell, approximately coincides with the total uncompensated charge Q^* within the star corona. The phenomenon of counterion localization in the intramolecular volume is typical for dilute salt-free solutions of highly branched polyions of arbitrary topology, including randomly branched, dendritic polyions, PE molecular brushes, etc.

The LEA can be applied to the analysis of conformations of PE stars with a sufficiently large number of arms. In contrast to neutral stars, for which the generalized Daoud–Cotton approach provides an accurate description of the star structure in terms of radial power law decay of polymer concentration and of local stretching of the arms, the nonlocal effects (related to the additional pulling force exerted by the terminal segments of the arms) are essential for PE stars in salt-free solutions.

Some peculiar effects arise in pH-sensitive stars because of a coupling between the conformations and the degree of ionization of the arms. In particular, the overall extension of the arms of the star depends in a non-monotonic fashion on the ionic strength in the bulk and on the number of the arms of the star.

The mean-spherical approximation provides an adequate description of the PE star conformation under conditions of good or theta-solvent. However, in contrast to some early theoretical predictions, simulations give evidence that conformational transition related to the collapse of hydrophobic or thermosensitive PE stars is accompanied by the formation of various intramolecular structures of low symmetry (pearl necklaces, bundles).

Experiments on PE stars show extremely low values of the osmotic coefficient in salt-free star solution, thus proving the concept of counterion localization. Potentiometric titration experiments confirm theoretical predictions concerning a shift of the effective pK_a upon an increase in the number of arms.

Acknowledgment The support of the European Union within the Marie Curie Research and Training Network POLYAMPHI and of the Russian Foundation for Basic Research, grant 08-03-33126a is gratefully acknowledged. OVB acknowledges the Alexander von Humboldt Foundation for support of his stay in the University of Bayreuth. We thank A.A. Polotsky, F.A. Plamper and P. Kosovan for creating Figs. 2,8, and 19, respectively.

Appendix: Local Electroneutrality Approximation

The local electroneutrality approximation (LEA) assumes that the local number density of charged monomer units in the PE corona is approximately equal to local (excess) number density of mobile counterions:

$$\sum_{j^-} c_{j^-}(r) + \alpha(r) c_{\mathrm{p}}(r) = \sum_{j^+} c_{j^+}(r) \tag{55}$$

We will focus on the case of a solution that contains, in addition to H^+ and OH^- ions (whose concentration is controlled by the pH in the bulk), also monovalent co- and counterions due to added salt (e.g., Na^+, Cl^-, etc.). Here, $c_j(r)$ is the local concentration of ions of type j, and $c_{\mathrm{p}}(r)$ and $\alpha(r)$ are the concentration of the monomer units and the degree of ionization in the corona at a distance r from the center of the star, respectively. Note that we assume that the star is negatively charged. The summation on the right-hand side of (55) includes all the cationic species (i.e. salt ions, c_{Na^+}, and hydrogen ions, c_{H^+}), whereas the summation on the left-hand side of (55) includes all the anionic species (i.e. salt ions, c_{Cl^-}, and hydroxyl ions, c_{OH^-}).

The concentrations c_{bj} (or, equivalently, the chemical potentials) of all the mobile ions are assumed to be constant in bulk solution, wherein the osmotic pressure is given by:

$$\Pi_{\mathrm{b}}/k_{\mathrm{B}}T = \Phi_{\mathrm{ion}} \equiv \sum_{j} c_{bj} \tag{56}$$

(Here, the summation is performed over all ion species including H^+ and OH^- ions).

In the framework of LEA, the electrostatic interactions manifest themselves through the entropy of ions disproportionated between the interior of a strongly branched macromolecule and bulk solution. Therefore, the driving force for swelling of a branched polyion can be formulated in terms of the differential osmotic pressure of small ions inside and outside of the macromolecule.

If the (excess) electrostatic potential $\Delta\Psi(r)$ is ascribed to the intramolecular volume of the star, then the concentrations of all mobile ions obey the Donnan rule (the Boltzmann law):

$$c_{j^-}(r)/c_{bj^-}(r) = c_{bj^+}(r)/c_{j^+}(r) = \exp(e\Delta\Psi(r)/k_{\mathrm{B}}T) \tag{57}$$

Note, that here all the small ions (co- and counterions) are assumed to be monovalent.

Combining (55) and (57), we find for the excess electrostatic potential:

$$\exp(e\Delta\Psi(r)/k_{\mathrm{B}}T) = \sqrt{1 + (\alpha(r)c_{\mathrm{p}}(r)/\Phi_{\mathrm{ion}})^2} - \alpha(r)c_{\mathrm{p}}(r)/\Phi_{\mathrm{ion}} \tag{58}$$

It follows from (57) and (58), that the total concentration of counterions inside the star is $\sum_{j^+} c_{j^+}(r) \cong \alpha(r)c_{\mathrm{p}}(r)$, provided that $\alpha(r)c_{\mathrm{p}}(r)/\sum_j c_{bj} \to \infty$. That is, in the

limit of low salt concentrations, the charge density created by the charged monomers is locally matched by that of the mobile counterions (osmotic regime).

Quenched Polyelectrolyte Corona

For a strongly dissociating (quenched) PE star, the density of the Gibbs free energy is given by:

$$f_{\text{ion,quenched}}\{c_{\text{p}}(r)\}/k_{\text{B}}T = \sum_j c_j(r)[\ln c_j(r) - 1] + \Pi_b/k_{\text{B}}T - \sum_j c_{bj} \ln c_{jb} =$$

$$\alpha_b c_{\text{p}}(r)\left(\left(1 - \sqrt{1 + (\alpha_{\text{b}} c_{\text{p}}(r)/\Phi_{\text{ion}})^2}\right)/(\alpha_b c_{\text{p}}(r)/\Phi_{\text{ion}})\right.$$

$$\left. + \text{Arsh}(\alpha_{\text{b}} c_{\text{p}}(r)/\Phi_{\text{ion}})\right) \tag{59}$$

where $\text{Arsh}(x) \equiv \ln(x + \sqrt{1+x^2})$. An expansion of $f_{\text{ion}}\{c_{\text{p}}(r)\}$ in series of $\alpha_b c_{\text{p}}(r)/\Phi_{\text{ion}}$ leads to the asymptotic power law dependencies:

$$\frac{f_{\text{ion}}\{c_{\text{p}}(r)\}}{k_{\text{B}}T} \cong \begin{cases} \alpha_{\text{b}} c_{\text{p}}(r) \ln(2\alpha_b c_{\text{p}}(r)/e\Phi_{\text{ion}}), & \alpha_b c_{\text{p}}(r)/\Phi_{\text{ion}} \gg 1 \\ \frac{\alpha_{\text{b}}^2 c_{\text{p}}^2(r)}{2\Phi_{\text{ion}}}, & \alpha_{\text{b}} c_{\text{p}}(r)/\Phi_{\text{ion}} \ll 1 \end{cases} \tag{60}$$

corresponding to the limits of low and high salt concentrations, respectively. As follows from (60), at low concentrations of added salt the free energy is dominated by the translational entropy of the counterions that are confined inside the PE corona. When the concentration of added ions far exceeds the average concentration of counterions in the PE corona (salt-dominated regime), the differential swelling pressure of the counterions can be described as excluded-volume (binary) monomer–monomer interactions with an effective second viral coefficient $\upsilon_{\text{eff}} = \alpha^2/2\Phi_{\text{ion}}$.

Annealing Polyelectrolyte Corona

For an annealing (weakly dissociating) PE star, one has to account for the shift in the local ionization equilibrium, whose free energy cost, $f_{\text{ionization}}$, must complement the free energy of the star:

$$f_{\text{ionization}}\{c_{\text{p}}(r)\}/k_{\text{B}}T = c_{\text{p}}(r)$$

$$\left[\alpha(r)\ln\alpha(r) + (1-\alpha(r))\ln(1-\alpha(r)) - \alpha(r)\ln\frac{K_a}{c_{\text{bH}^+}}\right] \tag{61}$$

This leads to:

$$f_{\text{ion,annealing}}\{c_{\text{p}}(r)\}/k_{\text{B}}T = \left(1 - \sqrt{1 + (\alpha(r)c_{\text{p}}(r)/\Phi_{\text{ion}})^2}\right)\Phi_{\text{ion}} + c_{\text{p}}(r)\ln\left(1 - \alpha(r)\right) \tag{62}$$

where $\alpha(r) = \alpha\{c_{\text{p}}(r), \Phi_{\text{ion}}\}$ is determined by the following equation:

$$\frac{\alpha(r)}{1-\alpha(r)} \cdot \frac{1-\alpha_{\text{b}}}{\alpha_{\text{b}}} = \sqrt{1 + (\alpha(r)c_{\text{p}}(r)/\Phi_{\text{ion}})^2} - \alpha(r)c_{\text{p}}(r)/\Phi_{\text{ion}} \tag{63}$$

and α_{b} is the degree of ionization of an isolated acidic monomer in the bulk solution at given pH. The detailed derivation of the free energy density for the annealing PE corona can be found in [159].

Equations (62) and (63) can be expanded in series of $\alpha(r)c_{\text{p}}(r)/\Phi_{\text{ion}}$, and the logarithm in (62) can be expanded up to linear order in $\alpha(r) \ll 1$. As a result, one gets:

$$\alpha(r) \cong \begin{cases} \left(\frac{\alpha_{\text{b}}}{1-\alpha_{\text{b}}} \cdot \frac{\Phi_{\text{ion}}}{2c_{\text{p}}(r)}\right)^{1/2}, & \alpha(r)c_{\text{p}}(r)/\Phi_{\text{ion}} \gg 1 \\ \alpha_{\text{b}}, & \alpha(r)c_{\text{p}}(r)/\Phi_{\text{ion}} \ll 1 \end{cases} \tag{64}$$

and:

$$\frac{f_{\text{ion}}\{c_{\text{p}}(r)\}}{k_{\text{B}}T} \cong \begin{cases} -\left(\frac{2\alpha_{\text{b}}}{1-\alpha_{\text{b}}}\Phi_{\text{ion}}c_{\text{p}}(r)\right)^{1/2}, & \alpha(r)c_{\text{p}}(r)/\Phi_{\text{ion}} \gg 1 \\ \frac{\alpha_{\text{b}}^2 c_{\text{p}}^2(r)}{2\Phi_{\text{ion}}} + c_{\text{p}}(r)\ln(1-\alpha_b), & \alpha(r)c_{\text{p}}(r)/\Phi_{\text{ion}} \ll 1 \end{cases} \tag{65}$$

As follows from (64), at low salt concentrations (annealing osmotic regime), the degree of ionization of the monomers in the corona is an increasing function of the salt concentration, Φ_{ion} and a decreasing function of local polymer concentration, $c_{\text{p}}(r)$.

References

1. Oosawa F (1971) Polyelectrolytes. Dekker, New York
2. Barrat JL, Joanny JF (1996) In: Prigogine I, Rice SA (eds) Advances in chemical physics. Wiley, New York
3. Dobrynin AV, Rubinstein M (2005) Pogr Polym Sci 30:1049
4. Ballauff M, Borisov OV (2006) Curr Opin Colloid Interface Sci 11:316
5. Ballauff M, Likos C (2004) Angew Chem Intl Ed 43:2998
6. Peppas NA (1997) Curr Opin Colloid Interface Sci 2:531
7. Mori H, Müller AHE (2003) Prog Polym Sci 28:1403
8. Zhang M, Müller AHE (2005) J Polym Sci Part A Polym Chem 43:3461
9. Xu Y, Plamper F, Ballauff M, Müller AHE (2010) Adv Polym Sci 228:1
10. Förster S, Abetz V, Müller AHE (2004) Adv Polym Sci 166:173
11. Abu-Lail NI, Camesano TA (2003) Biomacromolecules 4:1000

12. Ng L, Grodzinsky AJ, Patwari P, Sandy J, Plaas A, Ortiz C (2003) J Struct Biol 143:242
13. Fuchs E, Cleveland DW (1998) Science 279:514
14. Burchard W (1999) Adv Polym Sci 143:113
15. Birshtein TM, Mercurieva AA, Leermakers FAM, Rud OV (2008) Polym Sci A(Russia) 50:1673
16. Stockmayer WH, Zimm BH (1949) J Chem Phys 17:301
17. Benoit H (1953) J Polym Sci 11:507
18. Benoit H (1955) R Acad Sci 533
19. Candau F, Rempp R, Benoit H (1972) Macromolecules 5:627
20. Khokhlov AR (1978) Polymer 19:1387
21. Daoud M, Cotton JP (1982) J Phys (France) 43:531
22. Zhulina EB (1984) Polym Sci USSR 26:794
23. Birshtein TM, Zhulina EB (1984) Polymer 25:1453
24. Birshtein TM, Zhulina EB, Borisov OV (1986) Polymer 27:1079
25. Manning G (1969) J Chem Phys 51:3249
26. Pincus P (1991) Macromolecules 24:2912
27. Borisov OV (1996) J Phys II (France) 6:1
28. Borisov OV, Zhulina EB (1998) Europ Phys J B 4:205
29. Klein Wolterink J, Leermakers FAM, Fleer GJ, Koopal LK, Zhulina EB, Borisov OV (1999) Macromolecules 32:2365
30. Klein Wolterink J, van Male J, Cohen Stuart MA, Koopal LK, Zhulina EB, Borisov OV (2002) Macromolecules 35:9176
31. Borisov OV, Vilgis TA (1996) Europhys Lett 35:327
32. Borisov OV, Daoud M (2001) Macromolecules 34:8286
33. Klein Wolterink J, van Male J, Daoud M, Borisov OV (2003) Macromolecules 36:6624
34. Kramarenko EYu, Khokhlov AR, Yoshikawa K (1997) Macromolecules 30:3383
35. Levin Y, Deihl A, Fernandez-Nieves A, Fernandez-Barbero A (2002) Phys Rev E 65:036143
36. Alexander S, Chaikin PM, Grant P, Morales GJ, Pincus P, Hone D (1984) J Chem Phys 80:5776
37. Leermakers FAM, Ballauff M, Borisov OV (2008) Langmuir 24:10026
38. Roger M, Guenoun P, Muller F, et al (2002) Eur Phys J E 9:313
39. Jusufi A, Likos CN, Löwen H (2002) J Chem Phys 116:11011
40. Jusufi A, Likos CN, Ballauff M (2004) J Colloid Polym Sci 282: 910
41. Mei Y, Hoffmann M, Ballauff M, Jusufi A (2008) Phys Rev E 77:031805
42. Sandberg DJ, Carillo JY, Dobrynin AV (2007) Langmuir 23:12716
43. Plamper FA, Becker H, Lanzendörfer M, Patel M, Wittemann A, Ballauff M, Müller AHE (2005) Macromol Chem Phys 206:1813
44. Ballauff M (2007) Prog Polym Sci 32:1135
45. Guo X, Ballauff M (2001) Phys Rev E 64:015406
46. Karaky K, Reynaud S, Billon L, Francois J, Chreim Y (2005) J Polym Sci Part A Polym Chem 43:5186
47. Plamper FA, Ruppel M, Schmalz A, Borisov OV, Ballauff M, Müller AHE (2007) Macromolecules 40:8361
48. Plamper FA, Schmalz A, Penott-Chang E, Drechsler M, Jusufi A, Ballauff M, Müller AHE (2007) Macromolecules 40:5689
49. Plamper FA, Walther A, Müller AHE, Ballauff M (2007) Nano Lett 7:167
50. Mays JW (1990) Polym Commun 31:170
51. Heinrich M, Rawiso M, Zilliox JG, Lesieur P, Simon JP (2001) Eur Phys J E 4:131
52. Muller F, Guenoun P, Delsanti M, Deme B, Auvray L, Yang J, Mays JW (2004) Eur Phys J E 15:465
53. Muller F, Delsanti M, Auvray L, Yang J, Chen YJ, Mays JW, Demé B, Tirrell M, Guenoun P (2000) Eur Phys J E 3:45
54. Amiel C, Sikka M, Schneider JW, Tsao YH, Tirrell M, Mays JW (1995) Macromolecules 28:3125

55. Guenoun P, Delsanti M, Gaseau D, Auvray L, Cook DC, Mays JW, Tirrell M (1998) Eur Phys J B 1:77
56. Guenoun P, Davis HT, Tirrell M, Mays JW (1996) Macromolecules 29:3965
57. Guenoun P, Muller F, Delsanti M, Auvray L, Chen YJ, Mays JW, Tirrell M (1998) Phys Rev Lett 81:3872
58. Van der Maarel JRC, Groenewegen W, Egelhaaf SU, Lapp A (2000) Langmuir 16:7510
59. Groenewegen W, Egelhaalf SU, Lapp A, van der Maarel JRC (2000) Macromolecules 33:3283
60. Groenewegen W, Lapp A, Egelhaalf SU, van der Maarel JRC (2000) Macromolecules 33:4080
61. Kiserow D, Prochazka K, Ramireddy C, Tuzar Z, Munk P, Webber SE (1992) Macromolecules 25:461
62. Khougaz K, Astafieva I, Eisenberg A (1995) Macromolecules 28:7135
63. Förster S, Hemsdorf N, Leube W, Schnablegger H, Regenbrecht M, Akari S, Lindner P, Böttcher C (1999) J Phys Chem 103:6657
64. de Gennes PG (1979) Scaling concepts in polymer physics. Cornell University Press, Ithaca
65. Alexander S (1977) J Phys (France) 38:983
66. de Gennes PG (1980) Macromolecules 13:1069
67. Pincus P (1976) Macromolecules 9:386
68. Grest GA, Kremer K, Milner ST, Witten TA (1989) Macromolecules 22:1904
69. Grest GA (1994) Macromolecules 27:3493
70. Zifferer G (1999) Macromol Theory Simul 8:433
71. Havrankova J, Limpouchova Z, Prochaska K (2003) Macromol Theory Simul 12:512
72. Hsu HP, Nadler W, Grassberger P (2004) Macromolecules 37:4658
73. Förster S, Burger C (1998) Macromolecules 31:879
74. Bauer BI, Hadjichristidis N, Fetters LI, Roovers JE (1980) J Am Chem Soc 102:2410
75. Willner L, Jacknischke O, Richter D, Roovers J, Zhou LL, Toporowski PM, Fetters LJ, Huang JS, Lin MY, Hadjichrisitidis N (1994) Macromoleules 27:3821
76. Stellbrink J, Willner L, Richter D, Lindner P, Fetters LJ, Huang JS (1999) Macromoleules 32:5321
77. Cogan CA, Gast AP, Capel M (1991) Macromolecules 24:6512
78. Cogan CA, Gast AP, Butun V, Armes SP (1999) Macromolecules 32:4302
79. Held D, Müller AHE (2000) Macromol Symp 157:225
80. Witten TA, Pincus P (1986) Macromolecules 19:2509
81. Witten TA, Pincus PA, Cates ME (1986) Europhys Lett 2:137
82. Likos CN, Löwen H, Watzlawek M, Abbas B, Jucknischke O, Allgaier J, Richter D (1998) Phys Rev Lett 80:4450
83. Likos CN (2001) Phys Rep 348:267
84. Jusufi A, Likos CN (2009) Rev Mod Phys 81:1753
85. Marques CM, Izzo D, Charitat T, Mendes E (1998) Europ Phys J B 3:353
86. Beaudoin E, Borisov OV, Lapp A, Billon L, Hiorns RC, Francois J (2002) Macromolecules 35:7436
87. Beaudoin E, Borisov OV, Lapp A, Francois J (2003) Macromol Symp 191:89
88. Odijk T (1977) J Polym Sci Polym Phys Ed 15:447
89. Skolnick J, Fixman M (1977) Macromolecules 12:688
90. Flory PJ (1953) Principles of polymer chemistry. Cornell University Press, Ithaca
91. de Gennes PG, Pincus P, Velasco RM, Brochard F (1976) J Phys (France) 37:1461
92. Khokhlov AR, Khachaturian KA (1982) Polymer 23:1742
93. Shusharina NA, Rubinstein M (2008) Macromolecules 41:203
94. Kegler K, Salomo M, Kremer F (2007) Phys Rev Lett 98:058304
95. Kegler K, Konieczny M, Dominguez-Espinosa G, Gutsche C, Salomo M, Kremer F, Likos CN (2008) Phys Rev Lett 100:118302
96. Dominguez-Espinosa G, Synytska A, Drechsler A, Gutsche C, Kegler K, Uhlmann P, Stamm M, Kremer F (2008) Polymer 49:4802

97. Elmahdy MM, Synytska A, Drechsler A, Gutsche C, Uhlmann P, Stamm M, Kremer F (2009) Macromolecules 42:9096
98. Zhulina EB, Borisov OV (1997) J Chem Phys 107:5952
99. Isaacson J, Lubensky TC (1980) J Phys Lett 41:L-469
100. Daoud M, Joanny JF (1981) J Phys (France) 42:1359
101. Zimm BH, Stockmayer WH (1949) J Chem Phys 17:1301
102. Birshtein TM, Borisov OV, Zhulina EB, Khokhlov AR, Yurasova TA (1987) Polym Sci USSR 29:1293
103. Fredrickson G (1993) Macromolecules 26:2825
104. Rouault Y, Borisov OV (1996) Macromolecules 29:2605
105. Feuz L, Leermakers FAM, Textor M, Borisov OV (2005) Macromolecules 38:8891
106. Feuz L, Strunz P, Geue T, Textor M, Borisov OV (2007) Europ Phys J E 23:237
107. Hsu H-P, Paul W, Binder K (2010) Macromolecules 43:3094
108. Kiani C, Chen L, Wu YJ, Yee AJ, Yang BB (2002) Cell Res 12:19
109. Thornton DJ, Rousseau K, McGuckin MA (2008) Annu Rev Physiol 70:459
110. Janmey PA, Leterrier J-F, Herrmann H (2003) Curr Opin Colloid Interface Sci 8:40
111. Jones JB, Safinya CR (2008) Biophys J 95:723
112. Beck R, Deek J, Jones JB, Safinya CR (2010) Nat Mater 9:40
113. Mukhopadhyay R, Kumar S, Hoh JH (2004) BioEssays 26:1
114. Zhulina EB, Leermakers FAM (2009) Soft Matter 5:2836
115. Zhulina EB, Leermakers FAM (2007) Biophys J 93:1421
116. Zhulina EB, Leermakers FAM (2007) Biophys J 93:1452
117. Zhulina EB, Leermakers FAM (2010) Biophys 98:462
118. Leermakers FAM, Zhulina EB (2008) BRL 3:459
119. Leermakers FAM, Zhulina EB (2010) Eur Biophys J 39:1323
120. Fleer GJ, Cohen Stuart MA, Scheutjens JMHM, Cosgrove T, Vincent B (1993) Polymers at interfaces. Chapman and Hall, London
121. Borisov OV, Zhulina EB (1997) J Phys II 7:449
122. Semenov AN (1985) Sov Phys JETP 61:733
123. Zhulina EB, Birshtein TM, Borisov OV (2006) Eur Phys J E 20:243
124. Wijmans CM, Zhulina EB (1993) Macromolecules 26:7214
125. Dobrynin AV, Colby RH, Rubinstein M (1995) Macromolecules 28:1859
126. Zhulina EB, Birshtein TM, Borisov OV (1995) Macromolecules 28:1491
127. Wesley RD, Cosgrove T, Thompson L, Armes SP, Billingham NC, Baines FL (2000) Langmuir 16:4467
128. Prinz C, Muller P, Maaloum M (2000) Macromolecules 33:4896
129. Currie EPK, Sieval AB, Fleer GJ; Cohen Stuart MA (2000) Langmuir 16:8324
130. Biesalski M, Johannsmann D, Ruhe J (2002) J Chem Phys 117:4988
131. Matejicek P, Podhajewcka K, Humpolickova J, Uhlik F, Jelinek K, Limpouchova Z, Prochazka K (2004) Macromolecules 37:10141
132. Konradi R, Ruhe J (2005) Macromolecules 38:4345
133. Zhang HN, Ruhe J (2005) Macromolecules 38:4855
134. Xu L, Zhu Z, Borisov OV, Zhulina EB, Sukhishvili SA (2009) Phys Rev Lett 103:N118301
135. Zhulina EB, Borisov OV, Birshtein TM (1999) Macromolecules 32:8189
136. Birshtein TM, Zhulina EB (1996) Ber Bunsen Phys Chem 100:929
137. Mei Y, Lauterbach K, Hoffmann M, Borisov OV, Ballauff M, Jusufi A (2006) Phys Rev Let 97:158301
138. Toomey R, Tirrell M (2008) Annu Rev Phys Chem 59:493
139. Castelnovo M, Evilevitch A (2006) Europhys Lett 73:635
140. Borisov OV, Birshtein TM, Zhulina EB (1988) Polym Sci USSR 30:772
141. Zhulina EB, Borisov OV, Birshtein TM (1988) Polym Sci USSR 30:780
142. Meunier JC, Leemput R (1971) Makromolek Chem B147:191
143. Williams CE, Wafa E (1995) J Phys II (France) 5:1269
144. Aseyev VO, Tenhu H, Winnik FM (2006) Adv Poly Sci 196:1
145. Zeng Q, Pan CY (2006) Eur Polym J 42: 807

146. Lu Y, Witteman A, Ballauff M, Drechsler M (2006) Macromol Rapid Commun 27:1137
147. Khokhlov AR (1980) J Phys A 13:979
148. Raphael E, Joanny JF (1990) Europhys Lett 13:623
149. Dobrynin AV, Rubinstein M, Obukhov SP (1996) Macromolecules 29:2974
150. Lord Rayleigh (1882) Phil Mag 14:184
151. Borisov OV, Zhulina EB (2005) Macromolecules 38:2506
152. Halperin A, Zhulina EB (1991) Europhys Lett 15:417
153. Lyulin AV, Dünweg B, Borisov OV, Darinskii AA (1999) Macromolecules 32:3264
154. Micka U, Holm C, Kremer K (1999) Langmuir 15:4033
155. Borisov OV, Birshtein TM, Zhulina EB (1992) Prog Colloid Polym Sci 90:177
156. Ross R, Pincus P (1992) Macromolecules 25:2177
157. Misra S, Mattice WL, Napper DH (1994) Macromolecules 27:7090
158. Kosovan P, Kuldova J, Limpouchova Z, Prochazka K, Zhulina EB, Borisov OV (2010) Soft Matter 6:1872
159. Zhulina EB, Borisov OV (2002) Macromolecules 35:9191

Adv Polym Sci (2011) 241: 57–129
DOI:10.1007/12_2011_114

Published online: 8 April 2011

Self-Assembled Structures of Amphiphilic Ionic Block Copolymers: Theory, Self-Consistent Field Modeling and Experiment

Oleg V. Borisov, Ekaternia B. Zhulina, Frans A.M. Leermakers, and Axel H.E. Müller

Abstract We present an overview of statistical thermodynamic theories that describe the self-assembly of amphiphilic ionic/hydrophobic diblock copolymers in dilute solution. Block copolymers with both strongly and weakly dissociating (pH-sensitive) ionic blocks are considered. We focus mostly on structural and morphological transitions that occur in self-assembled aggregates as a response to varied environmental conditions (ionic strength and pH in the solution). Analytical theory is complemented by a numerical self-consistent field approach. Theoretical predictions are compared to selected experimental data on micellization of ionic/hydrophobic diblock copolymers in aqueous solutions.

O.V. Borisov (✉)
Institut Pluridisciplinaire de Recherche sur, l'Environnement et les Matériaux,
UMR 5254 CNRS/UPPA, Pau, France
and
Institute of Macromolecular Compounds of the Russian Academy of Sciences,
199004 St. Petersburg, Russia
e-mail: oleg.borisov@univ-pau.fr

E.B. Zhulina
Institute of Macromolecular Compounds of the Russian Academy of Sciences,
199004 St. Petersburg, Russia
e-mail: kzhulina@hotmail.com

F.A.M. Leermakers
Laboratory of Physical Chemistry and Colloid Science, Wageningen University Dreyenplein 6,
6703 HB Wageningen, The Netherlands
e-mail: frans.leermakers@wur.nl

A.H.E. Müller
Makromolekulare Chemie II and Bayreuther Zentrum für Kolloide und Grenzflächen,
Universität Bayreuth, 95440 Bayreuth, Germany
e-mail: axel.mueller@uni-bayreuth.de

Keywords Amphiphilic block copolymers · Micelles · Polyelectrolytes · Polymorphism · Self-assembly

Contents

1 Introduction

The assembly of amphiphilic (macro)molecules in aqueous environments is a generic mechanism of self-organization on multiple length scales that is amply exploited by nature. The spontaneous formation of self-assembled structures of phospholipids and biomacromolecules, exemplified by living cells, is the outcome

of a delicate balance between attractive and repulsive forces, among which hydrophobic attraction, hydrogen bonding, metal-coordination forces, and steric or electrostatic repulsion play dominant roles.

In the realm of technology, the self-assembly of synthetic amphiphilic molecules is also widely exploited. Many water-based industrial formulations include small amphiphilic molecules (surfactants) and polymeric amphiphiles, which self- and co-assemble with other molecules and colloidal (nano)particles.

In the past decade, significant progress has been made in terms of understanding the self-assembly of amphiphilic diblock copolymers in selective solvents [1–9]. In aqueous solutions, the assembly is driven by hydrophobic attraction between associating blocks and is counterbalanced by electrostatic and/or steric repulsions between ionic or neutral water-soluble blocks. As a result, diverse nanostructures emerge. Among them, spherical core–corona micelles, formed by copolymers with a relatively long solvophilic block, have been extensively studied. Similarly to low molecular weight amphiphiles (surfactants), block copolymers with more bulky (longer) solvophobic blocks may self-assemble in cylindrical wormlike micelles, bilayer vesicles ("polymersomes"), lamellar mesophases, etc.

Self-assembled nanoaggregates of amphiphilic block copolymers attract strong research interest due to the large number of emerging and potential applications. These include smart nanocontainers for encapsulation, delivery and controlled release of biologically active molecules in nanomedicine, food and personal care products, and agrochemistry. Uptake of heavy metal ions, radionuclides, and toxic organic compounds is being explored for water treatment and environment monitoring purposes. Polymeric nanostructures of different and controlled morphologies could serve as molecular templates for nanoelectronic devices.

Necessary requirements for many applications include: (1) precise control over the size (on nanometer length scale) and morphology of the assembled aggregates, and (2) pronounced stimuli-responsive properties. The latter imply that these structures can change their size, aggregation number, etc. in a significant way when the physical and/or chemical properties of the surroundings (temperature, pH, ionic strength, etc.) are varied smoothly, or that the structures recognize weak specific stimuli such as trace concentrations of biologically active or toxic molecules. Both requirements can be met by nanoaggregates that emerge as a result of the assembly of amphiphilic block copolymers with tailored molecular architecture. The latter implies properly chosen molecular weight of the blocks and the correct balance of intramolecular hydrophilic and hydrophobic interactions or, more specifically, an appropriate composition of the macromolecule in terms of non-ionic, ionic and pH-sensitive, and hydrophobic (thermosensitive) components.

Self-assembly of block copolymers that are made of poly(ethylene oxide), PEO, as the hydrophilic non-ionic block, has been extensively explored. The research interest in PEO-containing block copolymers was motivated, to a great extent, by potential biomedical applications, which rely on the finding that PEO moieties are biocompatible. Because amphiphilic block copolymers of PEO and poly(propylene oxide) PPO (pluronics) are produced on an industrial scale, research on these non-ionic polymeric surfactants resulted in many technological applications. Both PPO and PEO are thermoresponsive, having a low solution critical temperature (LSCT),

so nanostructures formed from pluronics also demonstrate thermoresponsive features. Unfortunately, they do not show a pronounced response to salt or pH changes in the solution.

Structures formed by amphiphilic block copolymers composed of a hydrophilic block with ionic and, in particular, pH-sensitive (weak polyelectrolyte) segments, linked to a hydrophobic block, are more responsive. This is because the strength of repulsive Coulomb interactions between the polyelectrolyte (PE) segments can be efficiently tuned by variations in pH or/and ionic strength in the aqueous solution, while their thermoresponsive nature can be maintained if the hydrophobic block is well chosen.

The responsive features of micelles with a PE corona, e.g., the ability of micelles to change their size, aggregation number and morphology, as a response to variations in ionic strength and pH, were demonstrated and studied experimentally. However, association of the hydrophobic blocks in water often results in a dense core wherein structural rearrangements are hindered by high energy barriers (the cores are found in a glassy state). In this state, the dynamic equilibrium between copolymers in the micelle and freely dispersed in solution (unimers) does not exist, and these micelles must be characterized as out-of-equilibrium "frozen" aggregates. Under preparation conditions, either the temperature is very high or mixtures of water and a common (organic) co-solvent are used. In these mixed solvents or at high temperatures, the dynamic equilibrium between unimers and aggregates is attained and the responsive features can be exploited.

The response of frozen micelles to varied ionic strength and pH is thus limited to conformational changes in the hydrated PE corona domains, and is similar to that discussed for PE stars in [10].

One of the possible solutions for design of truly responsive ("dynamic") micelles is to use copolymers with "soft" hydrophobic blocks. For example, at the stage of copolymer synthesis, one can incorporate a small fraction of pH-sensitive comonomer units in the hydrophobic moiety. This opens up the possibility of turning on some repulsive contributions in a net attractive domain, leading to a softer core. Alternatively, one can opt for copolymers that are made of a PE block that is linked to a thermosensitive block [11]. This gives the possibility of triggering the formation and dissociation of micelles by variations in the temperature [12].

In spite of significant experimental efforts made in the last decade, it remains difficult to provide an unambiguous proof of the dynamic (equilibrium) nature of polymeric micelles. A review of selected experimental results on the stimuli-responsive behavior of PE micelles is presented at the end of this chapter.

A number of theoretical studies have been devoted to analysis of the self-assembly of amphiphilic ionic/hydrophobic diblock copolymers [13–24]. Most of these studies considered copolymers with strongly dissociating (also referred to as "quenched") PE blocks [13–18, 20] and extensively exploited the analogy between the conformation of PE blocks in a corona and that in a spherical PE brush [25–33] or PE stars (see [10] for a review). The micellization and the responsive behavior of nanostructures formed by copolymers with pH-sensitive PE blocks have also been systematically studied in recent years [19, 21–23].

We present an overview of the statistical thermodynamic theories of self-assembly in aqueous media for amphiphilic diblock copolymers that are composed of one PE block and one hydrophobic block. In all theoretical models, the hydrophobic block is assumed to be "soft" enough to ensure the equilibrium character of self-assembly. We outline here the arguments that were presented in more detail in the corresponding original papers [18–23].

We start with a brief reminder of the theory of self-assembly in a selective solvent of non-ionic amphiphilic diblock copolymers. Here, the focus is on polymorphism of the emerging copolymer nanoaggregates as a function of the intramolecular hydrophilic/hydrophobic balance. We then proceed with a discussion of the structure of micelles formed by block copolymers with strongly dissociating PE blocks in salt-free and salt-added solutions. Subsequently, we analyze the responsive behavior of nanoaggregates formed by copolymers with pH-sensitive PE blocks. The predictions of the analytical models are systematically complemented by the results of a molecularly detailed self-consistent field (SCF) theory. Finally, the theoretical predictions are compared to the experimental data that exist to date.

2 Thermodynamic Principles of Micellization

2.1 Critical Micelle Concentration and Aggregation Number

The general principles of self-assembly of amphiphilic molecules into finite-sized aggregates (micelles) are described in a number of classic books [34–36]. In our analysis of micelle formation we apply the equilibrium "close association" model. That is, we assume first that only one population of micelles, with an aggregation number p (number of copolymers in one aggregate), is present in the system at any given concentration of amphiphiles in the solution, or that there are no micelles at all; and second, that the free energy per molecule in a micelle, F_p, exhibits a minimum at a certain value of the aggregation number, $p = p_0$.

The thermodynamic model of micellization, presented here, describes the association of any amphiphilic molecules, including low molecular weight surfactants or polymeric amphiphiles. The physical origin of the minimum in the free energy, as a function of p, is specified by the molecular architecture and the interactions between amphiphilic molecules involved in the assembly, and will be discussed in the corresponding sections. An extension of the model for the case of a continuous distribution of micelles with respect to aggregation number (polydispersity of the aggregates) involves the value of $\partial^2 F_p/\partial p^2$. If this quantity is small in the vicinity of $p = p_0$, then the micelle distribution is wide, and vice versa [37]. The approximation of micelle monodispersity is essential for application of the numerical SCF model which is discussed in Sect. 9.

We consider a solution with a volume V that contains N_p amphiphilic block copolymer molecules. The total number density of the amphiphiles is $c = N_p/V$. We assume that c_1 is the concentration (number density) of the amphiphiles that are

found in the unimer (nonassociated) state, whereas $c_{\mathrm{mic}} = (c - c_1)/p$ is the number density of the monodisperse micelles with aggregation number p. The relevant thermodynamic potential is the Helmholtz free energy $F(V,N_p,T)$. Assuming that the solution is dilute and that intermicelle and micelle–unimer interactions can be ignored, the free energy of the system can be presented as:

$$F/Vk_{\mathrm{B}}T = pc_{\mathrm{mic}}F_p/k_{\mathrm{B}}T + c_{\mathrm{mic}}(\ln c_{\mathrm{mic}} - 1) + c_1F_1/k_{\mathrm{B}}T + c_1(\ln c_1 - 1), \quad (1)$$

wherein k_{B} is the Boltzmann constant and T is the temperature. Here, the first term represents the free energy of the micelles (F_p is the free energy of one amphiphile in a micelle comprising p molecules), the second term is the translational entropy of micelles, the third term is the free energy of unimers, and the last term is the translational entropy of unimers.

The minimization of the Helmholtz free energy, F, with respect to p and c_{mic}, ($\partial F/\partial p = 0$, $\partial F/\partial c_{\mathrm{mic}} = 0$) leads to the following equations:

$$p\frac{\partial F_p}{\partial p} = \frac{k_{\mathrm{B}}T}{p}\ln c_{\mathrm{mic}}, \quad (2)$$

$$F_p + p\frac{\partial F_p}{\partial p} \equiv \frac{\partial (pF_p)}{\partial p} = \mu_1(c_1), \quad (3)$$

where:

$$\mu_1(c_1) = F_1 + k_{\mathrm{B}}T\ln c_1 \quad (4)$$

is the chemical potential of unimer, and (3) implies the equality of chemical potentials of a free unimer and an amphiphile incorporated in a micelle.

Equations (2)–(4) determine the equilibrium aggregation number, p_{eq}, the number densities of unimers, c_1, and of micelles, c_{mic}, at a given value of the total number density of amphiphiles, c. With the account of (4), we can rewrite (2) as:

$$k_{\mathrm{B}}T\ln c_{\mathrm{mic}} = -[pF_p - p\mu_1(c_1)] = -\Omega(c_1), \quad (5)$$

where Ω is (by definition) the grand potential of a micelle.

Note that the condition of thermodynamic stability requires that the free energy of a micelle, $F_{\mathrm{micelle}} \equiv pF_p$, is a concave function of the aggregation number, p. That is:

$$\frac{\partial^2 (pF_p)}{\partial p^2} > 0. \quad (6)$$

Therefore, as follows from (3) and (5), in a thermodynamically stable system:

$$\partial \mu_1(c_1)/\partial p \geq 0 \quad (7)$$

and:

$$\frac{\partial \Omega}{\partial p} = -p\frac{\partial \mu_1(c_1)}{\partial p} \leq 0. \quad (8)$$

Hence, under equilibrium conditions, the chemical potential of a unimer must be an increasing function of the aggregation number p, and the grand potential of a micelle, $\Omega(p)$, must be a decreasing function of p.

The minimal aggregation number, $p = p_{\min}$, in a thermodynamically stable micelle, is determined by the condition:

$$\left(\frac{\partial^2(pF_p)}{\partial p^2}\right)_{p=p_{\min}} = 0. \tag{9}$$

That is, $\partial\Omega/\partial p = \partial\mu_1/\partial p = 0$ at $p = p_{\min}$, and the micelles with $p < p_{\min}$ are thermodynamically unstable.

A minimal micelle with $p_{\text{eq}} = p_{\min}$ appears in the system at a certain (minimal) threshold concentration, $c_{\min}$, which can be identified as the "theoretical critical micellization concentration". Below this threshold, $c \le c_{\min}$, no micelles and only unimers are found in the solution. At amphiphile concentration $c = c_{\min}$, the number density of micelles, $c_{\text{mic}}^{(\min)} = \exp[-\Omega(p_{\min})/k_{\text{B}}T]$, is negligible with respect to the unimer density, $c_1^{(\min)}$. A subsequent increase in the concentration of amphiphiles, $c \ge c_{\min}$, leads to an increase in both the concentration of micelles, c_{mic}, and the concentration of unimers, c_1, and an increase in both the chemical potential of unimers and the aggregation number, p_{eq}.

Often, the critical micelle concentration (CMC) is defined as the total concentration of amphiphiles at which the number of unimers is equal to the number of amphiphiles incorporated into the micelles, $pc_{\text{mic}} = c_1 = \text{CMC}/2$. In this case, the CMC is specified by the equation:

$$k_{\text{B}}T \ln\left(\frac{\text{CMC}}{2}\right) = \left(\frac{\partial(pF_p)}{\partial p}\right)_{p=p_{\text{eq}}(\text{CMC})} - F_1, \tag{10}$$

where F_p is the free energy per chain in the equilibrium micelle with $p = p_{\text{eq}}(\text{CMC})$.

A frequently used simplifying approximation is based on neglecting the translational entropy of micelles (i.e., the second term in (1) is omitted). This approximation is justified as long as the aggregation number in an equilibrium micelle is large. Then, (2)–(4) reduce to:

$$\frac{\partial F_p(p)}{\partial p} = 0, \tag{11}$$

$$c_1 = \exp[(F_p(p_0) - F_1)/k_{\text{B}}T], \tag{12}$$

$$c_{\text{mic}} = \frac{c - c_1}{p_0}. \tag{13}$$

Within this approximation, (11) specifies the equilibrium aggregation number p_0, corresponding to the minimum of function $F_p(p)$, which does not depend on the concentration of amphiphiles. According to (12), the concentration of unimers, c_1, remains constant at $c \ge \text{CMC}$, irrespective of the total concentration of amphiphiles, c.

According to the above definition of CMC, an approximate expression for the CMC is given by:

$$k_{\mathrm{B}}T \ln\left(\frac{\mathrm{CMC}}{2}\right)_{\mathrm{approx}} = F_p(p_0) - F_1 = \left(\frac{\partial(pF_p)}{\partial p}\right)_{p=p_0} - F_1. \tag{14}$$

As follows from (2), $(\partial F_p/\partial p)_{p=p_{\mathrm{eq}}} < 0$. Because F_p exhibits a minimum at $p = p_0$, the equilibrium micelle is always smaller than that predicted by the approximate theory, i.e., $p_{\mathrm{eq}} \leq p_0$. An increase in the concentration of amphiphiles beyond the c_{min} threshold results in a progressive increase in the equilibrium aggregation number p_{eq}, that asymptotically approaches the value of p_0.

A comparison of (10) and (14) indicates that because of the stability condition, (8), the exact CMC [defined by (10)] is smaller than the CMC obtained from the approximate analytical model, (14). Accounting for the translational entropy of micelles leads, therefore, to a lower value of the aggregation number, $p_{\mathrm{eq}}(c) < p_0$, and a lower CMC.

The statistical thermodynamic theory of self-assembly of amphiphilic ionic/hydrophobic diblock copolymers, reviewed in this chapter, is based on the simplifying approximation (11)–(13), which neglects the translational entropy of the micelles. In particular, we pre-assume that at the copolymer concentration beyond the CMC, the solution contains only micelles with the "optimal" aggregation number, $p = p_0$, which corresponds to the minimum of the free energy, F_p. As a result, the fluctuations around the most probable ground state, $p = p_0$, which give rise to the equilibrium distribution with respect to the aggregation number (polydispersity of the aggregates), are also neglected.

The simplified model enables one to account, in a straightforward way, for the effects of charge on the micellization of ionic amphiphiles. The electrostatic interactions between ionic groups of the amphiphilic molecules in a micelle are included in the free energy term, F_p. In a salt-free solution, the association of amphiphiles in aggregates is accompanied by the localization ("condensation") of counterions, which are necessarily present in the system to ensure its total electroneutrality. While in solution of unimers (below the CMC), the counterions are distributed fairly uniformly, the formation of large aggregates leads to a restriction in the mobility of counterions. More specifically, a significant fraction of counterions are "trapped" in the vicinity of an aggregate due to the large local attractive electrostatic potential. This effect is well known for simple ionic amphiphiles, but becomes much more pronounced for polymeric species. Consistent with the discussion in [10], a major fraction of the counterions in PE micelles are entrapped in the highly hydrated PE coronas. Hence, the aggregation of PE copolymers in micelles is opposed not only by losses in the translational entropy of the polyamphiphiles but, much more significantly, by losses in the translational entropy of mobile counterions. Formally, the effect of counterions can be accounted for by adding the term:

$$F_{\mathrm{ions}}/Vk_{\mathrm{B}}T = c_1 Q[\ln(Qc_1) - 1] \tag{15}$$

to the free energy in (1). Here, Q is the number of elementary charged groups in one polyamphiphile and we assume that the "bare" charge, pQ, in the corona of a micelle with p copolymers, is totally neutralized by the localized counterions. The validity of this approximation is discussed in [10]. A more accurate analysis indicates that the degree of neutralization of the micelle charge by its counterions (the fraction of trapped counterions) is a function of p, which, however, approaches the plateau value of unity at large $p \gg 1$.

The free energy, (1), complemented by the contribution due to counterions, cf. (15), can be minimized with respect to c_{mic} and p. When the translational entropy of micelles is neglected, the optimal aggregation number, $p = p_0$, is still given by (11). The concentration of unimers that coexist with micelles, and thus the CMC, is, however, significantly larger than for neutral (uncharged) amphiphiles:

$$c_1 \approx \frac{1}{Q} \exp\left[(F_p(p_0) - F_1)/Qk_{\mathrm{B}}T\right] \tag{16}$$

provided that $Q \gg 1$. This increase in the CMC upon an increase in Q is a direct consequence of the loss in translational entropy of a large number of counterions upon the aggregation of polyamphiphiles. A similar effect of significant increase in the CMC for ionic low molecular weight surfactants has been discussed in [38]. An addition of salt to the solution results in the decrease of excess electrostatic potential associated with the PE corona and, at sufficiently high ionic strengths, (11)–(13) apply for ionic polyamphiphiles.

2.2 Block Copolymer Micelles

As follows from Sect. 2.1, in order to find the optimal (equilibrium) aggregation number and the CMC, a theoretical model has to specify the functional form of the free energy F_p per amphiphile as a function of p in an aggregate of a given morphology. This free energy depends on the molecular architecture as well as on the interaction parameters, which, in general, can be affected by the environmental conditions (temperature, ionic strength, pH, etc.).

We consider a dilute solution of diblock copolymer, which is composed of a hydrophilic (non-ionic or ionic) block with a degree of polymerization N_A and a hydrophobic (associating) block with a degree of polymerization N_B. Here, we focus mostly on the specifics of self-assembly of the copolymer whose hydrophilic block A is charged.

A poor solubility of the hydrophobic blocks B in water provides the driving force for self-assembly of polymeric amphiphiles in aqueous media. This driving force is counterbalanced by repulsive interactions between the hydrophilic blocks, which ensure the formation of finite-sized aggregates in favor of a macroscopic phase separation at concentrations above the CMC. In these aggregates, blocks B associate in a dense hydrophobic core that is surrounded by a hydrated corona, formed by the

soluble blocks A. The preferred morphology of the core domain in the equilibrium aggregate is controlled by a subtle balance of solvophilic–solvophobic interactions, and the conformational entropy of both blocks.

Due to the strong hydrophobicity of the blocks B, the interface between the collapsed hydrophobic domain and the surrounding aqueous environment is narrow compared to the size of the core. Therefore, the coronal blocks A can be envisioned as tethered to the interface to form a polymer brush [33, 39, 40]. The hydration of the corona and the repulsion between different coronae ensure the solubility (aggregative stability) of the micelles in water.

2.2.1 Corona Domain

The conformational characteristics of the corona-forming blocks are controlled by the balance between repulsive monomer–monomer interactions and the conformational entropy penalty for chain stretching.

For uncharged coronal blocks A, the short-ranged (van der Waals) interactions between monomer units are described in terms of a virial expansion. The latter accounts for the monomer–monomer binary (pair) interactions, with second virial coefficient $v_A a^3$, or the ternary interactions with third virial coefficient $w_A a^6$. We assume that the monomer unit length, a, is the same for both blocks A and B. In the following, we use a as a unit length to make all lengths dimensionless and eliminate a in further equations. We also assume that the (dimensionless) second virial coefficient $v_A \geq 0$ and that the third virial coefficient $w_A \simeq 1$.

The ionization of the soluble blocks A of the polymeric amphiphile introduces long-ranged repulsive interactions in the corona of a micelle. We discuss separately the cases of amphiphilic diblock copolymers containing strongly dissociating ("quenched") and weakly dissociating ("annealing" or pH-sensitive) PE block A linked to the associating hydrophobic block B. In the former case, the fraction of charged monomer units, α_b, in the block A is quenched according to its chemical sequence (as in the case of, e.g., partially sulfonated polystyrene). In the latter case, the fraction of charged monomer units, $\alpha(\mathbf{r})$, is controlled by the local pH (i.e., minus the log of the proton molar concentration), which depends on the bulk (buffer) pH, and the local electrostatic potential $\Psi(\mathbf{r})$. The degree of dissociation of the monomer unit, $\alpha(\mathbf{r})$, of a weak polyacid depends on the local concentration $c_{H^+}(\mathbf{r})$ of hydrogen ions via the mass action law:

$$\frac{\alpha(\mathbf{r})}{1-\alpha(\mathbf{r})} = \frac{K_{\mathrm{a}}}{c_{H^+}(\mathbf{r})}, \tag{17}$$

where K_a is the acidic ionization constant for an isolated monomer. For a polybase, the ionization occurs through the protonation of the monomers, and a generalization of the theory is straightforward.

2.2.2 Core Domain

The compact core of a micelle is characterized by a uniform polymer density, $\varphi(\chi_{BS})$, chemical potential per monomer unit, $k_{\mathrm{B}}T\mu_B(\chi_{BS})$, and excess free energy per unit area of the core–water interface, $k_{\mathrm{B}}T\gamma(\chi_{BS})$. Here, $\chi_{BS}(T)$ is the Flory–Huggins parameter of monomer (B)–solvent (S) interaction, and $\chi_{BS}(T) \geq \chi_{BS}(\theta) = 1/2$ under poor solvent conditions for the monomer units of block B. Although the solubility of polymers in organic solvents usually decreases with a decrease in temperature, $\partial\chi(T)/\partial T \leq 0$, the situation is more complex in aqueous solutions. In particular, it appears that the solubility of thermosensitive block B in water typically decreases with an increase in temperature [11], and hence $\partial\chi_{BS}(T)/\partial T \geq 0$. In this case, the collapse of blocks B and the aggregation of the block copolymers into micelles occur at $T \geq$ LCST, where LCST is the lower critical solution temperature.

Within this so-called volume approximation [41], all the partial parameters, $\varphi(\chi_{BS})$, $\mu_B(\chi_{BS})$, and $\gamma(\chi_{BS})$ are independent of the core size. This approximation is applicable as long as the width of the core–water interface, Δ, is much smaller than the core size, R_{core}, i.e., $R_{\mathrm{core}} \gg \Delta$. The excess free energy of the core–water interface originates from an enhanced probability of unfavorable contacts between solvophobic monomer units of block B and solvent (water) molecules in the interfacial region. The surface tension γ also accounts for local conformational entropy losses in the segments of blocks B localized close to the core–solvent interface.

The explicit dependencies of $\varphi(\chi_{BS})$, $\mu_B(\chi_{BS})$, and $\gamma(\chi_{BS})$ on the χ_{BS} parameter can be obtained [42] within the Flory theory of polymer solutions [43]. However, in the vicinity of the theta point (or LCST) for the core-forming block B, $|\chi(\theta) - \chi(T)|/\chi(\theta) \approx |T-\theta|/\theta \ll 1$, all the partial parameters can be expressed [41, 44] as power law functions of the dimensionless virial coefficients of monomer–monomer interactions for block B:

$$\varphi \approx -v_B/2w_B \cong \tau, \tag{18}$$

$$\gamma/k_{\mathrm{B}}T \approx v_B^2/2^{7/2}3^{1/2}w_B^{3/2} \cong \tau^2. \tag{19}$$

Here, the second virial coefficient (excluded-volume parameter), $v_B \cong [1 - 2\chi(T)] \leq 0$, is negative because water is a poor solvent for the hydrophobic block B. The third virial coefficient, w_B, is positive, and $\tau \equiv |T-\theta|/\theta$ is the relative deviation from the theta temperature. At small deviations from the theta point, $\tau \ll 1$, the surface tension γ and the polymer volume fraction φ are related as $\gamma/k_{\mathrm{B}}T \cong \varphi^2$. However, at larger deviations from the theta point, φ becomes comparable to unity and the latter relationship breaks down. Because in a typical experimental situation $\varphi \cong 1$, we treat φ and γ as two independent parameters. Note that in a general case, surface tension γ and width Δ of the core–corona interface depend on both the polymer–solvent interaction parameter $\chi_{BS}(T)$ for the core-forming block and the incompatibility χ_{AB} between monomers of blocks A and B. That is, γ could depend on the concentration of monomers of the coronal block A near the core surface. We, however, neglect this (weak) dependence and assume that the surface tension γ is not affected by conformations of the coronal blocks in a micelle.

The combination of packing constraints (constant concentration of B segments in the core and the localization of junctions between blocks B and A at the core–corona interface) implies the stretching of the core-forming blocks in the radial direction. This stretching leads to conformational entropy losses in the core-forming blocks. For a given core surface area per molecule, the stretching of a core block is maximal in a spherical geometry, and it decreases with decreasing curvature, i.e. going from spherical to cylindrical to lamellar geometries. Explicit expressions for the conformational entropy of core-forming blocks are presented below.

2.2.3 Free Energy

The free energy F per one block copolymer in a micelle can be presented as:

$$F = F_{\text{corona}} + F_{\text{interface}} + F_{\text{core}}. \tag{20}$$

Here, the term F_{corona} includes contributions due to the conformational entropy of the coronal blocks and the (repulsive) interactions in the coronal domain. The term $F_{\text{interface}}$ is the excess free energy of the core–water interface. It is proportional to the interfacial area, s, per copolymer molecule:

$$F_{\text{interface}}/k_{\text{B}}T = \gamma s. \tag{21}$$

Finally, the term $F_{\text{core}} \sim k_{\text{B}}TR_{\text{core}}^2/N_B$ accounts for the conformational entropy of stretched core-forming blocks, for which the numerical prefactor depends on the particular morphology of the aggregate.

The volume contribution, $N_B\mu_B$, to the free energy of the collapsed core-forming block is independent of the aggregation number, p, and therefore is disregarded in subsequent equations.

The second term in (20) favors larger micelles (the area per chain, s, is a decreasing function of the aggregation number, p), whereas the first and the last terms are increasing functions of p, and thus limit the growth of micelles.

As discussed below, the first two terms in (20) always dominate over the last term, i.e., the area per chain, s, is determined by the balance between the repulsive interactions in the corona and the excess free energy of the interface. The conformational entropy of the core-forming blocks, however, controls the morphology of the aggregates if the size of the core exceeds that of the corona (so-called crew-cut micelles, vesicles).

A minimization of the free energy, (20), with respect to its structural parameters, i.e., the aggregation number p or, equivalently, the core radius or area of the core–water interface per molecule, enables one to specify the values of structural parameters, corresponding to the minimum in the free energy of an aggregate of a given morphology. A subsequent comparison of the free energies, corresponding to the "optimal" aggregates of different morphologies, allows one to identify which morphology has the lowest free energy, i.e., which is the equilibrium morpholigy.

Finally, making use of the theory of polymer and PE brushes of different morphologies, one can calculate experimentally observable properties such as the radius of gyration and/or hydrodynamic radius of equilibrium aggregates.

3 Scaling Theory of Non-ionic Block Copolymer Micelles

3.1 Spherical Non-ionic Micelles

We first review the main results of the scaling theory for micelles formed by block copolymers with a neutral (non-ionic) soluble block [37, 45–50].

In the case of strongly asymmetric block copolymers ($N_A \gg N_B$), the size of the micellar core, R_{core}, is much smaller than the radius R_{corona} of the corona. In this case, "starlike" micelles with spherical cores are formed (Fig. 1a). In the opposite limit of short hydrophilic block, $N_A \ll N_B$, the size of micellar core, R_{core}, exceeds by far the thickness of the corona. The coronae of these crew-cut micelles can be viewed as quasi-planar polymer brushes [51, 52], see Fig. 1b.

In the framework of the scaling theory, the corona of a spherical micelle can be envisioned [53–56] as an array of concentric spherical shells of closely packed blobs. The blob size, $\xi(r) \cong r/p^{1/2}$, grows as a function of the radial distance r from the center of the core. Each blob comprises a segment of the chain within the local correlation length of the monomer density fluctuations [57], and corresponds to a $\sim k_{\text{B}}T$ contribution to the free energy of steric repulsion between the coronal chains. After calculating the total number of blobs in the micellar corona, one finds the free energy (per coronal chain) as:

$$F_{\text{corona}}(p)/k_{\text{B}}T \cong p^{1/2} \ln\left(\frac{R_{\text{corona}}}{R_{\text{core}}}\right), \tag{22}$$

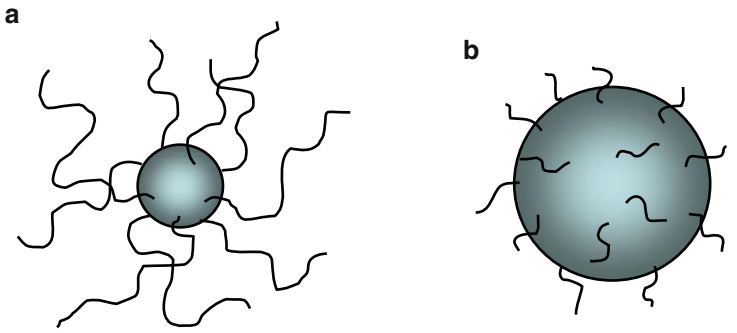

Fig. 1 Spherical starlike (**a**) and crew-cut (**b**) block copolymer micelles

where:

$$R_{\text{core}} \cong (pN_B/\varphi)^{1/3} \tag{23}$$

is the radius of micellar core, R_{corona} is the outmost radius of the corona, and $H_{\text{corona}} = R_{\text{corona}} - R_{\text{core}}$ is its thickness. The excess free energy of the core–corona interface is given by:

$$F_{\text{interface}}(p)/k_{\text{B}}T \cong \gamma s \cong \gamma \left(\frac{N_B}{\varphi}\right)^{2/3} p^{-1/3}, \tag{24}$$

where:

$$s \cong R_{\text{core}}^2/p \cong (N_B/\varphi)^{2/3} p^{-1/3} \tag{25}$$

is the area of the core–corona interface per chain.

Finally, the conformational entropy contribution of stretching in the radial direction of the core-forming block B scales as:

$$F_{\text{core}}(p)/k_{\text{B}}T \cong R_{\text{core}}^2/N_B. \tag{26}$$

3.1.1 Starlike Spherical Non-ionic Micelles

For strongly asymmetric copolymers, $N_A \gg N_B$, the structure of a micelle is controlled by the balance of the coronal free energy, F_{corona}, and the excess free energy of the core–corona interface, $F_{\text{interface}}$.

The minimization of the free energy with respect to p results in the equilibrium aggregation number:

$$p_{\text{eq}} \cong \gamma^{6/5} (N_B/\varphi)^{4/5} \left(\ln \frac{R_{\text{corona}}}{R_{\text{core}}}\right)^{-6/5}. \tag{27}$$

Here, $R_{\text{corona}} \cong N_A^{\nu} p^{(1-\nu)/2} v_A^{2\nu-1}$ is the external radius of the corona, and ν is the Flory exponent for the coronal block A ($\nu \approx 3/5$ and $\nu = 1/2$ under good and theta-solvent conditions, respectively).

With the accuracy of the logarithmic factors, the corona and the core radii are given by:

$$R_{\text{corona}} \cong N_A^{\nu} v_A^{2\nu-1} \gamma^{3(1-\nu)/5} \left(\frac{N_B}{\varphi}\right)^{2(1-\nu)/5} \tag{28}$$

and:

$$R_{\text{core}} \cong \gamma^{2/5} \left(\frac{N_B}{\varphi}\right)^{3/5} \tag{29}$$

respectively.

An important feature of (27), (29) is the absence of a power law dependence of the aggregation number p_{eq} and R_{core} on the length N_A of the coronal block. Micelles are starlike, i.e., $R_{corona} \gg R_{core}$, provided that:

$$N_A \gg \gamma^{(3\nu-1)/5\nu} v_A^{(1-2\nu)/\nu} \left(\frac{N_B}{\varphi}\right)^{(2\nu+1)/5\nu}. \tag{30}$$

By using (22), (24), and (27), one can calculate the free energy of the equilibrium micelle, and, by using (14), estimate the CMC as:

$$\ln \mathrm{CMC} \approx -\gamma \left(\frac{N_B}{\varphi}\right)^{2/3} + \gamma^{3/5} \left(\frac{N_B}{\varphi}\right)^{2/5} \left(\ln \frac{R_{corona}}{R_{core}}\right)^{2/5}, \tag{31}$$

where $F_{interface}(p=1)/k_BT \cong \gamma(N_B/\varphi)^{2/3} \cong (N_B\tau^2)^{2/3}$ is the excess interfacial free energy of an individual block B collapsed in water. The latter provides the dominant contribution to the CMC [the first term in (31)]. The second term in (31) describes the repulsive interactions in the corona, balanced with the excess interfacial free energy, (24). As long as the aggregation number in the equilibrium micelle $p_{eq} \gg 1$, the second term in (31) is relatively small with respect to the first (dominant) term. Hence, in the case of non-ionic copolymer micelles, the CMC is determined mostly by the solubility of hydrophobic block B and is weakly affected by the properties of the coronal block A. An increase in length of the soluble block A leads to the logarithmic increase in the CMC via the increase in R_{corona}. These theoretical predictions are in qualitative agreement with experimental findings [58].

3.1.2 Crew-Cut Spherical Non-ionic Micelles

In the case of crew-cut micelles, $H_{corona} \ll R_{core}$ and the logarithm in (22) can be expanded up to the term linear in H_{corona}/R_{core}, to give $F_{corona}/k_BT \cong H_{corona}/s^{1/2} \cong H_{corona}/\xi$. The thickness of the corona, H_{corona}, scales as $H_{corona} \cong N_A s^{-(1-\nu)/2\nu} v_A^{(2\nu-1)/\nu}$. In the framework of the Alexander–de Gennes blob model [51, 52], the micellar corona (the planar brush) can be envisioned as an array of closely packed blobs with size $\xi \cong s^{1/2}$, equal to the average distance between the coronal blocks. We note that a constant size of the blobs implies $H_{corona} \sim N_A$. The number of coronal blobs per chain $\sim H_{corona}/\xi$ is proportional to the free energy of the interchain repulsion that equals $F_{corona}/k_BT \cong N_A s^{-1/2\nu} v_A^{(2\nu-1)/\nu}$.

Taking the relation $s \cong (N_B/\varphi_B)^{2/3} p^{-1/3}$ into account and minimizing the free energy with respect to p, one obtains the equilibrium aggregation number:

$$p_{eq} \cong \left(\frac{N_B}{\varphi}\right)^2 \left(\frac{N_A}{\gamma}\right)^{-6\nu/(2\nu+1)} v_A^{-6(2\nu-1)/(2\nu+1)} \tag{32}$$

and the core radius, which determines the overall size of the crew-cut micelle:

$$R_{\text{core}} \cong \frac{N_B}{\varphi}\left(\frac{N_A}{\gamma}\right)^{-2\nu/(2\nu+1)} v_A^{-2(2\nu-1)/(2\nu+1)}. \tag{33}$$

The core–corona surface area per chain is given by

$$s_{\text{eq}} \cong \left(\frac{N_A}{\gamma}\right)^{2\nu/(2\nu+1)} v_A^{2(2\nu-1)/(2\nu+1)}. \tag{34}$$

Interestingly, this area is independent of the length of core-forming block B. In contrast to the case of starlike micelles, the equilibrium aggregation number and the core radius in a crew-cut micelle strongly decrease upon an increase in the degree of polymerization of the coronal block, N_A. The thickness of the corona is given by:

$$H_{\text{corona}} \cong N_A^{3\nu/(2\nu+1)} v_A^{3(2\nu-1)/(2\nu+1)} \gamma^{(1-\nu)/(2\nu+1)} \tag{35}$$

and it is easy to check that $H_{\text{corona}} \leq R_{\text{core}}$ provided that:

$$N_A \leq \gamma^{(3\nu-1)/5\nu} v_A^{(1-2\nu)/\nu} (N_B/\varphi)^{(2\nu+1)/5\nu}. \tag{36}$$

Similarly to the case of starlike micelles, the CMC is controlled by the gain in free energy upon association of blocks B and is only weakly affected by the properties of coronal block A:

$$\ln \text{CMC} \cong -\gamma(N_B/\varphi)^{2/3} + (\gamma N_A^{2\nu})^{1/(2\nu+1)} v_A^{2(2\nu-1)/(2\nu+1)}. \tag{37}$$

An increase in the length of the core-forming block B leads to the progressive increase in the conformational entropy penalty for their stretching, $F_{\text{core}}(p)$, given by (26). However, before $F_{\text{core}}(p)$ becomes comparable to the dominant terms in the free energy, $F_{\text{corona}} + F_{\text{interface}}$, the spherical crew-cut micelles change their morphology, i.e., they undergo a thermodynamic transition into cylindrical micelles, as discussed in the following section.

3.2 *Polymorphism of Aggregates of Non-ionic Block Copolymers*

For strongly asymmetric block copolymers with long hydrophobic blocks, $N_B \gg N_A$, the conformational entropy losses in the stretched core-forming blocks B determine the equilibrium morphology of an aggregate. Because for given surface area s per chain, the stretching of the core-forming blocks decreases from the spherical to the cylindrical and to the lamellar topology, one anticipates that copolymers with longer blocks B might form nonspherical aggregates.

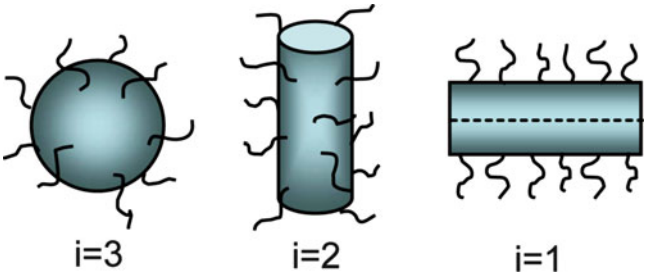

Fig. 2 Self-assembled block-copolymers aggregates of different morphologies: spherical ($i = 3$), cylindrical ($i = 2$), lamellar ($i = 1$). Hydrophobic blocks B and polyelectrolyte blocks A form the core and the corona of the micelle, respectively

The polymorphism of non-ionic block copolymer aggregates was theoretically analyzed by Zhulina and Rubinstein [50], and here we briefly summarize the main results.

The morphology of a block copolymer aggregate is specified by index i. We distinguish between spherical ($i = 3$), cylindrical ($i = 2$), and planar ($i = 1$) morphologies (see Fig. 2). The latter describes lamellae, vesicles, discs, etc. Edge effects for nonspherical aggregates ($i = 1, 2$) can be incorporated on the level of correction terms.

The condition of constant core density φ imposes a relation between the core radius, R_{core}, and the interfacial area per chain, $s(R_{\text{core}})$, in an aggregate of morphology i as:

$$s = s(R_{\text{core}}) = \frac{iN_B}{\varphi R_{\text{core}}} \qquad i = 1, 2, 3. \tag{38}$$

The latter determines the excess interfacial free energy per chain as:

$$\frac{F^{(i)}_{\text{interface}}(R_{\text{core}})}{k_{\text{B}}T} = \gamma s(R_{\text{core}}), \qquad i = 1, 2, 3. \tag{39}$$

The elastic free energy of a stretched block B in the core of an aggregate with morphology i yields:

$$\frac{F^{(i)}_{\text{core}}(R_{\text{core}})}{k_{\text{B}}T} = b_i \frac{R^2_{\text{core}}}{N_B}, \tag{40}$$

where:

$$b_i = \begin{cases} \pi^2/8, & i = 1 \\ \pi^2/16, & i = 2 \\ 3\pi^2/80, & i = 3 \end{cases}. \tag{41}$$

The values of the numerical coefficients in (41) account for the nonuniform and nonequal extension of the core blocks in micelles of different morphologies. They were first calculated by Semenov [59] for a dense micellar core, $\varphi = 1$, within

the so-called strong stretching approximation, i.e., when the chains are noticeably stretched with respect to their Gaussian size. The coefficients b_i in (41) remain valid also for a condensed core with $\varphi \leq 1$ (provided that the polymer density profile in the core is uniform).

Finally, the coronal contribution, $F^{(i)}_{\text{corona}}(R_{\text{core}})$, to the free energy of an aggregate of morphology i is calculated as the free energy of a planar ($i = 1$) or curved ($i = 2, 3$) polymer brush. This is attained by a generalization of the blob model for the case of an arbitrary (finite) curvature of the grafting surface:

$$F^{(i)}_{\text{corona}}/k_{\text{B}}T = \int_{R_{\text{core}}}^{R_{\text{core}}+H_{\text{corona}}} \frac{s(r)dr}{\xi^3(r)}. \tag{42}$$

Here:

$$s(r) = s(R_{\text{core}}) \left(\frac{r}{R_{\text{core}}} \right)^{i-1}, \qquad i = 1, 2, 3 \tag{43}$$

is the area per chain at a distance $(r - R_{\text{core}})$ from the surface of the core, and $k_{\text{B}}T\xi^{-3}(r) = f(r)$ is the free energy density in the corona. The latter accounts, in the scaling approximation, both for the conformational entropy losses and the monomer–monomer interactions, where $\xi(r) \cong s(r)^{1/2}$ is the local correlation length in the corona. Note that at $i = 3$, (42) and (43) lead to (22).

It can be demonstrated that a spherical starlike micelle is always thermodynamically stable with respect to nonspherical aggregates. It has a lower free energy than the cylindrical micelle or the lamella, as long as the size of the corona exceeds that of the core, $H_{\text{corona}} \gg R_{\text{core}}$.

Morphological transitions sphere–cylinder–lamella occur, therefore, when the aggregates acquire the crew-cut shape. It is instructive to consider first a lamellar aggregate, $i = 1$. Here, the coronal contribution is given by the number of blobs per chain in a planar brush:

$$\frac{F^{(1)}_{\text{corona}}}{k_{\text{B}}T} \cong N_A s^{-1/(2\nu)} \nu_A^{(2\nu-1)/\nu}. \tag{44}$$

By balancing $F^{(1)}_{\text{corona}} \simeq F^{(1)}_{\text{interface}}$, one finds the equilibrium area per chain s in a planar lamella:

$$s \cong \left(\frac{N_A}{\gamma} \right)^{2\nu/(1+2\nu)} \nu_A^{2(2\nu-1)/(1+2\nu)}. \tag{45}$$

The thickness $H^{(1)}_{\text{corona}}$ of the corona is given by:

$$H^{(1)}_{\text{corona}} \cong \gamma^{(1-\nu)/(1+2\nu)} N_A^{3\nu/(1+2\nu)} \nu_A^{3(2\nu-1)/(2\nu+1)} \tag{46}$$

while the free energy per chain yields:

$$\frac{F^{(1)}}{k_{\mathrm{B}}T} \cong \gamma^{1/(1+2\nu)} N_A^{2\nu/(1+2\nu)} v_A^{2(2\nu-1)/(2\nu+1)}. \tag{47}$$

In a spherical or cylindrical crew-cut micelle ($i = 2,3$), the coronal free energy is lower than in a planar brush. At small curvatures of the core, the coronal contribution, given by (42), can be expanded with respect to the small parameter $H^{(1)}_{\mathrm{corona}}/R_{\mathrm{core}} \ll 1$, with an account of the normalization condition:

$$N_A = \int_{R_{\mathrm{core}}}^{R_{\mathrm{core}}+H_{\mathrm{corona}}} c_p(r) s(r) \mathrm{d}r. \tag{48}$$

Here, $c_p(r)$ is the polymer concentration (number density of the A monomers) at a distance $(r - R_{\mathrm{core}})$ from the core, and one can use the scaling relation [57] between the local polymer concentration and the correlation length, $c_p(r) \cong \xi^{(1-3\nu)/\nu}(r) v_A^{(1-2\nu)/\nu}$. Retention of the first (linear in $H^{(1)}_{\mathrm{corona}}/R_{\mathrm{core}}$) term provides an approximate expression:

$$\begin{aligned} \frac{F^{(i)}_{\mathrm{corona}}}{k_{\mathrm{B}}T} &\approx \frac{F^{(1)}_{\mathrm{corona}}}{k_{\mathrm{B}}T} \left[1 - \frac{1}{2} \left(\frac{\partial \ln c_p(r)}{\partial \ln r} - \frac{\partial \ln f(r)}{\partial \ln r} \right) \frac{H^{(1)}_{\mathrm{corona}}}{R_{\mathrm{core}}} \right] = \\ &= \frac{F^{(1)}_{\mathrm{corona}}}{k_{\mathrm{B}}T} \left[1 - \frac{(i-1)}{4\nu} \frac{H^{(1)}_{\mathrm{corona}}}{R_{\mathrm{core}}} \right], \end{aligned} \tag{49}$$

where $f(r) \sim \xi^{-3}(r) \sim r^{-3(i-1)/2}$ is the free energy density in the corona, $H^{(1)}_{\mathrm{corona}}$ is given by (46), and R_{core} is related to i and s via (38).

Within this line of approximations, the total free energy per chain in a crew-cut aggregate of morphology i yields:

$$\begin{aligned} \frac{F^{(i)}}{k_{\mathrm{B}}T} = \frac{F^{(1)}}{k_{\mathrm{B}}T} - b_0 \frac{(i-1)}{2i} \gamma^{(2-3\nu)/(1+2\nu)} N_A^{7\nu/(1+2\nu)} v_A^{7(2\nu-1)/(2\nu+1)} \frac{\varphi}{N_B} \\ + b_i i^2 \frac{N_B}{\varphi^2} \left(\frac{N_A}{\gamma} \right)^{-4\nu/(1+2\nu)} v_A^{4(1-2\nu)/(2\nu+1)}. \end{aligned} \tag{50}$$

In this equation, the first (dominant) term is the free energy per chain in the equilibrium planar lamella ($i = 1$). The second term is a decrease in coronal free energy due to curvature of the core (the numerical coefficient $b_0 \simeq 1$ does not depend on i). The third term gives the elastic free energy of the core block [the numerical coefficients b_i are specified in (41)]. The radius R_{core} of the core in a cylindrical ($i = 2$) or spherical ($i = 3$) micelle is calculated via (38) and (45), whereas the corona thickness $H^{(i)}_{\mathrm{corona}} \approx H^{(1)}_{\mathrm{corona}}$, cf. (46).

A morphological transition $(i+1) \Longrightarrow i$ is specified by the condition $F^{(i+1)} = F^i$, to give the following equation for the binodals:

$$\frac{b_0}{2i(i+1)[b_{i+1}(i+1)^2 - b_i i^2]} \frac{\varphi^3}{N_B^2} \gamma^{(2-7\nu)/(1+2\nu)} N_A^{11\nu/(1+2\nu)} \nu_A^{11(2\nu-1)/(2\nu+1)} = 1 \tag{51}$$

By substituting $i = 1$ in (51) and solving it with respect to N_B, one finds the degree of polymerization of the insoluble block, $N_B^{(l-c)}$, corresponding to a lamella-to-cylinder transition:

$$N_B^{(\mathrm{l-c})} = \frac{\sqrt{2b_0}}{\pi} \varphi^{3/2} \gamma^{(2-7\nu)/(2+4\nu)} N_A^{11\nu/(2+4\nu)} \nu_A^{11(2\nu-1)/(4\nu+2)}. \tag{52}$$

Substitution of $i = 2$ in (51) gives the degree of polymerization $N_B^{(c-s)}$, corresponding to a cylinder-to-sphere transition:

$$N_B^{(\mathrm{c-s})} = \frac{\sqrt{\frac{20}{21} b_0}}{\pi} \varphi^{3/2} \gamma^{(2-7\nu)/(2+4\nu)} N_A^{11\nu/(2+4\nu)} \nu_A^{11(2\nu-1)/(4\nu+2)}. \tag{53}$$

Because both binodals $N_B^{(\mathrm{l-c})}$ and $N_B^{(\mathrm{c-s})}$ obey the same power law dependencies on N_A, γ, ν_A, and φ, the region of thermodynamic stability of the cylindrical micelles ($N_B^{(\mathrm{c-s})} < N_B < N_B^{(\mathrm{l-c})}$) constitutes a narrow corridor with the boundaries that differ only in the numerical prefactor. Remarkably, the relative width of this corridor:

$$\frac{\Delta N_B}{N_B^{(\mathrm{l-c})}} = \frac{N_B^{(\mathrm{l-c})} - N_B^{(\mathrm{c-s})}}{N_B^{(\mathrm{l-c})}} = 1 - \sqrt{\frac{10}{21}} \approx 0.31 \tag{54}$$

is independent of the solvent strength (the value of ν). However, a weak dependence on the solvent quality is found for the inverted binodals (i.e., the degrees of polymerization of the coronal block, $N_A^{(\mathrm{l-c})}(N_B, \gamma, \varphi)$ and $N_A^{(\mathrm{c-s})}(N_B, \gamma, \varphi)$, corresponding to the lamella-to-cylinder and the cylinder-to-sphere transitions, respectively):

$$\frac{\Delta N_A}{N_A^{(\mathrm{l-c})}} = \frac{N_A^{(\mathrm{c-s})} - N_A^{(\mathrm{l-c})}}{N_A^{(\mathrm{l-c})}} = \left(\frac{21}{10}\right)^{(1+2\nu)/11\nu} - 1 \approx \begin{cases} 0.28, & \nu = 3/5, \\ 0.31, & \nu = 1/2. \end{cases} \tag{55}$$

Hence, upon a progressive decrease in the solvent strength, a slight increase is predicted for the relative interval of molecular weights of soluble block A that corresponds to thermodynamically stable cylindrical micelles.

In Fig. 3 we present the theoretical diagram of states in N_A, N_B coordinates, which specifies the stability regions of spherical (S), cylindrical (C), and lamellar (L) aggregates in dilute solutions of non-ionic block copolymer [50]. The binodals (solid lines) are calculated using the full expressions for the corresponding free energy of an aggregate of morphology i. The latter involves the numerical

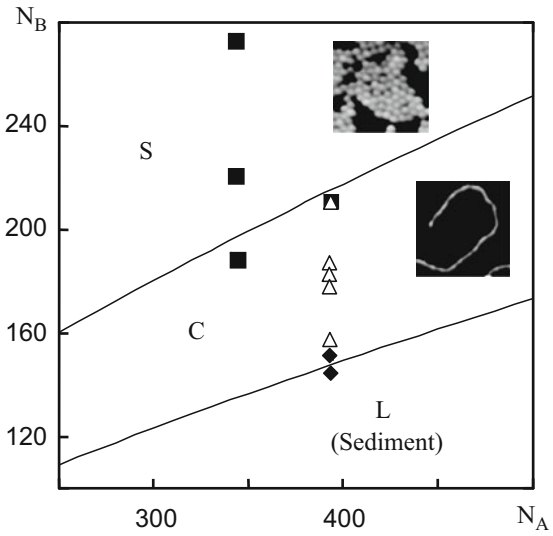

Fig. 3 Diagram of states for non-ionic block copolymer with soluble *A* and insoluble *B* blocks with theoretically predicted stability regions of spherical (S), cylindrical (C), and lamellar (L) aggregates. Values of the theoretical parameters are adjusted for PS-PI copolymer in *n*-heptane [50]. Different symbols specify morphology of the experimental samples: spherical micelles (*squares*), cylindrical micelles (*triangles*), and insoluble aggregates, presumably lamellae (*diamonds*). AFM images of spherical and cylindrical micelles are adopted from [50]

values of all the parameters, adjusted for a specific block copolymer system, namely polyisoprene(PI)-polystyrene(PS) in *n*-heptane. Samples with different molecular weights of the soluble (PI) and insoluble (PS) blocks were examined by static and dynamic light scattering. The morphology i of the aggregates in each sample, specified by respective degrees of polymerization, N_A and N_B, of PI and PS blocks is indicated in the diagram by squares (spheres, $i = 3$), triangles (cylinders, $i = 2$), and diamonds (insoluble aggregates). The latter presumably correspond to associated lamellae ($i = 1$) in the sediment. The shapes of soluble aggregates (spherical and cylindrical micelles of PI–PS diblock copolymer) are visualized by atomic force microscopy (AFM).

Note that for spherical (starlike as well as crew-cut) micelles, the most probable aggregation number [specified by (11)] is close to the average aggregation number. For large $p \gg 1$, the concentration-dependent corrections arising due to translational entropy of micelles are negligible. The thermal (equilibrium) fluctuations in the aggregation number (polydispersity of micelles) are controlled by the shape, $\partial^2 F(p)/\partial p^2$, of the free energy near the bottom of the minimum attained at $p = p_0$. By contrast, in the solution containing cylindrical micelles (at the total polymer concentration $c \geq$ CMC), the distribution with respect to the length (the aggregation number) is wide and follows an exponentially decaying function [35, 37]. The average length of a cylindrical micelle increases proportionally to the square root of the total polymer concentration, c, and grows exponentially as a function of excess free energy of the end-cap of the cylindrical micelle [35, 60].

4 Scaling Theory of Micelles with Polyelectrolyte Corona

The structure and the basic thermodynamics of micelles formed by amphiphilic block copolymers with a PE coronal block A can be analyzed using the blob model. However, the ionization of block A in a polymeric amphiphile introduces long-ranged repulsive interactions in the corona of a micelle. As a result, the blob picture for the micellar corona has to be modified, as explained in this section.

4.1 Starlike Micelles with Quenched Polyelectrolyte Corona

We start with the case of a salt-free dilute solution that contains asymmetric ($N_A \geq N_B$) ionic/hydrophobic block copolymers with a long quenched PE block. These copolymers associate into starlike micelles. The corona of such micelle resembles a star-branched PE [61–64], discussed in detail in [10].

Long-ranged repulsive Coulomb interactions between the coronal blocks A dominate over short-ranged excluded-volume monomer–monomer repulsions, provided that the fraction of charged monomer units is sufficiently large. The block copolymer solution also contains mobile counterions that spread fairly uniformly over the volume of the solution if the aggregation number p is small, $p \leq \alpha_b^{-1/2} l_B^{-1}$. Here, $l_B = e^2/a\varepsilon k_B T$ is the Bjerrum length measured in units of monomer length a, e is the elementary charge, and ε is the dielectric permittivity of the solvent. By contrast, a micelle with large aggregation number, $p \gg \alpha_b^{-1/2} l_B^{-1}$, retains the majority of its counterions inside the corona. The coronal contribution to the free energy is dominated by Coulomb repulsions between charged blocks A in the former case, and by the translational entropy of counterions confined in the corona in the latter case (the so-called osmotic regime). The combined action of Coulomb repulsion and osmotic pressure of counterions entrapped in the corona results in a uniform radial stretching of the coronal blocks A, $R_{\text{corona}} \sim N_A$. If Gaussian entropic elasticity of the coronal chains is assumed, $F_{\text{elastic}} \cong k_B T R_{\text{corona}}^2 / N_A$, then each coronal block can be envisioned as a string of Gaussian electrostatic blobs with constant size:

$$\xi \cong \begin{cases} (\alpha_b^2 l_B)^{-1/3} p^{-1/3}, & p \ll \alpha_b^{-1/2} l_B^{-1}, \\ \alpha_b^{-1/2}, & p \gg \alpha_b^{-1/2} l_B^{-1}. \end{cases} \tag{56}$$

Hence, the radius of the corona is given by:

$$R_{\text{corona}}(p) \cong \frac{N_A}{\xi} \cong \begin{cases} N_A (\alpha_b^2 l_B)^{1/3} p^{1/3}, & p \ll \alpha_b^{-1/2} l_B^{-1}, \\ N_A \alpha_b^{1/2}, & p \gg \alpha_b^{-1/2} l_B^{-1} \end{cases} \tag{57}$$

and the free energy is given by:

$$F_{\text{corona}}/k_B T \cong \frac{N_A}{\xi^2}. \tag{58}$$

Balancing the coronal free energy, F_{corona}, with the excess free energy of the core–corona interface [cf. (24)] leads to the equilibrium aggregation number:

$$p_{\text{eq}} \cong \begin{cases} \gamma(N_B/\varphi)^{2/3} N_A^{-1} (\alpha_b^2 l_B)^{-2/3}, & p_{\text{eq}} \ll \alpha_b^{-1/2} l_B^{-1}, \\ \gamma^3 (N_B/\varphi)^2 (N_A \alpha_b)^{-3}, & p_{\text{eq}} \gg \alpha_b^{-1/2} l_B^{-1} \end{cases} \tag{59}$$

the radius of the core:

$$R_{\text{core}} \cong \begin{cases} \gamma^{1/3} (N_B/\varphi)^{5/9} N_A^{-1/3} (\alpha_b^2 l_B)^{-2/9}, & p_{\text{eq}} \ll \alpha_b^{-1/2} l_B^{-1}, \\ \gamma (N_B/\varphi)(N_A \alpha_b)^{-1}, & p_{\text{eq}} \gg \alpha_b^{-1/2} l_B^{-1} \end{cases} \tag{60}$$

and the corresponding radius of the corona:

$$R_{\text{corona}} \cong \begin{cases} N_A^{2/3} \gamma^{1/3} (N_B/\varphi)^{2/9} (\alpha_b^2 l_B)^{1/9}, & p_{\text{eq}} \ll \alpha_b^{-1/2} l_B^{-1}, \\ N_A \alpha_b^{1/2}, & p_{\text{eq}} \gg \alpha_b^{-1/2} l_B^{-1} \end{cases} \tag{61}$$

which determines the experimentally measurable (e.g., in dynamic light scattering experiments) size of the micelle.

As in the case of micelles formed by copolymers with non-ionic coronal blocks, the aggregation number p increases as a power law function of the length N_B of the core-forming block. A new feature, introduced by ionic interactions in the corona, is, however, a strong decrease in the aggregation number as a function of the length N_A of the coronal block A and its degree of ionization, α_b. As follows from (59), micelles with a small aggregation number, $p_{\text{eq}} \leq \alpha_b^{-1/2} l_B^{-1}$, that release counterions from their barely charged coronae into the bulk of the solution, are formed if $N_A^3 \alpha_b^{5/2} \geq \gamma^3 (N_B/\varphi)^2 l_B$. In the case of shorter coronal and/or longer core-forming blocks, $N_A^3 \alpha_b^{5/2} \ll \gamma^3 (N_B/\varphi)^2 l_B$, osmotic micelles with larger aggregation numbers, $p_{\text{eq}} \gg \alpha_b^{-1/2} l_B^{-1}$ are formed, which retain most of their counterions in the coronal domain. This situation usually occurs in experimental systems. Remarkably, as follows from (61), the radius of the micellar corona in the osmotic regime is controlled (in terms of its power law dependence) solely by the length, N_A, and the degree of ionization, α_b, of the coronal block.

Another specific feature of osmotic micelles in salt-free solutions is the strong increase of the CMC as a function of N_A and α_b. As follows from (16), the dominant term for the CMC of micelles in the osmotic regime is given by:

$$\ln \text{CMC} \approx -\gamma (N_B/\varphi)^{2/3} (\alpha_b N_A)^{-1}. \tag{62}$$

As discussed in Sect. 2.1, the origin of this increase in the CMC is the translational entropy penalty for the localization of counterions in the corona upon the association of block copolymers into micelles.

For micelles with a small aggregation number, $p \leq \alpha_b^{-1/2} l_B^{-1}$, screening effects of low molecular weight salt that is added to the micellar solution, become important when the salt-controlled Debye screening length becomes smaller than the

micellar size, $r_D \leq R_{\text{corona}}$. For micelles with a large aggregation number, whose coronae are found in the osmotic regime, the effect of salt on the self-assembly becomes essential when the (bulk) salt concentration Φ_{ion} exceeds the concentration of counterions entrapped in the corona, $\Phi_{\text{ion}} \geq p\alpha_b^{-1/2}N_A^{-2}$. As discussed in detail in [18, 62], in the salt-dominated regime, the micellar corona can be subdivided into several concentric regions that differ with respect to local structural properties (e.g., radial dependence of the coronal blob size). Importantly, the size of the coronal blobs in salt added solution is an increasing function of the distance from the center of a micelle, though the blobs are not closely packed [18, 62]. However, with a good (experimentally accessible) accuracy, the effect on the self-assembly of the screening of the electrostatic interactions in the micellar corona, can be accounted for within the mean-field approximation, as explained in Sect. 6.

4.2 Crew-Cut Micelles with Quenched Polyelectrolyte Corona

Strongly asymmetric copolymers with long hydrophobic blocks form crew-cut micelles with $H_{\text{corona}} \ll R_{\text{core}}$. The coronae of such micelle can be treated as quasi-planar PE brushes [25–33].

A detailed analysis shows [30] that when the surface area per coronal chain is sufficiently small, the majority of counterions are localized inside the brush. The free energy of such corona is dominated by the translational entropy loss of the entrapped counterions (the corona is equivalent to the "osmotic" PE brush). More specifically, this is the case when $H_{\text{corona}} \gg \Lambda$, where $\Lambda = s/2\pi l_B \alpha_b N_A$ is the Gouy–Chapman length. In the opposite limit of a relatively sparsely "grafted" corona formed by blocks A that have few charged groups, $H_{\text{corona}} \ll \Lambda$, and most of the counterions escape from the corona, but are retained in the proximity of the core within a distance $\sim \Lambda$ provided that $\Lambda \ll R_{\text{core}}$. We assume that the corona of a crew-cut PE micelle is in the osmotic regime (this situation is typical for experimental systems).

For crew-cut PE micelles, the coronal chains can be presented as being composed of strings of Gaussian electrostatic blobs of size $\xi \cong \alpha_b^{-1/2}$. The average distance between the coronal chains, $\sim s^{1/2}$ exceeds the blob size ξ. This implies that the electrostatic blobs in the quasi-planar corona of a crew-cut micelle are also not closely packed. Remarkably, in the osmotic regime, the size of the electrostatic blob and, consequently, the corona thickness, $H_{\text{corona}} \cong N_A/\xi \cong N_A\alpha_b^{1/2}$, are independent (in terms of power law dependencies) of the aggregation number p (i.e., independent of area $s(R_{\text{core}})$ per PE block A at the core–corona interface).

As a result, the equilibrium aggregation number and the core radius in a crew-cut spherical micelle are given (with the accuracy of numerical factors) by the same expressions [second lines in (59) and (60)] as for a starlike spherical micelle in the osmotic regime:

$$p_{\text{eq}} \cong \gamma^3 (N_B/\varphi)^2 (N_A\alpha_b)^{-3}, \tag{63}$$

$$R_{\text{core}} \cong \gamma (N_B/\varphi)(\alpha_b N_A)^{-1}. \tag{64}$$

The aggregation number and the core size increase as a function of the length of the hydrophobic block, N_B and decrease as a power law function of the length of the PE block, N_A. The surface area per chain:

$$s_{\text{eq}} \cong \alpha_b \frac{N_A}{\gamma} \tag{65}$$

is independent of the length N_B of the core block [cf. (34)]. The CMC for the crew-cut micelles in a salt-free solution is also given by (62).

The condition $H_{\text{corona}} \ll R_{\text{core}}$ holds as long as $N_A \ll (N_B\gamma/\varphi)^{1/2}\alpha_b^{-3/4}$. In the opposite limit, $N_A \gg (N_B\gamma/\varphi)^{1/2}\alpha_b^{-3/4}$, the micelles are starlike, $H_{\text{corona}} \gg R_{\text{core}}$.

Addition of salt in the solution leads to the screening of electrostatic repulsions between the coronal chains and a decrease in the excess osmotic pressure, as soon as the corona is found in the salt-dominated regime [28]. This regime is entered when the bulk concentration of added salt exceeds significantly the concentration of counterions trapped inside the corona, $\Phi_{\text{ion}} \gg \alpha_b^{1/2}s^{-1} \cong \gamma\alpha_b^{-1/2}N_A^{-1}$. Here, one can use the local electroneutrality mean-field approximation, discussed in Sect. 5.

5 Mean-Field Theory of Block Copolymer Micelles: Boxlike Model

The mean-field approach provides a convenient framework for the analysis of copolymer self-assembly leading to micellar structures. Combining the mean-field approach with the local electroneutrality approximation (LEA) enables us to generalize the theory for micelles with ionic coronal blocks that feature stimuli-responsive properties.

The LEA assumes that the charge of coronal chains is compensated by the (excess) local concentration of counterions. The LEA is applicable provided that the number of copolymer chains in one micelle is sufficiently large that the excess electrostatic potential is great enough to retain the mobile counterions inside the corona, even at low salt concentrations in the solution. In the LEA framework, the electrostatic interactions manifest themselves through the entropy of the ions, disproportionated between the interior of the corona and the bulk solution. The mean-field theory in combination with the LEA scheme gives a route wherein one can account explicitly for the ionization equilibrium and the interplay of electrostatic and nonelectrostatic interactions in the micellar corona. This is of key importance for the analysis of stimuli-induced structural transitions in micelles formed by copolymer that contains a weakly ionizable (pH-sensitive) PE block. The latter demonstrate a strong coupling between the ionization and aggregation state of the block copolymer.

Within a mean-field approximation, the interaction part of the free energy density in the corona, $f_{\text{int}}\{c_p(r)\}$, can be presented as a function of the local concentration

of monomer units, $c_p(r)$. It comprises the contributions $f_{\rm ev}\{c_p(r)\}$ and $f_{\rm ion}\{c_p(r)\}$ that arise due to the repulsive short-ranged (excluded volume) monomer–monomer interactions and due to the charges along the coronal chains:

$$f_{\rm int}\{c_p(r)\} = f_{\rm ev}\{c_p(r)\} + f_{\rm ion}\{c_p(r)\}. \tag{66}$$

Here:

$$f_{\rm ev}\{c_p(r)\}/k_{\rm B}T = v_A c_p^2(r) + w_A c_p^3(r) + \cdots, \tag{67}$$

whereas the ionic contribution, $f_{\rm ion}\{c_p(r)\}$, is specified below in Sects. 6 and 7. Since solvent is assumed to be good for uncharged monomer units of the block A, we retain only the first term in (67) (to account for binary short-ranged repulsions).

At this stage, we neglect the radial gradients in the polymer density distribution within the corona and in the elastic stretching of the A and B chains. In other words, we implement a boxlike model wherein the average concentration of monomer units inside the corona is given by:

$$c_p = \frac{3pN_A}{4\pi(R_{\rm corona}^3 - R_{\rm core}^3)} \tag{68}$$

and the free energy of a spherical micelle with arbitrary size ratio, $R_{\rm corona}/R_{\rm core} \equiv H_{\rm corona}/R_{\rm core} + 1$, can be presented as:

$$\frac{F}{k_{\rm B}T} \cong \frac{3R_{\rm core}^2}{2N_B} + \frac{3(R_{\rm corona} - R_{\rm core})^2}{2N_A} + \frac{3\gamma N_B}{R_{\rm core}\varphi} + \frac{F_{\rm int}(c_p)}{k_{\rm B}T}. \tag{69}$$

In this equation, the first and the second terms describe the respective conformational entropies of stretched core and coronal blocks, whereas the third term, $\sim\gamma s(R_{\rm core})$, accounts for excess interfacial free energy [here, $s(R_{\rm core})$ is specified by (38)]. The last term in (69) accounts for repulsive interactions in the corona,

$$F_{\rm int}(c_p) = (4\pi/3)(R_{\rm corona}^3 - R_{\rm core}^3) f_{\rm int}(c_p). \tag{70}$$

The radii of the core, $R_{\rm core}$, and of the corona, $R_{\rm corona}$, are related as:

$$\frac{R_{\rm corona}}{R_{\rm core}} = \left(1 + \frac{N_A\varphi}{N_B c_p}\right)^{1/3}. \tag{71}$$

When (71) is substituted into (69), one can formulate the free energy of a micelle as a function of two independent variables, $R_{\rm core}$ and c_p. The minimization of this free energy with respect to $R_{\rm core}$ provides a relation between c_p and $R_{\rm core}$:

$$R_{\rm core} = \left(\frac{\gamma N_B^2}{\varphi}\right)^{1/3} \left\{1 + \frac{N_B}{N_A}\left[\left(1 + \frac{N_A\varphi}{N_B c_p}\right)^{1/3} - 1\right]^2\right\}^{-1/3} \tag{72}$$

and [using the packing condition, (23)] between c_p and the aggregation number p:

$$p = \frac{4\pi\gamma N_B}{3}\left\{1+\frac{N_B}{N_A}\left[\left(1+\frac{N_A\varphi}{N_B c_p}\right)^{1/3}-1\right]^2\right\}^{-1} \tag{73}$$

in the equilibrium micelle. Correspondingly, the free energy per chain in a micelle becomes a function of a single structural parameter, c_p:

$$\frac{F(c_p)}{k_B T} = \frac{9}{2}\left(\frac{\gamma}{\varphi}\right)^{2/3} N_B^{1/3}\left\{1+\frac{N_B}{N_A}\left[\left(1+\frac{N_A\varphi}{N_B c_p}\right)^{1/3}-1\right]^2\right\}^{1/3} + \frac{F_{\text{int}}(c_p)}{k_B T}. \tag{74}$$

In the limiting cases of starlike ($N_A\varphi/N_B c_p \gg 1$) and crew-cut ($N_A\varphi/N_B c_p \ll 1$) micelles, the free energy in (74) can be approximated as:

$$\frac{F(c_p)}{k_B T} \approx \frac{F_{\text{int}}(c_p)}{k_B T} + \begin{cases} \frac{9}{2}\gamma^{2/3}\left(\frac{N_B}{\varphi}\right)^{4/9} N_A^{-1/9} c_p^{-2/9}, & N_A\varphi/N_B c_p \gg 1, \\ \frac{9^{2/3}}{2}\gamma^{2/3} N_A^{1/3} c_p^{-2/3}, & N_A\varphi/N_B c_p \ll 1. \end{cases} \tag{75}$$

A closer inspection of the free energy (74) and (75) as a function of c_p allows us to specify the structural properties (aggregation number and size) of the equilibrium micelle as a function of the copolymer composition (values of N_B and N_A) and the external parameters that control the strength of interactions in the coronal domain.

5.1 Non-ionic Block Copolymer Micelles

In the case of non-ionic or weakly charged coronal chains, the excluded-volume repulsions in the corona dominate over ionic interactions. In this case, the ionic contribution can be neglected and the corresponding contribution to the free energy can be presented as:

$$\frac{F_{\text{int}}(c_p)}{k_B T} = v_A N_A c_p. \tag{76}$$

The minimization of the free energy, (74) or (75), with respect to c_p gives the structural properties of a spherical micelle with a quasi-neutral corona. For a starlike micelle one finds:

$$p_{\text{eq}} \cong \gamma^{15/11}\left(\frac{N_B}{\varphi}\right)^{10/11} N_A^{-3/11} v_A^{-6/11}, \tag{77}$$

$$R_{\text{corona}} \cong \gamma^{3/11} \left(\frac{N_B}{\varphi} \right)^{2/11} N_A^{6/11} v_A^{1/11}, \tag{78}$$

$$R_{\text{core}} \cong \gamma^{5/11} \left(\frac{N_B}{\varphi} \right)^{7/11} N_A^{-1/11} v_A^{-2/11}. \tag{79}$$

The micelles are starlike, i.e. $R_{\text{core}} \ll R_{\text{corona}}$, as long as block A is sufficiently long:

$$N_A \gg \gamma^{2/7} \left(\frac{N_B}{\varphi} \right)^{5/7} v_A^{-3/7} \tag{80}$$

In the range of block lengths specified by (80), starlike spherical micelles are thermodynamically most favorable. Copolymer aggregates with other morphologies (cylindrical micelles, vesicles) are metastable (i.e., have a larger free energy per chain). The most important factor that contributes to the stability of spherical micelles with relatively long N_A is that overlap, and therefore repulsions, between coronal blocks are minimal in the spherical geometry. The ionization of coronal chains results in their additional stretching as compared to quasi-neutral micelles. Therefore, the micelles with ionized corona remain spherical (starlike), provided (80) is fulfilled.

For the crew-cut quasi-neutral micelles with $H_{\text{corona}} \ll R_{\text{core}}$, that are formed by strongly asymmetric copolymers with short coronal blocks, $N_A \ll \gamma^{2/7} (\frac{N_B}{\varphi})^{5/7} v_A^{-3/7}$, one finds:

$$p_{\text{eq}} \cong (\gamma / N_A)^{9/5} \left(\frac{N_B}{\varphi} \right)^{2} v_A^{-6/5}, \tag{81}$$

$$R_{\text{core}} \cong (\gamma / N_A)^{3/5} \left(\frac{N_B}{\varphi} \right) v_A^{-2/5}, \tag{82}$$

$$H_{\text{corona}} \cong \gamma^{1/5} N_A^{4/5} v_A^{1/5}. \tag{83}$$

Due to the mean-field approximation used to account for excluded-volume interactions in the coronal domain, the power law exponents in (77)–(82) differ slightly from those obtained in the scaling framework in Sect. 3.1. This is because the mean-field approach neglects the local density correlations and overestimates the free energy of the micellar corona.

6 Mean-Field Theory of Block Copolymer Micelles with Quenched Polyelectrolyte Corona

Structural rearrangements in a micelle with quenched PE corona can be investigated using the mean-field approach (described in Sect. 5) in combination with the local electroneutrality approximation (LEA). As before, we neglect here the radial gradients in the polymer density and mobile ion distributions (i.e., implement the boxlike model). Moreover, we omit the contribution due to nonelectrostatic

(excluded volume) repulsions. In such a framework, the free energy of a quenched PE corona is formulated as:

$$\frac{F_{\text{ion}}(c_p)}{k_{\text{B}}T} = \alpha_b N_A \left[\left(1 - \sqrt{1 + (\alpha_b c_p/\Phi_{\text{ion}})^2} \right) \Big/ (\alpha_b c_p/\Phi_{\text{ion}}) + \text{Arsh}(\alpha_b c_p/\Phi_{\text{ion}}) \right]$$
$$\approx \begin{cases} \alpha_b N_A [\ln(2\alpha_b c_p/\Phi_{\text{ion}}) - 1], & \alpha_b c_p/\Phi_{\text{ion}} \gg 1, \\ N_A \frac{\alpha_b^2 c_p}{2\Phi_{\text{ion}}}, & \alpha_b c_p/\Phi_{\text{ion}} \ll 1, \end{cases} \tag{84}$$

where:

$$\Phi_{\text{ion}} \equiv \sum_j c_{bj} \tag{85}$$

is the total concentration of (monovalent) ionic species in the bulk of the solution (including H^+ and OH^- ions) and $\text{Arsh}(x) \equiv \ln(x + \sqrt{x^2+1})$ is the inverse hyperbolic sine function.

Combining (84) and (74), one finds a closed expression for the free energy of a spherical micelle with a quenched PE corona as a function of a single structural parameter, c_p.

In the low salt limit, $\alpha_b c_p \gg \Phi_{\text{ion}}$, the coronal contribution to the free energy is dominated by the translational entropy of counterions entrapped inside the corona, $F_{\text{int}} \cong k_{\text{B}}T\alpha_b N_A(\ln c_p - 1)$. In this case, all results of the blob model are recovered both for osmotic starlike and crew-cut spherical micelles (59), (61), and (62).

In the high salt limit, $\alpha_b c_p \ll \Phi_{\text{ion}}$, the contribution of the translational entropy of mobile ions, disproportionated between the interior and the exterior of the corona, is equivalent to a renormalization of the second virial coefficient of monomer–monomer interactions, as $v_A \to v_{\text{eff}} = v_A + \alpha_b^2/2\Phi_{\text{ion}}$, [see (84)].

At any salt concentration, Φ_{ion}, the $F(c_p)$ curve exhibits a single minimum as a function of c_p that corresponds to a single population of equilibrium micelles. Using approximate expressions in (75), one can derive the power law dependencies for the structural properties of starlike and crew-cut micelles on the block lengths, N_A and N_B, the degree of ionization α_b, the hydrophobicity of the block B, and the salt concentration, as discussed in the following section.

6.1 Starlike Micelles with Quenched Polyelectrolyte Corona

Within the mean-field approximation, the coronal contribution to the free energy in the salt-dominated regime can be calculated as:

$$F_{\text{int}}(p)/k_{\text{B}}T \cong v_{\text{eff}} N_A c_p = \left(v_A + \frac{\alpha_b^2}{2\Phi_{\text{ion}}} \right) N_A c_p, \tag{86}$$

where $v_{\text{eff}} = v_A + \alpha_b^2/2\Phi_{\text{ion}}$ is the salt-dependent effective second virial coefficient. The equilibrium aggregation number and the core size in a starlike PE micelle

increase as a function of the salt concentration Φ_{ion} according to the following equations:

$$p_{\text{eq}}(\Phi_{\text{ion}}) \cong \gamma^{15/11}(N_B/\varphi)^{10/11}N_A^{-3/11}\left(v_A + \frac{\alpha_b^2}{\Phi_{\text{ion}}}\right)^{-6/11}, \tag{87}$$

$$R_{\text{core}}(\Phi_{\text{ion}}) \cong \gamma^{5/11}(N_B/\varphi)^{7/11}N_A^{-1/11}\left(v_A + \frac{\alpha_b^2}{2\Phi_{\text{ion}}}\right)^{-2/11}. \tag{88}$$

An increase in the aggregation number $p_{\text{eq}}(\Phi_s) \sim \Phi_{\text{ion}}^{6/11}$, accompanied by a decrease in the strength of repulsive electrostatic interactions (due to added salt ions), results in a very weak decrease in the coronal size in a starlike PE micelle as a function of the salt concentration:

$$R_{\text{corona}}(\Phi_{\text{ion}}) \cong \gamma^{3/11}(N_B/\varphi)^{2/11}N_A^{6/11}\left(v_A + \frac{\alpha_b^2}{2\Phi_{\text{ion}}}\right)^{1/11}. \tag{89}$$

The micelles are starlike, i.e., $R_{\text{corona}} \gg R_{\text{core}}$ as long as $N_A \gg \gamma^{2/7}(N_B/\varphi)^{5/7}(v_A + \alpha_b^2/2\Phi_{ion})^{-3/7}$.

Under the so-called salt dominance conditions, the association of block copolymers into micelles does not lead to significant losses in the translational entropy of counterions (whose concentrations inside the corona and in the bulk of the solution are approximately equal). Therefore, within the accuracy of the main term, the CMC is controlled by the hydrophobicity of the block B:

$$\ln \text{CMC} \approx -\gamma(N_B/\varphi)^{2/3} + \gamma^{6/11}(N_B/\varphi)^{4/11}N_A^{1/11}\left(v_A + \frac{\alpha_b^2}{2\Phi_{\text{ion}}}\right)^{2/11}. \tag{90}$$

An increase in the salt concentration Φ_{ion}, leads only to a decrease in the second (correction) term and to a mild decrease in the CMC.

At high salt concentrations $\Phi_{\text{ion}} \gg v_A^{-1}\alpha_b^2$, the structural properties (e.g., $p_{\text{eq}}(\Phi_{\text{ion}})$, and $R_{\text{corona}}(\Phi_{\text{ion}})$) approach the values that are found for starlike micelles with non-ionic corona, (77), (78).

Because an increase in salt concentration leads to the increase in the core size, R_{core}, and in the simultaneous decrease in the corona size, R_{corona}, the starlike micelle can transform into the crew-cut micelle with an increase in the salt concentration.

6.2 Crew-Cut Micelles with Quenched Polyelectrolyte Coronae

In the salt-dominated regime, the free energy of the quasi-planar corona of a crew-cut micelle is given by:

$$F_{\text{int}}/k_{\text{B}}T \cong N_A s^{-2/3} v_{\text{eff}}^{2/3} = N_A s^{-2/3}\left(v_A + \frac{\alpha_b^2}{2\Phi_{\text{ion}}}\right)^{2/3}. \tag{91}$$

It decreases as a function of the salt concentration. Balancing the free energy, (91), with the excess free energy of the core–corona interface, (24), gives the equilibrium interfacial area per copolymer chain:

$$s_{\mathrm{eq}} \cong (N_A/\gamma)^{3/5} \left(v_A + \frac{\alpha_b^2}{2\Phi_{\mathrm{ion}}} \right)^{2/5} \tag{92}$$

and the equilibrium aggregation number in a salt-dominated crew-cut micelle:

$$p_{\mathrm{eq}}(\Phi_{\mathrm{ion}}) \cong (\gamma/N_A)^{9/5} (N_B/\varphi)^2 \left(v_A + \frac{\alpha_b^2}{2\Phi_{\mathrm{ion}}} \right)^{-6/5}. \tag{93}$$

As expected, the aggregation number increases with increasing salt concentration Φ_{ion}. The corresponding power law exponent, $6/5$, is remarkably larger than in the case of starlike micelles. This is due to stronger repulsive interactions between PE blocks in the quasi-planar corona of a crew-cut micelle as compared to those in a starlike corona. Similarly to the case of a starlike micelle, the thickness of the corona, H_{corona}, in a crew-cut micelle decreases as a function of the salt concentration, Φ_{ion}, although the area $s(\Phi_{\mathrm{ion}})$ per PE chain at the core–corona interface decreases:

$$H_{\mathrm{corona}}(\Phi_{\mathrm{ion}}) \cong \gamma^{1/5} N_A^{4/5} \left(v_A + \frac{\alpha_b^2}{2\Phi_{\mathrm{ion}}} \right)^{1/5}. \tag{94}$$

The size of the core, which dominates the overall dimensions of a crew-cut micelle, grows upon an increase in salt concentration as:

$$R_{\mathrm{core}}(\Phi_{\mathrm{ion}}) \cong (\gamma/N_A)^{3/5} (N_B/\varphi) \left(v_A + \frac{\alpha_b^2}{2\Phi_{\mathrm{ion}}} \right)^{-2/5}. \tag{95}$$

Upon further increase in the salt concentration, $\Phi_{\mathrm{ion}} \gg v_A^{-1}\alpha_b^2$, the structural properties of crew-cut micelles with a quenched PE corona asymptotically approach these of micelles with a non-ionic corona, (81)–(83).

Similarly to the case of crew-cut micelles composed of non-ionic block copolymers, an increase in the length of the core-forming block B leads to an increase in entropic penalty for stretching the chains. As a result, copolymers with longer insoluble block B might associate in nonspherical aggregates (e.g., cylindrical crew-cut micelles). These morphological changes will be discussed in detail in Sect. 10.

7 Mean-Field Theory of Block Copolymer Micelles with Annealing Polyelectrolyte Corona

Within the framework of the boxlike model, the free energy of the corona of micelle with annealing PE block can be formulated as:

$$\frac{F_{\text{ion}}(c_p)}{k_{\text{B}}T} = N_A\left[\left(1-\sqrt{1+(\alpha c_p/\Phi_{\text{ion}})^2}\right)+\ln(1-\alpha)\right]$$
$$\approx N_A\cdot\begin{cases}-\alpha+\ln(1-\alpha), & \alpha_b c_p/\Phi_{\text{ion}}\gg 1,\\ \frac{\alpha_b^2 c_p}{2\Phi_{\text{ion}}}+\ln(1-\alpha_b), & \alpha_b c_p/\Phi_{\text{ion}}\ll 1.\end{cases} \tag{96}$$

Here, the average degree of ionization α of the coronal block A depends not only on the pH (via α_b), but also on the ionic strength in the bulk solution (buffer), and the average polymer concentration in the corona, c_p, as:

$$\frac{\alpha}{1-\alpha}\cdot\frac{1-\alpha_b}{\alpha_b}=\sqrt{1+(\alpha c_p/\Phi_{\text{ion}})^2}-\alpha c_p/\Phi_{\text{ion}}, \tag{97}$$

where α_b is the degree of ionization of a single monomer in the bulk solution of given pH:

$$\alpha_b=\frac{10^{\text{pH}-\text{p}K_{\text{a}}}}{10^{\text{pH}-\text{p}K_{\text{a}}}+1}. \tag{98}$$

Equation (97) can be used to obtain approximate expressions for the degree of ionization of the monomer units of the coronal block A in the limiting cases of low and high salt concentrations:

$$\alpha\cong\begin{cases}\left(\frac{\alpha_b}{1-\alpha_b}\cdot\frac{\Phi_{\text{ion}}}{2c_p}\right)^{1/2}, & \alpha c_p/\Phi_{\text{ion}}\gg 1,\\ \alpha_b\left[1-\frac{\alpha_b c_p}{\Phi_{\text{ion}}}(1-\alpha_b)\right], & \alpha c_p/\Phi_{\text{ion}}\ll 1.\end{cases} \tag{99}$$

The coupling between the ionization of the coronal block A and the association equilibrium of the copolymers gives rise to unique features for the self-assembly of amphiphilic block copolymers with a weak (pH-sensitive) PE block. In other words, the levels of ionization for unimers in solution and for copolymers incorporated in micelles, can be noticeably different due to different values of the pH inside micellar corona and in the bulk solution. Furthermore, the strength of the electrostatic repulsion in the corona can be affected not only by variations in the ionic strength (as it is for micelles with quenched PE corona), but also by variations in the pH, which affect the ionization of the coronal chains.

Moreover, the effect of added salt on the self-assembly of block copolymers with an annealing PE block is more complicated than for copolymers with a quenched PE block. The reason for this is that at pH $\cong pK$, an addition of small amounts of salt into the bulk solution leads to substitution of H^+ (or OH^-) counterions in the micellar corona by salt ions. The latter promotes ionization of the coronal chains and affects the strength of repulsive interactions between the corona-forming blocks. At low salt concentrations, ionization of the monomer units in coronae of micelles formed by copolymers with an annealing PE block can be strongly suppressed. As a result, the coronal contribution to the free energy of the micelle might be dominated by nonelectrostatic excluded-volume repulsions between corona-forming blocks (the so-called quasi-neutral micelle regime).

7.1 Structural Transitions in Starlike Micelles with Annealing PE Corona

The block copolymer chains with a strongly asymmetric composition, $N_A \gg \gamma^{2/7}(N_B/\varphi)^{5/7}v_A^{-3/7}$, form starlike micelles at an arbitrary small degree of ionization of the coronal block. The free energy per chain in a starlike micelle with an annealing PE coronal block is given by:

$$\frac{F}{k_{\mathrm{B}}T} \cong \frac{9}{2}\gamma^{2/3}\left(\frac{N_B}{\varphi}\right)^{4/9} N_A^{-1/9} c_p^{-2/9} + N_A\left[v_A c_p + \left(1-\sqrt{1+(\alpha c_p/\Phi_{\mathrm{ion}})^2}\right) + \ln(1-\alpha)\right], \tag{100}$$

where the degree of ionization $\alpha(\alpha_b, \Phi_{\mathrm{ion}}, c_p)$ is determined from (97).

Further analysis of the free energy as a function of c_p (or α), (100) and (97), indicates the existence of a single minimum at both low, $\Phi_{\mathrm{ion}} \ll \alpha_b c_p$, and high, $\Phi_{\mathrm{ion}} \gg \alpha_b c_p$, salt concentrations. This minimum corresponds to a single population of micelles that coexist with unimers either at low or at high salt concentration in the solution. At intermediate salt concentrations, $F(c_p)$ might exhibit two minima as a function of c_p. The presence of two minima in the free energy indicates the possibility of abrupt (quasi-first order) salt- and pH-induced structural transitions in block copolymer micelles. These transitions are discussed below in Sect. 7.1.3.

7.1.1 Quasi-neutral Micelles

At low salt concentrations, $\Phi_{\mathrm{ion}} \ll \alpha_b c_p$, the ionization of A segments in the micelle corona is low, $\alpha \ll \alpha_b$. In this case, the excluded-volume repulsions (binary interactions) give the dominant contribution to the free energy of the corona. As a result, the structural properties of the quasi-neutral micelles approximately coincide with those formed by non-ionic block copolymers and are given by (77) and (78).

An increase in the salt concentration leads to the progressive replacement of H^+ ions in the micellar corona by, e.g., Na^+ ions of the added salt (i.e., increases the local pH in the corona). This promotes the increase in the degree of ionization α of the coronal blocks as:

$$\alpha \cong \left(\frac{\alpha_b}{1-\alpha_b}\cdot\Phi_{\mathrm{ion}}\right)^{1/2}\gamma^{-3/11}\left(\frac{N_B}{\varphi}\right)^{-2/11} N_A^{5/11} v_A^{9/22}. \tag{101}$$

The latter leads to a slight decrease (on the level of the correction terms) in the aggregation number, and an increase in the radius of the corona.

The free energy per chain in a quasi-neutral micelle is given by:

$$F_{\mathrm{quasi-neutral}}/k_{\mathrm{B}}T \cong \gamma^{6/11}(N_B/\varphi)^{4/11}N_A^{1/11}v_A^{2/11} + N_A\ln(1-\alpha). \tag{102}$$

Here, the first term is dominant because α, given by (101), is small.

Although at low salt concentrations the structural parameters of quasi-neutral micelles formed by copolymers with an annealing PE block are close to those of micelles formed by non-ionic block copolymers, the CMC for the former is significantly larger than that for the latter. Indeed, the degree of ionization of the annealing PE blocks in the unimer state of copolymer, α_b, is significantly larger than that of the copolymers incorporated in micelles. Hence, the association of copolymers into micelles is accompanied by an additional free energy penalty (recombination of significant fraction of counterions with the acidic groups of the annealing PE blocks). As a result, the CMC increases as a function of N_A and α_b according to the equation:

$$\begin{aligned}\ln \mathrm{CMC}_{\mathrm{quasi-neutral}} &\approx -\gamma(N_B/\varphi)^{2/3} + \gamma^{6/11}(N_B/\varphi)^{4/11} N_A^{1/11} v_A^{2/11} - N_A \ln(1-\alpha_b) \\ &= \ln \mathrm{CMC}_{\mathrm{neutral}} - N_A \ln(1-\alpha_b). \end{aligned} \tag{103}$$

Here, the first two terms specify the CMC for equivalent uncharged (neutral) block copolymer with lengths of blocks, N_A and N_B:

$$\ln \mathrm{CMC}_{\mathrm{neutral}} \approx -\gamma(N_B/\varphi)^{2/3} + \gamma^{6/11}(N_B/\varphi)^{4/11} N_A^{1/11} v_A^{2/11}, \tag{104}$$

and we have neglected the $N_A(1-\alpha)$ term in the free energy of the coronae of the quasi-neutral micelles as well as the contribution due to intramolecular repulsive interactions and the stretching of the block A in unimers.

Equation (103) demonstrates that the CMC for quasi-neutral micelles is a strongly increasing function of α_b, i.e., it is strongly affected by the value of the bulk pH. When $-N_A \ln(1-\alpha_b) \geq \gamma(N_B/\varphi)^{2/3}$, quasi-neutral micelles do not form at any copolymer concentration in the solution.

7.1.2 Charged Micelles

In the opposite limit of high salt concentration, $\Phi_{\mathrm{ion}} \gg \alpha_b c_p$, the difference between the pH in the bulk solution and inside the micellar corona is negligible. At a given solution pH, α_b is specified according to (98), and the monomer units of blocks A in the micellar corona approach their maximal at given pH degree of ionization, $\alpha \approx \alpha_b$. The corona is indistinguishable from that formed by quenched PE chains with a degree of ionization α_b in the salt-dominated regime. The evolution of the structural parameters of the micelles follows the same trends as described above: the aggregation number increases and the coronal dimensions decrease upon an increase in the salt concentration according to (87) and (89), respectively. An increase in α_b (an increase in the pH) enhances repulsive interactions in the corona and thus leads to a progressive decrease in the aggregation number and an increase in the coronal dimensions.

The free energy of micelles in the salt-dominated regime is formulated as:

$$F/k_{\mathrm{B}}T \cong \gamma^{6/11}(N_B/\varphi)^{4/11}N_A^{1/11}(\alpha_b^2/2\Phi_{\mathrm{ion}} + v_A)^{2/11} + N_A\ln(1-\alpha_b), \qquad (105)$$

whereas the CMC is given by:

$$\begin{aligned}\ln \mathrm{CMC}_{\mathrm{charged}} &\approx -\gamma(N_B/\varphi)^{2/3} + \gamma^{6/11}(N_B/\varphi)^{4/11}N_A^{1/11}\left(v_A + \frac{\alpha_b^2}{2\Phi_{\mathrm{ion}}}\right)^{2/11} \\ &= \ln \mathrm{CMC}_{\mathrm{neutral}} + \gamma^{6/11}(N_B/\varphi)^{4/11}N_A^{1/11}v_A^{2/11} \\ &\quad \times \left[\left(1 + \frac{\alpha_b^2}{2\Phi_{\mathrm{ion}}v_A}\right)^{2/11} - 1\right]. \end{aligned} \qquad (106)$$

7.1.3 Micelle-to-Micelle Transition

Remarkably, in the intermediate range of salt concentrations, starlike micelles formed by block copolymer with an annealing PE block exhibit a discontinuous variation of their structural parameters upon a smooth variation in either the salt concentration, Φ_{ion}, or the pH of the solution.

Analysis of (100) indicates that at moderate salt concentrations, the free energy versus c_p curves might exhibit two minima, one corresponding to a quasi-neutral (weakly ionized) micelle with high aggregation number, and the other corresponding to a micelle with strongly charged corona, $\alpha \approx \alpha_b$, and low aggregation number. These two minima correspond to two populations of micelles that coexist in the solution in a certain range of salt concentrations.

When the two minima are equally deep, the transition from large (quasi-neutral) to small (charged) micelle occurs as a jump-wise quasi-first order phase transition. (A more accurate analysis [23] points at a finite interval of salt concentrations wherein the two types of micelles coexist). Using (102) and (105) for the free energy of quasi-neutral and charged micelle, and assuming $\alpha_b^2/\Phi_{\mathrm{ion}}v_A \gg 1$, the characteristic salt concentration at the transition point can be evaluated as:

$$\Phi^*_{\mathrm{ion}} \cong \alpha_b^{-7/2}\gamma^3\left(\frac{N_B}{\varphi}\right)^2 N_A^{-5}. \qquad (107)$$

Decomposition of large micelles into many smaller ones is accompanied by an abrupt increase in the degree of ionization of the corona from $\alpha \approx \alpha_b(\Phi^*_{\mathrm{ion}}/\alpha_b c_p)^{1/2}$ to α_b, accompanied by a substantial drop in the aggregation number:

$$\frac{p_{\mathrm{quasi-neutral}}}{p_{\mathrm{charged}}} \cong \left(1 + \frac{\alpha_b^2}{2v_A\Phi^*_{\mathrm{ion}}}\right)^{6/11}. \qquad (108)$$

A combined action of the decrease in the number of coronal chains and the increase in their ionization results in a relatively small jump up in the coronal dimensions:

$$\frac{R_{\text{corona,charged}}}{R_{\text{corona,quasi-neutral}}} \cong \left(1+\frac{\alpha_b^2}{2\nu_A \Phi^*_{\text{ion}}}\right)^{1/11}. \tag{109}$$

The diagram of states of the solution of block copolymer that forms starlike micelles is presented using as coordinates either polymer concentration versus salt concentration (Φ_{ion}) (Fig. 4a) or polymer concentration versus bulk degree of ionization (α_b) (Fig. 4b).

When the polymer concentration is below $\text{CMC}_{\text{quasi-neutral}}$ (CMC_{qn}), micelles do not form in the range of Φ_{ion} to the left of the $\text{CMC}_{\text{charged}}$ (CMC_{ch}) line. When the CMC_{ch} line is crossed, starlike micelles with charged, $\alpha \approx \alpha_b$ coronae appear in the solution.

When the polymer concentration exceeds CMC_{qn}, quasi-neutral micelles with weakly ionized, $\alpha \ll \alpha_b$, coronae are found in the range of low salt concentrations (small Φ_{ion}). At the transition concentration, $\Phi_{\text{ion}} = \Phi^*_{\text{ion}}$, these micelles abruptly rearrange into micelles with smaller aggregation number, but stronger charged coronae. Further increase in salt content, $\Phi_{\text{ion}} > \Phi^*_{\text{ion}}$, leads to progressive increase in the micelle aggregation number.

Alternatively, decomposition of large quasi-neutral micelles into smaller charged micelles (upon crossing of $\Phi^*_{\text{ion}}(\alpha_b)$ line) may be triggered by an increase in the pH (i.e., in α_b) at the polymer concentration above CMC_{qn}. An increase in the pH both below and above the transition threshold, leads to a continuous decrease in the aggregation number and an increase in the span of the corona. At polymer concentrations below CMC_{ch}, only unimers are found in the solution at high pH ($\alpha_b \approx 1$). A decrease in pH leads to a decrease in chain ionization and in Coulomb repulsions between unimers, and may trigger micellization upon crossing the CMC_{ch} or the CMC_{qn} lines.

Figure 5 demonstrates the diagram of states for starlike micelles in the $\Phi_{\text{ion}}, \alpha_b$ coordinates. We delineate four regions, denoted as S_{qn}, $S_{\text{qn}'}$, S_{ch} and U. In region S_{qn}, the starlike micelles are quasi-neutral, and their structural parameters are given by (77), (78), and (101). The dotted line divides region S_{qn} into two parts. To the left of the dotted line, the CMC_{qn} is virtually unaffected by the polyelectrolyte nature of the coronal chains (it coincides with the CMC for the equivalent neutral copolymer). To the right of the dotted line, the CMC_{qn} is shifted according to (103).

In region S_{ch}, the coronal blocks are charged, $\alpha \approx \alpha_b$, and the parameters of equilibrium micelles are given by (87) and (89). The bold line separating regions S_{ch} and S_{qn} is the line of abrupt rearrangements of the micelles, $\Phi_{\text{ion}} = \Phi^*_{\text{ion}}(\alpha_b)$. In region $S_{\text{qn}'}$, the coronal blocks A are ionized, $\alpha \approx \alpha_b$, but the electrostatic interactions are strongly screened due to the high salt concentration. As a result, the structural parameters of the micelles are the same as in region S_{qn}.

Finally, in region U the micelles are unstable, and only free ionized unimers (with $\alpha = \alpha_b$) are found in the solution for any polymer concentration.

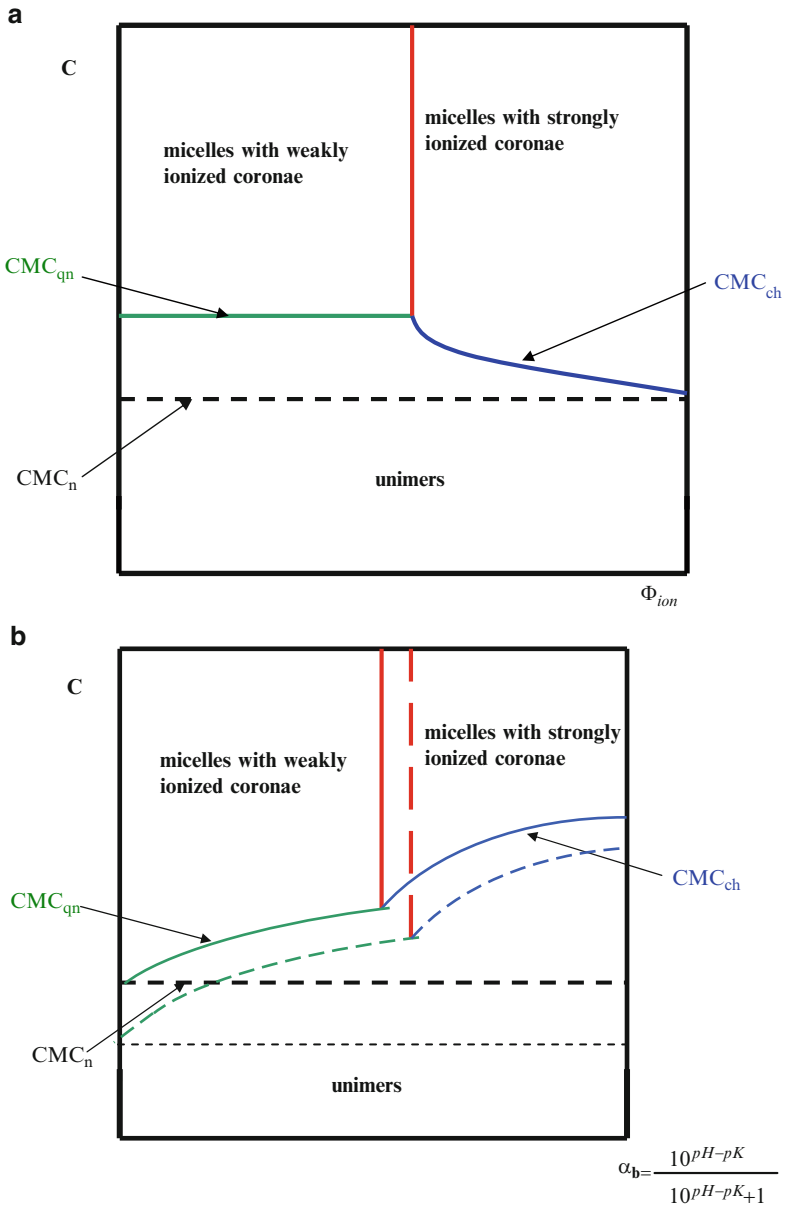

Fig. 4 Diagram of states for solution of block copolymers with pH-sensitive PE blocks. Coordinates are (**a**) polymer concentration C and salt concentration Φ_{ion} (at constant buffer pH); (**b**) polymer concentration C and pH (at constant salt concentration). *Dashed lines* in (**b**) indicate shift of the boundaries of different regimes upon increasing hydrophobicity of the blocks B

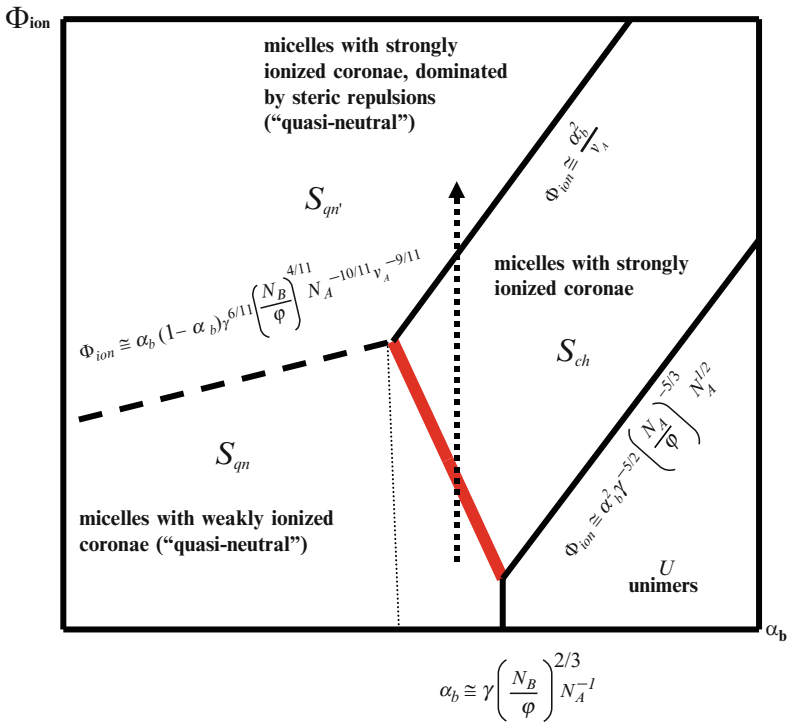

Fig. 5 Diagram of states in α_b, Φ_{ion} coordinates for dilute solution of block copolymers with pH-sensitive PE blocks, that associate in starlike micelles, $N_A \gg \gamma^{2/7}(\frac{N_B}{\varphi})^{5/7}\nu_A^{-3/7}$. The *dotted arrow* indicates cross-section of the diagram corresponding to the evolution of the micelle parameters as a function of salt concentration presented in Fig. 6a, b

Figure 6 shows the evolution of both the aggregation number and the radius of the corona for starlike micelles upon variations in the salt concentration (6a, b) and in the pH (6c,d). All the structural properties of starlike micelles with pH-sensitive coronal blocks exhibit a non-monotonous and discontinuous variation as a function of Φ_{ion}: the aggregation number exhibits a minimum (with a jump down at $\Phi_{ion} \approx \Phi^*$), whereas the coronal dimensions exhibit a weak maximum (with a jump up at $\Phi_{ion} \approx \Phi^*$).

7.2 *Crew-Cut Micelles with Annealing Polyelectrolyte Coronae*

Crew-cut micelles with $H_{corona} \ll R_{core}$ are formed by copolymers with comparatively long hydrophobic and short hydrophilic blocks, $N_A \ll \gamma^{2/7}(\frac{N_B}{\varphi})^{5/7}\nu_A^{-3/7}$. The latter condition ensures that quasi-neutral micelles have a crew-cut shape. As we

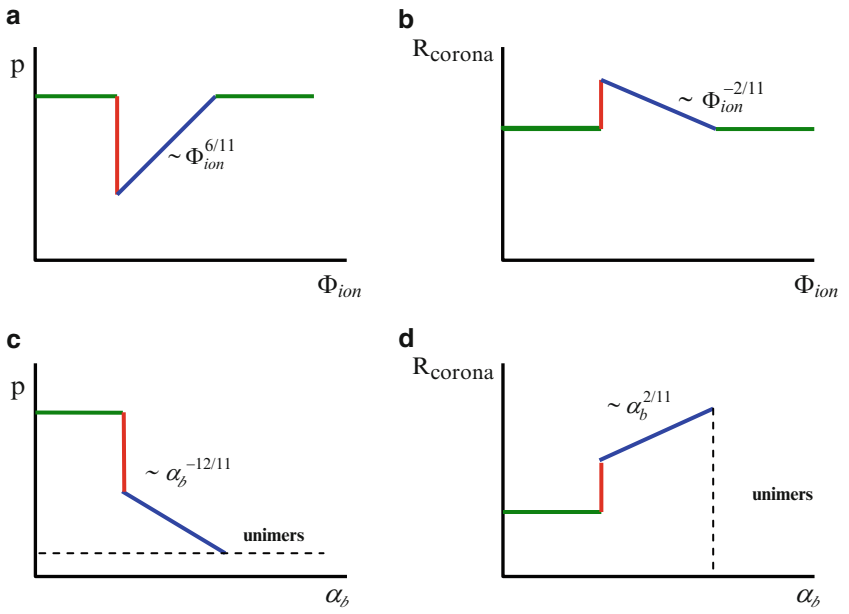

Fig. 6 Dependency of (**a**) aggregation number p; (**b**) radius of the corona R_{corona} for starlike micelles with annealing coronal block as a function of salt concentration. The pH is fixed according to the position of the dotted arrow in Fig. 5. Dependency of (**c**) p and (**d**) R_{corona} as a function of pH

will show, the progressively increasing role of electrostatic interactions at intermediate salt concentrations leads to the decrease in the size ratio, $R_{\text{core}}/H_{\text{corona}}$, which suggests possible transformation of crew-cut into starlike micelles.

The corona of a crew-cut micelle can be viewed as a quasi-planar annealing PE brush, as long as $R_{\text{core}} \gg H_{\text{corona}}$. The ionization-recombination balance and the structural properties of a planar PE brush were discussed in detail in [31]. Here, we focus on the evolution of crew-cut micelles caused by an increase in the salt concentration, Φ_{ion}, and pH.

Using (75) (at $N_A\varphi_B/N_Bc_p \ll 1$) and (96), we find that with the accuracy of numerical coefficients:

$$\frac{F}{k_BT} \cong \frac{9^{2/3}}{2}\gamma^{2/3}N_A^{1/3}c_p^{-2/3} + N_A\left[v_Ac_p + \ln(1-\alpha) - \frac{\Phi_{\text{ion}}}{c_p}\left(\sqrt{1+(\alpha c_p/\Phi_{\text{ion}})^2}-1\right)\right], \quad (110)$$

where $\alpha(c_p, \Phi_{\text{ion}})$ is determined by (97).

In the low salt limit, $\Phi_{\rm ion} \ll \alpha_b c_p$, the coronal chains are weakly ionized, i.e., $\alpha \ll \alpha_b \leq 1$. Making use of (96), we represent the free energy in (110) as:

$$\frac{F}{k_{\rm B}T} \cong \frac{9^{2/3}}{2}\gamma^{2/3}N_A^{1/3}c_p^{-2/3} + N_A[v_A c_p + \ln(1-\alpha) - \alpha]. \tag{111}$$

At very low salt concentrations $\alpha \ll \alpha_b \leq 1$, and the last two terms in (111) are negligible compared to the second term (steric repulsions). The structure of micelles is determined by the competition between steric repulsions (the second term) and excess free energy of the core–corona interface (the first term). Balance of these terms indicates that the structural parameters are given by (81)–(83) for quasi-neutral crew-cut micelles.

The degree of ionization of the coronal chains increases as a function of the salt concentration (99) and is given by:

$$\alpha \cong \left(\frac{\alpha_b \Phi_{\rm ion}}{1-\alpha_b}\right)^{1/2} \frac{N_A^{1/5} v_A^{3/10}}{\gamma^{1/5}}. \tag{112}$$

As long as steric repulsions $\sim c_p v_A$ in the corona dominate over the ionic contributions $\sim \alpha$, the increase in α does not affect the structure of the micelles.

The ionic contributions start to dominate over steric repulsions at:

$$\Phi_{\rm ion} \geq \Phi_{\rm ion}^{(1)} \equiv \frac{1-\alpha_b}{\alpha_b}\left(\frac{\gamma}{N_A}\right)^{6/5} v_A^{1/5}. \tag{113}$$

The equilibrium structure of the micelle is now determined by a balance between the osmotic pressure of counterions in the corona and excess interfacial free energy of the core–corona boundary. Here, the micellar corona is equivalent to a quasi-planar PE brush in the annealing osmotic regime [31].

The aggregation number and the thickness of the corona depend on the degree of ionization α in the same way as for crew-cut micelles with osmotic quenched PE corona:

$$p \cong \gamma^3 (N_B/\varphi)^2 (N_A \alpha)^{-3}, \tag{114}$$

$$H_{\rm corona} \cong a N_A \alpha^{1/2}, \tag{115}$$

$$s \cong \alpha \frac{N_A}{\gamma}, \tag{116}$$

but now the degree of ionization α of the coronal blocks depends on the ionic strength, $\Phi_{\rm ion}$, and on the polymer concentration in the corona $c_p \cong N_A/sH_{\rm corona}$ via (99), which leads to:

$$\alpha \cong \left(\frac{\alpha_b}{1-\alpha_b}\frac{N_A \Phi_{\rm ion}}{\gamma}\right)^2. \tag{117}$$

Hence, α rapidly increases as a function of $\Phi_{\rm ion}$.

An increase in the degree of ionization of blocks A leads to an increase in osmotic repulsion in the corona, and the aggregation number rapidly decreases as:

$$p_{\rm eq} \cong \left(\frac{N_B}{\varphi}\right)^2 \left(\frac{\gamma}{N_A}\right)^9 \left(\frac{1-\alpha_b}{\alpha_b \Phi_{\rm ion}}\right)^6. \tag{118}$$

The extension of coronal chains is therefore given by:

$$H_{\rm corona} \cong \alpha^{1/2} N_A \cong \frac{N_A^2}{\gamma} \frac{\alpha_b \Phi_{\rm ion}}{1-\alpha_b}, \tag{119}$$

i.e., the corona thickness increases with increasing salt concentration $\Phi_{\rm ion}$, while the size of the core:

$$R_{\rm core} \cong \left(\frac{N_B}{\varphi}\right) \left(\frac{\gamma}{N_A}\right)^3 \left(\frac{1-\alpha_b}{\alpha_b \Phi_{\rm ion}}\right)^2 \tag{120}$$

decreases with $\Phi_{\rm ion}$ due to the decrease in aggregation number, (118). As a result, the ratio $R_{\rm core}/H_{\rm corona}$ decreases with increasing salt concentration as $\sim 1/(\Phi_{\rm ion})^3$.

The annealing osmotic regime holds as long as $\alpha \ll \alpha_b$, i.e., in the range of salt concentrations:

$$\Phi_{\rm ion} \ll \Phi_{\rm ion}^{(2)} \equiv \frac{\gamma}{N_A} \alpha_b^{-1/2} (1-\alpha_b). \tag{121}$$

At $\Phi_{\rm ion} \cong \Phi_{\rm ion}^{(2)}$, the coronal blocks reach maximal ionization, $\alpha \approx \alpha_b$, and maximal extension, $H_{\rm corona} \cong \alpha_b^{1/2} N_A$. In contrast, the aggregation number reaches its minimal value, which coincides with the aggregation number for a quenched PE micelle with $\alpha = \alpha_b$ in a salt-free solution and is given by (63).

The ratio $R_{\rm core}/H_{\rm corona}$ also passes through a minimum at $\Phi_{\rm ion}^{(2)}$:

$$\left(\frac{R_{\rm core}}{H_{\rm corona}}\right)_{\Phi_{\rm ion}^{(2)}} \cong \frac{N_B}{\varphi} \frac{\gamma}{N_A^2} \alpha_b^{-3/2}. \tag{122}$$

At larger salt concentrations, $\Phi_{\rm ion} \gg \Phi_{\rm ion}^{(2)}$, the corona is found in the salt-dominated regime. Here, $\alpha \approx \alpha_b$ and the structural parameters of these micelles coincide with those of crew-cut micelles with a quenched PE coronal block, given by (93)–(95). The CMC of copolymers with an annealing PE block at high salt concentration also coincides with that for copolymers with quenched PE block.

In the range of salt concentrations $\Phi_{\rm ion}^{(2)} \ll \Phi_{\rm ion} \ll \alpha_b^2/v_A$, the electrostatic contribution of $v_{\rm eff}$ dominates over the steric contribution, and $v_{\rm eff} = v_A + \alpha_b^2/\Phi_{\rm ion} \cong \alpha_b^2/\Phi_{\rm ion}$. At higher salt content, $\Phi_{\rm ion} \gg \alpha_b^2/v_A$, the electrostatic interactions are screened, and the micelles are found in the quasi-neutral regime (81)–(83).

The scenario of crew-cut micelle evolution (described above) holds if $H_{\rm corona} \ll R_{\rm core}$ in the whole range of salt concentrations (including $\Phi_{\rm ion}^{(2)}$, where $R_{\rm core}$ and $H_{\rm corona}$ reach their minimal and maximal values, respectively).

The condition $H_{\text{corona}} \ll R_{\text{core}}$ can, however, break down at relatively high values of α_b and/or for moderately asymmetric block copolymers, i.e., at $\alpha_b \geq (\gamma N_B / N_A^2 \varphi)^{2/3}$. In this case, the stronger electrostatic interactions in the corona transform crew-cut micelles whose coronae are in the osmotic annealing regime, $\Phi_{\text{ion}} \geq \Phi_{\text{ion}}^{(1)}$, into salt-dominated starlike micelles when the bulk concentration of salt reaches the value of $\Phi_{\text{ion}} = \Phi_{\text{ion}}^{*} \leq \Phi_{\text{ion}}^{(2)}$.

The transition point Φ_{ion}^{*} is specified by (107), and this rearrangement occurs abruptly (as the first-order phase transition). In the transition range two population of micelles, quasi-neutral crew-cut micelles and charged starlike micelles coexist in the solution.

The equilibrium parameters of the micelles after the transition coincide with those for charged starlike micelles.

In Fig. 7 the diagram of states for crew-cut micelles is presented in the Φ_{ion}, α_b coordinates. The diagram contains regions CC_{qn}, $\text{CC}_{\text{qn}'}$, CC_{osm}, CC_{ch} and S_{ch}. In region CC_{qn}, the micelles are quasi-neutral, and the coronae are weakly ionized, $\alpha \ll \alpha_b$. The dotted line indicates the value of α_b above which the CMC_{qn}

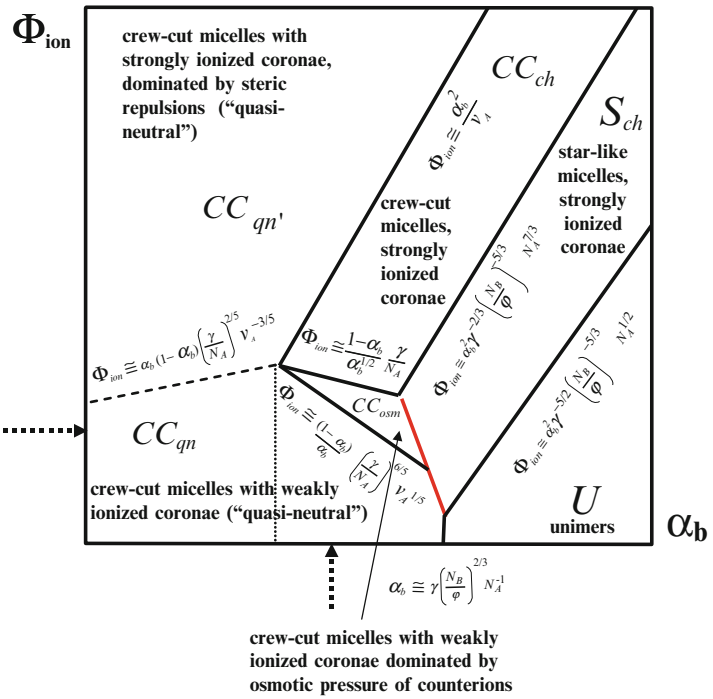

Fig. 7 Diagram of states in α_b, Φ_{ion} coordinates for dilute solution of block copolymers with pH-sensitive PE blocks, that associate in crew-cut spherical micelles, $N_A \ll \gamma^{2/7} (\frac{N_B}{\varphi})^{5/7} \nu_A^{-3/7}$. Vertical and horizontal *dotted arrows* indicate fixed values of pH and salt concentration corresponding to Fig. 8a, b and Fig. 8c, d, respectively

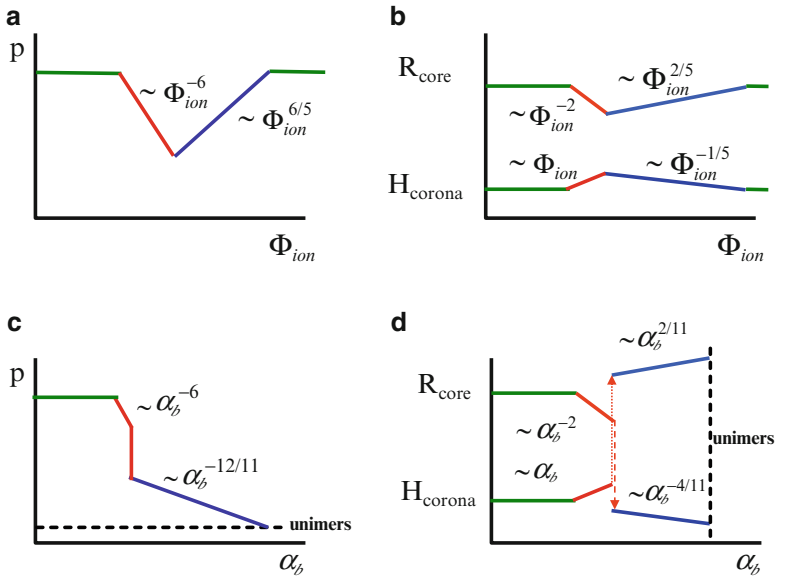

Fig. 8 Dependency of (**a**) aggregation number p; (**b**) radius of the core R_{core} and thickness of the corona H_{corona} in crew-cut spherical micelles with pH-sensitive coronal block as a function of salt concentration. The pH is fixed according to the position of the vertical dotted arrow in Fig. 5. Dependency of (**c**) p, and (**d**) R_{core} and H_{corona} as a function of pH. Salt concentration is fixed according to the position of horizontal dotted arrow in Fig. 7

deviates from CMC_n, cf. (103). In region $\text{CC}_{\text{qn}'}$, the coronal blocks are ionized, $\alpha \approx \alpha_b$, but the electrostatic interactions are strongly screened due to high salt concentration, and structural parameters of the micelles are the same as in region CC_{qn}. Line $\Phi_{\text{ion}}^{(1)}$ separates regions CC_{qn} and CC_{osm}. The bold line indicates the transition line $\Phi_{\text{ion}} = \Phi_{\text{ion}}^{*}(\alpha_b)$, where weakly ionized osmotic crew-cut micelles abruptly transform into strongly charged starlike micelles (region S_{ch}). In region CC_{ch}, the charged micelles acquire crew-cut shape. Line $\Phi_{\text{ion}}^{(2)}$ separates regions CC_{osm} from CC_{ch}. Upon crossing this line, a continuous transformation of micelles occurs.

The evolution in aggregation number, core radius, degree of dissociation, and extension of the coronal chains in a crew-cut micelle, as a function of salt concentration and pH, are schematically presented in Fig. 8.

In contrast to a nonmonotonous behavior of the equilibrium parameters of crew-cut micelles, the CMC decreases monotonously as a function of the bulk salt concentration, Φ_{ion}. Namely:

$$\ln \text{CMC}_{\text{CC}} \cong -\gamma(N_B/\varphi)^{2/3} + \begin{cases} -N_A \ln(1-\alpha_b) - N_A^3[\alpha_b \Phi_{\text{ion}}/\gamma(1-\alpha_b)]^2, & \Phi_{\text{ion}} \ll \Phi_{\text{ion}}^{(2)}, \\ N_A^{3/5}\gamma^{2/5}(v_A + \alpha_b^2/2\Phi_{\text{ion}})^{2/5}, & \Phi_{\text{ion}} \gg \Phi_{\text{ion}}^{(2)}. \end{cases} \quad (123)$$

8 Micelles with Quenched and Annealing Polyelectrolyte Coronae: Nonlocal Mean-Field Approach

The mean-field approach combined with the local electroneutrality approximation (LEA) can be extended beyond the boxlike model. To calculate the free energy of a micellar corona with the radial gradients in polymer density, we assume that all the free ends of blocks A are located at the corona periphery and are equally stretched. Within this model, the free energy of a micelle of morphology i ($i = 1,2,3$), can be explicitly calculated for both quenched and annealing PE coronae. We outline here only a general scheme of the approach, whereas the details can be found in [22, 32].

The Gibbs free energy per chain in the corona of morphology i is formulated as:

$$F_{\text{corona}}^{(i)} = \frac{3k_{\text{B}}T}{2}\int_{R_{\text{core}}}^{R_{\text{corona}}}\left(\frac{\mathrm{d}r}{\mathrm{d}n}\right)\mathrm{d}r + \int_{R_{\text{core}}}^{R_{\text{corona}}} f_{\text{int}}\{c_p(r)\}s(r)\mathrm{d}r. \tag{124}$$

Here, the first term accounts for the nonuniform stretching of the coronal block, whereas the second term accounts for the excluded-volume interactions, the translational entropy of mobile ions, and (in the case of an annealing PE block) the free energy gain due to corona ionization, as specified by (66), (67).

The local chain stretching at distance r from the center of micelle, dr/dn, is related to local polymer density, $c_p(r)$, as:

$$c_p(r) = \frac{\mathrm{d}n}{s(r)\mathrm{d}r}, \tag{125}$$

where:

$$s(r) = s(R_{\text{core}})\left(\frac{r}{R_{\text{core}}}\right)^{i-1}, \qquad i = 1,2,3. \tag{126}$$

This enables one to represent the free energy of the corona, (124), in the form:

$$F_{\text{corona}}^{(i)} = \int_{R_{\text{core}}}^{R_{\text{corona}}} f\{c_p(r), r\}s(r)\mathrm{d}r, \tag{127}$$

where the free energy density in the corona is given by:

$$f\{c_p(r), r\} = \frac{3k_{\text{B}}T}{2c_p(r)s^2(r)} + f_{\text{int}}\{c_p(r)\}. \tag{128}$$

The outermost radius R_{corona} of the corona follows from the normalization condition:

$$\int_{R_{\text{core}}}^{R_{\text{corona}}} c_p(r)s(r)\mathrm{d}r = N_A. \tag{129}$$

Minimization of the coronal free energy, (127), under the constraint given by (129) leads to the following equations for polymer density profile, $c_p(r)$, and for the radius of the corona, R_{corona}:

$$\frac{\delta}{\delta c_p(r)} f\{c_p(r), r\} = \lambda, \tag{130}$$

$$\left(c_p(r) \frac{\delta}{\delta c_p(r)} f\{c_p(r), r\} - f\{c_p(r), r\} \right)_{r=R_{\text{corona}}} = 0, \tag{131}$$

where λ is the (exchange) chemical potential of monomer unit of the coronal block. For specified density of the interaction free energy, $f_{\text{int}}\{c_p(r) = f_{\text{ev}}\{c_p(r)\} + f_{\text{ion}}\{c_p(r)\}$, the coronal free energy, $F^{(i)}_{\text{corona}}$, can be calculated with the account of (127)–(131) at arbitrary radius of the core, R_{core}. The density of the free energy of non-ionic interactions, $f_{\text{ev}}\{c_p(r)\}$, is given by (66). Within the LEA, the ionic contribution, $f_{\text{ion}}\{c_p(r)\}$, can be obtained from (84) or (96) for a quenched and an annealing corona, respectively, by replacing $c_p \to c_p(r), \alpha \to \alpha(r)$. In the latter case, the degree of ionization of the coronal chains $\alpha(r)$ becomes also a function of the radial coordinate, r, and is related to local polymer concentration, $c_p(r)$, by (97) and (99).

Compared to the boxlike model, the nonlocal mean-field approach provides deeper insights in the structure of a micellar corona. In particular, in starlike micelles ($R_{\text{corona}} \gg R_{\text{core}}$), the polymer density, $c_p(r)$, decays as a power law function of r in the central regions of the corona. At low salt concentration, the local degree of ionization in the corona increases as a power law function of r, according to the relation between $c_p(r)$ and $\alpha(r)$, specified by (99). In both limits of starlike ($H_{\text{corona}} \gg R_{\text{core}}$) and crew-cut ($H_{\text{corona}} \ll R_{\text{core}}$) micelles, the asymptotic power law expressions for the coronal size and the free energy, obtained in the framework of the boxlike model, are recovered. In addition, explicit numerical prefactors for both properties can be calculated [22].

Analysis of the radial gradients in polymer and free energy densities in the corona of aggregate with morphology i enables one to obtain linear in curvature correction terms for the coronal free energy of crew-cut micelles, $H_{\text{corona}} \ll R_{\text{core}}$. As we demonstrate below in Sects. 10 and 11, the magnitude of these curvature-dependent terms can be tuned by variations in the pH and ionic strength in the solution. As a result, morphological transformations of block copolymer aggregates can take place.

9 Self-Consistent Field Modeling of Micelle Formation

Scaling approaches to predicting structural dependencies for micelles are useful to reveal power law behavior, but lack the precision with respect to numerical coefficients. The mean-field theory for self-assembly, as discussed above, unravels the general trends for these complex micellar systems, but implements major approximations. In particular, the boxlike model neglects gradients in the local densities in both the core and corona regions. A more advanced nonlocal mean field model

accounts for radial gradients in the coronal density profile and in local stretching of both the coronal and the core-forming blocks, but implements the strong stretching approximation. Moreover, large-scale fluctuations in stretching of the coronal chains (distribution of the free ends) are neglected. Therefore, one cannot expect truly accurate molecularly detailed results from these analytical theories. In this section we discuss the numerical self-consistent field (SCF) approach to self-assembly of block copolymers [65–69]. The SCF approach is also of the mean-field type and thus has a known tendency to overestimate the free energy of the unimers, as well as the free energy for the polymer brushes that make up the micelle coronae. In contrast to the box model, one can account for all relevant gradients in densities in the micelle [70–73] because it includes the statistical weights of all possible chain conformations within a freely jointed chain approximation [74] and therefore is able to account for molecular details. Not surprisingly, the equations need to be solved numerically [75], and the calculations really become challenging for weakly charged and pH-dependent systems, especially in the limit of low salt concentrations. As computations are more demanding, the SCF approach should be seen to complement the analytical approaches rather than to replace them.

The scaling laws and the analytical dependencies that are discussed in this review, are expected to hold in the limit of long chains. In stark contrast, well-defined block copolymers that form responsive micelles often have a limited molecular weight. The analytical theory is only expected to give some guidance and trends for micelles composed of short polymers because several of its premises are not met. From this perspective, there exists a need to forward approaches that can give accurate information on self-assembly for relatively short copolymers [76]. As computational difficulties are gradually overcome, Monte Carlo and molecular dynamics computer simulations are used to generate results for self-assembly of copolymers in selective solvents. Accurate results are expected for short copolymers, but detailed analysis for micellization of amphiphilic ionic copolymers is not yet available.

Numerical SCF theory can be used to probe the self-assembly of both long and short copolymers [72, 73, 77], for non-ionic [78–82] as well as ionic systems [83–86]. For long polymers, we can use the numerical SCF theory to check the scaling predictions and to test the validity of the analytical approximations. For short chains, the numerical theory is still expected to give reasonable predictions and results can be used to analyze experiments on the one hand, and to complement computer simulation results on the other hand.

9.1 Spherical Micelles: Implementation of Numerical SF-SCF Method

Here, we discuss results from the SF-SCF model wherein the SCF equations are implemented using the discretization scheme of Scheutjens and Fleer. Details of this approach have been presented in the literature [74]. Here, we only specify the

main approximations of the model and focus on diblock copolymers $A_{N_A}B_{N_B}$ in a selective monomeric solvent S that may contain monovalent salt ions as well as hydroxyl and hydrogen ions.

Calculations are done in a spherical coordinate system wherein lattice sites are organized in layers with spherical geometry [70, 87, 88], resulting in measurable radial volume fraction profiles for all the components $\varphi(r)$. Generalizations to other geometries are straightforward and one can therefore use the SCF approach to study micelle–cylinder–lamelle transitions. To date, the SCF work in this direction has been limited to surfactant systems [70, 88]. In this review, we thus focus on the block copolymer micelles of spherical geometry. Besides the volume fractions $\varphi(r)$, the SCF theory features radial segment potential profiles $u(r)$ for each type of segment $X = A, B, S, \cdots$. Using these profiles, the free energy F can be computed. The optimization of this free energy results in the self-consistent field machinery:

$$u[\varphi(r)] \leftrightarrow \varphi[u(r)]. \tag{132}$$

The left-hand side of this equation indicates that the segment potentials are uniquely computed from the volume fractions. First of all we have a Lagrange field, which is coupled to the incompressibility relation $\sum_X \varphi_X(r) = 1$ implemented for all coordinates r. In addition there are the excluded volume interactions. These are accounted for using the Bragg–Williams approximation, where the interactions are parameterized by Flory–Huggins χ parameters. When the segments are charged they give rise to an electrostatic contribution, $e\Psi(r)/k_BT$, where Ψ is the local electrostatic potential. The potentials follow from solving, for a specified charge distribution $q(r)$, the Poisson equation. In these systems we introduce a 1:1 electrolyte wherein the ions take up the same volume as a solvent molecule [89]. A two-state model is implemented when the A segments are weakly charged. Depending on the local proton concentration and the pK_a value, a segment can either be in the state with a negative charge or in a neutral form. These two states are equilibriated with the account of the autodissociation of water. In this way, the degree of dissociation of a monomer unit A, α, is a function of the radial coordinate [90]. For such system, we introduce proton and hydroxyl ions (both of the same size as the water molecules) into the system and fix the bulk concentration of hydrogen ions to set the (bulk) pH.

The right-hand side of (132) indicates that the segment volume fractions are uniquely computed from the segment potentials. As mentioned above, we implement a freely jointed chain model, which ensures the chain connectivity, but which does not prevent backfolding of the chain to previously occupied lattice sites. For this chain model, the volume fractions can be computed efficiently using a propagator formalism, which is intimately related to the Edwards equation [91].

The free energy of n micelles in a volume (which is assumed to be incompressible) that has a solvent, copolymers, etc. ($j = 1, 2, \ldots$) as its molecular species, is given by $F = \Omega n + \sum_j n_j \mu_j$ where n_j and μ_j are the number and chemical potential of molecules of type j. The optimization of the free energy with respect to the number of micelles leads to the condition of equilibrium for micelles, i.e., $\Omega = 0$ [36, 92]. The SCF model gives access to the grand potential Ω_m of the micelle that

is pinned at the center of the computational box. When the micelle is sufficiently large, we may ignore the translational entropy and define stable micelles having $\Omega_m \approx \Omega = 0$ (cf. (5) with $\ln c_{mic} \approx 0$). Unless mentioned otherwise, we follow this Ansatz in this section. By doing so we give an upper limit of the micelle size and aggregation number (see discussion in Sect. 2.1).

We will focus on spherical micelles formed by copolymers in a monomeric solvent. The default parameters are consistent with a selective solvent $\chi_{BS} = \chi_{AB} = 1.5$ and $\chi_{AS} = 0$. The discretization length (size of a lattice site = size of a segment) a is equal to 0.5 nm, which is chosen to be close to the Bjerrum length for aqueous solutions around room temperature. The relative dielectric constant ϵ is set equal to 80 for all species except for apolar species, for which $\epsilon_B = 2$. Further details are given in the relevant sections.

The radial density profile (polymer volume fraction φ_A) in the corona of micelle can unambiguously be used to find the aggregation number p. The sizes of core and corona are less trivially obtained. To help define the micellar dimensions we have incorporated two molecular markers at both ends of the hydrophilic block, named X_2 (at the junction between A and B segments) and X_1 (at the free end of the A block). The first moment $< X_k >$:

$$\langle X_k \rangle \equiv \frac{\sum_r L(r) r \varphi_{X_k}(r)}{\sum_r L(r) \varphi_{X_k}(r)} \qquad k = 1, 2, \tag{133}$$

where $L(r) \propto r^2$ is the number of lattice sites at coordinate r, is a measure for the average position of the marker. The X_2 is typically at the boundary between the core and the corona and $\langle X_2 \rangle$ is a measure for the core size, R_{core}. The average position of the first marker is a measure of the overall size of the micelle, R_{corona}. The difference between these two average positions is a measure for the dimension of the corona, H_{corona}.

The CMC of the copolymer system can also be extracted from the radial profile φ_A because it corresponds to the concentration of copolymers in the limit of $r \to \infty$.

9.2 Neutral Micelles of Amphiphilic Block Copolymers

The SF-SCF approach has been used to consider many aspects of amphiphile self-assembly [77, 82, 88, 93–96]. Here, we focus on results that are relevant for the self-assembly of non-ionic copolymers in spherical micelles. The self-assembly of non-ionic copolymers is characterized by relatively few parameters, and we will use this system to show the micellar properties as a function of the most relevant molecular parameters.

In Fig. 9 we give, as an example, the radial density (volume fraction) profiles through a spherical micelle composed of $A_{200}B_{50}$ copolymers with a four times longer hydrophilic block than the hydrophobic block. Inspection of the radial profile

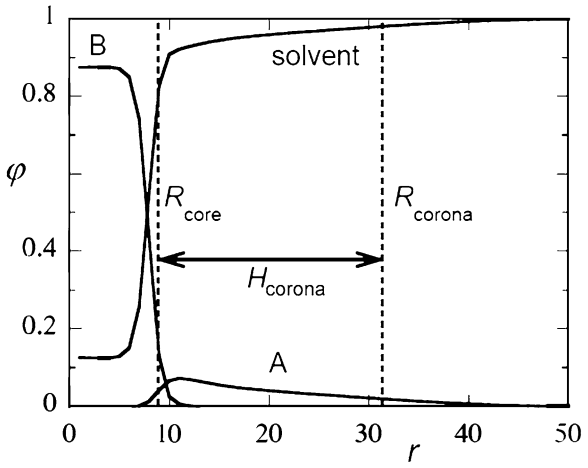

Fig. 9 Radial volume fraction profiles for the core-forming (B) segments, the corona-forming (A) segments, and the monomeric solvent S for copolymer $A_{200}B_{50}$. The vertical *dashed lines* specify the core size R_{core}, the overall size of the micelle R_{corona}, and the size of the corona H_{corona}. These measures are found by two markers placed in the molecule. One of the markers, X_1, is positioned between blocks A and B; the second marker, X_2, is at the end of the hydrophilic block A. The first moments of the density distributions of these markers are indicated by the two vertical *dashed lines*. The Flory–Huggins parameters have the default values $\chi_{BS} = \chi_{AB} = 1.5$ and $\chi_{AS} = 0$. The grand potential $\Omega_m = 0$, which represents equilibrium when translational entropy of the micelle is ignored

for the core-forming block B exemplifies that, as anticipated above, the core has a homogeneous density. The density in the core is an increasing function of χ_{BS}. In contrast to the assumption in the boxlike model, the volume fraction profile in the corona has a clear dependence on r. Analysis of the latter profile indicates the following generic features: For very small cores, the profile represents that of a starlike micelle and the volume fraction of monomers A decays as a power law near the micelle center, in accordance to the predictions of the analytical theory. At larger distances (at the periphery of the corona), the profile is quasi-parabolic. The core–solvent interface is sharp and becomes progressively sharper with increasing χ_{BS}, but also when the repulsion between A and B (specified by the value of χ_{AB}) increases. In Fig. 9 we also show the sizes of the micelle, R_{corona}, and of the core, R_{core} (dashed vertical lines), and the thickness of the corona, H_{corona}, obtained as explained above.

The dependence of the aggregation number and the CMC on the lengths of the polar blocks are given in Fig. 10a, b, respectively, for two values of the core-forming block and for two values of the solvent quality of the corona-forming block. The scaling theory and also the boxlike model give different dependencies for these quantities, depending on the geometry of micelle (crew-cut or starlike). The size of the core, R_{core}, and that of the corona, H_{corona}, are presented as a function of the length of the soluble block A in Fig. 10c. As can be seen in Fig. 10c, the size of the core decreases and that of the corona increases with increasing length of the coronal

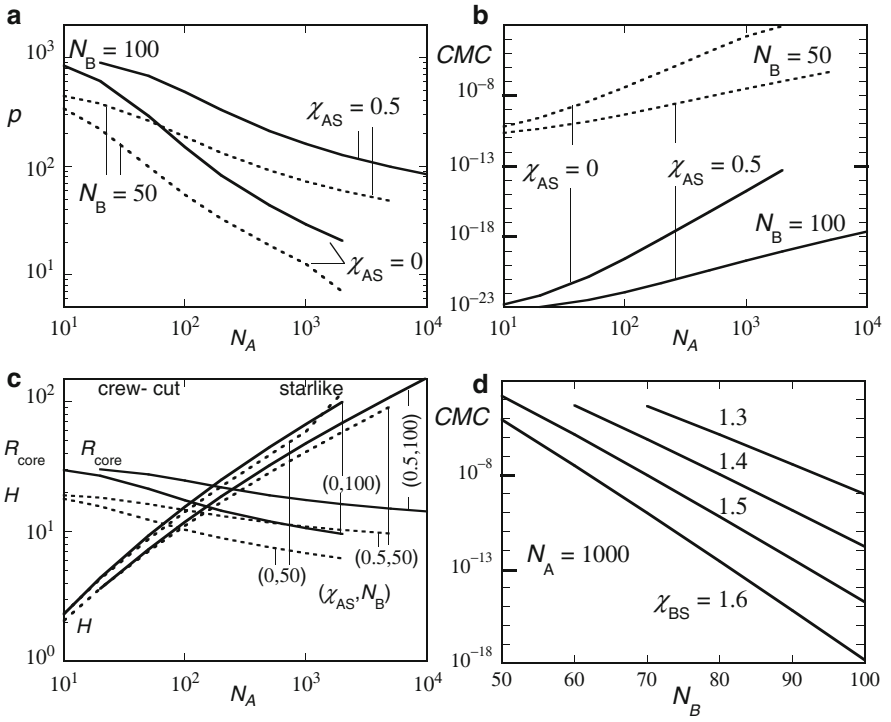

Fig. 10 (**a**) The micellar aggregation number p as a function of the length of the polar block N_A; (**b**) CMC (volume fraction of copolymer in the bulk) as a function of the block length N_A; and (**c**) the core size R_{core} and corona size H as a function of N_A for equilibrium micelles ($\Omega_m = 0$) with $N_B = 50$ (*dotted lines*) and $N_B = 100$ (*solid lines*) and χ_{AS} values of 0 (good solvent) and 0.5 (theta solvent). Other parameters have the default values. (**d**) CMC as a function of the length of the core-forming block N_B for $N_A = 1000$ and for different values of the solvent quality of the core-forming block χ_{BS} as indicated

block. The boundary from crew-cut to starlike shape appears around $N_A \approx 100$ for $N_B = 50$ and is about twice as high for $N_B = 100$. Over a wide range of N_A values, the core and corona dimensions are comparable and therefore there is a wide range of parameters for which the micelle is in the crossover from crew-cut to starlike regimes. Starlike micelles occur over a wider range of parameters when the solvent quality for the corona chains is better.

From Fig. 10a, b it is difficult to extract clear power law dependencies. Therefore, we only qualitatively discuss the trends that are in qualitative agreement with the scaling analysis. The longer the polar block A, the smaller the aggregation number and the higher the CMC, (31). Inferior solvent quality for the polar block makes these trends less pronounced. The decrease in the aggregation number with increasing length of the polar block approximately follows a power law dependence, where the apparent exponent is highest in the crossover regime. The slope of the dependence $p(N_A)$ is not a strong function of the length of the core-forming block. It is more steep for good solvent than for theta solvent conditions.

In Fig. 10d we show that the CMC depends exponentially on the length N_B of the core-forming block. The slope of this dependence is proportional to the χ_{BS}, and is well documented in the surfactant literature. We note that the dependence of the CMC on the length of the core block (Fig. 10d) is much stronger than that of the corona (Fig. 10b). In passing, we note that the SCF theory assumes that the chains in the bulk are ideal and are fully surrounded by the solvent. The method thus ignores the possibility that the core-forming block of unimers is collapsed. In such a state, the unimer also avoids most contacts with the solvent and we conclude that the SF-SCF approach overestimates the free energy of unimers. Collapse of the hydrophobic block of unimer would increase CMC according to (31), (37).

9.3 Micelles with Quenched Polyelectrolyte Corona

For block copolymers comprising ionic hydrophilic blocks one has, in addition to the parameters discussed in the previous section, several new parameters that influence the micelle characteristics. Here, we focus on how these new parameters, i.e., the charge density in the corona and the ionic strength influence the micelle characteristics. In this section we therefore focus on a given molecular composition and we opt for a symmetric case, $A_{200}B_{200}$, and fixed the values for the excluded-volume interactions parameters: $\chi_{BS} = \chi_{NaB} = \chi_{ClB} = \chi_{AB} = 1.5$ and $\chi_{AS} = \chi_{NaS} = \chi_{ClS} = 0$. Hence, we choose for the scenario that the ions have similar excluded-volume interactions with the polymer segments as the solvent. Note that in practice ions might have some specific affinity for either the core or the coronal blocks, and this situation could be also addressed in frames of the SF-SCF model.

In Fig. 11 we show an example of the relevant radial distributions for an equilibrium micelle composed of a symmetric ionic/non-ionic diblock copolymer with a

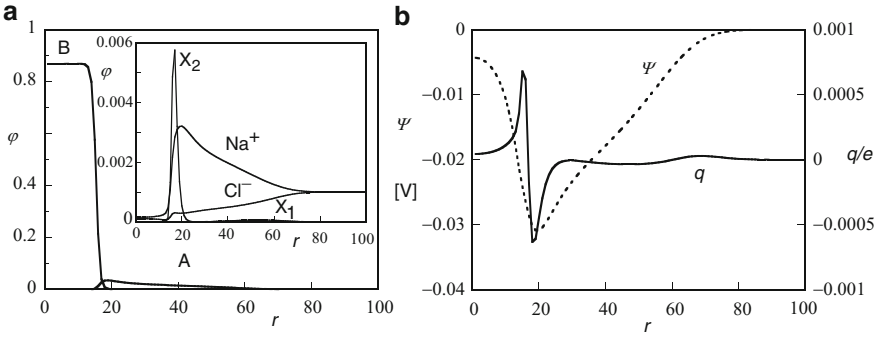

Fig. 11 (**a**) Radial volume fraction profiles for apolar block B and charged coronal block A with $\alpha = 0.2$ (every fifth segment along the coronal block has a negative charge $-e$). *Inset* shows radial distributions for the two markers and for the 1:1 electrolyte for which the bulk concentration is $\Phi_s = 0.001$. (**b**) Corresponding radial electrostatic potential profile $\Psi(r)$ (*left ordinate*) in volts and the dimensionless radial charge density $q(r)/e$ (*right ordinate*)

charge density of -0.2 charges per segment in the coronal chain in a $\Phi_s = 0.001$ salt solution. In Fig. 11a, the volume fractions of the polar and apolar blocks are shown in combination with that of the two markers. The distributions of the salt ions are given as well (in the inset). Compared to Fig. 9 we show here a result for which the core is larger. In the corona the counterions (Na) accumulate and the co-ions (Cl) are depleted with respect to the bulk concentrations. Both co- and counterions avoid the core because they interact with B monomers as molecules of a poor solvent.

In Fig. 11b the radial distribution of the electrostatic potential is shown in combination with the overall distribution of the charge density. As, in this case, the charge along the chain is quenched, the charge distribution due to the polymers in the micelle simply follows the distribution of the A segments. The total charge profile is now computed from $q(r)/e = -0.2\varphi_A(r) + \varphi_{Na}(r) - \varphi_{Cl}(r)$. As seen in Fig. 11b, the overall charge in the corona chain is very low, proving that the LEA is accurate in this case. The radial electrostatic potential in the micelle is negative throughout the micelle, as expected. One can systematically investigate the radial profile of the electrostatic potential and one then finds that the electrostatic potential is approximately parabolic in the corona region. As compared to Fig. 9 the average density of segments in the corona is significantly lower in the case of the charged micelle than for the non-ionic case. The accumulation of counterions in the corona causes a local high osmotic pressure, which, in turn, swells the corona region. This is typical for micelles with a PE corona.

Copolymers with quenched PE blocks form micelles that strongly respond to variations in the ionic strength in solution. To illustrate this behavior, which is already anticipated above from the scaling theory and the boxlike model, we show the micelle characteristics in Fig. 12. In these graphs, we plot the aggregation number, the CMC and the sizes of the core and corona as a function of the fractional charge along the corona block for various values of the salt concentration Φ_s.

Inspection of the results of Fig. 12 shows that in the limit of high ionic strength and low charge density, the micelle parameters go to the limit of non-ionic micelles. With increasing charge and decreasing ionic strength, rather dramatic changes in micellar properties are predicted. As illustrated in Fig. 12a, the aggregation number dramatically drops to very low values. More specifically, when $\Phi_s = 10^{-4}$ the micelles disappear when the fractional charge is more negative than -0.1. Correspondingly, the CMC is a very strong function of the charge density along the A chain, especially when the ionic strength is low. This strong dependence is traced to the loss in translational entropy of the entrapped counterions. As the density of segments in the core is not a strong function of the aggregation number, the size of the core follows the aggregation number. Hence, R_{core} is a strongly decreasing function of the charge density. On the other hand, the size of the corona increases with increasing charge density. The higher the charge density in the corona, the more counterions are localized in the corona, with corresponding consequences for the osmotic driving force that swells the corona. At the same time, the effective second virial coefficient of monomer–monomer interactions in the corona is a strongly increasing function of the charge density and a decreasing function of the ionic strength.

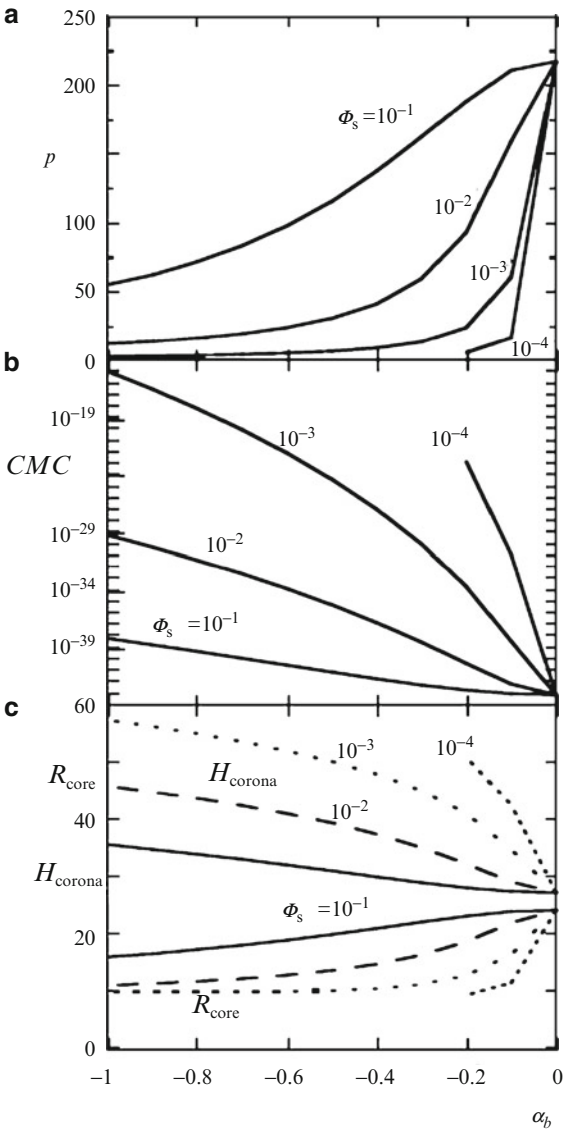

Fig. 12 (**a**) Dependence of the aggregation number p; (**b**) CMC; and (**c**) core size R_{core} and corona size H_{corona} as a function of the fractional charge α_b for quenched PE block at Φ_s values of 10^{-1}, 10^{-2}, 10^{-3}, and 10^{-4}. Both blocks have the length of 200 segments. $\Omega_m = 0$ and the interaction parameters have the default values

From the above it is clear that one needs relatively long core-forming blocks in order to generate a strong enough associating force to keep highly charged coronal chains in the micelle. This observation explains why, in the next section, we focus on copolymers with a longer apolar block.

9.4 Micelles with Annealing Polyelectrolyte Corona

When the charge density in the corona chains is pH-dependent (i.e., the charges are annealing), the micelles are even more responsive. Here, we consider micelles composed of a relatively long hydrophobic block, $N_B = 300$, and a shorter acidic coronal block, $N_A = 100$, to illustrate the properties of these systems. It is assumed that the A segments have an (intrinsic) pK_a and when the $pH \gg pK_a$, all the segments release a proton so that each one acquires a negative charge $(-e)$ and $\alpha_b = 1$. For $pH \ll pK_a$ all segments are in the protonated (neutral) state, i.e. $\alpha_b = 0$. The difference $\Delta pH = pK_a - pH$ is important. When the chargeable segments are isolated in the bulk solution, half the segments will be charged at $pH = pK_a$ (i.e., $\alpha_b = 0.5$), as described by (98). In the corona, however, the locally high electrostatic potential suppresses the degree of dissociation and, typically, the effective pK_a^{eff} (defined as the pH at which half the groups are titrated) is shifted by several pH units with respect to the intrinsic pK_a.

The radial volume fraction profiles of monomer units in such micelle at a pH one unit below the intrinsic pK_a and for a salt concentration of $\Phi_s = 10^{-3}$ are shown in Fig. 13. In this case, the degree of dissociation in the bulk is $\alpha_b \approx 0.1$. As shown in Fig. 13 (right ordinate), the degree of dissociation is significantly suppressed in the corona region of the micelle. This is due to the negative electrostatic potential in the corona. As shown for quenched micelles, the electrostatic potential is low outside the corona of the micelle (i.e., both in the core and in the bulk solution) and this is why $\alpha(r)/\alpha_b \approx 1$ in these regions. In this particular example, the corona block is rather small and the ionic strength is not too low. This is why in this case the core size exceeds that of the corona. Hence in this example the micelle is in the crew-cut regime. For such a micelle, the curvature in the coronal part of the micelle is not very important and the profile is close to that in a planar PE brush. Such a brush is known [30] to have a parabolic profile of the electrostatic potential.

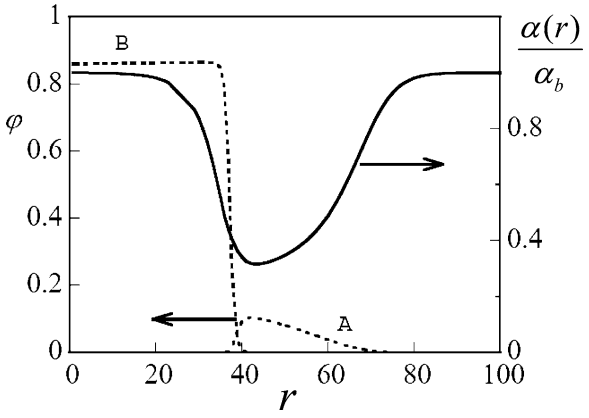

Fig. 13 Radial density profiles for A and B segments (*left ordinate*), and radial distribution of the degree of dissociation normalized to the dissociation of an A segment in the bulk, $\alpha(r)/\alpha_b \approx 1$ (*right ordinate*), for $A_{100}B_{300}$, $\Phi_s = 10^{-3}$, and $pH - pK_a = -1$

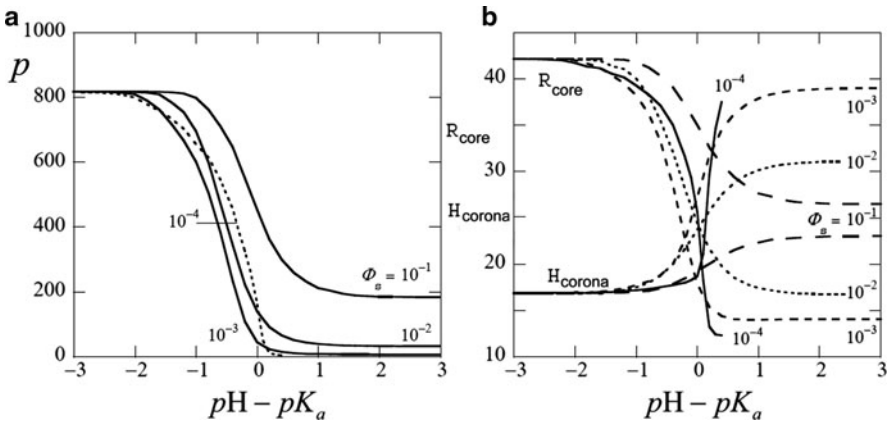

Fig. 14 (**a**) Aggregation number p, and (**b**) core size R_{core} and corona size H_{corona} as a function of the difference between pH and pK_{a} for $\Phi_s = 10^{-4}$, 10^{-3}, 10^{-2}, and 10^{-1} as indicated. The copolymer chain $A_{100}B_{300}$ has polar A segments with annealing charges. Other parameters have the default values

For micelles composed of diblock copolymers with pH-sensitive coronal blocks, all measurable characteristics become a strong function of the pH and ionic strength in solution. In Fig. 14 we show how the aggregation number and the sizes of the core and corona change over a wide range of these parameters. With increasing pH, the polyacid chains become gradually more charged, (117), and the response of the micelles is to decrease the aggregation number as well as the core size [cf. (118), (120)]. At the same time the corona size increases, (119) so that the overall size of the micelle is a much weaker function of the pH.

As illustrated in Fig. 14 there is a nontrivial salt concentration dependence for the aggregation number and core size: both pass through a minimum at low salt concentration, if pH $\approx$ pK_{a} (cf. predictions of the analytical theory schematically depicted in Fig. 8). In all cases, the drop in aggregation number, as well as the size changes are more dramatic for lower ionic strengths. Furthermore, the major changes occur near pH $\approx$ pK_{a}; however, in the series $\Phi_s = 10^{-1}$, 10^{-2} and 10^{-3} the drop in p and R_{core} and the rise in H_{corona} occur at gradually lower pH values, but this trend reverses for even lower ionic strength. More specifically, for $\Phi_s = 10^{-4}$ the drop occurs very close to pH $\approx$ pK_{a} at a value of the pH that is larger than for $\Phi_s = 10^{-3}$. For even lower ionic strengths this upward shift continues (not shown). It is relevant to mention that for these low ionic strengths, no stable micelles are present when pH is much larger than pK_{a}.

Comparing the core and corona sizes as presented in Fig. 14 we see that for these rather asymmetric copolymers with a much longer apolar block than polar block, the micelles remain in the crew-cut regime for all pH values ($R_{\text{core}} > H_{\text{corona}}$) at high ionic strength. For lower ionic strengths, there is a transition from a crew-cut to a starlike micelle that takes place around pH $\approx$ pK_{a}. Typically, the overall size of the crew-cut micelles ($R_{\text{corona}} = R_{\text{core}} + H_{\text{corona}}$) decreases with pH due to the dominant decrease in R_{core}. However, for very low ionic strengths, the overall micelle size

goes through a minimum around the crossover from crew-cut to starlike micelles. This minimum appears due to interplay of the opposite trends in evolution of R_{core} and H_{corona} as a function of pH. The transition from crew-cut to starlike micelles becomes progressively sharper the lower the ionic strength in the solution.

From Fig. 14 it is noticed that the crew-cut to starlike micelle transition becomes sharper with decreasing ionic strength. In Fig. 14 we focused on micelles with a vanishing grand potential, and that have the property that $\partial\Omega_m/\partial p < 0$ [see (8)]. As discussed in Sect. 7.2, below some threshold ionic strength the crew-cut to starlike micelle transition becomes jump-like and, under certain conditions, both the starlike and the crew-cut micelles coexist in equilibrium. We illustrate this coexistence with a study on micelles at low salt concentration, $\Phi_s = 10^{-5}$. For more details we refer to the literature where the transition is analyzed in depth for a slightly different case [23].

The coexistence between crew-cut and starlike micelles is demonstrated for micelles composed of $A_{50}B_{300}$ copolymers using the default solvency parameters. We selected the low ionic strength conditions, $\Phi_s = 10^{-5}$. In this case, the pH-induced micelle-to-micelle jump-like transition occurs around pH $-\text{p}K_\text{a} \approx 1$, i.e., for a pH just above the pK_a. It is illustrated in Fig. 15a that in a narrow pH range, the grand potential Ω_m develops a new region of stability at small values of p (indicated by the conditions $\Omega_m > 0$ and $\partial\Omega_m/\partial p < 0$). For lower values of the pH (upper curve in Fig. 15a), the grand potential becomes an increasing function of p, which signals that these micelles are unstable. For higher values of the pH (lower curves in Fig. 15a), the grand potential becomes negative for small values of p, implying that these small micelles spontaneously disintegrate. For coexistence between starlike and crew-cut micelles, it is further necessary that the chemical potentials of the copolymers in both aggregates match. As proven in Fig. 15b, it is possible to find such conditions. For stable micelles, the condition $\partial \ln \varphi^b/\partial p > 0$ should be fulfilled and, as can be seen in Fig. 15b, this occurs both for small values of p (starlike micelle) and for much larger values (crew-cut micelle). For the value of pH $-\text{p}K_\text{a} = 1$, we therefore find a corridor of micelle sizes for which the two types of micelles coexist at the same chemical potential (indicated by the shaded area). For lower values of the pH, it is found from the chemical potentials that crew-cut micelles are more favorable than the starlike micelles (not shown), whereas at higher pH values the opposite occurs. Indeed, the coexistence region (in terms of a pH interval) is very narrow.

In Fig. 15c,d we show the radial volume fraction profiles for A and B segments. By visual inspection of the two profiles, it is clear that the coronal size is much larger than the core size in Fig. 15c (starlike micelle) and the opposite occurs in Fig. 15d (crew-cut micelle). For the starlike micelle, the density in the corona is much lower than in the crew-cut case. Due to the curvature, the corona of a starlike micelle layer has two regions: near the core the density drops as a power law function of the distance from the center of the core and near the periphery the shape of the profile resembles that in a planar-like corona. These trends are in line with predictions of the analytical theory.

In the SCF results discussed in this section, it was pre-assumed that the geometry of the micelles is spherical. Especially for the cases that the micelles are in the crew-

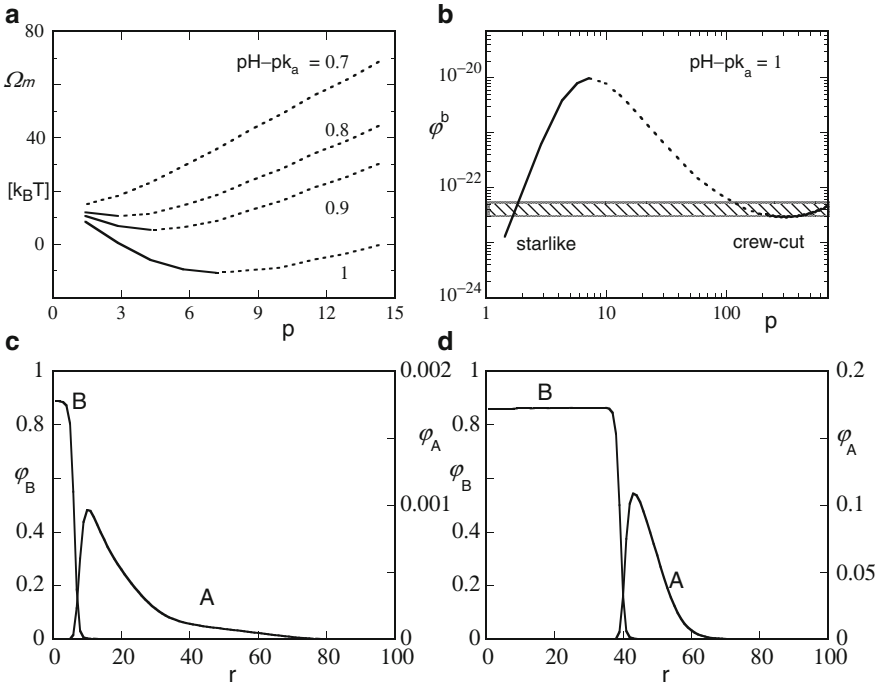

Fig. 15 (**a**) Grand potential Ω_m of a micelle composed of $A_{50}B_{300}$ copolymers and fixed in the center of the coordinate system as a function of the aggregation number p. (**b**) The volume fraction of the unimers φ^b that are in equilibrium with the micelles, as a function of the aggregation number p for given values of pH. The unstable parts of the curves of (**a**) and (**b**) are *dotted*. The stable parts are shown by *solid lines*. The *shaded area* in (**b**) represents the coexistence region where starlike and crew-cut micelles coexist. In (**c, d**), the radial volume fraction profiles for the apolar (B) and annealing charged (A) segments are shown for a typical starlike ($p = 3$) and a typical crew-cut ($p = 700$) micelle, respectively. The two micelles have almost identical grand potential Ω_m (very close to zero) and their copolymers have (almost) the same chemical potentials. In all panels $\Phi_s = 10^{-5}$

cut regime, one should consider the relative stability of the aggregates of the same copolymers, being in the same physical chemical conditions, but with a different geometry (cylindrical or lamellar). Although such analysis is possible, systematic SCF analysis of nonspherical block copolymer aggregates is currently lacking in the literature.

10 Polymorphism of Self-Assembled Aggregates of Block Copolymers with Quenched Polyelectrolyte Blocks

Similarly to the case of non-ionic micelles, micelles with a charged corona can demonstrate shape transformations. The physical origin of these morphology

changes is the same as in non-ionic micelles. That is, an increase in curvature of the micellar core decreases the coronal electrostatic interactions (with respect to a planar PE corona) at the cost of an additional stretching of the insoluble core blocks. These changes in the coronal and core free energies become comparable when the size of the core, $R_{\rm core}$, becomes larger than that of the corona, $R_{\rm core} \geq H_{\rm corona}$. Therefore, one anticipates morphological transformations (under both low and high salt conditions), when spherical micelles acquire the crew-cut shape. In the case of ionic coronal block, the morphological transitions can be triggered by tuning the strength of repulsive interactions in the corona, e.g., by variation in the ionic strength of the solution.

To specify the range of thermodynamic stability of micelles with morphology i, at a given salt concentration, $\Phi_{\rm ion}$, we go beyond the boxlike model and incorporate polymer density gradients in the coronal domain and account for a nonuniform stretching of the blocks. We follow here the arguments of [20, 22].

In a crew-cut aggregate with morphology i, the free energy per chain is given by $F^{(i)} = F^{(i)}_{\rm core} + F^{(i)}_{\rm interface} + F^{(i)}_{\rm corona}$, where the first two terms are specified by (40), (41), and (39), whereas the coronal contribution is approximated if the core of the aggregate is weakly curved, $H_{\rm corona}/R_{\rm core} \approx H^{(1)}_{\rm corona}/R_{\rm core} \ll 1$, as:

$$F^{(i)}_{\rm corona} \approx F^{(1)}_{\rm corona} - \frac{3(i-1)}{2}\left(\frac{H^{(1)}_{\rm corona}}{N_A^{1/2}}\right)^2 \frac{H^{(1)}_{\rm corona}}{R_{\rm core}}. \tag{134}$$

Here, $H^{(1)}_{\rm corona}$ and $F^{(1)}_{\rm corona}$ are the respective thickness and free energy (per chain) in a planar brush with grafting area $s(R_{\rm core}) = iN_B/\varphi R_{\rm core}$. The specific expressions for $H^{(1)}_{\rm corona}$ and $F^{(1)}_{\rm corona}$ are determined by the state of a PE brush (osmotic, salt-dominated, or quasi-neutral). By substituting the corresponding expressions for $H^{(1)}_{\rm corona}$ and $F^{(1)}_{\rm corona}$ in (134), one finds the coronal free energy per chain, $F^{(i)}_{\rm corona}$, in an aggregate of morphology i and, subsequently, the equilibrium value of the free energy, $F^{(i)}$, in a weakly curved crew-cut aggregate. The binodals, separating stability regions of aggregates with morphologies i and $i+1$, are derived from the condition $F^{(i)} = F^{(i+1)}$.

10.1 Salt-Free Solution

We first find the binodals in a salt-free solution of block copolymers with a quenched PE block A. Assuming Gaussian elasticity of the stretched coronal blocks, and taking advantage of the LEA (all mobile counterions are entrapped inside the corona), one finds [22]:

$$\frac{F^{(1)}_{\rm corona}}{k_{\rm B}T} = \alpha_b N_A \left[\ln\left(\frac{\sqrt{3\alpha_b}}{s(R_{\rm core})}\right) - \frac{1}{2}\right] \tag{135}$$

and:

$$H_{\text{corona}}^{(1)} = \frac{1}{\sqrt{3}} \alpha_b^{1/2} N_A. \tag{136}$$

Note that the LEA can be safely applied in salt-free solutions of the ionic/hydrophobic block copolymers at concentrations sufficiently larger than the CMC to insure finite electrostatic screening length in the solution.

The free energy per chain, $F^{(i)}$, in an aggregate of morphology i yields:

$$\frac{F^{(i)}}{k_B T} \approx \frac{F_{\text{corona}}^{(1)}}{k_B T} + \gamma s(R_{\text{core}}) - \frac{(i-1)}{2i\sqrt{3}} \frac{\alpha_b^{5/2} N_A^3 \varphi}{\gamma N_B} + b_i \frac{i^2 N_B \gamma^2}{\varphi^2 \alpha_b^2 N_A^2}. \tag{137}$$

Here, the first two terms are the free energy of the planar corona and core–water interface, respectively. The third term is the reduction of coronal free energy due to curvature, while the last term accounts for the elastic stretching of the core blocks. Similarly to the case of non-ionic micelles, the area s per chain is determined by balancing the dominant free energy contributions (the first and the second terms in (137)). Correspondingly, the binodals are specified from balancing the correction terms [the third and forth terms in (137)] in the free energies of aggregates with morphology i and $i+1$, as:

$$\frac{\alpha_b^{9/2} N_A^5 \varphi^3}{N_A^2 \gamma^3} = 2\sqrt{3} i(i+1) \left[b_{i+1}(i+1)^2 - b_i i^2 \right] \qquad i = 1, 2. \tag{138}$$

The transition from morphology i to $i+1$ (i.e., lamella to cylinder or cylinder to sphere) occurs upon an increase in the degree of ionization of the coronal blocks, α_b, and/or an increase in N_A/decrease in N_B. These molecular parameters are specified by the block copolymer composition. Therefore, to detect the predicted structural transformations, one has to use a series of block copolymer with finely tuned molecular weights of the blocks. As follows from (138), the relative width of the corridor, delineating the stability range of cylindrical micelles in a low salt solution, $(N_A^{(\text{c-s})} - N_A^{(\text{l-c})})/N_A^{(\text{l-c})} \approx 0.16$, is rather small. Moreover, the absolute width of the corridor, $N_A^{(\text{c-s})} - N_A^{(\text{l-c})}$, is also small due to the typically short length of block A. A more practical route to search for morphological transitions in diblock copolymers with quenched PE block is to exploit the response of charged micelles to variations in the content of added salt.

10.2 Salt-Dominated Solution

Under salt dominance conditions (i.e., when the concentration of salt, Φ_{ion}, exceeds by the far the concentration of counterions in salt-free osmotic corona), the electrostatic interactions in the corona are described via an effective second

virial coefficient of binary monomer–monomer interactions, v_{eff}. The structure of a planar brush, wherein the interactions are determined by binary contacts between monomers, is specified by the free energy per chain:

$$\frac{F^{(1)}_{\text{corona}}}{k_{\text{B}}T} = \frac{3^{4/3}}{2} N_A v_{\text{eff}}^{2/3} s(R_{\text{core}})^{-2/3} \tag{139}$$

and the brush thickness:

$$H^{(1)}_{\text{corona}} = \frac{1}{3^{1/3}} N_A v_{\text{eff}}^{1/3} s(R_{\text{core}})^{-1/3}, \tag{140}$$

where $s(R_{\text{core}})$ is the grafting area per chain. By using (39), (40), (41), and (134), and by optimizing the free energy with respect to area s, we find the equilibrium free energy per chain, $F^{(i)}$, in a weakly curved crew-cut aggregate of morphology i [20]. Within the accuracy of linear in curvature terms:

$$\frac{F^{(i)}}{k_{\text{B}}T} \approx \frac{5}{2} 3^{1/5} N_A^{3/5} v_{\text{eff}}^{2/5} \gamma^{2/5} - \frac{(i-1)}{2i} \frac{N_A^2 \varphi v_{\text{eff}}}{N_B} + b_i \frac{i^2 N_B}{3^{2/5} \varphi^2} \left(\frac{\gamma}{N_A v_{\text{eff}}^{2/5}} \right)^{6/5} \tag{141}$$

for $i = 1, 2, 3$. Here, the first term is the free energy of a planar PE corona balanced with the surface free energy, the second term specifies the reduction in coronal free energy caused by the core curvature, and the third term is due to elastic stretching of core blocks B. An approximate expression for the binodals that separate regions of thermodynamic stability of aggregates with morphology i and $i+1$, are given by:

$$v_{\text{eff}} = v_A + \alpha_b^2 / 2\Phi_{\text{ion}} \approx \frac{N_B^{10/9}}{N_A^{16/9}} \frac{\gamma^{2/3}}{\varphi^{5/3}} \left\{ \frac{2i(i+1)}{3^{2/5}} \left[b_{i+1}(i+1)^2 - b_i i^2 \right] \right\}^{5/9} \qquad i = 1, 2. \tag{142}$$

A progressive increase in the salt concentration, Φ_{ion}, leads first to the sphere-to-cylinder and then to cylinder-to-lamella transitions, which occur almost at a constant surface area per chain, s.

The regions of thermodynamic stability of the aggregates of different morphologies are presented in Fig. 16a, b as a function of variable length of the ionic and hydrophobic blocks, respectively. As follows from Fig. 16, spherical micelles are stable in a wide range of salt concentrations if $N_A \gg N_B$ and even if $N_A \leq N_B$. Cylindrical micelles and vesicles (or lamellar structures) are found in a narrow range of (high) salt concentration for strongly asymmetric, $N_B \gg N_A$ copolymers. For each morphology i, an increase in salt concentration leads to the progressive decrease in the corona thickness, H_{corona}, and in a simultaneous increase in the radius of the core R_{core}. At the transition (sphere-to-cylinder and cylinder-to-lamella) points, these smooth dependencies are interrupted by a drop in the core size (which enables relaxation of the elastic tension in the core blocks) and in a simultaneous jump up in the thickness of the corona. The ratio $H_{\text{corona}}/R_{\text{core}}$ monotonically decreases as a

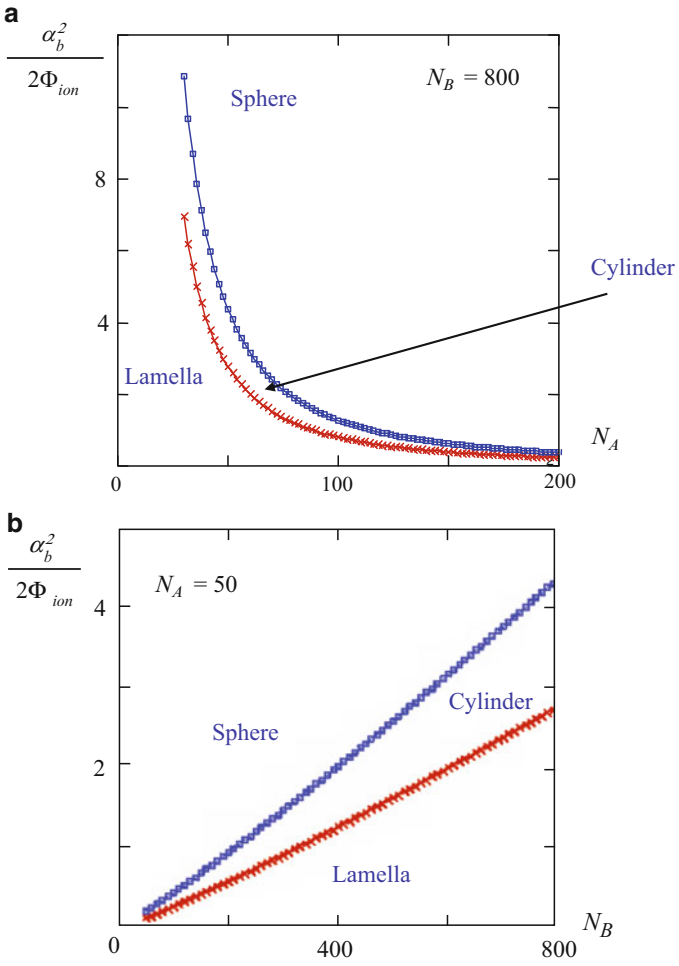

Fig. 16 Phase diagrams of the solution of ionic/hydrophobic diblock copolymers as a function of salt concentration and the length of the hydrophilic (*A*) (**a**) and hydrophobic (*B*) (**b**) blocks

function of salt concentration for each particular morphology, but jumps up at the transition point, as demonstrated in Fig. 17.

We emphasize that it is a reduction in elastic stretching of the core blocks *B*, that drives the change in micelle morphology. Similarly to the case of salt-free solutions, both the elastic stretching of the core blocks and the reduction in electrostatic interactions in weakly curved corona constitute only small corrections to the major free energy terms: the surface free energy at core–corona interface, balanced with the ionic contribution in a quasi-planar corona [the first term in (141)]. However, the interplay between these corrections dictate the morphology *i* of crew-cut aggregates.

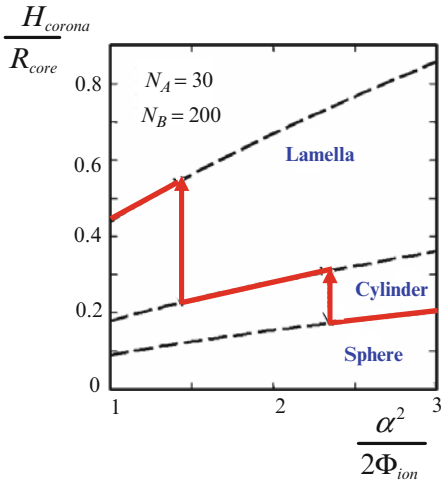

Fig. 17 Ratio of the coronal thickness H_{corona} to the core radius R_{core}, as a function of the salt concentration (via the effective second virial coefficient $\alpha_b^2/2\Phi_{ion}$) in the aggregates of different morphologies. *Arrows* indicate transitions from spherical to cylindrical, and from cylindrical to lamellar morphology

Salt-induced transitions between charged aggregates of different morphologies were also considered in [17]. In contrast to our findings, the transitions sphere-to-cylinder and cylinder-to-lamella were predicted in the starlike regime of charged aggregates with corona thickness $H_{\text{corona}} \geq R_{\text{core}}$. (We refer to such aggregates as starlike irrespective of morphology *i*.) The origin of this discrepancy is traced to an inadequate extrapolation of the asymptotic expressions for the free energy of a starlike corona (that are valid only in the limit $H_{\text{corona}} \gg R_{\text{core}}$) to the range $H_{\text{corona}} \simeq R_{\text{core}}$. As a result of such treatment, the free energies of the spherical ($i = 3$), cylindrical ($i = 2$), and lamellar ($i = 1$) starlike aggregates intersect when $H_{\text{corona}} \geq R_{\text{core}}$, resulting in improper location of the sphere-to-cylinder and cylinder-to-lamella morphological transitions. These transitions were erroneously attributed in [17] to the gain in entropy of counterions. Remarkably, if the finite size of the core is taken into account, but the conformational entropy of the core-forming blocks *B* is disregarded, a spherical shape of the micelle provides the minimal free energy at any values of the interaction parameters. As emphasized earlier, the driving force for morphological transitions is the successive relaxation of the elastic stretching of the core blocks going from a spherical to cylindrical and finally to the lamellar topology. Without this effect, a spherical micelle with a quenched PE corona would be stable at any salt concentration [20].

11 Re-entrant Morphological Transitions in Aggregates of Block Copolymers with Annealing Polyelectrolyte Block

Remarkably, in micelles with weakly dissociating (pH-sensitive) coronae an increase in the salt concentration, Φ_{ion}, might invert the sequence of morphological transformations from sphere–cylinder–lamella to lamella–cylinder–sphere [21].

This "unusual" sequence of transitions occurs under low salt conditions, when the coronal ionization is strongly coupled to the conformations of the soluble block *A*. The physical origin of inverted morphological transitions is the same as for non-ionic micelles and micelles with quenched PE corona. The elastic stretching of the core-forming blocks increases in the series lamella–cylinder–sphere, whereas the average coronal concentration of ionizable monomer units decreases upon an increase in curvature of coronal domain. As a result, the ionization of the coronal blocks, α, increases, and the corresponding ionic contribution to the free energy decreases. When gains in the ionic contribution in the corona of micelle become comparable to the losses in elastic stretching of core blocks, micelles might change morphology. To specify the binodals, separating the regions of thermodynamic stability for aggregate of morphology *i*, we use (134). As is discussed earlier, this equation approximates the coronal free energy of a crew-cut aggregate with a weakly curved core, $R_{\text{core}} \gg H_{\text{corona}}$. Recall that $H^{(1)}_{\text{corona}}$ and $F^{(1)}_{\text{corona}}$ in (134) are the thickness and the free energy of a planar corona under the corresponding conditions (i.e., for pH-sensitive chains with varying α).

When the degree of ionization of monomer units in the corona is relatively small, $\alpha << \alpha_b \leq 1$, the effect of short-ranged interactions is not negligible. Therefore, in a weakly dissociating corona, both ionic and nonelectrostatic binary interactions (specified by the second virial coefficient v_A) should be taken into account. In this case, the corresponding expressions for $H^{(1)}_{\text{corona}}$ and $F^{(1)}_{\text{corona}}$ can be represented as [22, 97]:

$$H^{(1)}_{\text{corona}} = \frac{1}{3^{1/3}} N_A v_A^{1/3} s(R_{\text{core}})^{-1/3} \frac{z^{1/3}}{\left(\sqrt{1+z}-1\right)^{2/3}}, \tag{143}$$

$$\frac{F^{(1)}_{\text{corona}}}{k_{\text{B}}T} = \frac{3^{4/3}}{2} N_A v_A^{2/3} s(R_{\text{core}})^{-2/3} \frac{\sqrt{1+z}-3}{z^{1/3}\left(\sqrt{1+z}-1\right)^{1/3}}, \tag{144}$$

where the combination of parameters:

$$z = \frac{24 v_A}{s(R_{\text{core}})^2} \frac{1-\alpha_b}{\alpha_b \Phi_{\text{ion}}}$$

depends on both area per chain, $s(R_{\text{core}})$, and the strength of steric and electrostatic repulsions (via v_A and α_b).

The coronal free energy in a weakly curved aggregate of morphology *i* is then specified as [22]:

$$F^{(i)}_{\text{corona}} \approx F^{(1)}_{\text{corona}} \left[1 - (i-1) \frac{H^{(1)}_{\text{corona}}}{3R_{\text{core}}} \frac{z}{\left(\sqrt{1+z}-3\right)\left(\sqrt{1+z}-1\right)}\right]. \tag{145}$$

We now introduce the new combinations of the parameters, t and u:

$$t = \frac{s(R_{\text{core}})}{3^{1/5} v_A^{2/5}} \left(\frac{\gamma}{N_A}\right)^{3/5}; \quad u = \frac{24 v_A^{1/5}}{3^{2/5}} \left(\frac{\gamma}{N_A}\right)^{6/5} \frac{1-\alpha_b}{\alpha_b \Phi_{\text{ion}}}. \tag{146}$$

Here, t is proportional to the still-unknown area per chain, $s(R_{\text{core}})$, whereas u specifies the relative strength of non-ionic and ionic interactions. When electrostatic interactions are weak compared to nonelectrostatic interactions, $u \to \infty$. In the opposite limit, i.e., when electrostatic interactions dominate, $u \to 0$.

By balancing the dominant contribution in the coronal free energy, $F^{(i)}_{\text{corona}} \approx F^{(1)}_{\text{corona}}$, with the surface free energy, $F^{(i)}_{\text{interface}} = \gamma s k_{\text{B}} T$, we find the equilibrium area, $s(R_{\text{core}})$, or, equivalently, the relation between t and u:

$$\frac{u^{2/3}}{t^3\left(\sqrt{1+u/t^2}-1\right)^{4/3}} = 1. \tag{147}$$

The equation for binodals is obtained along the same lines as before. One finds [22]:

$$\frac{N_B^2\gamma^{6/5}}{\varphi^3 N_A^{16/5} v_A^{9/5} t(u)^{9/2}}\left\{\frac{2}{3^{2/5}} i(i+1)\left[(i+1)^2 b_{i+1} - i^2 b_i\right]\right\} = 1 \qquad i = 1,2, \tag{148}$$

where $t(u)$ is the solution of (147).

When electrostatic interactions are weak, $u \to \infty$ (or, equivalently, $\alpha_b \to 0$), the solution of (147), $t(u) \to 1$, and one finds asymptotic expressions for the binodals in the quasi-neutral limit. Note that due to the mean-field nature of the model used here, the exponents are slightly different from these in (51), obtained for non-ionic micelles in the scaling framework. The difference is, however, minor.

When $u \to 0$ (the so-called osmotic annealing limit), $t(u) \approx 16/u^2$. Here, one finds the asymptotic expressions for the binodals as:

$$\frac{\alpha_b \Phi_{\text{ion}}}{1-\alpha_b} = 3^{5/9} 2^{10/9} \frac{N_B^{2/9}\gamma^{4/3}}{\varphi^{1/3} N_A^{14/9}} i(i+1)\left[(i+1)^2 b_{i+1} - i^2 b_i\right] \qquad i = 1,2. \tag{149}$$

As follows from (149), an increase in Φ_{ion} triggers the lamella–cylinder–sphere transformations in a crew-cut micelle with an annealing osmotic corona. As discussed earlier, an increase in Φ_{ion} leads to an enhanced ionization of the coronal blocks, driven by the substitution of hydrogen ions by the salt ions and, thereby, decreasing local pH inside the corona. As a result, the ionic contribution to the coronal free energy decreases, and the spherical shape of the aggregate is stabilized. In other words, in order to transform a cylindrical aggregate into spherical micelles, one has to increase the concentration of salt ions in the solution. Recall that such behavior is expected only under low salt conditions, when salt-induced screening of electrostatic interactions is negligible.

In a salt-dominated solution, the behavior of weakly and strongly dissociating PEs becomes indistinguishable, $\alpha \approx \alpha_b$. Here, the addition of salt leads predominantly to an enhanced screening of electrostatic interactions in the corona (via the decrease in the effective virial coefficient, $v_{\text{eff}} = v_A + \alpha_b^2/2\Phi_{\text{ion}}$). Therefore,

block copolymer with a pH-sensitive block demonstrates under these conditions the conventional sequence of morphological transitions (see Sect. 10). The corresponding binodals are specified by (142).

Figure 18a demonstrates the diagram of states in N_B, Φ_{ion} coordinates for block copolymer with the length of pH-sensitive block $N_A = 50$, and $\text{pH} = \text{p}K_{\text{a}}$ (i.e., for $\alpha_b = 0.5$). Solid lines indicate the binodals calculated according to (148) and (142). A smaller value of $\alpha_b = 0.1$ is used in Fig. 18b The diagrams localize the stability regions of three main morphologies of block copolymer aggregates: spherical, S ($i = 3$), and cylindrical C ($i = 2$) micelles, and lamellae L ($i = 1$). The latter can further associate due to Van der Waals forces, and precipitate from the solution.

Comparison of diagrams of Fig. 18a, b indicates that morphology i of aggregate formed by pH-sensitive block copolymers can be tuned by variations in both concentration of added salt, Φ_{ion} and pH in solution. For example, when $\text{pH} < \text{p}K_{\text{a}}$ (e.g., at $\alpha_b = 0.1$, Fig. 18b), a copolymer with lengths of the blocks, $N_A = 50$ and $N_B = 125$, retains the cylindrical (C) morphology at any salt concentration, Φ_{ion}. In contrast, when $\text{pH} = \text{p}K_{\text{a}}$ ($\alpha_b = 0.5$, Fig. 18a), the same copolymer makes cylindrical (C) micelles only at low salt concentrations, and associates into spherical (S) micelles upon a further increase in Φ_{ion}.

In addition to three canonical morphologies of aggregates (S, C, and L), more complex associations of block copolymer molecules could be found in certain regions of the diagram. In particular, a recent theoretical study [24] predicts the existence of branched cylinders in the vicinity of the S–C binodal line. The latter occupy a narrow corridor and coexist with cylindrical and spherical micelles. Branched structures and networks of aggregates formed by diblock copolymer with quenched PE block were also considered in [17].

12 Experiment Versus Theory

In this last section of the review, we compare the theoretical results with the available experimental data. Clearly, we can not discuss here all the relevant papers on self-assembly of ionic/hydrophobic block copolymers. A comprehensive discussion of experimental developments and trends in this field can be found elsewhere (see, e.g., [8, 9]). Instead, we focus here on selected experimental findings that are used to confront the predictions of theoretical models formulated above.

The assembly of amphiphilic ionic/hydrophobic block copolymers in aqueous media suggests that the effective (hydrophobic) attraction between the associating blocks is sufficiently strong to counterbalance repulsions between the PE blocks. That is, the corresponding cohesive free energies for the hydrophobic core-forming blocks are significantly larger than those involved in the assembly of non-ionic block copolymers in selective organic solvents. In order to assure the stability of micelles in wide ranges of temperature and salinity, polymers with high T_{g}, e.g., PS or poly(*tert*-butyl sterene) are often chosen for core-forming block [98–114]. The hydrophobic domains in these aggregates are found in a glassy (“frozen”) state and can hardly rearrange once micelles are formed. Moreover, assembly of the

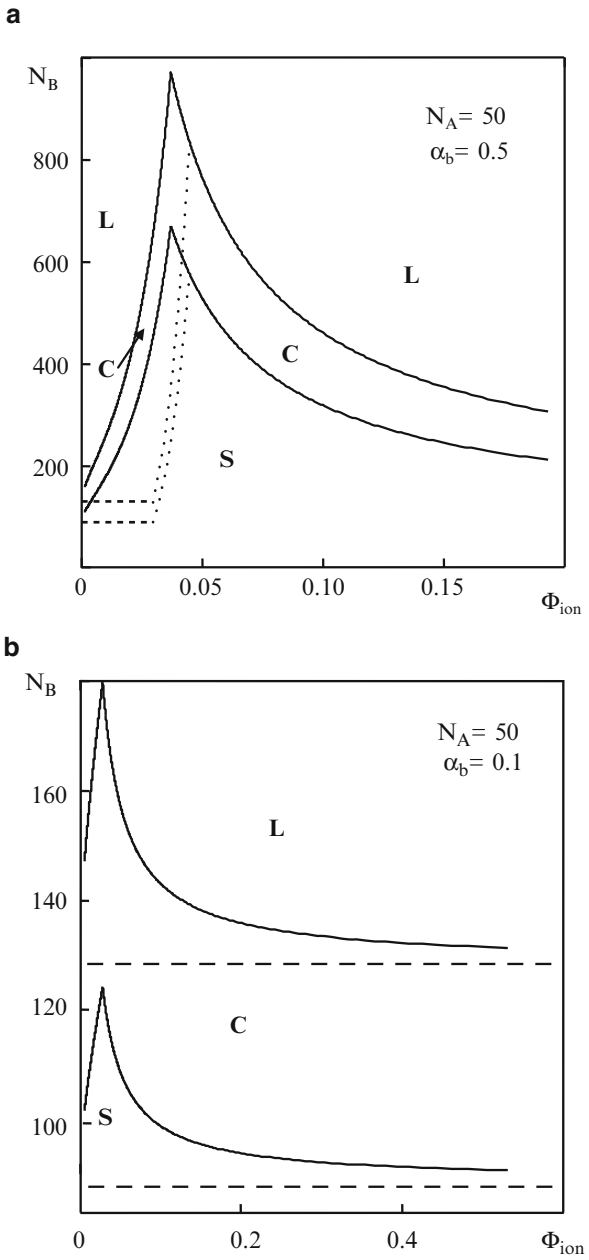

Fig. 18 Diagram of states in N_B, Φ_{ion} coordinates for diblock copolymer solution at different values of $\text{pH} - \text{p}K_{\text{a}}$, corresponding to $\alpha_b = 0.5$ (**a**) and $\alpha_b = 0.1$ (**b**). Other parameters are $\gamma = 1$, $\varphi = 1$, $v_A = 0.4$, $N_A = 50$. *Dashed and dotted lines* correspond to asymptotic expressions for the binodal lines given by (142) (at $\alpha_b = 0$) and (149)

ionic/hydrophobic block copolymers in water may lead to out-of-equilibrium frozen aggregates, even for copolymers with a core-forming block that exhibits relative low T_g, e.g., poly(*n*-butyl acrylate) [115–119]. The nonequilibrium nature of the aggregates with non-glassy cores is often explained by high activation energy barriers for exchange between copolymers included in the micelles and those existing in unimer state in the solution [120].

Depending on the intramolecular hydrophilic/hydrophobic balance, micelles with frozen cores can be obtained either by direct dissolution of the copolymers in water (at elevated temperature) or by dialysis of the molecular solution of the copolymer from common solvent (e.g., dioxane) to water. The "freezing" of the core (quenching of the aggregation state) occurs below a certain temperature or upon a decrease of the content of the common solvent in the mixture with water.

The aggregation number (and the size of core domain) in micelles with glassy core, is little affected by variations in environmental conditions. Moreover, the frozen micelles retain their integrity at arbitrary low concentration, i.e., exhibit no CMC. Since the aggregation number is fixed, variations in the ionic strength and/or in pH may lead to only conformational changes in the corona. Depending on the ratio between the lengths of the hydrophobic and PE blocks, the coronae of frozen micelles are similar to colloidal PE brushes or to multiple-arm PE stars.

Structural characterization of block copolymer aggregates by dynamic and static light scattering (DLS and SLS) in combination with small angle neutron scattering (SANS) at variable ionic strength and pH in the solution enables one to discriminate between frozen and dynamic (equilibrium) micelles. In particular, SANS provides direct information about the core size and shape because of relatively low scattering density of the corona.

The theory predicts that in the case of frozen starlike micelles with strongly dissociating PE corona, the hydrodynamic radius of the micelle (measured by DLS) is expected to decrease as $R_{corona} \sim c_s^{-1/5}$ upon an increase in salt concentration c_s [10]. This theoretical prediction is in agreement with findings in [106] on poly(*tert*-butyl sterene)-*block*-poly(sodium styrene sulfonate) micelles, that proves the frozen nature of these aggregates. Starlike micelles with frozen PS core and pH-sensitive poly(acrylic acid) coronae were systematically studied in [112–114]. Conformational changes in the corona induced by variations in the ionic strength and pH in the solution were analyzed by SANS, and a good agreement with theoretical predictions [62, 64] concerning conformations of pH-sensitive PE stars was established.

Hence, it is still a challenging experimental task to produce dynamic, equilibrium micelles. The dynamic nature of micelles is inherently linked to the stimuli-responsive properties, i.e., an ability to change reversibly the aggregation number and morphology of the aggregate in response to specific variation in the environmental conditions. An ability of micelles to disintegration, triggered by external stimuli, is most valuable in certain applications, e.g., drug delivery and controlled release systems [121, 122].

Most experimental studies searching for dynamic micelles have focused on the proper choice of "soft" hydrophobic block to assure equilibrium,i.e., reversible association of the ionic/hydrophobic block copolymers. Copolymers with such soft

hydrophobic blocks as poly(ethylethylene) [123], poly(isobutylene) [124–127], or poly(diethyleneglycol ethylether acrylate) [128] have been extensively explored.

The solution behavior of poly(ethylethylene)-*block*-poly(styrene sulfonic acid) was studied by combining DLS, SLS, cryo-TEM, and SANS [123]. Here, the combination of a soft hydrophobic block (with $T_g \approx -25°C$) with a strongly dissociating PE block was chosen to analyze the effect of ionic strength on the block copolymer assembly in a wide range of salt concentrations (three orders of magnitude in c_s). It was found that an increase in concentration of added salt leads to an increase in the aggregation number (and in core size) and in a simultaneous decrease in the hydrodynamic radius of the micelle as $R_{\text{corona}} \sim c_s^{-x}$ with the apparent exponent $x \approx 0.12$. The latter value is close to the theoretical exponent $1/11 \approx 0.09$ (89), which is expected for equilibrium micelles in which the aggregation number increases upon an increase in salt concentration (87). Note that the value of experimental exponent is noticeably smaller than the 0.2, predicted for frozen micelles (PE stars). This suggests that micelles of poly(ethylethylene)-*block*-poly(styrene sulfonic acid) copolymer in aqueous solution might be close to equilibrium.

Micellization of poly(isobutylene)-*block*-poly(methacrylic acid) copolymers with short hydrophobic and long PE blocks has been studied [124–127] by DLS, SLS, SANS, and pyrene titration experiments supported by cryo-TEM imaging. It was unambiguously demonstrated that at high pH, when the poly(methacrylic acid) blocks are fully ionized, the aggregation number increases whereas the hydrodynamic radius decreases as a function of salt concentration. Both dependencies can be approximated by power laws with exponents close to those predicted by theory (87), (89), which again points to the dynamic nature of these micelles.

Micellization of poly[2-(dimethylamino)ethyl methacrylate]-*block*-poly[2-(diethylamino)ethyl methacrylate] (DMAEMA/DEAEMA) gives rise to pH-responsive spherical micelles that are found in aqueous solution above a certain critical pH [129, 130]. Under acidic conditions, protonation of the amino groups transforms the block copolymers in PEs and keeps them as unimers in solution. Deprotonation of the DEAEMA block by addition of base makes this block hydrophobic and causes formation of micelles, with the corona formed by still-protonated (annealing) DMAEMA blocks. The electrostatic properties of the micellar corona were additionally tailored by using copolymer with the DMAEMA block selectively quaternized with benzyl chloride (Q-DMAEMA/DEAEMA), and by substituting the DMAEMA block by a PEO block. In the former case, one finds strongly charged (quenched) corona whereas in the latter case the hydrophilic micellar corona is electroneutral [130]. The data obtained from potentiometric titrations, DLS, SLS, and SANS allowed the probing of the dependence of aggregation number p as a function of the degree of chain ionization, $\alpha \sim \alpha_b$. The starlike DMAEMA/DEAEMA micelles demonstrated a power law decrease in aggregation number, $p \sim \alpha_b^{-y}$ with apparent exponent $y = 1.5$, upon an increase in α_b (a decrease in pH). The equilibrium theory predicts the value of exponent $y = 12/11 \approx 1.1$ for starlike micelles in the salt-dominated regime, (87). The theoretical exponent is reasonably close to the experimental exponent, specified for DMAEMA/DEAEMA micelles at the boundary between osmotic and salt-dominated regimes [130]. At the same time, the rearrangements of these micelles

due to additions of salt ions after micellization were hindered, suggesting the lack of full equilibrium. "Softness" of the core-forming DEAEMA block was also demonstrated by the salt-induced rearrangements in Q-DMAEMA/DEAEMA micelles. Here, the degree of ionization of the coronal blocks, $\alpha \sim 1$, was not sensitive to variations in solution pH, but the forming micelles responded to additions of salt both before and after micellization.

We remark, however, that a soft hydrophobic block alone does not necessarily ensure the dynamic (equilibrium) nature of the forming aggregate. On the contrary, there are experimental indications that a combination of softness of the core-forming block with "intrinsic hydrophobicity" of the PE block [e.g., in the cases of poly(styrene sulfonic) or poly(methacrylic) acid] might be important. A tentative explanation assumes the influence of the coronal block on the core–corona interfacial energy. In addition, we also note that in experimental studies of dynamic micelles, mostly asymmetric or nearly symmetric block copolymers with longer PE block were investigated. These block copolymers form starlike aggregates in aqueous solutions. Currently, we are not aware of reliable experimental evidence of dynamic crew-cut micelles formed by copolymers with long hydrophobic core-forming block.

An alternative strategy for design of dynamic, stimuli-responsive PE micelles is to use block copolymers with thermosensitive associating blocks, e.g., poly(*N*-isopropylacrylamide) [131, 134, 135] poly(*N*,*N*-diethylacrylamide) [131–133], and poly(*N*,*N*-dimethylacrylamide) [134]. In this case, reversible micellization–dissociation can be triggered by temperature variations that affect the solubility of the core-forming blocks. For example, in [131] it was shown that poly(acrylic acid)-*block*-poly(*N*-isopropylacrylamide) copolymers can form micelles with poly(*N*-isopropylacrylamide) core and poly(acrylic acid) corona at pH 6 and $T \geq 45^{\circ}$C, whereas at pH 4 and room temperature "inverse" micelles are formed.

Moreover, in the vicinity of the LCST (or UCST) the insoluble core is soft enough to undergo structural transformations in response to variations in strength of ionic interactions in the corona. In [135], micellization of poly(*N*-isopropylacrylamide)-*block*-poly(DMAEMA) in aqueous solution was studied as a function of pH and temperature. Predicted by the theory [19], a pH-induced, jump-wise transition between spherical micelles with distinctively different aggregation numbers was observed by combination of DLS and AFM at temperatures T > LCST for the core-forming *N*-isopropylacrylamide block. To the best of our knowledge, to date this study is the only experimental evidence of abrupt structural transformations in spherical micelles with annealing PE corona.

Nonspherical aggregates (cylindrical micelles, vesicles, lamellae, etc.) were detected experimentally for a number of non-ionic block copolymers (see, e.g., [50, 136–139]) and copolymers with weakly dissociating PE block [102, 140]. Morphological transformations in non-ionic PI-*block*-PS micelles were triggered by variations in molecular weight of the PS block [50] or by variations in the solvent composition [137, 138]. The latter studies clearly indicate the possibility of stimuli-responsive transitions (sphere → cylinder → vesicle) for non-ionic block copolymer aggregates in mixed organic solvents. It was also demonstrated [58] that

mild swelling of PS core of the micelle in a single solvent *n*-heptane (a preferential solvent for PI block) leads to the decrease in T_g of the core-forming block down to $\simeq$28°C, and allows for a close to equilibrium state of the aggregates at temperatures slightly elevated above T_g.

Experimental observations on stimuli-induced equilibrium morphological transitions in aggregates formed by amphiphilic ionic/hydrophobic block copolymers, are still lacking. Nanoaggregates of different morphologies (spherical starlike and crew-cut micelles, cylinders, vesicles and "complex" micelles) were obtained by Eisenberg et al [102, 140] via dialysis of the molecular solution of poly(acrylic acid)-*block*-PS copolymers from a common solvent (dioxane) into water at different pH. The aggregates (spherical or cylindrical micelles) were formed by copolymers with different ratios of the lengths of PE and hydrophobic blocks at a certain composition of the mixed solvent. Copolymer with shorter PS blocks formed spheres, and longer hydrophobic blocks gave rise to cylinders. However, below a certain content of dioxane, the PS core was kinetically frozen. Hence once formed, the aggregates could not change the morphology (aggregation state) upon variations in the ionic strength and pH, but rather responded by conformational changes in the corona.

Acknowledgment The support of the European Union within the Marie Curie Research and Training Network POLYAMPHI and of the Russian Foundation for Basic Research, grant 08-03-336 is gratefully acknowledged. OVB acknowledges the Alexander von Humboldt Foundation for support of his stay in the University of Bayreuth.

References

1. Galaev I, Mattiasson B (ed) (2008) Smart polymers: applications in biotechnology and biomedicine, CRC, Boca Raton
2. Dai L (2003) Intelligent macromolecules for Smart devices: from material synthesis to device application. Springer, London
3. Minko S (2006) Responsive polymer materials: design and applications. Backwell, Oxford
4. Lazzari M, Liu G, Lecommandoux S (ed) (2006) Block copolymers in nanoscience. Wiley, Weinheim
5. Hamley IW (1998) The physics of block copolymers. Oxford University Press, New York
6. Riess G (2003) Micellization of block copolymers. Prog Polym Sci 28:1107–1170
7. Gohy JF (2005) Adv Polym Sci 190:65
8. Förster S, Abetz V, Müller AHE (2004) Adv Polym Sci 166:267
9. Cohen Stuart MA, Hofs B, Voets IK, de Keizer A (2005) Curr Opin Coll Int Sci 10:30
10. Borisov OV, Zhulina EB, Leermakers FAM, Müller AHE, Ballauff M (2011) Adv Polym Sci DOI: 12_2010_104
11. Aseyev VO, Tenhu H, Winnik FM (2006) Adv Polym Sci 196:1
12. Dimitrov I, Trzebicrf B, Müller AHE, Dworak A, Tsvetanov CD (2007) Prog Polym Sci 32:1275
13. Marko JF, Rabin Y (1992) Macromolecules 25:1503
14. Wittmer J, Joanny J-F (1993) Macromolecules 26:2691
15. Shusharina NP, Nyrkova IA, Khokhlov AR (1996) Macromolecules 29:3167
16. Huang C, Olivera de la Cruz M, Delsanti M, Guenoun P (1997) Macromolecules 30:8019
17. Netz RR (1999) Europhys Lett 47:391
18. Borisov OV, Zhulina EB (2002) Macromolecules 35:4472

19. Zhulina EB, Borisov OV (2002) Macromolecules 35:9191
20. Borisov OV, Zhulina EB (2003) Macromolecules 36:10029
21. Borisov OV, Zhulina EB (2005) Langmuir 21:3229
22. Zhulina EB, Borisov OV (2005) Macromolecules 38:6726
23. Lauw Y, Leermakers FAM, Cohen Stuart MA, Borisov OV, Zhulina EB (2006) Macromolecules 39:3628
24. Viktorov AI, Plotnikov NV, Hong P-D (2010) J Phys Chem B 114:8846
25. Pincus PA (1991) Macromolecules 24:2912
26. Ross R, Pincus P (1992) Macromolecules 25:2177
27. Borisov OV, Birshtein TM, Zhulina EB (1991) J Phys II (France) 1:521
28. Borisov OV, Zhulina EB, Birshtein TM (1994) Macromolecules 27:4795
29. Zhulina EB, Borisov OV (1996) Macromolecules 29:2618
30. Zhulina EB, Borisov OV (1997) J Chem Phys 107:5952
31. Zhulina EB, Birshtein TM, Borisov OV (1995) Macromolecules 28:1491
32. Zhulina EB, Birshtein TM, Borisov OV (2006) Eur Phys J E 20:243
33. Ballauff M, Borisov OV (2006) Curr Opin Colloid Interface Sci 11:316
34. Tanford C (1973) The hydrophobic effect: formation of micelles and biological membranes. Wiley-Interscience, New York
35. Israelachvili JN (1985) Intermolecular and surface forces. Academic, London
36. Hill TL (1994) Thermodynamics of small systems. Dover, New York
37. Izzo D, Marques CM (1993) Macromolecules 26:7189
38. Konop AJ, Colby RH (1999) Langmuir 15:58
39. Halperin A, Tirrell M, Lodge T (1990) Adv Polym Sci 100:31
40. Borisov OV, Zhulina EB (2008) Responsive polymer brushes: a theoretical outlook. In: Galaev I, Mattiasson B (eds) Smart polymers: applications in biotechnology and biomedicine. CRC, Boca Raton, p 53
41. Grosberg AY, Khokhlov AR (1994) Statistical physics of macromolecules. AIS, New York
42. Polotsky AA, Daoud M, Borisov OV, Birshtein TM (2010) Macromolecules 43:1629
43. Flory P (1953) Principles of polymer chemistry. Cornell University Press, Ithaca
44. Ushakova AS, Govogun EN, Khokhlov AR (2006) J Phys Condens Matter 18:915
45. Zhulina YB, Birshtein TM (1985) Polym Sci USSR 27:570
46. Halperin A (1987) Macromolecules 20:2943
47. Halperin A (1989) Europhys Lett 8:351
48. Halperin A, Alexander S (1989) Macromolecules 22:2403
49. Birshtein TM, Zhulina EB (1989) Polymer 30:170
50. Zhulina EB, Adam M, Sheiko S, LaRue I, Rubinstein M (2005) Macromolecules 38:5330
51. Alexander S (1977) J Phys (France) 38:983
52. de Gennes PG (1980) Macromolecules 13:1069
53. Daoud M, Cotton JP (1982) J Phys (France) 43:531
54. Zhulina YB (1984) Polym Sci USSR 26:794
55. Birshtein TM, Zhulina EB (1984) Polymer 25:1453
56. Birshtein TM, Zhulina EB, Borisov OV (1986) Polymer 27:1079
57. de Gennes PG (1979) Scaling concepts in polymer physics. Cornell University Press, Ithaca
58. LaRue I, Adam M, Zhulina EB, Rubinstein M, Pitsikalis M, Hadjichristidis N, Hammouda B, Lin MY, Ivanov DA, Gearba RI, Anokhin DV, Sheiko SS (2008) Macromolecules 41:6555
59. Semenov AN (1985) Sov Phys JETP 61:733
60. Wang Z-G, Safran SA (1988) J Chem Phys 89:5323
61. Borisov OV (1996) J Phys II (France) 6:1
62. Borisov OV, Zhulina EB (1998) Europ Phys J B 4:205
63. Klein Wolterink J, Leermakers FAM, Fleer GJ, Koopal LK, Zhulina EB, Borisov OV (1999) Macromolecules 32:2365
64. Klein Wolterink J, van Male J, Cohen Stuart MA, Koopal LK, Zhulina EB, Borisov OV (2002) Macromolecules 35:9176
65. Noolandi J, Hong KM (1983) Macromolecules 16:1443
66. Leermakers FAM, Scheutjens JMHM (1988) J Chem Phys 89:3264

67. Leermakers FAM, Scheutjens JMHM (1989) J Phys Chem 93:7417
68. Leermakers FAM, Scheutjens JMHM (1988) J Chem Phys 89:6912
69. Leermakers FAM, Scheutjens JMHM (1990) Biochim Biophys Acta 1024:139
70. Leermakers FAM, Scheutjens JMHM (1990) J Colloid Interface Sci 136:231
71. Leermakers FAM, Lyklema J (1992) Colloids Surf 67:239
72. Cogan KA, Leermakers FAM, Gast AP (1992) Langmuir 8:429
73. Leermakers FAM, Wijmans CM, Fleer GJ (1995) Macromolecules 28:3434
74. Fleer GJ, Cohen Stuart MA, Scheutjens JMHM, Cosgrove T, Vincent B (1993) Polymers at interfaces. Chapman and Hall, London
75. Evers OA, Scheutjens JMHM, Fleer GJ (1990) Macromolecules 23:5221
76. Leermakers FAM, Rabinovich AL (2007) Phys Rev E 76:031904/1
77. Charlaganov MI, Borisov OV, Leermakers FAM (2008) Macromolecules 41:3668
78. Jódar-Reyes AB, Ortega-Vinuesa JL, Martin-Rodriguez A, Leermakers FAM (2003) Langmuir 19:878
79. Lauw Y, Leermakers FAM, Cohen Stuart MA (2003) J Phys Chem 107:10912
80. Oversteegen SM, Leermakers FAM (2000) Phys Rev E 62:8453
81. Jódar-Reyes AB, Leermakers FAM (2006) J Phys Chem B 110:6300
82. Li F, Marcelis ATM, Sudholter EJR, Cohen Stuart MA, Leermakers FAM (2009) Soft Matter 5:4173
83. Meijer LA, Leermakers FAM, Lyklema J (1994) Recl Trav Chim Pays-Bas 113:167
84. Claessens MMAE, van Oort BF, Leermakers FAM, Hoekstra FA, Cohen Stuart MA (2004) Biophys J 87:3882
85. Lauw Y, Leermakers FAM, Cohen Stuart MA (2006) J Phys Chem B 110:465
86. Lauw Y, Leermakers FAM, Cohen Stuart MA (2007) J Phys Chem B 111:8158
87. Leermakers FAM, van der Schoot PPAM, Scheutjens JMHM, Lyklema J (1990) In: Mittal KL (ed) Surfactants in solution, vol 7. Plenum, New York, pp 43–60
88. Leermakers FAM, Eriksson JC, Lyklema J (2005) Association colloids and their equilibrium modelling. In: Lyklema J (ed) Fundamentals of interface and colloid science, vol V: Soft colloids. Elsevier, Amsterdam, pp 4.1–4.121
89. Israëls R, Leermakers FAM, Fleer GJ, Zhulina EB (1994) Macromolecules 27:3249
90. Israëls R, Leermakers FAM, Fleer GJ (1994) Macromolecules 27:3087
91. Edwards SF (1966) Proc Phys Soc 88:265
92. Hall DG, Pethica BA (1967) In: Schick MJ (ed) Nonionic surfactants. Marcel Dekker, New York, pp 515–557
93. Voets IK, Leermakers FAM (2008) Phys Rev E 78:061801
94. Meijer LA, Leermakers FAM, Lyklema J (1999) J Chem Phys 110:6560
95. Kik RA, Leermakers FAM, Kleijn JM (2005) Phys Chem Chem Phys 7:1996
96. Kik RA, Leermakers FAM, Kleijn JM (2010) Phys Rev E 81:021915
97. Biesheuvel PM (2004) J Colloid Interface Sci 275:97
98. Kiserow D, Prochazka K, Ramireddy C, Tuzar Z, Munk P, Webber SE (1992) Macromolecules 25:461
99. Qin A, Tian M, Ramireddy C, Webber SE, Munk P (1994) Macromolecues 27:120
100. Matějíček P, Podhájecká K, Humpolíčková J, Uhlík F, Jelínek K, Limpouchová Z, Procházka K (2004) Macromolecules 37:10141
101. Khougaz K, Astafieva I, Eisenberg A (1995) Macromolecules 28:7135
102. Zang L, Eisenberg A (1995) Science 268:1728
103. Zang L, Barlow RJ, Eisenberg A (1995) Macromolecules 28:6055
104. Gao Z, Yarshney SK, Wong S, Eisenberg A (1994) Macromolecules 27:7923
105. Shen H, Eisenberg A (2000) Macromolecules 33:2561
106. Guenoun P, Davis HT, Tirrell M, Mays JW (1996) Macromolecules 29:3965
107. Guenoun P, Muller F, Delsanti M, Auvray L, Chen YJ, Mays JW, Tirrell M (1998) Phys Rev Lett 81:3872
108. Guenoun P, Delsanti M, Gaseau D, Auvray L, Cook DC, Mays JW, Tirrell M (1998) Eur Phys J B 1:77

109. Förster S, Hemsdorf N, Leube W, Schnablegger H, Regenbrecht M, Akari S, Lindner P, Böttcher C (1999) J Phys Chem 103:6657
110. Muller F, Delsanti M, Auvray L, Yang J, Chen YJ, Mays JW, Demé B, Tirrell M, Guenoun P (2000) Eur Phys J E 3:45
111. Muller F, Guenoun P, Delsanti M, Deme B, Auvray L, Yang J, Mays JW (2004) Eur Phys J E 15:465
112. Van der Maarel JRC, Groenewegen W, Egelhaaf SU, Lapp A (2000) Langmuir 16:7510
113. Groenewegen W, Egelhaalf SU, Lapp A, van der Maarel JRC (2000) Macromolecules 33:3283
114. Groenewegen W, Lapp A, Egelhaalf SU, van der Maarel JRC (2000) Macromolecules 33:4080
115. Müller AHE, Cai Y, Hartenstein M, Gradzielski M, Zhang M, Mori H, Pergushov DV (2004) Polymer Prepr (Am Chem Soc, Div Polym Chem) 45:267
116. Eghbali E, Colombani O, Drechsler M, Müller AHE, Hoffmann H (2006) Langmuir 22:4766
117. Schumacher M, Ruppel M, Burkhardt M, Drechsler M,Colombani O, Schweins R, Müller AHE (2007) Polym Mater Sci Eng 96:374
118. Colombani O, Ruppel M, Schubert F, Zettl H, Pergushov DV, Müller AHE (2007) Macromolecules 40:4338
119. Colombani O, Ruppel M, Burkhardt M, Drechsler M, Schumacher M, Schweins R, Müller AHE (2007) Macromolecules 40:4351
120. Won YY, Davis HT, Bates FS (2003) Macromolecules 36:953
121. Kataoka K, Harada A, Nagasaki Y (2001) Adv Drug Deliv Rev 47:113
122. Gillies ER, Fréchet MJ (2004) Pure Appl Chem 76:1295
123. Förster S, Hemsdorf N, Böttcher C, Lindner P (2002) Macromolecules 35:4096
124. Schuch H, Klingler J, Rossmanith P, Frechen T, Gerst N, Feldthusen J, Müller AHE (2000) Macromolecules 33:1734
125. Pergushov DV, Remizova EV, Gradzielski M, Lindner P, Feldthusen J, Zezin AB, Müller AHE (2004) Polymer 45:367
126. Burkhardt M, Martinez-Castro N, Tea S, Drechsler M, Babin I, Grishagin I, Schweins R, Pergushov DV, Gradzielski M, Zezin AB, Müller AHE (2007) Langmuir 23:12864
127. Burkhardt M, Ruppel M, Tea S, Drechsler M, Schweins R, Pergushov DV, Gradzielski M, Zezin AB, Müller AHE (2008) Langmuir 24:1769
128. Jacquin M, Muller P, Cottet H, Théodoly O (2010) Langmuir 26:18681
129. Lee AS, Gast AP, Bütün V, Armes SP (1999) Macromolecules 32:4302
130. Lee AS, Bütün V, Vamvakaki M, Armes SP, Pople JA, Gast AP (2002) Macromolecules 35:8540
131. Schilli CM, Zhang M, Müller AHE, Rizzardo E, Thang SH, Chong YK, Edwards K, Karlsson G (2004) Macromolecules 37:7861
132. André X, Zhang M, Müller AHE (2005) Macromol Rapid Commun 26:558
133. André X, Burkhardt M, Drechsler M, Lindner P, Gradzielski M, Müller AHE (2007) Polym Mater Sci Eng 96:560
134. Lokitz BS, York AW, Stempka JE, Treat ND, Li Y, Jarrett WL, McCormick CL (2007) Macromolecules 40:6473
135. Xu L, Zhu Z, Borisov OV, Zhulina EB, Sukhishvili SA (2009) Phys Rev Lett 103:N118301
136. Won YY, Bates FS (2006) In: Zana R, Kaler EW (eds) Giant micelles: properties and applications. CRC, Boca Raton
137. Lodge TP, Bang J, Li Z, Hillmayer MA, Talmon YR (2005) Soc Chem Faraday Discuss 128:1
138. Bang J, Jain S, Li Z, Lodge PT (2006) Macromolecules 39:1199
139. Larue I, Adam M, Sheiko S, Rubinstein M (2003) Polym Mater Sci Eng 88:236
140. Khougaz K, Zhang L, Moffitt M, Eisenberg A (1996) Polymer Science 38A:331

Adv Polym Sci (2011) 241: 131–161
DOI:10.1007/12_2010_102

Published online: 12 November 2010

Interpolyelectrolyte Complexes Based on Polyionic Species of Branched Topology

Dmitry V. Pergushov, Oleg V. Borisov, Alexander B. Zezin, and Axel H.E. Müller

Abstract This review reports advances in experimental and theoretical research on interpolyelectrolyte complexes based on polyionic species of star-shaped polyelectrolytes, cylindrical polyelectrolyte brushes, and micelles of ionic amphiphilic block co- and terpolymers.

Keywords Co-assembly · Cylindrical polyelectrolyte brushes · Interpolyelectrolyte complexes · Ionic amphiphilic block copolymers · Micelles · Polyelectrolytes · Star-shaped polyelectrolytes

Contents

D.V. Pergushov (✉) and A.B. Zezin
Department of Polymer Science, School of Chemistry, Moscow State University,
119991 Moscow, Russia
e-mail: pergush@genebee.msu.ru; pergushov@vms.chem.msu.ru; zezin@genebee.msu.ru

O.V. Borisov
Institute of Macromolecular Compounds, Russian Academy of Sciences,
199004 St. Petersburg, Russia
and
Institut Pluridisciplinaire de Recherche sur l'Environnement et les Matériaux
UMR 5254 CNRS/UPPA, Pau, France
e-mail: oleg.borisov@univ-pau.fr

A.H.E. Müller (✉)
Makromolekulare Chemie II and Bayreuther Zentrum für Kolloide und Grenzflächen,
Universität Bayreuth, 95440 Bayreuth, Germany
e-mail: axel.mueller@uni-bayreuth.de

Abbreviations

AFM	Atomic force microscopy
AUC	Analytical ultracentrifugation
Cryo-TEM	Cryogenic transmission electron microscopy
DLS	Dynamic light scattering
GPE	Guest polyelectrolyte
HPE	Host polyelectrolyte
IPEC	Interpolyelectrolyte complex
MD	Molecular dynamics
$P2VPH^+$	Protonated poly(2-vinylpyridine)
P2VPQ	Quaternized poly(2-vinylpyridine)
P4VPQ	Quaternized poly(4-vinylpyridine)
PAA	Poly(acrylic acid)
PANa	Poly(sodium acrylate)
PB	Poly(butadiene)
PDMAEMAQ	Quaternized poly[2-(dimethylamino)ethyl methacrylate]
PDVB	Poly(divinylbenzene)
PE	Polyelectrolyte
PEI	Poly(ethylene imine)
PEO	Poly(ethylene oxide)
PIB	Poly(isobutylene)
PMA^*Na	Fluorescently labeled poly(sodium methacrylate)
PMAA	Poly(methacrylic acid)
PMANa	Poly(sodium methacrylate)
PS	Poly(styrene)
PSSNa	Poly(sodium styrene sulfonate)
PVBTAC	Poly(ar-vinylbenzyl)trimethylammonium chloride
SANS	Small-angle neutron scattering
SEM	Scanning electron microscopy
SFM	Scanning (atomic) force microscopy
SLS	Static light scattering
TEM	Transmission electron microscopy

1 Introduction

During the last few years, polymer scientists have focused considerable attention on the easy and straightforward design of multifunctional macromolecular architectures with a specific combination of properties required for their desired end-use applications. One of the possible and most robust approaches for building up such architectures is to apply co-assembly processes, which proceed in multicomponent polymer systems comprising complementary macromolecular components. In particular, one can exploit the electrostatically driven co-assembly occurring upon the simple mixing of aqueous solutions of oppositely charged polyelectrolytes (PEs), often referred to as interpolyelectrolyte complexation. This process results in the formation of so-called interpolyelectrolyte complexes (IPECs) [1], which represent macromolecular co-assemblies stabilized by a cooperative system of interpolymer salt bonds. Hydrogen bonding, hydrophobic interactions, charge-transfer interactions, and van der Waals forces can also contribute to their stabilization, thereby modulating the electrostatic attraction between the oppositely charged polymeric components.

IPECs are of considerable interest because of their numerous promising (potential) applications in agriculture, water treatment, biotechnology, and medicine. Some examples include effective and available binders for dispersed systems and flocculants of colloidal dispersions [2], biocompatible coatings [3, 4], components of membranes [5–11], carriers of biologically active compounds (including enzymes and DNA) [12–16], matrices for metal ions and metal nanoparticles [17–22], and the formation of multilayered PE films and capsules using layer-by-layer techniques [23–32].

The general rules for the formation of such macromolecular co-assemblies, as well as their properties and behavior in solution and in bulk, have been extensively investigated by a number of research groups and the results of their studies have been exhaustively reviewed, e.g., in [33–36]. It has been recognized that one of the main driving forces for interpolyelectrolyte complexation in aqueous media is the gain in translational entropy of small counterions released into the bulk solution due to the strong electrostatic attraction between ionic groups of oppositely charged polymeric components interacting in a cooperative manner. The structure and properties of IPECs are determined by a number of factors, such as characteristics of the polymeric components (e.g., the nature of their ionic groups, degrees of polymerization, topology, charge densities) and their concentrations, the ratio between amounts of the oppositely charged groups of PEs (i.e., base-molar stoichiometry of a mixture of oppositely charged PEs), the conditions of the surrounding solution (e.g., ionic strength, pH, temperature) and, in some cases, the procedure or method employed for the preparation of such macromolecular co-assemblies.

Up to now, studies on IPECs have mostly been focused on the macromolecular co-assemblies formed by the oppositely charged linear polyions, both synthetic and natural (e.g., DNA). However, in recent years there have also been reports of IPECs based on nonlinear polyionic species, such as slightly cross-linked PE

hydrogels [37–51], dendrimers bearing ionic groups [47–64], micelles of ionic amphiphilic (di/tri)block (co/ter)polymers [65–78], star-shaped PEs [79–81], cylindrical PE brushes [64, 82–85], and planar PE brushes [86–88].

Depending on the above-mentioned parameters, IPECs formed by oppositely charged linear polyions can be either insoluble or soluble in aqueous media. If ionic groups of the polymeric components are incorporated in these co-assemblies in an equivalent ratio (1:1 base-molar stoichiometry), the generated IPECs are insoluble in aqueous media and form precipitates that are rather swollen because water acts as an effective plasticizer for such macromolecular co-assemblies. However, if one of the polymeric components involved (the lyophilizing or so-called host PE, HPE) is present in a certain base-molar excess compared to its polymeric counterpart (the blocking or so-called guest PE, GPE), one can prepare IPECs that are soluble in aqueous media, typically provided that the degree of polymerization of the HPE exceeds that of the GPE. Such water-soluble IPECs are often referred to as water-soluble nonstoichiometric IPECs.

The domain of water-soluble IPECs was thoroughly and systematically investigated by Kabanov and Zezin and their coworkers, who suggested that such macromolecular co-assemblies can be considered as peculiar amphiphilic block copolymers whose solubility in aqueous media results from charged fragments of the HPE that do not form interpolymer salt bonds with their polymeric counterparts [33]. The structure of water-soluble nonstoichiometric IPECs with ladder-like sequences of interpolymer salt bonds proposed by Zezin and Kabanov is schematically depicted in Fig. 1.

The significant progress in the controlled synthesis of well-defined polymers achieved during the few last years has offered unique possibilities for designing novel and, as yet, unexplored macromolecular co-assemblies comprising PE species with nonlinear architectures. These co-assemblies considerably increase the complexity of the IPECs, into which new properties and/or functionalities can be imparted. Studies on the formation and properties of IPECs incorporating polyionic species with a higher level of structural organization (nanostructured polyionic species) are highly required for rapidly developing nanotechnologies because such macromolecular co-assemblies appear to be valuable candidates for the construction of nanodevices, nanocontainers, and nanoreactors.

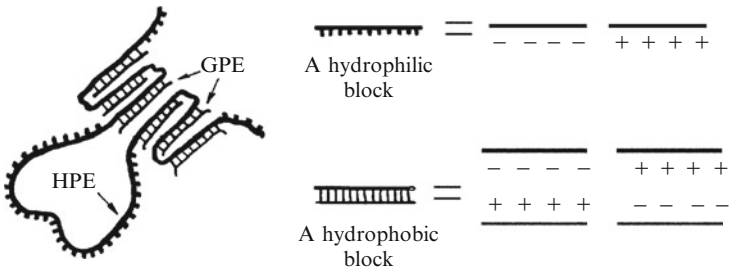

Fig. 1 Structure of water-soluble nonstoichiometric IPECs formed by oppositely charged linear PEs with considerably different degrees of polymerization. *HPE* host PE, *GPE* guest PE [33]

This review deals with recently obtained experimental results on IPECs based on branched PE species, specifically including PE stars, star-like micelles generated in aqueous solutions of ionic amphiphilic block co- and terpolymers, and cylindrical PE brushes. In addition, we will also present the results of molecular dynamics (MD) simulations performed for some of these systems, which enable the possible structural organization of the formed macromolecular co-assemblies to be revealed.

2 IPECs Based on Polyelectrolyte Stars

2.1 Experimental Results

The advances in controlled polymerization achieved in recent years have opened up the possibility of synthesizing well-defined star-shaped PEs, particularly those containing a large number of arms. To the best of our knowledge, no publications on the interaction of PE stars with oppositely charged macromolecules or investigations on the properties of the resulting macromolecular co-assemblies can be found in the literature to date, except for a few papers [79–81] that are discussed below.

Pergushov et al. [79] demonstrated for the first time that the interaction of poly(acrylic acid) stars [$(PAA)_X$, where X denotes the number of arms] with relatively long cationic PEs, namely quaternized poly(4-vinylpyridine) (P4VPQ), at pH 7 can lead to the formation of water-soluble IPECs in which the star-shaped PEs play a lyophilizing role, i.e., they act as HPEs, providing solubility of the whole macromolecular co-assemblies in aqueous media. Specifically, it was observed that the addition of P4VPQ into an aqueous solution of the $(PAA)_X$ stars causes macroscopic phase separation of the mixture of oppositely charged polymeric components only if their base-molar ratio Z ($Z = [N^+]/[COO^- + COOH]$, $Z < 1$) exceeds a certain threshold value Z_M (Fig. 2), thereby strongly suggesting the formation of water-soluble IPECs at $Z < Z_M$. The values of Z_M were found to increase with an increase in the number of arms (Fig. 2, inset). This tendency, as shown by the same authors [79], became more pronounced at higher ionic strengths of the aqueous mixtures of oppositely charged polymeric components.

It is remarkable that an aqueous solution of the reference linear PAA becomes turbid after adding the first portion of the aqueous solution of P4VPQ (Fig. 2, inset). This clearly indicates that the reference linear PAA, in contrast to the $(PAA)_X$ stars, cannot form water-soluble IPECs via this method under the same conditions and also clearly manifests a pronounced effect of the topology of the polymeric component involved in interpolyelectrolyte complexation on the possibility of preparing water-soluble macromolecular co-assemblies.

A detailed examination of the homogeneous mixtures of $(PAA)_X$ stars and P4VPQ [79] by dynamic light scattering (DLS) provided evidence of a distinct coexistence of the two populations of macromolecular co-assemblies: (1) A dominant fraction comprising particles of water-soluble IPECs that result from interactions between oppositely charged polymeric components; their hydrodynamic size was

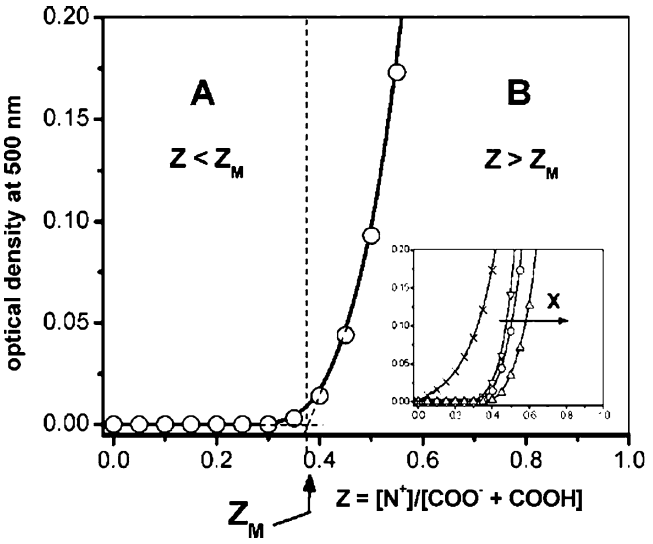

Fig. 2 Turbidimetric titration curve of an aqueous solution of $(PAA)_8$ stars with an aqueous solution of P4VPQ. *Inset* shows the corresponding turbidimetric titration curves for aqueous solutions of $(PAA)_X$ stars with $X = 5$ (*down triangles*), 8 (*circles*), and 21 (*up triangles*), as well as the reference linear PAA (*crosses*). Z is the base-molar ratio of components and Z_M is the threshold value at which phase transition occurs. Reprinted from [79] with permission from the American Chemical Society

very close to that of the original $(PAA)_X$ stars. (2) A minor fraction comprising some large but rather compact complex aggregates that were concomitantly generated in such mixtures.

These authors [79] proposed two tentative scenarios for interpolyelectrolyte complexation (schematically depicted in Fig. 3). In the case of $(PAA)_X$ stars with a small number of arms (i.e., the total number of ionic groups of a single PE star is lower than or comparable to the total number of ionic groups of a chain of the oppositely charged linear PE), each dominant complex species is assumed to contain several $(PAA)_X$ stars per $P4VPQ^+$ chain (Fig. 3a). This suggests that association of several molecules of the star-shaped PE can be induced via their interaction with a chain of the oppositely charged linear polyion. In the case of $(PAA)_X$ stars with a large number of arms (i.e., the total number of ionic groups of a single PE star is considerably larger than the number of ionic groups of a chain of the oppositely charged linear PE), each dominant complex species is considered to comprise one $(PAA)_X$ star and one or more $P4VPQ^+$ chains (Fig. 3b).

Further studies carried out by the same authors [80] demonstrated that for a specific system, namely aqueous mixtures of $(PAA)_X$ with a large number of arms $(X = 21)$ and very short quaternized poly(2-vinylpyridine) (P2VPQ), the fraction of the large complex aggregates generated at $Z < Z_M$ is quite negligible, thus making static light scattering (SLS) measurements feasible. The weight-average molecular weight of such macromolecular co-assemblies determined by SLS indicates that

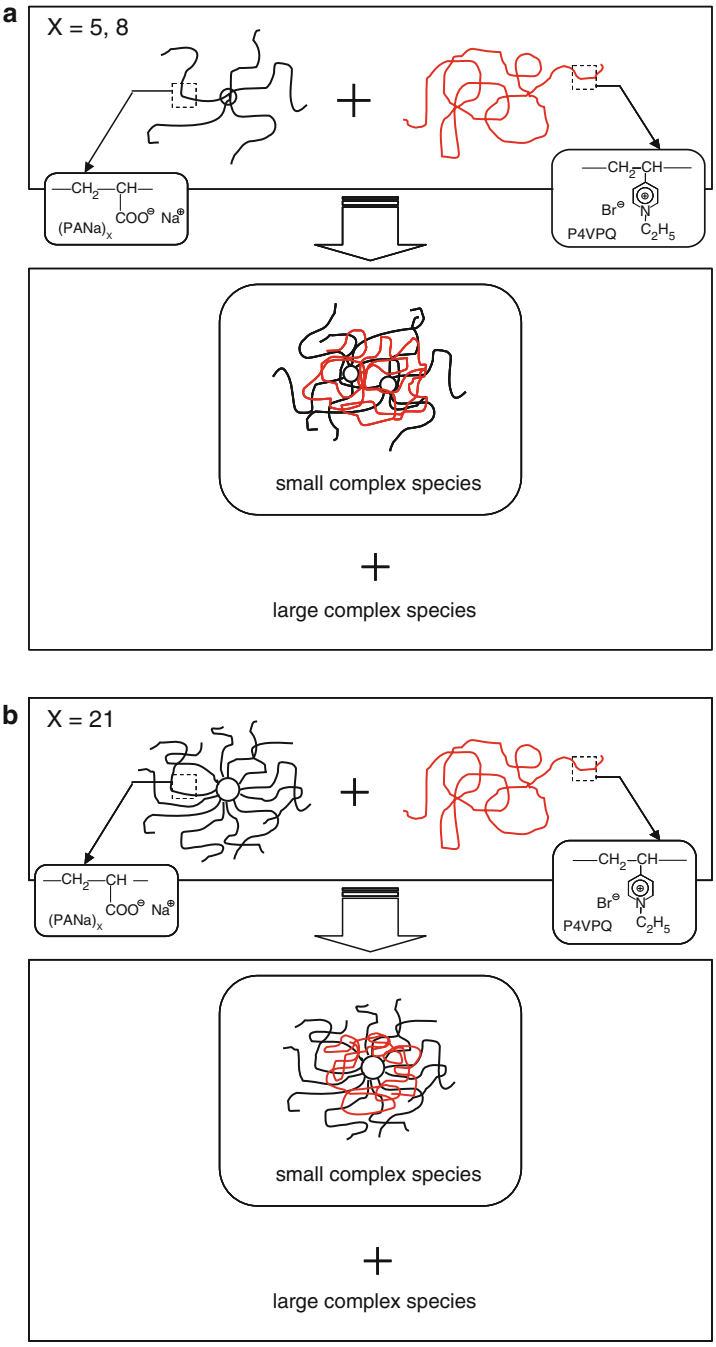

Fig. 3 Hypothetical representation of the interpolyelectrolyte complexation between $(PAA)_X$ stars (in the form of sodium salts) and P4VPQ for $(PAA)_X$ stars with (**a**) a small number of arms and (**b**) a large number of arms. Reprinted from [79] with permission from the American Chemical Society

each of them only contains one $(PAA)_X$ star, whose charge is partially compensated by the $P2VPQ^+$ chains. It was suggested that the $P2VPQ^+$ chains are predominantly located in the central region (near the branching point) of the star-shaped PE, thereby forming an inhomogeneous core–corona structure. A relatively hydrophobic core of such macromolecular co-assembles is assembled from coupled fragments of oppositely charged polymeric components (the so-called complex coacervate domain), which incorporates the opposite charges in a ratio of nearly 1:1. Meanwhile, a hydrophilic (ionic) corona is built up from the excess fragments of $(PAA)_X$ (those not involved in interpolyelectrolyte complexation), providing solubility of the whole complex species in aqueous media (Fig. 4).

Two different possible structural organizations of the IPECs based on PE stars can be proposed. As schematically depicted in Fig. 4, the first scenario (structure I) assumes that the arms of the star-shaped HPE split into two populations upon interpolyelectrolyte complexation. Some of the arms are completely embedded into

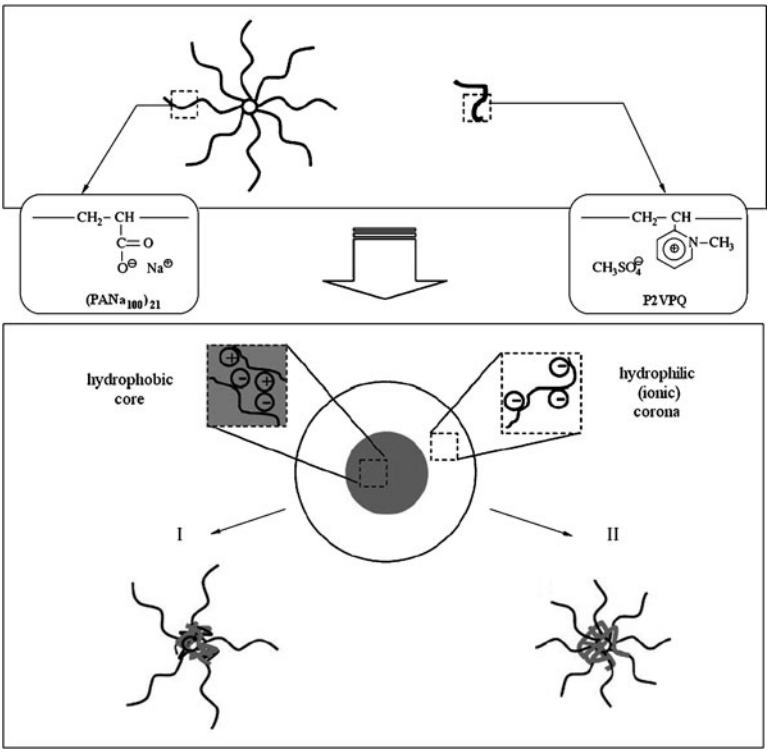

Fig. 4 Proposed inhomogeneous core–corona structure of the macromolecular co-assemblies formed in aqueous mixtures of $(PAA)_{21}$ stars (in the form of sodium salt) and P2VPQ. In *structure I*, some of the arms of the star-shaped HPE are embedded in the core and others are extended. In *structure II*, all of the arms contribute segments of equal length to the core. Reprinted from [80] with permission from Springer

the complex coacervate core, whereas the others remain extended and form the hydrated corona of the co-assemblies. Experimental observation that the hydrodynamic radius of the formed co-assemblies only weakly depends on their base-molar stoichiometry (degree of charge compensation of the branched HPE by GPE chains) supports this first scenario. An alternative possibility (structure II) assumes that all of the branches of the star-shaped HPE contribute segments of equal length to the central core (complex coacervate) domain. The lyophilizing corona is formed by the terminal segments of the star-shaped HPE that are not involved in the complexation with chains of the linear GPE. Obtaining experimental proof of the thermodynamically preferred structure of such macromolecular co-assemblies is a challenging task; a deeper insight into this problem has been enabled by MD simulations and scaling arguments, as discussed in Sect. 2.2.

An interesting example of macromolecular co-assemblies derived from star-shaped polyionic species was reported by Ge et al. [81]. The authors found that a star-shaped double hydrophilic poly(methacrylic acid)-poly(ethylene oxide) heteroarm copolymer [$(PMAA)_X$-PDVB-$(PEO)_X$, with PDVB being poly(divinylbenzene) and X denoting the number of PMAA and PEO arms] can interact in alkaline media with a double hydrophilic poly(ethylene oxide)-*block*-quaternized poly[2-(dimethylamino)ethyl methacrylate] (PEO-*b*-PDMAEMAQ) diblock copolymer. At $Z = [PDMAEMAQ]/[PMAA] = 1$, well-defined water-soluble onion-like (core–shell–corona) macromolecular co-assemblies are formed, with a hydrophobic core consisting of a PDVB microgel. The interaction of the PMA^- arms of the hybrid coronas of such copolymer stars with the $PDMAEMAQ^+$ blocks of the diblock copolymer generates an insoluble inner layer (shell) around a PDVB core. Meanwhile, PEO blocks from both PEO-*b*-PDMAEMAQ and $(PMAA)_X$-PDVB-$(PEO)_X$ build up a hydrophilic nonionic corona that stabilizes the whole complex in aqueous media.

2.2 Molecular Dynamics Simulations

A pioneering attempt to unravel the internal structural organization of IPECs formed from the interaction between oppositely charged star-shaped PEs (HPEs) and linear PEs (GPEs) was recently made by Larin et al. [89]. The total number of ionic groups of a single PE star was taken to considerably exceed the total number of ionic groups of a chain of an oppositely charged linear PE. Using MD simulations (coarse-grained bead–rod model), the authors showed the stable inhomogeneous structure of the formed macromolecular co-assemblies. Specifically, they demonstrated that the resulting IPEC species comprise three distinct domains: (a) a dense central domain where chains of the linear PE partially compensate the local charge of the arms of the star-shaped PE; (b) a complex coacervate domain where the local charge of the arms of the star-shaped PE is nearly fully compensated by chains of the linear PE, the majority of which are found here; and (c) a periphery domain where the charge of the arms of the star-shaped PE is considerably undercompensated.

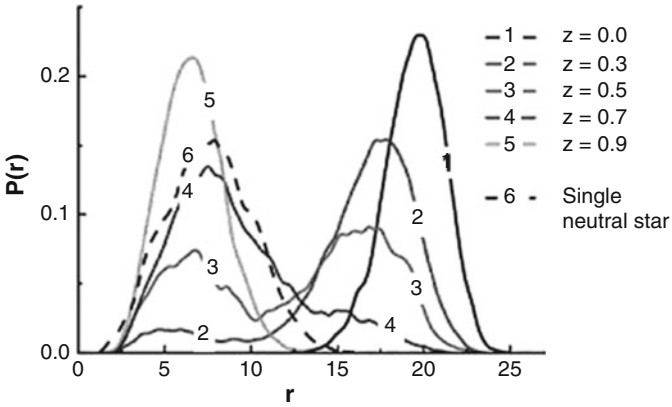

Fig. 5 Fraction P of the terminal monomer units located at a distance r from the center of a star-shaped PE at different contents of a linear PE. z is the degree of charge compensation, which reflects the linear PE content. Reprinted from [89] with permission from the American Chemical Society

Thus, the results of MD simulations provide ultimate support for the core–corona [the core comprises domains (a) and (b), as revealed in MD simulations] model of the structural organization of IPECs based on the star-shaped PEs, which was suggested on the basis of experimental findings [80]. Together, experimental results and MD simulations provide evidence for a compartmentalized micelle-like structure that results from a pronounced nonuniform distribution of chains of the linear PE within the volume occupied by a molecule of the star-shaped PE.

The MD simulations [89] also gave another very important insight into the structure of IPECs based on the star-shaped PEs that would be difficult to obtain experimentally. Following from the radial distributions of the end monomer units demonstrated in Fig. 5, a progressive repartitioning of the arms of the star-shaped PE from the periphery region to the complex coacervate domain was observed with an increase in content of the linear PE. Figure 6 clearly illustrates the pronounced segregation of the arms of the star-shaped PE into two populations, one of which forms the complex coacervate domain together with chains of the linear PE, and the other builds up the corona domain.

The MD-predicted intramolecular segregation of the arms of the star-shaped PE into two populations (collapsed and extended ones) provides an explanation for the experimentally observed absence of a dependence (or relatively weak dependence) of the hydrodynamic size of the IPEC species on the number of incorporated chains of the linear PE.

Simple scaling arguments [89] enable a rationalization of the origin of the partitioning of arms of the star-shaped HPE between the core and the corona domains: the free energy of the core (complex coacervate) domain is controlled (in the main part) by the total number of positively and negatively charged monomer units forming the complex coacervate core, i.e., by the degree of charge compensation of the

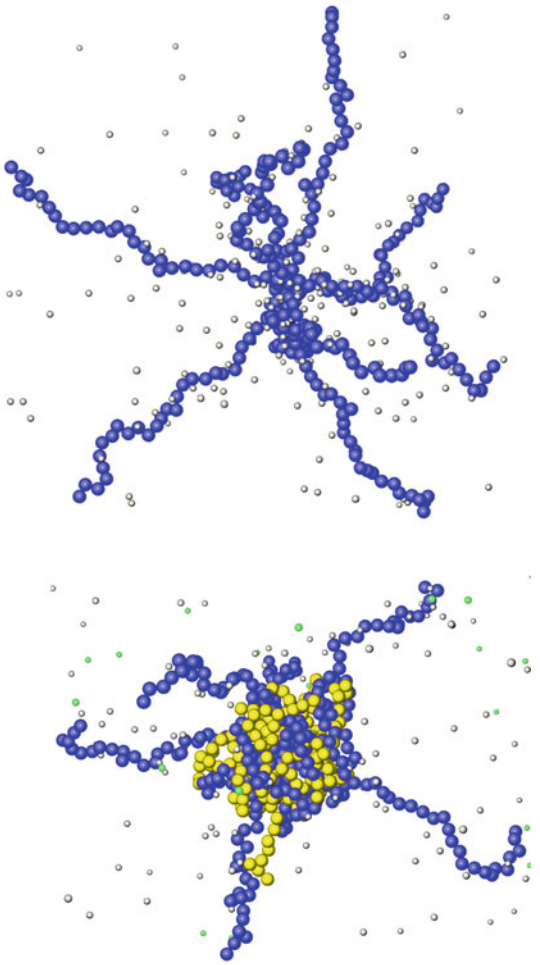

Fig. 6 Snapshot of the typical conformations of a bare PE star (*top*) and its IPEC with the oppositely charged linear PE (*bottom*). Chains of linear PE are shown by the *light-colored* beads. Reprinted from [89] with permission from the American Chemical Society

star-shaped HPE by chains of the linear GPE. At the same time, at a given number of monomer units of HPE in the coronal domain, the free energy of the corona is lower when it is formed by a smaller number of longer arms than by a larger number of shorter arms. This is the case, for example, when the Coulomb repulsions or osmotic pressure of the entrapped counterions dominate the interactions in the corona region.

We should emphasize that the trends discussed in this section are also expected to manifest for IPECs based on other types of branched PE species acting as HPEs. In particular, they can be related to IPECs derived from star-like micelles of ionic amphiphilic block copolymers. These are considered from the experimental point of view in Sect. 4.

3 IPECs Based on Cylindrical Polyelectrolyte Brushes

3.1 Experimental Results

Cylindrical PE brushes represent another type of PE with a branched topology. They consist of long backbones with densely attached, relatively short PE side chains, and are thus highly anisotropic polymeric objects. To the best of our knowledge, only a few studies devoted to IPECs based on cylindrical PE brushes have been reported so far [64, 82–85].

Ishizu et al. [82, 83] described macromolecular co-assemblies formed through the interaction of a so-called anionic prototype copolymer brush, namely the poly(ethylene oxide)/poly(sodium styrene sulfonate) (PEO/PSSNa) brush, with a linear cationic PE, P4VPQ. The authors found that the macromolecular co-assemblies resulting from the interactions of such oppositely charged polymeric components in aqueous media were very large aggregates with a hydrodynamic diameter of ca. 250 nm and a rod-like cylindrical morphology, as shown in scanning electron microscopy (SEM) micrographs. The authors considered these aggregates to be highly anisotropic supramolecular polymeric architectures (supermicelles) (Fig. 7).

In a paper by Störkle et al. [64], the co-assembly between DNA and cationic cylindrical PE brushes with P2VPQ side chains and poly(ethylene imine) (PEI) side chains was investigated. The authors showed that macromolecular co-assemblies formed in diluted solutions exhibited a similar size (30–55 nm) in terms of the mean square radius of gyration, regardless of the cationic cylindrical PE brush. The extremely large charge density mismatch between DNA and the P2VPQ and PEI brushes was claimed to be a reason for the formation of strongly "overcharged" cationic complex species when there was an excess of charged groups of the cationic cylindrical PE brushes compared to the charged groups of DNA, or for formation of slightly negatively charged complex species when there was excess of the charged groups of DNA.

The analytical ultracentrifugation (AUC) and DLS experiments for the mixtures of an anionic cylindrical PAA brush acting as the HPE and a linear P4VPQ acting as the GPE demonstrated that at $Z < Z_M$ ($Z = [N^+]/[COO^- + COOH]$, $Z < 1$), a single type of colloidally stable IPEC with a hydrodynamic size nearly coinciding with that of the original cylindrical PE brush is formed in the solution [84]. Similarly to the IPECs derived from the star-shaped PEs, this system also undergoes macroscopic phase separation at $Z > Z_M$. The colloidal stability of the IPECs based on the cylindrical PE brush suggests that such macromolecular co-assemblies have a core–

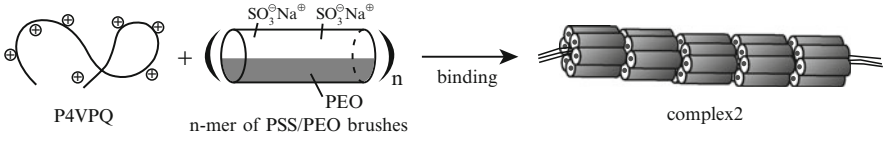

Fig. 7 Interaction between a PEO/PSSNa prototype copolymer brush and P4VPQ in aqueous medium. Reprinted from [82] with permission from the American Chemical Society

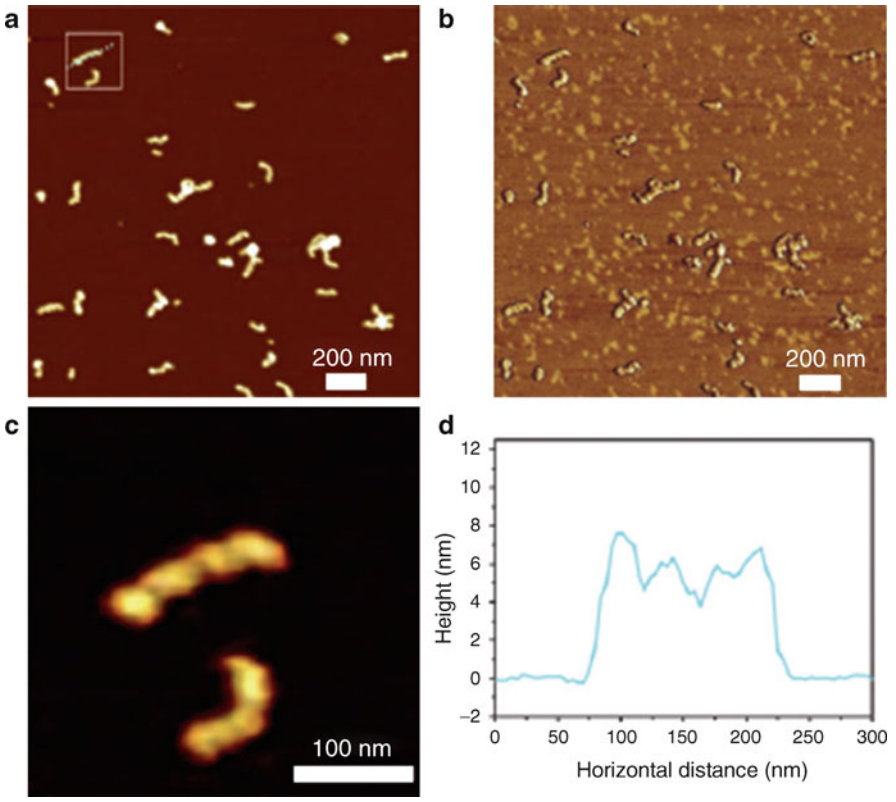

Fig. 8 AFM images of IPEC formed by the PDMAEMAQ brush complexed with PSSNa at $Z = [SO_3^-]/[N^+] = 0.75$: (**a**) height image, Z range 20 nm; (**b**) phase image, Z range 25°; (**c**) magnified image of a selected area from **a**. (**d**) Section analysis of the cursors displayed in **a**. Reprinted from [85] with permission from the American Chemical Society

corona structure, and intuition would predict a cylindrical complex coacervate core. However, the results of the MD simulations presented in Sect. 3.2 indicate that the complex core appears to be split into a necklace of complex coacervate pearls.

Using atomic force microscopy (AFM), Xu et al. [85] showed that similar macromolecular co-assemblies derived from the cylindrical PE brush based on quaternized poly[2-(dimethylamino) ethyl methacrylate] (PDMAEMAQ) complexed with short poly(sodium styrene sulfonate) (PSSNa) have distinct longitudinal undulations (Fig. 8), thereby apparently providing experimental proof of a peculiar pearl-necklace structure of IPECs based on such branched PEs.

3.2 Molecular Dynamics Simulations

The structural organization of IPECs resulting from interactions between the cylindrical PE brush acting as a HPE and oppositely charged chains of the linear GPE was recently investigated by Larin et al. using MD simulations [84].

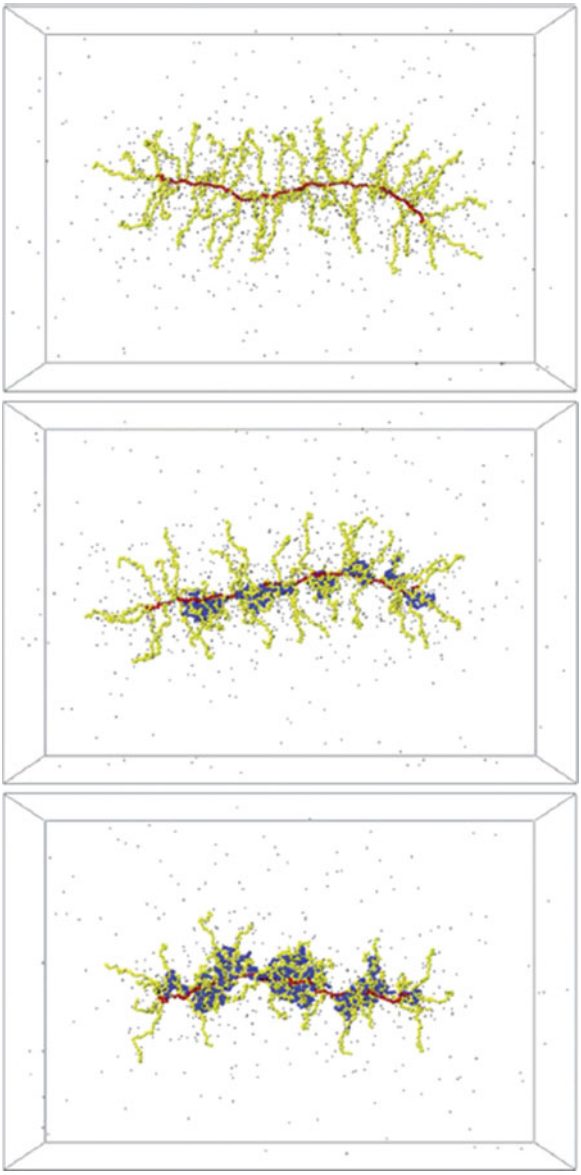

Fig. 9 Snapshots of the typical conformations of the bare cylindrical PE brush (*top*) and of IPECs of the cylindrical PE brush with linear GPE at the degrees of charge compensation of 0.25 (*middle*) and 0.5 (*bottom*). *Red* PE brush backbone, *yellow* PE brush side chains, *blue* chains of the linear GPE. Reprinted from [84] with permission from the Royal Society of Chemistry

A very similar computational model to the one used for simulations of IPECs based on the star-shaped HPE and described in Sect. 2.2 was applied. Typical equilibrium conformations of the bare cylindrical PE brush and of the IPECs with the degree of charge compensations of 0.25 and 0.5 are presented in Fig. 9. The simulation results

confirmed the core–corona structure of the formed co-assemblies, which is in accordance with experimental observations and explains the colloidal stability of the IPECs in aqueous media. However, instead of the intuitively expected cylindrical core, the snapshots clearly demonstrate that the core domain splits into a necklace of complex coacervate pearls. The pearls are decorated by a hydrophilic corona formed by the excess side chains of the cylindrical PE brush, which do not form interpolymer salt bonds with the chains of oppositely charged linear GPE.

The longitudinal instability of the cylindrically uniform complex coacervate core domain is a manifestation of the Rayleigh instability. The latter occurs when surface tension at the core–water interface is counterbalanced by long-range repulsive forces stretching the core. For the specific system considered here, the effective long-range repulsions arise because of interactions between the side chains forming the cylindrical corona of the IPEC. Similar pearl-necklace structures have previously been theoretically predicted and experimentally observed for amphiphilic cylindrical brushes in selective solvents [90–92].

Figure 10 presents the radial distributions of the terminal segments of the side chains of the cylindrical PE brush in the complex with oppositely charged linear GPE chains. As can be seen, a single maximum typical for the bare cylindrical PE brush splits into two maxima: the proximal maximum corresponds to the side chains of the cylindrical PE brush being completely embedded into complex coacervate domains, and the distal maximum corresponds to the side chains constituting the corona of the complex. As described for IPECs based on star-shaped PEs (Sect. 2.2), the side chains of the cylindrical PE brush demonstrate progressive repartitioning from the corona to the collapsed complex coacervate domains with increasing content of linear PE (Fig. 10).

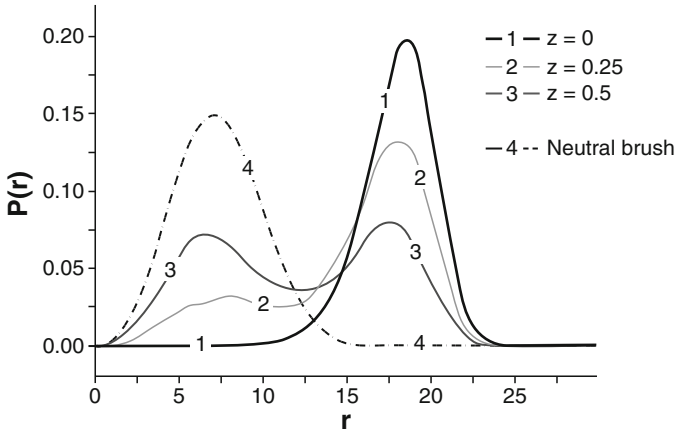

Fig. 10 Radial distribution (P) of the terminal monomer units of side chains as a function of the distance (r) from the backbone at different degrees of charge compensation (z). Reprinted from [84] with permission from the Royal Society of Chemistry

4 IPECs Based on Star-like Micelles of Ionic Amphiphilic Block Co- and Terpolymers

4.1 IPECs Based on Micelles of Ionic Amphiphilic Diblock Copolymers

The core–corona micelles generated via self-assembly in aqueous solutions of ionic amphiphilic diblock copolymers resemble star-shaped PEs with a high number of arms, provided that the radius of the hydrophobic core is considerably smaller than the thickness of the PE corona. The properties of these micelles are reviewed in detail elsewhere [93]. In most cases, the core domain formed upon association of strongly hydrophobic blocks is found in a kinetically "frozen" state, e.g., poly(styrene) (PS) associating blocks are in a glassy state. These "frozen" micelles do not change their aggregation numbers with variations in the environmental conditions; therefore, their behavior in solution is equivalent to that of PE stars with a fixed number of arms. Recently, significant efforts have been made to obtain "dynamic" or equilibrium micelles with PE coronas. In these micelles, there is a dynamic equilibrium between macromolecules of diblock copolymers self-assembled into micelles and those existing in the form of unimers in solution. These micelles are expected to respond to changing environmental conditions by tuning the strength of electrostatic interactions in the PE corona (e.g., by variations in pH or ionic strength) or by varying the strength of attraction between associating blocks (e.g., by varying the temperature) through a variation in their aggregation number.

The core–corona micelles with PE coronas are naturally expected to interact with oppositely charged macromolecules, thereby generating IPECs. Although only structural changes are anticipated to take place in the PE corona (as in the case of the PE stars) upon interpolyelectrolyte complexation of frozen micelles, the dynamic micelles might exhibit more complex responsive behaviors, e.g., undergo rearrangement of their nonpolar cores and a variation in their aggregation number.

To the best of our knowledge, the pioneering attempt to investigate the formation of IPECs in such systems and to determine the characteristics of the generated co-assemblies was realized by Talingting et al. [65], who described interpolyelectrolyte complexation of protonated poly(styrene)-*block*-poly(2-vinylpyridine) (PS-*b*-P2VPH$^+$) micelles with PSSNa in strongly acidic media. By means of laser microelectrophoretic and SLS measurements, these authors [65] demonstrated considerable mass overcompensation of the PS-*b*-P2VPH$^+$ micelles by PSSNa, even under a low concentration regime, which apparently enabled the formation of bridged structures to be avoided. The molecular weight increased by a factor of about 5–6, which corresponds to about 4.7–5.5 sulfonate groups per pyridinium group. This was accompanied by a concomitant and remarkable charge inversion for the PS-*b*-P2VPH$^+$ micelles. Although the molecular weight of PSSNa varied from 5.00×10^3 to 8.01×10^5 g/mol (corresponding to the degree of polymerization, which ranged from about 0.1 to about 15 times the degree of polymerization of the P2VPH$^+$ block), only a minor effect on the characteristics of the generated

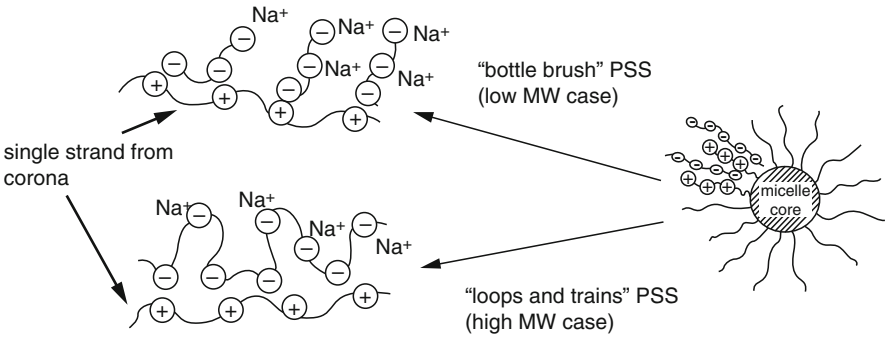

Fig. 11 Structure of co-assemblies resulting from the interactions between PS-*b*-P2VPH$^+$ micelles and PSSNa of low and high molecular weights. Reprinted from [65] with permission from the American Chemical Society

macromolecular co-assemblies was revealed. Talingting et al. suggested that some of the PSS$^-$ chains were strongly associated with P2VPH$^+$ blocks while some of them were not, thereby forming "loop and train" structures. For the longer PSS$^-$ chains, the authors expected parts of the PSS$^-$ chains to be extended outside the micellar coronas, providing additional overcompensation, whereas they proposed the formation of "bottle-brush" structures for the shorter PSS$^-$ chains (Fig. 11). As also indicated by the authors, the formation of the massively overcharged complex species could be a result of the "kinetic trapping" of PSS$^-$ chains in the coronas of PS-*b*-P2VPH$^+$ micelles due to the strong binding of oppositely charged polymeric components and, therefore, to the rather low rate of macromolecular rearrangements that would lead to alignment of the PSS$^-$ chains along P2VPH$^+$ blocks, thereby providing a charge balance for the formed complex species.

Further investigations in this field, specifically studies on the interaction of poly(isobutylene)-*block*-poly(sodium methacrylate) (PIB-*b*-PMANa) micelles with P4VPQ in alkaline media by Pergushov et al. [66–68] and Burkhardt et al. [69], demonstrated for the first time the possibility of formation of novel macromolecular co-assemblies in which the original diblock copolymer micelles apparently play a lyophilizing role. Such micelles act as the HPE and provide solubility (stability against aggregation and precipitation) of the whole complex in aqueous media. To explain the experimental observations, the onion-like (core–shell–corona) structural model of these IPECs was proposed. In contrast to the previous paper by Talingting et al. [65], the PIB-*b*-PMANa micelles were used in excess compared to P4VPQ so that the molar concentration of their ionic groups in the aqueous mixtures of the oppositely charged polymeric components exceeded that of the linear PE.

The addition of P4VPQ into an aqueous solution of the PIB-*b*-PMANa micelles was found to induce macroscopic phase separation of the aqueous mixtures of oppositely charged polymeric components only if the ratio between the molar concentrations of their ionic groups Z ($Z = [N^+]/[COO^-]$, $Z < 1$) exceeded the certain threshold value of Z_M (Fig. 12). At $Z < Z_M$, the aqueous mixtures of the PIB-*b*-

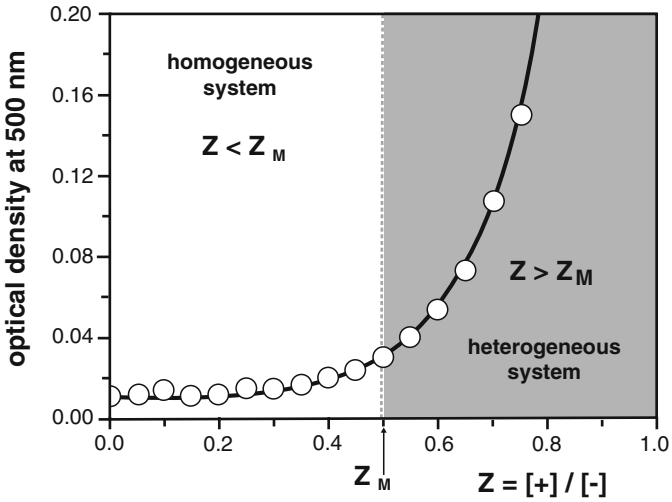

Fig. 12 Turbidimetric titration curve of the aqueous solution of PIB-*b*-PMANa micelles with the aqueous solution of P4VPQ. *Z* is the ratio of the concentrations of the ionic groups, $[N^+]/[COO^-]$ of the polymeric components. Phase separation occurred above the threshold value Z_M. Reprinted from [66] with permission from the American Chemical Society

PMANa micelles and P4VPQ remained transparent, thus strongly suggesting the formation of water-soluble IPECs enriched by ionic groups of the micelle-forming polymeric component. This trend is very similar to that discussed in Sect. 2.1 for the formation of IPECs between star-shaped HPE and linear GPE chains.

The examination of homogeneous mixtures of the PIB-*b*-PMANa micelles and P4VPQ at $Z < Z_M$ carried out using various techniques, including AUC [66, 67], fluorescence spectroscopy (with the use of pyrene as a polarity probe) [66, 67], DLS [67–69], small-angle neutron scattering (SANS) [67–69], and cryogenic transmission electron microscopy (cryo-TEM) [69], provided evidence that the formed water-soluble IPECs have peculiar onion-like (or multilayer) micellar structure. It is remarkable that the hydrodynamic sizes [67–69] and morphologies [69] of such macromolecular co-assemblies were found to be quite close to or virtually the same as those of the original PIB-*b*-PMANa micelles. These observations suggest that, similarly to IPECs based on star-shaped HPEs, the co-assembly between micelles with PE coronas and chains of oppositely charged linear GPE results in intra-coronal disproportionation of PE blocks. A certain fraction of such blocks is completely embedded in the complex coacervate shell, whereas the rest of the coronal blocks only contribute a small number of their monomer units in the shell domain and form the lyophilizing corona.

According to the authors of [66–69], each of the water-soluble complex species contains a hydrophobic core formed by PIB blocks (A in Fig. 13), which is surrounded by a compact complex coacervate inner shell assembled from oppositely charged fragments of the polymeric components (PMA^- blocks and $P4VPQ^+$ chains) (B in Fig. 13) and by a hydrophilic (ionic) corona built up from excess

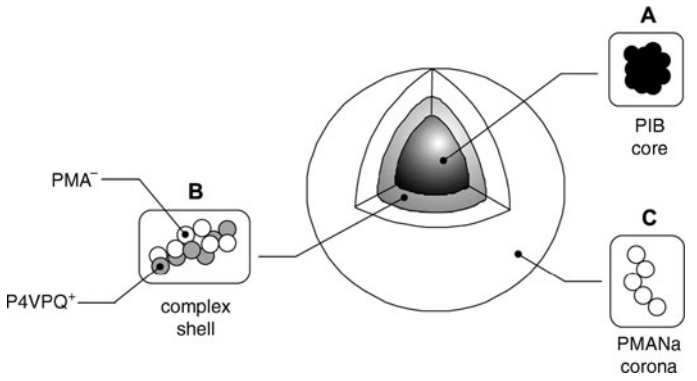

Fig. 13 Onion-like core (**A**)–shell (**B**)–corona (**C**) structure of the micellar IPEC formed upon interaction between PIB-*b*-PMANa micelles and P4VPQ. Reprinted from [67] with permission from Elsevier

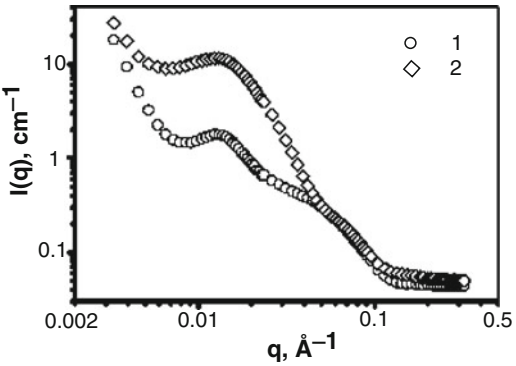

Fig. 14 SANS intensity (I) as a function of the scattering vector (**q**) for alkaline aqueous solutions of the PIB-*b*-PMANa micelles (*1*) and their IPEC with P4VPQ at $Z = [N^+]/[COO^-] = 0.4$ (*2*). Reprinted from [67] with permission from Elsevier

PMANa blocks that are not involved in interpolyelectrolyte complexation with $P4VPQ^+$ (C in Fig. 13).

Detailed analysis of the scattering curves obtained by SANS (Fig. 14) strongly suggest that the aggregation number of the original PIB-*b*-PMANa micelles hardly changes upon their interaction with P4VPQ [67–69], i.e., upon formation of the complex particles, although the original micelles exhibit "dynamic" properties [94]. Apparently, interpolyelectrolyte complexation of such micelles with oppositely charged linear PE does not make them "frozen" structures as their aggregation numbers remain sensitive to variations in the pH of the surrounding solution [69].

The time-dependent turbidity measurements carried out by the authors of [69] suggest that the mixing of aqueous solutions of PIB-*b*-PMANa micelles and P4VPQ is at first accompanied by the formation of large multimicellar aggregates, which gradually split into smaller ones. At the same time, $P4VPQ^+$ chains initially bound

to peripheral (outmost) parts of micellar coronas penetrate deeper inside them to eventually become located at the core–corona interface. This structure enables the interface between the complex coacervate domain and the hydrated ionic corona in the formed macromolecular co-assemblies to be minimized. Finally, these rearrangements lead (typically, within tens of minutes) to the formation of equilibrium water-soluble macromolecular co-assemblies from the nonequilibrium large aggregates that were initially generated.

Another example of core–shell–corona macromolecular co-assemblies resulting from poly(styrene)-*block*-quaternized poly(4-vinylpyridine) (PS-*b*-P4VPQ) micelles interacting with poly(sodium methacrylate) (PMANa) [or fluorescent pyrenyl-labeled PMANa (PMA*Na)] in alkaline media was reported by Lysenko et al. [70, 72] and Chelushkin et al. [71]. They showed that the formation of water-soluble IPECs can either be realized in a certain excess of positively charged groups of the PS-*b*-P4VPQ micelles (Fig. 15, region I) or in a certain excess of negatively charged groups of PMA*Na (Fig. 15, region V) compared to the amount of the charged groups of the corresponding polymeric counterparts (PMANa or PS-*b*-P4VPQ, respectively). Otherwise, the aqueous mixtures of the oppositely charged

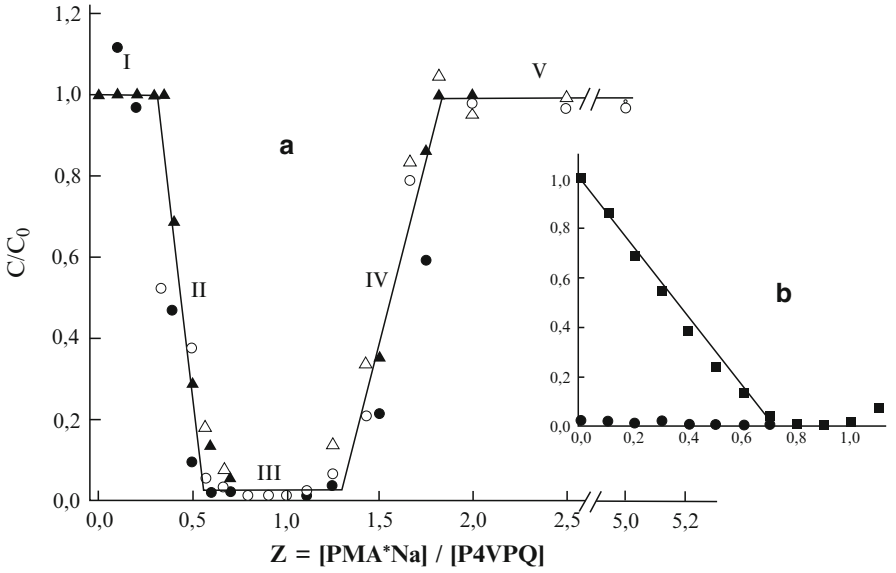

Fig. 15 Solubility diagram of the mixtures of (**a**) PS-*b*-P4VPQ micelles and PMA*Na and (**b**) P4VPQ and PMA*Na, presented as the dependence of the relative concentrations (C/C_0) of the PEs remaining in solution on the base-molar stoichiometry (Z) of the mixtures of oppositely charged polymeric components $(Z = [COO^-]/[N^+])$. The data shown are (**a**) for PS-*b*-P4VPQ (*triangles*) and PMA*Na (*circles*) for different mixing orders: the PMA*Na solution was added to the solution of PS-*b*-P4VPQ micelles (*closed symbols*) or the solution of PS-*b*-P4VPQ micelles was added to the solution of PMA*Na (*open symbols*) and (**b**) for P4VPQ (*squares*) and PMA*Na (*circles*); the solution of PMA*Na was added to the solution of P4VPQ. Water-soluble IPECs are formed in regions *I* and *V*, phase separation occurs in regions *II* and *IV*, and there is precipitation of insoluble IPECs in region *III*. Reprinted from [72] with permission from the American Chemical Society

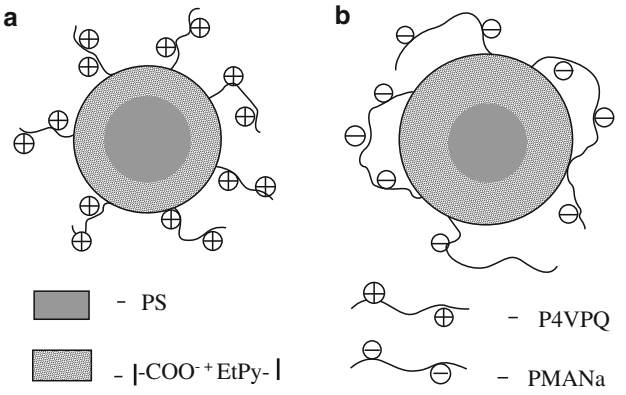

Fig. 16 Structure of (**a**) positively charged (excess of PS-*b*-P4VPQ) or (**b**) negatively charged (excess of PMANa) micellar IPEC formed upon the interaction of PS-*b*-P4VPQ micelles with PMANa. Reprinted from [72] with permission from the American Chemical Society

polymeric components undergo distinct macroscopic phase separation: the PS-*b*-P4VPQ micelles become colloidally unstable and precipitate as insoluble IPECs (Fig. 15, regions II–IV).

On the basis of the results obtained by SLS and transmission electron microscopy (TEM), it was concluded that binding of PMANa to the PS-*b*-P4VPQ micelles hardly affected the structure of the PS core, i.e., no disaggregation, fusion, or flocculation of the original micelles occurred as a result of their interaction with the oppositely charged linear PE [70–72]. The water-soluble macromolecular co-assemblies have also been considered as multilayer IPECs with a core–shell–corona structure (Fig. 16), for which the original PS-*b*-P4VPQ micelles act as peculiar "nucleating" particles. Depending on the lyophilizing polymeric component (PS-*b*-P4VPQ micelle or PMANa), the particles of such multilayer IPECs are stabilized in aqueous solutions by coronas built up either by excess fragments of P4VPQ blocks (positively charged micellar IPECs, Fig. 16a) or by excess fragments of PMANa chains (negatively charged micellar IPECs, Fig. 16b).

Further investigations carried out by Chelushkin et al. [73] for various combinations of micelles formed in aqueous media by ionic amphiphilic diblock copolymers [PS-*b*-P4VPQ, poly(styrene)-*block*-poly(sodium acrylate) (PS-*b*-PANa), and PS-*b*-PMANa)] with oppositely charged linear PEs (polycarboxylates, polysulfonates, polyphosphates, and aromatic, aliphatic, and alicyclic quaternized polyamines) have demonstrated that the solubility of IPECs is decisively determined by (1) the aggregation state of the excess polymeric component (micelles versus individual polymeric coils) and (2) the procedure or method employed for the preparation of such macromolecular co-assemblies.

When the diblock copolymer micelles play a lyophilizing part (i.e., when they act as HPEs), water-soluble micellar IPECs can be typically obtained via at least one of the preparation routes described by the authors [73]. In this case, the chemical

nature and the degree of polymerization of the linear PE determines whether such IPECs can be obtained independently of the procedure used for their preparation (e.g., PS-*b*-P4VPQ/polycarboxylates) or via the specific procedure comprising mixing of the oppositely charged polymeric components at high values of ionic strength (to prevent interpolyelectrolyte complexation) followed by dilution with a solvent to lower the ionic strength (to switch on interpolyelectrolyte complexation). The latter procedure would be followed for, e.g., PS-*b*-PANa/aromatic, aliphatic, and alicyclic quaternized polyamines. Furthermore, the hydrodynamic characteristics (hydrodynamic size and sedimentation coefficient) of the formed macromolecular co-assemblies are predominantly determined by the corresponding hydrodynamic characteristics of the original diblock copolymer micelles.

When the linear PE plays a lyophilizing role (i.e., when it acts as an HPE), water-soluble micellar IPECs can only be generated for some selected combinations of oppositely charged polymeric components, namely if the linear PE can form water-soluble IPECs with the corresponding linear analog of the PE block of the ionic amphiphilic diblock copolymer (e.g., PS-*b*-P4VPQ/PMANa, where PMANa as the HPE forms water-soluble IPECs with P4VPQ). In this case, the hydrodynamic characteristics (hydrodynamic size and sedimentation coefficient) of the formed macromolecular co-assemblies are decisively determined by the molecular weight and chemical nature of the excess linear PE.

4.2 IPECs Based on Micelles of Ionic Amphiphilic Block Terpolymers

A fascinating example of water-soluble micellar IPECs was recently found and thoroughly investigated by Schacher et al. [74]. In particular, it was demonstrated that polyampholytic amphiphilic polybutadiene-*block*-quaternized poly(2-vinylpyridine)-*block*-poly(methacrylic acid) (PB-*b*-P2VPQ-*b*-PMAA) triblock terpolymers can generate peculiar multicompartment self-assemblies in aqueous media. According to these authors, each micelle comprises a hydrophobic poly(butadiene) (PB) core, multiple $PMA^-/P2VPQ^+$ domains [patches, or intramicellar IPECs] on the PB core that are caused by electrostatic interaction between both oppositely charged PE blocks, and a corona composed of excess fragments of the longer PE block (either PMAA or P2VPQ depending on their degrees of polymerization). The ionic corona provides solubility (stability against intermicellar aggregation and precipitation) of the whole macromolecular self-assembly in aqueous media (Fig. 17). In contrast to the considerations in Sect. 4.1 for IPECs formed by micelles of ionic amphiphilic diblock copolymers interacting with the oppositely charged linear PE, the $PMA^-/P2VPQ^+$ shell in this case appears to be distinctly noncontinuous (patchy), as shown in the cryo-TEM micrographs (Fig. 17A, B, E).

The PB-*b*-P2VPQ-*b*-PMAA micelles are apparently dynamic colloids because they change their aggregation numbers upon variations in ionic strength of the surrounding solution. Specifically, the aggregation number of such micelles was found to decrease with increasing ionic strength, which was attributed to the salt-induced

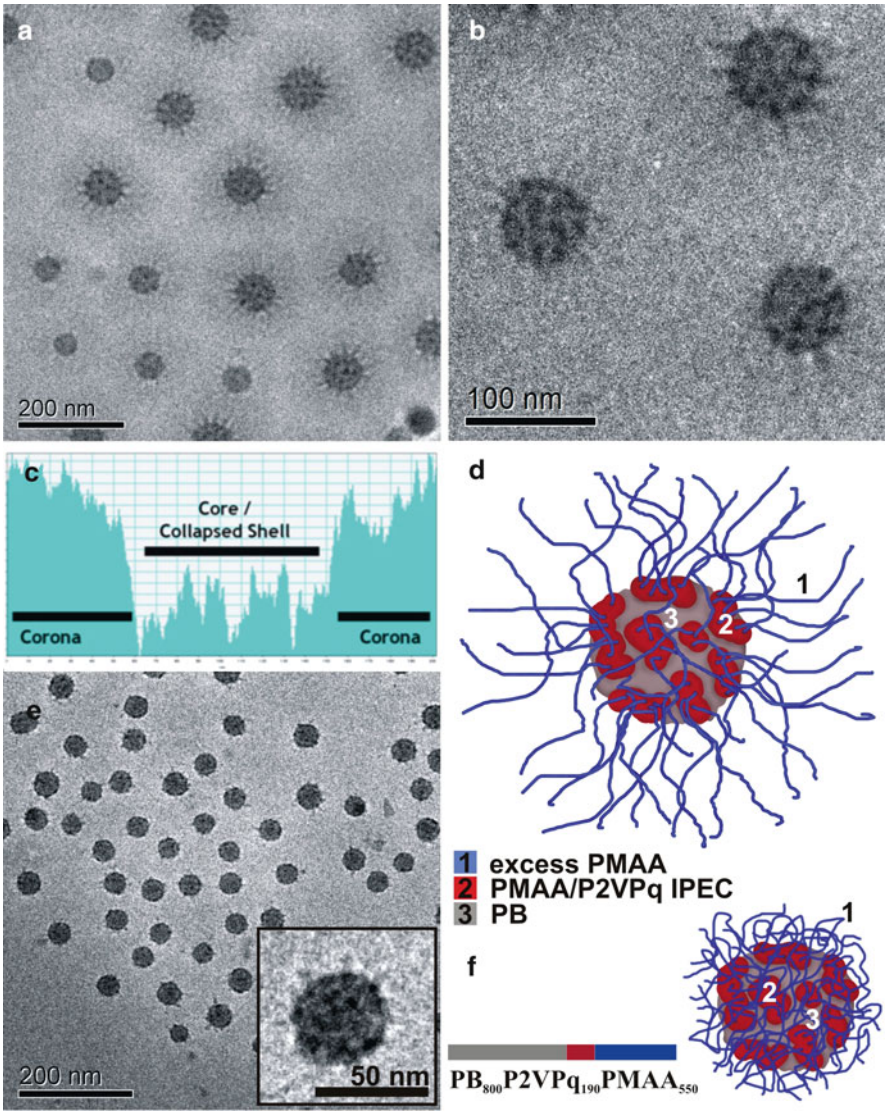

Fig. 17 (**a, b**) Cryo-TEM micrographs of PB-*b*-P2VPQ-*b*-PMAA micelles (the PMAA block is longer than the P2VPQ block) in aqueous solution at pH 10. (**c**) Gray scale analysis of a micellar cross-section for the PB-*b*-P2VPQ-*b*-PMAA micelles at pH 10. (**d**) Proposed structure of the PB-*b*-P2VPQ-*b*-PMAA micelles at high pH. (**e**) Cryo-TEM micrograph of the PB-*b*-P2VPQ-*b*-PMAA micelles (the PMAA block is longer than the P2VPQ block) in aqueous solution at pH 4; *inset* shows an enlargement of a single micelle. (**f**) Proposed solution structure of the PB-*b*-P2VPQ-*b*-PMAA micelles at low pH. Reprinted from [74] with permission from the American Chemical Society

dissociation of the intramicellar IPECs. In that way, both PE compartments of the PB-*b*-P2VPQ-*b*-PMAA block terpolymers are uncomplexed, resulting in a higher hydrophilicity and the formation of classical core–shell–corona micelles.

As recently shown by Schacher et al. [75], the preformed, negatively charged, PB-*b*-P2VPQ-*b*-PMAA micelles with PMAA corona (where the PMAA block is longer than the P2VPQ block) in alkaline media can further interact with positively charged, double hydrophilic ionic/nonionic diblock copolymers, namely a quaternized poly(2-vinylpyridine)-*block*-poly(ethylene oxide) (P2VPQ-*b*-PEO). The occurring complexation reaction generates a "second" shell that consists of oppositely charged fragments from both polymeric building blocks (the excess PMA^- of PB-*b*-P2VPQ-*b*-PMAA and the $P2VPQ^+$ blocks of P2VPQ-*b*-PEO) and that buries the "first" original patchy shell. The obtained core–first shell/second shell–corona complex macromolecular species are thought to be stabilized by the PEO blocks, or by both the PEO blocks and the remaining excess PMAA if a charge balance is not reached. The schematic representation of the proposed structure of the multicompartment micellar IPEC formed at $Z = [N^+]/[COO^-] = 1$ is given in Fig. 18.

Such micellar IPECs were also shown to exhibit an interesting slow structural rearrangement within about 10 days, changing from the initially star-shaped objects with patchy shells and ray-like protrusions (Fig. 19) to a final (presumably equilibrium) core–first shell/second shell–corona structure with thick, fuzzy, continuous shells (Fig. 20), as revealed by cryo-TEM and scanning (atomic) force microscopy (SFM). It is remarkable that the sizes of the PB cores of the original PB-*b*-P2VPQ-*b*-PMAA micelles and the final multicompartment micellar IPEC appear to coincide, thereby suggesting that no changes in the aggregation number occur during their interactions with the P2VPQ-*b*-PEO chains.

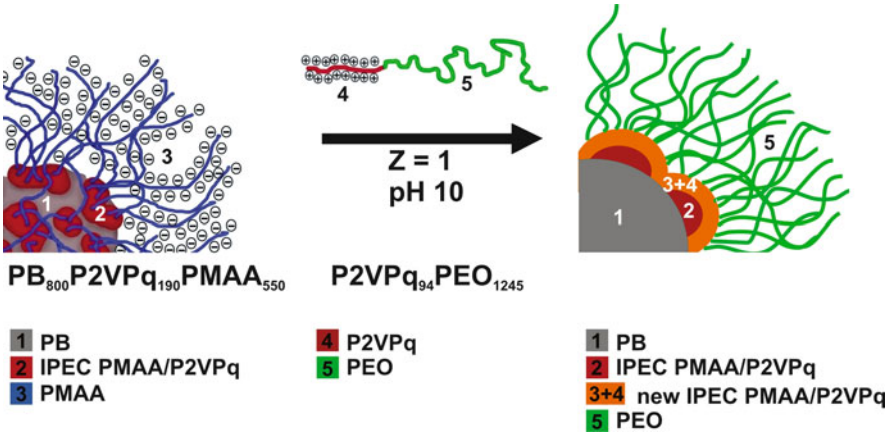

Fig. 18 Multicompartment micellar IPEC formed by the interaction between negatively charged PB-*b*-P2VPQ-*b*-PMAA micelles and P2VPQ-*b*-PEO at $Z = [N^+]/[COO^-] = 1$. Reprinted from [75] with permission from the American Chemical Society

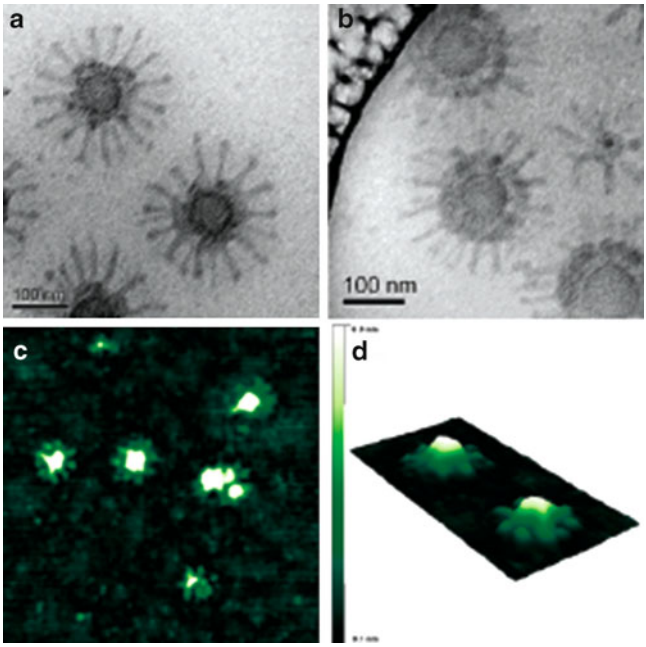

Fig. 19 (**a, b**) Cryo-TEM micrographs of the micellar IPEC formed upon interaction between negatively charged PB-*b*-P2VPQ-*b*-PMAA micelles and P2VPQ-*b*-PEO in alkaline media at $Z = [N^+]/[COO^-] = 1$ after a mixing time of 1 h at different locations of the same sample. (**c, d**) SFM height images of the same micellar IPEC deposited onto a carbon-coated TEM grid. Reprinted from [75] with permission from the American Chemical Society

Another example of multicompartment micellar IPECs is the macromolecular co-assembly of the triblock terpolymer poly(*N*,*N*-dimethylacrylamide)-*block*-poly(*N*-acryloylalanine)-*block*-poly(*N*-isopropylacrylamide) or the diblock terpolymer poly(*N*,*N*-dimethylacrylamide)-*block*-poly(*N*-isopropylacrylamide)-stat-(*N*-acryloylvaline), interacting in aqueous media with poly(ar-vinylbenzyl) trimethylammonium chloride (PVBTAC) [76, 77]. The authors demonstrated that interpolyelectrolyte complexation of such assemblies formed with PVBTAC within specific pH and temperature ranges makes them stable with respect to the disassembly induced by cooling below critical micellization temperatures.

4.3 Polyion Interchange Reactions Involving Micellar IPECs

One of the very characteristic features of IPECs is their ability to participate in so-called polyion interchange (exchange and substitution) reactions, previously investigated for aqueous mixtures of oppositely charged linear PEs by Kabanov

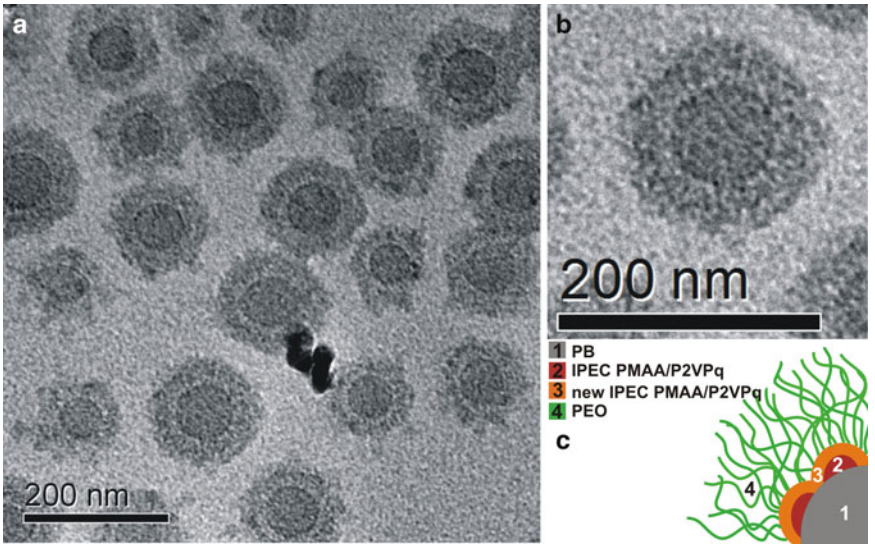

Fig. 20 (**a**) Cryo-TEM micrographs of the micellar IPEC formed by the interaction between negatively charged PB-*b*-P2VPQ-*b*-PMAA micelles and P2VPQ-*b*-PEO in alkaline media at $Z = [N^+]/[COO^-] = 1$ after a mixing time of 10 days; (**b**) enlargement of a single micellar IPEC. (**c**) Proposed structure of the macromolecular co-assembly. Reprinted from [75] with permission from the American Chemical Society

and Zezin and their coworkers [95]. As revealed by Chelushkin et al. [78], the aggregation state of the polymeric component(s) involved in such reactions has a significant effect on the reaction rates.

In particular, by means of fluorescence measurements with the use of 4′-(aminomethyl) fluorescein-labeled PMANa and PS-*b*-PMANa (PMA*Na and PS-*b*-PMA*Na, respectively) they studied the following polyion interchange reactions:

$$\mathrm{IPEC(PMA^-/P4VPQ^+) + PMA^*Na \rightarrow PMANa + IPEC(PMA^{*-}/P4VPQ^+)} \tag{1a}$$

$$\mathrm{IPEC(PMA^{*-}/P4VPQ^+) + PMANa \rightarrow PMA^*Na + IPEC(PMA^-/P4VPQ^+)} \tag{1b}$$

$$\mathrm{IPEC(PS-\mathit{b}-PMA^-/P4VPQ^+) + PMA^*Na \rightarrow PS-\mathit{b}-PMANa + IPEC(PMA^{*-}/P4VPQ^+)} \tag{2a}$$

$$\mathrm{IPEC(PS-\mathit{b}-PMA^{*-}/P4VPQ^+) + PMANa \rightarrow PS-\mathit{b}-PMA^*Na + IPEC(PMA^-/P4VPQ^+)} \tag{2b}$$

$$\mathrm{IPEC(PS-}b\mathrm{-PMA^{-}/P4VPQ^{+}) + PS-}b\mathrm{-PMA^{*}Na \rightarrow PS-}b\mathrm{-PMANa} + \mathrm{IPEC(PS-}b\mathrm{-PMA^{*-}/P4VPQ^{+})} \quad (3a)$$

$$\mathrm{IPEC(PS-}b\mathrm{-PMA^{*-}/P4VPQ^{+}) + PS-}b\mathrm{-PMANa \rightarrow PS-}b\mathrm{-PMA^{*}Na} + \mathrm{IPEC(PS-}b\mathrm{-PMA^{-}/P4VPQ^{+})} \quad (3b)$$

where PMANa, PMA*Na, PS-*b*-PMANa, and PS-*b*-PMA*Na play the role of HPEs. These polyion interchange reactions result in the migration of $P4VPQ^{+}$ chains between PMANa coils (1a, 1b), between PS-*b*-PMANa micelles and PMANa coils (2a, 2b), and between PS-*b*-PMANa micelles (3a, 3b).

It was demonstrated that all these reactions have the same basic features as revealed earlier for the mixtures of oppositely charged linear PEs [95], regardless of the aggregation state of the excess polymeric component. The reaction rates increase with the decreasing degree of polymerization of P4VPQ, as well as with the increasing ionic strength of the solution. At the same time, if at least one of the excess polymeric components participating in such reactions exists in such mixtures in the aggregated (i.e., self-assembled into micelles) state, they become considerably slower. Specifically, the rates of the polyion interchange reaction decrease in the following order: coil/coil (seconds) > coil/micelle (tens of seconds) > micelle/micelle (thousands of seconds).

The authors explained the observed differences in the rates of such polyion interchange reactions in terms of the "collision" model [95]. This model considers the transfer of the GPE from the original to the added HPE to proceed via a short-living intermediate ternary complex. Such a ternary complex is formed due to the diffusion-controlled approach and interpenetration of the HPE species occupied by chains of GPE and of free HPE species. Because the electrostatic and steric repulsions upon the approach and interpenetration of the reacting species for the coil/micelle combination (2a, 2b) and, especially, for the micelle/micelle combination (3a, 3b) are obviously much stronger than for the coil/coil combination (1a, 1b), the rates of the polyion interchange reactions show a pronounced decrease in the abovementioned order.

A similar trend was also found for the following polyion coupling reactions (4–6) [78]:

$$\mathrm{PMA^{*}Na + P4VPQ \rightarrow IPEC(PMA^{*-}/P4VPQ^{+})} \quad (4)$$

$$\mathrm{PS-}b\mathrm{-PMA^{*}Na + P4VPQ \rightarrow IPEC(PS-}b\mathrm{-PMA^{*-}/P4VPQ^{+})} \quad (5)$$

$$\mathrm{PS-}b\mathrm{-P4VPQ + PMA^{*}Na \rightarrow IPEC(PS-}b\mathrm{-P4VPQ^{+}/PMA^{*-}})} \quad (6)$$

where either PMA*Na or PS-*b*-PMA*Na were taken as HPEs, i.e., reactions (5, 6) involving one of the polymeric components in the aggregated (micellar) state were much slower than similar reactions involving the polymeric coils (4). The polyion coupling reaction is considered to involve two stages: first, a fast coupling of oppositely charged polymeric components that results in nonequilibrium macromolecular co-assemblies; and second, a slower stage leading to equilibrium macromolecular

co-assemblies via polyion interchange reactions [95]. Thus, the observed trend can be reasonably explained, as for the polyion interchange reactions discussed above.

5 Conclusions

The results of experimental and theoretical research on water-soluble (nonstoichiometric) IPECs based on nonlinear (branched) polyionic species (HPE) complexed with oppositely charged linear PEs (GPE) demonstrated that the main feature of such macromolecular co-assemblies is their pronounced compartmentalized structure, which results from a distinctly nonuniform distribution of the linear GPE chains within the intramolecular volume of the branched HPE. In the case of star-shaped PEs or star-like micelles of ionic amphiphilic block copolymers, this compartmentalization leads to the formation of water-soluble IPECs with core–corona (complex coacervate core) or core–shell–corona (complex coacervate shell) structures, respectively. Water-soluble IPECs based on cylindrical PE brushes appear to exhibit longitudinally undulating structures (necklace) of complex coacervate pearls decorated by the cylindrical PE corona.

An important inherent feature of IPECs comprising branched HPEs is the intramolecular segregation of its branches: a certain fraction of the branches whose charge is compensated by chains of the linear GPE is nearly completely embedded into the complex coacervate domains, whereas other branches that are virtually free of linear GPE chains form the hydrated corona.

Finally, the enormous number of possible combinations of oppositely charged polymeric components that can be involved in interpolyelectrolyte complexation offers attractive perspectives for the preparation of water-soluble multicompartment nanosized macromolecular co-assemblies with desired properties. We believe that such novel IPECs are very promising and will be in demand for their future applications in nanomedicine (e.g., gene and drug delivery, and diagnostic systems), biotechnology, and nanotechnology as nanocontainers, nanoreactors, and molecular templates for nanoelectronic devices.

Acknowledgments Support from the EU Marie Curie Research and Training Network "Self-Organized Nanostructures of Amphiphilic Copolymers" (POLYAMPHI) (project MCRTN-CT-2003-505027), the Deutsche Forschungsgemeinschaft, and the Russian Foundation for Basic Research (projects nos. 03-03-32511-a, 06-03-32696-a, 08-03-00336-a, 09-03-00851-a) is gratefully acknowledged. Dr. F. Schacher (Friedrich-Schiller-Universität Jena, Germany) and Dr. S.V. Larin (Institute of Macromolecular Compounds, Russian Academy of Sciences, St. Petersburg, Russia) are gratefully acknowledged for their help with preparation of the figures.

References

1. Smid J, Fish D (1988) In: Mark, HF; Kroschwitz, JI (eds) Encyclopedia of polymer science and engineering, vol 11. Wiley, New York, p 720
2. Kabanov VA, Zezin AB, Kasaikin VA, Yaroslavov AA, Topchiev DA (1991) Usp Khim 60:595
3. Zezin AB, Eltsefon BS, Rudman AR, Vengerova NA, Kalyuzhnaya RI, Valueva SP, Kopylova EM, Chepurov AK, Efimov VS, Kabanov VA (1987) Khim-Farm Zh 21:788
4. Valueva SP, Efimov VS, Rozkin MY, Gulyaeva ZG, Zezin AB, Kopylova EM, Eltsefon BS, Lopukhin YM (1981) Khim-Farm Zh 15:88
5. Kalyuzhnaya RI, Rudman AR, Vengerova NA, Razvodovskii EF, Eltsefon BS, Zezin AB (1975) Vysokomol Soed Ser A 17:2786
6. Kalyuzhnaya RI, Volynskii AL, Rudman AR, Vengerova NA, Razvodovskii EF, Eltsefon BS, Zezin AB (1976) Vysokomol Soed Ser A 18:71
7. Rudman AR, Vengerova NA, Kalyuzhnaya RI, Eltsefon BS, Zezin AB (1979) Khim-Farm Zh 13:82
8. Bromberg LE (1991) J Memb Sci 62:117
9. Bromberg LE (1991) J Memb Sci 62:131
10. Bromberg LE (1991) J Memb Sci 62:145
11. Bromberg LE (1991) J Memb Sci 62:155
12. Zezin AB, Izumrudov VA, Kabanov VA (1989) Makromol Chem Macromol Symp 26:249
13. Kabanov AV, Kabanov VA (1995) Bioconjug Chem 6:7
14. Kabanov AV, Kabanov VA (1998) Adv Drug Delivery Rev 30:49
15. Oana H, Kishimura A, Yonehara K, Yamasaki Y, Sashizu M, Kataoka K (2009) Angew Chem Int Ed 48:4613
16. Anraku Y, Kishimura A, Oba M, Yamasaki Y, Kataoka K (2010) J Am Chem Soc 132:1631
17. Zezin AB, Kabanov NM, Kokorin AI, Rogacheva VB (1977) Vysokomol Soed Ser A 19:118
18. Kabanov NM, Kokorin AI, Rogacheva VB, Zezin AB (1979) Vysokomol Soed Ser A 21:209
19. Kabanov NM, Kozhevnikova NA, Kokorin AI, Rogacheva VB, Zezin AB, Kabanov VA (1979) Vysokomol Soed Ser A 21:1891
20. Kabanov NM, Khvan AM, Rogacheva VB, Zezin AB, Kabanov VA (1979) Vysokomol Soed Ser B 21:535
21. Zezin AA, Feldman VI, Shmakova NA, Valueva SP, Ivanchenko VK, Nikanorova NI (2007) Nucl Instrum Methods Phys Res B 265:334
22. Zezin AA, Feldman VI, Dudnikov AV, Zezin SB, Abramchuk SS, Belopushkin SI (2009) High Energy Chem 43:100
23. Decher G (1997) Science 277:1232
24. Decher G, Eckle M, Schmitt J, Struth B (1998) Curr Opin Colloid Interface Sci 3:32
25. Shi XY, Schen MW, Möhwald H (2004) Prog Polym Sci 29:987
26. Johnston APR, Cortez C, Angelatos AS, Caruso F (2006) Curr Opin Colloid Interface Sci 11:203
27. Tang ZY, Wang Y, Podsiadlo P, Kotov NA (2006) Adv Mater 18:3203
28. Sukhorukov GB, Möhwald H (2007) Trends Biotechnol 25:93
29. De Geest BG, Sanders NN, Sukhorukov GB, Demeester J, De Smedt SC (2007) Chem Soc Rev 36:636
30. Wang Y, Angelatos AS, Caruso F (2008) Chem Mater 20:848
31. De Geest BG, De Koker S, Sukhorukov GB, Kreft O, Parak WJ, Skirtach AG, Demeester J, De Smedt SC, Hennink WE (2009) Soft Matter 5:282
32. De Gesest BG, Sukhorukov GB, Möhwald H (2009) Expert Opin Drug Deliv 6:613
33. Kabanov VA, Zezin AB (1984) Pure Appl Chem 56:343
34. Philipp B, Dautzenberg H, Linow K-J, Koetz J, Dawydoff W (1989) Prog Polym Sci 14:91
35. Kabanov VA (1994) In: Dubin P, Bock J, Davis R, Schulz DN, Thies C (eds) Macromolecular complexes in chemistry and biology. Springer, Berlin, p 151
36. Thünemann B, Müller M, Dautzenberg H, Joanny JF, Löwen H (2004) Adv Polym Sci 166:113

37. Kabanov VA, Zezin AB, Rogacheva VB, Litmanovich EA (1986) Doklady Akadem Nauk SSSR 288:1408
38. Kabanov VA, Zezin AB, Rogacheva VB, Prevysh VA (1988) Doklady Akadem Nauk SSSR 303:399
39. Rogacheva VB, Prevysh VA, Zezin AB, Kabanov VA (1988) Vysokomol Soed Ser A 30:2120
40. Kabanov VA, Zezin AB, Rogacheva VB, Prevysh VA (1989) Makromolek Chem Macromol Chem Phys 190:2211
41. Kabanov VA, Zezin AB, Rogacheva VB, Prevysh VA, Chupyatov AM (1990) Vysokomol Soed Ser B 32:83
42. Chupyatov AM, Rogacheva VB, Zezin AB, Kabanov VA (1994) Vysokomol Soed Ser B 36:212
43. Zezin AB, Rogacheva VB, Kabanov VA (1994) J Intell Mater Syst Struct 5:144
44. Zezin AB, Rogacheva VB, Kabanov VA (1998) Macromol Symp 126:123
45. Sergeev VG, Novoskol'tseva OA, Zinchenko AA, Pyshkina OA, Rogacheva VB, Zezin AB, Kabanov VA (2001) Doklady Phys Chem 379:218
46. Sergeyev VG, Novoskoltseva OA, Pyshkina OA, Zinchenko AA, Rogacheva VB, Zezin AB, Yoshikawa K, Kabanov VA (2002) J Am Chem Soc 124:11324
47. Panova TM, Bykova EV, Rogacheva VB, Joosten J, Brackman J, Zezin AB, Kabanov VA (2004) Polym Sci Ser A 46:471
48. Kabanov VA, Zezin AB, Rogacheva VB, Panova TV, Bykova EV, Joosten JGH, Brackman J (2005) Faraday Discuss 128:341
49. Panova TM, Rogacheva VB, Zezin SB, Joosten J, Brackman J, Zezin AB, Kabanov VA (2006) Polym Sci Ser A 48:124
50. Zansokhova MF, Rogacheva VB, Gulyaeva ZG, Zezin AB, Joosten J, Brackman J (2008) Polym Sci Ser A 50:656
51. Rogacheva VB, Panova TV, Bykova EV, Zezin AB, Joosten J, Brackman J (2009) Polym Sci Ser A 51:242
52. Li Y, Dubin PL, Spindler R, Tomalia DA (1995) Macromolecules 28:8426
53. Zhang H, Dubin PL, Ray J, Manning GS, Moorefield CN, Newkome GR (1999) J Phys Chem B 103:2347
54. Miura N, Dubin PL, Moorefield CN, Newkome GR (1999) Langmuir 15:4245
55. Kabanov VA, Zezin AB, Rogacheva VB, Gulyaeva ZG, Zansochova MF, Joosten JGH, Brackman J (1999) Macromolecules 32:1904
56. Kabanov VA, Sergeyev VG, Pyshkina OA, Zinchenko AA, Zezin AB, Joosten JGH, Brackman J, Yoshikawa K (2000) Macromolecules 33:9587
57. Stapert HR, Nishiyama N, Jiang D-L, Aida T, Kataoka K (2000) Langmuir 16:8182
58. Kabanov VA (2001) Macromol Symp 175:265
59. Zhang G-D, Nishiyama N, Harada A, Jiang D-L, Aida T, Kataoka K (2003) Macromolecules 36:1304
60. Zhang G-D, Harada A, Nishiyama N, Jiang D-L, Koyama H, Aida T, Kataoka K (2003) J Control Release 93:141
61. Leisner D, Imae T (2003) J Phys Chem B 107:8078
62. Leisner D, Imae T (2003) J Phys Chem B 107:13158
63. Leisner D, Imae T (2004) J Phys Chem B 108:1798
64. Störkle D, Duschner S, Heimann N, Maskos M, Schmidt M (2007) Macromolecules 40:7998
65. Talingting MR, Voigt U, Munk P, Webber SE (2000) Macromolecules 33:9612
66. Pergushov DV, Remizova EV, Feldthusen J, Zezin AB, Müller AHE, Kabanov VA (2003) J Phys Chem B 107:8093
67. Pergushov DV, Remizova EV, Gradzielski M, Lindner P, Feldthusen J, Zezin AB, Müller AHE, Kabanov VA (2004) Polymer 45:367
68. Pergushov DV, Gradzielski M, Remizova EV, Burkhardt M, Zezin AB, Kabanov VA, Müller AHE (2004) Polym Prepr 45(2):236
69. Burkhardt M, Ruppel M, Tea S, Drechsler M, Schweins R, Pergushov DV, Gradzielski M, Zezin AB, Müller AHE (2008) Langmuir 24:1769

70. Lysenko EA, Chelushkin PS, Bronich TK, Eisenberg A, Kabanov VA, Kabanov AV (2004) Polym Prepr 45(2):244
71. Chelushkin PS, Lysenko EA, Bronich TK, Eisenberg A, Kabanov AV, Kabanov VA (2004) Doklady Phys Chem 395:72
72. Lysenko EA, Chelushkin PS, Bronich TK, Eisenberg A, Kabanov VA, Kabanov AV (2004) J Phys Chem B 108:12352
73. Chelushkin PS, Lysenko EA, Bronich TK, Eisenberg A, Kabanov VA, Kabanov AV (2007) J Phys Chem B 111:8419
74. Schacher F, Walther A, Müller AHE (2009) Langmuir 25:10962
75. Schacher F, Betthausen E, Walther A, Schmalz H, Pergushov DV, Müller AHE (2009) ASC Nano 3:2095
76. Lokitz BS, Convertine AJ, Ezell RG, Heidenreich A, Li Y, McCormick CL (2006) Macromolecles 39:8594
77. Lokitz BS, York AW, Stempka JE, Treat ND, Li Y, Jarrett WL, McCormick CL (2007) Macromolecles 40:6473
78. Chelushkin PS, Lysenko EA, Bronich TK, Eisenberg A, Kabanov VA, Kabanov AV (2008) J Phys Chem B 112:7732
79. Pergushov DV, Babin IA, Plamper FA, Zezin AB, Müller AHE (2008) Langmuir 24:6414
80. Pergushov DV, Babin IA, Plamper FA, Schmalz H, Müller AHE, Zezin AB (2009) Doklady Phys Chem 425:57
81. Ge Zh, Xu J, Wu D, Narain R, Liu S (2008) Macromol Chem Phys (2008) 209:754
82. Ishizu K, Toyoda K, Furukawa T, Sogabe A (2004) Macromolecules 37:3954
83. Ishizu K (2005) Polym Degrad Stabil 90:386
84. Larin SV, Pergushov DV, Xu Y, Darinskii AA, Zezin AB, Müller AHE, Borisov OV (2009) Soft Matter 5:4938
85. Xu Y, Borisov OV, Ballauff M, Müller AHE (2010) Langmuir 26:6919
86. Zhang H, Rühe J (2003) Macromol Rapid Commun 24:576
87. Zhang H, Rühe J (2003) Macromolecules 36:6593
88. Zhang H, Rühe J (2005) Macromolecules 38:10743
89. Larin SV, Darinskii AA, Zhulina EB, Borisov OV (2009) Langmuir 25:1915
90. Borisov OV, Zhulina EB (2005) Macromolecules 38:2506
91. Polotsky AA, Charlaganov MI, Xu Y, Leermakers FAM, Daoud M, Müller AHE, Dotera T, Borisov OV (2008) Macromolecules 41:402
92. Košovan P, Kuldová J, Limpouchova Z, Procházka K, Zhulina EB, Borisov OV (2009) Macromolecules 42:6748
93. Borisov OV, Zhulina EB, Leermakers FAM, Ballauff M, Müller AHE (2010) Adv Polym Sci doi: 10.1007/12_2010_104
94. Burkhardt M, Martinez-Castro N, Tea S, Drechsler M, Babin IA, Grishagin IV, Schweins R, Pergushov DV, Gradzielski M, Zezin AB, Müller AHE (2007) Langmuir 23:12864
95. Bakeev KN, Izumrudov VA, Kuchanov SI, Zezin AB, Kabanov VA (1992) Macromolecules 25:4249

Adv Polym Sci (2011) 241: 163–185
DOI:10.1007/12_2010_100

Published online: 11 November 2010

Co-assembly Towards Janus Micelles

Ilja K. Voets, Frans A. Leermakers, Arie de Keizer, Marat Charlaganov, and Martien A. Cohen Stuart

Abstract In this paper, we report on our recent findings concerning the structure of complex coacervate core micelles composed of two types of (complementary) block copolymers. Both copolymers have a polyelectrolyte (one cationic and the other anionic) block combined with a neutral one. The opposite charges attract and form a close-to-electroneutral core. The two neutral blocks form the corona of the micelles. Here, we focus on the structure of the corona, which among other possibilities assumes the Janus configuration. Corresponding self-consistent field calculations confirm the rich behaviour of these systems. Unless the solvent quality of one of the corona chains is poor, we do not expect an onion-like corona with a clear interface between the layers. Disparities in chain length and solvent quality may only lead to gradual differences (local enrichments) in radial distributions. In the case that both corona chains are in good solvent, an unfavourable mixing of the two chains leads to the formation of Janus micelles, where the two blocks occupy different hemispheres. The interface that separates the two regions exerts a force on the core, which will deform when the core surface tension is not too high. In line with experimental results, the core flattens like a disk and the corona chains extend most in the direction of the poles.

I.K. Voets (✉)
Laboratory of Physical Chemistry and Colloid Science, Wageningen University,
Dreijenplein 6, 6703 HB Wageningen, The Netherlands
and
Adolphe Merkle Institute, University of Fribourg, Route de l'ancienne Papeterie,
1723 Marly 1, Switzerland
e-mail: ilja.voets@unifr.ch

F.A. Leermakers, A. de Keizer, M. Charlaganov, and Martien A. Cohen Stuart
Laboratory of Physical Chemistry and Colloid Science, Wageningen University,
Dreijenplein 6, 6703 HB Wageningen, The Netherlands
e-mail: frans.leermakers@wur.nl; arie.dekeizer@wur.nl; martien.cohenstuart@wur.nl

M. Charlaganov
Soft Matter Chemistry, Faculty of Science, Leiden Institute of Chemistry, University of Leiden,
Gorlaeus Laboratories, Einsteinweg 55, 2333 CC Leiden
e-mail: charlaganovm@umail.leidenuniv.nl

Keywords Coacervate · Co-assembly · Janus · Micelle · Polyelectrolyte · Polymer · Scattering · Segregation · Self-assembly · Self-consistent field calculations

Contents

1 Introduction

Self-assembly of identical molecules, such as amphiphilic surfactants or polymers, into micelles or vesicles has long been a topic of great interest. Although the vast majority of amphiphilic molecules give rise to spherical micelles consisting of two distinguishable domains (i.e. a core consisting of solvophobic units and a shell consisting of solvophilic units), other morphologies may also be encountered. For example, if the chain length of the solvophobic part of the molecules is increased relative to the chain length of the solvophilic part, the micellar morphology may exhibit a transition from sphere to cylinder to vesicle [1–4]. The introduction of exotic units (such as sugars, amino acids, crystalline monomers, halogens), topology (graft, dendritic, random copolymers instead of block copolymers, miktoarm stars), or multiple solvophilic and solvophobic units, such as in terpolymers, may likewise induce a deviation from the classical spherical core–shell type micelle [5–11].

Alternatively, the level of structural complexity may be affected in a totally different manner: employing co-assembly of chemically unlike molecules instead of self-assembly of chemically identical molecules [12–20]. We refer to the resultant micelles as mixed micelles or co-micelles to indicate that this type of micelle consists of more than one type of molecule, whereas classical micelles consist of identical molecules (polydispersity effects not taken into account). Consider two chemically distinguishable amphiphilic molecules A–B and C–D. Self-assembly into A/C or B/D micelles consisting of a core–shell structure, with a core solely consisting of A or C units and a shell solely consisting of B or D units, will only occur if the A or C units are solvophobic and the B or D units are solvophilic. However, if all units (A and B, or C and D) are solvophobic, phase separation will occur on a macroscopic level and result in a macroscopically inhomogeneous two-phase system. Conversely, if all units (A and B, or C and D) are solvophilic, phase separation

will not occur at all. Hence, only the combination of hydrophobic and hydrophilic units within one molecule will lead to an assembly process. By contrast, co-assembly may occur in solutions containing (1) solvophilic–solvophobic molecules [12, 19, 21–25], (2) solvophilic–solvophilic molecules [15–17, 20, 26–30] and (3) a mixture of solvophilic–solvophobic and solvophilic–solvophilic molecules [25]. Note that we limit our discussion here to mixtures of diblock copolymers, i.e. we do not include combinations of block copolymers and homopolymers, terpolymers and homopolymers, etc. (see for example [31–37]). It is clear that the number of possible arrangements of four different units (A, B, C and D) into one aggregate is larger than that of two different units (either A and B, or C and D). Thus, mixed micelles can be employed as a route towards more complicated micellar architectures.

Let us elaborate on this line of thought with a model system consisting of two block copolymers A–B and C–D. The monomers A and C are oppositely charged in all cases, while the neutral monomers B and D are (I) both hydrophobic, (II) both hydrophilic, or (III) hydrophobic (B) and hydrophilic (D). In aqueous solutions of oppositely charged ionic–hydrophobic block copolymers (system I), co-precipitation of B and D monomers may give rise to a core consisting of B and D units, while A and C reside in the shell. In system II, electrostatic interaction between fully water-soluble A and C units will induce an associative phase separation, while the water-soluble C and D units restrict this phase separation to the microscopic domain, i.e. resulting in the formation of mixed A–B/C–D micelles. Intuitively, one may anticipate that in both of these systems, dependent on the miscibility of A and C (and likewise, B and D) monomers, the mixed micelles may exhibit a certain segregation into multiple domains, via segregation of the core and/or shell into several domains. Alternatively, a vesicular structure with the A and C monomers residing on either side of the mixed B/D membrane may be envisioned. In system III, the micelles are likely to exhibit a three-layered structure, with a core consisting of hydrophobic B units, surrounded by a mixed A/C shell, which in turn is encapsulated in a hydrophilic D corona. This type of micelle is generally referred to as an onion-like micelle or core–shell-corona micelle [22–24, 38, 39]. In the above discussion, we have considered electrostatically driven co-micellisation of diblock copolymers. The resultant mixed micelles are generally termed complex coacervate core micelles, C3Ms [15, 32, 40, 41], polyion complex (PIC) micelles [26, 42], block ionomer complex (BIC) micelles [34] and interpolyelectrolyte complexes [37]. Other types of non-covalent interactions that may likewise be employed as a driving force are π–π stacking, donor–acceptor interactions, metal–ligand coordination and hydrogen bonding [12, 25, 27, 28, 39, 43, 44].

In this contribution, we describe our recent experimental and theoretical findings on complex coacervate core micelles. We have investigated the co-assembly of several types of oppositely charged ionic–hydrophilic block copolymers into mixed micelles. In particular, we have focused on chain mixing/segregation in the micellar corona as a function of monomer type and (the ratio between the) chain length of the polymer blocks in the corona. Our aim has been to employ co-assembly in such systems as a route towards formation of reversible Janus micelles. These are micelles with a corona that exhibits two distinguishable sides (hemispheres in the case

of spherical Janus micelles), referring to the two-faced Roman deity Janus. Another important keyword is the term "reversible", indicating that we are interested in micelles that can associate and dissociate upon a change in environmental parameters, such as ionic strength, pH, and/or block copolymer mixing fraction.

2 Characteristic Features of Complex Coacervate Core Micelles

Since the pioneering work of Harada and Kataoka in 1995 [26], many characteristic features of complex coacervate core micelles (C3Ms) have been described in the literature. One of the most fundamental is their tendency towards local charge compensation, i.e. the number of cationic and anionic segments within the micellar core is approximately equal. This is a consequence of the driving force for micellisation: Coulombic attraction and entropy gain occur through release of many small, monovalent counterions as they are replaced by a large counterion (the oppositely charged copolymer). Hence, C3Ms are typically formed under charge stoichiometric conditions. Mathematically, these can be captured in the formula:

$$f_+ \alpha_+ = f_- \alpha_- \tag{1}$$

where f_+ is the mixing fraction and α the degree of dissociation. Here, the mixing fraction is defined as the number of positively chargeable monomers divided by the total number of chargeable monomers, so that $f_+ = 1 - f_-$. From (1), it follows that the association and dissociation of micelles is affected by both the mixing fraction [41] and the degree of dissociation of the chargeable monomers. In the case of weak polyelectrolytes, this translates into a dependence on the pH [34, 45–47]. Additionally, the ionic strength is an important parameter. The driving force for micellisation decreases with increasing ionic strength, as electrostatic interactions become increasingly screened. Experimentally, one can determine a (concentration-dependent) critical ionic strength, I_c, above which micelles can no longer be observed [20, 29, 33, 37].

Because C3Ms are intrinsically responsive to several parameters, such as mixing fraction, ionic strength and pH (in the case of weak polyelectrolytes) [17, 20, 29, 32–34, 37, 40, 41, 48], they may be termed stimuli-responsive. Additionally, it has been shown that C3Ms can be rendered temperature-responsive via the introduction of temperature-sensitive polymer blocks, such as poly(2-isopropyl-2-oxazoline), PiPrOx [30] or poly(isopropyl acrylamide), PNIPAAm [17]. Intuitively, one anticipates a relatively low micellar stability as the (usually) undesirable counterpart of a responsive nature. Indeed, block copolymer C3Ms exhibit several hallmarks of a relatively weak driving force: rather high critical micellisation concentrations, size polydispersities and solvent fractions, as well as rather low aggregation numbers, as compared to micelles consisting of amphiphilic block copolymers [20]. Considerable effort has thus been devoted (rather successfully) to increasing the stability of C3Ms through incorporation of chargeable monomers that have a relatively

hydrophobic backbone (sometimes referred to as hydrophobic ionomers) [49, 50] and crosslinking of the oppositely charged monomers in the micellar core [51–54]. These studies have been particularly important for the application of C3Ms as containers for drugs and other active compounds. It goes without saying that tunability of the micellar stability (preventing premature release) and its response to environmental parameters (enabling controlled release on the target location) is ideal when tailoring the protective delivery system for a particular application. For further details, we refer to some recent reviews on several aspects of complex coacervate core micelles [40, 55–57].

3 Experimental Results

As we are interested in *reversible* Janus micelles, i.e. non-centrosymmetric nanoparticles with compartmentalised shells (Fig. 1), complex coacervate core micelles are a rather natural choice. As described in the previous section, electrostatic interaction is a rather weak driving force as compared to hydrophobic interaction. C3Ms may thus form under full thermodynamic control. Although ABC triblock copolymers in selective solvents (poor solvent for B; good solvent for both A and C) may also yield Janus micelles, they most frequently aggregate into micelles with a quenched rather than a dynamic nature, such that the aggregation number is fixed and no reversible association/dissociation is observed (on experimental time scales).

Now that we have established the requirements for the formation of reversible Janus micelles, we turn our attention to the choice of ionic–hydrophilic block copolymers. The ionic blocks have to be oppositely charged to ensure co-assembly in aqueous solutions, whereas the neutral blocks have to be water-soluble. Furthermore, the unlike water-soluble polymer blocks need to segregate, not mix within the micellar corona. Since the classical works of Flory and Huggins, extended by Scott to describe binary polymer solutions [58], it is well known that two unlike polymers

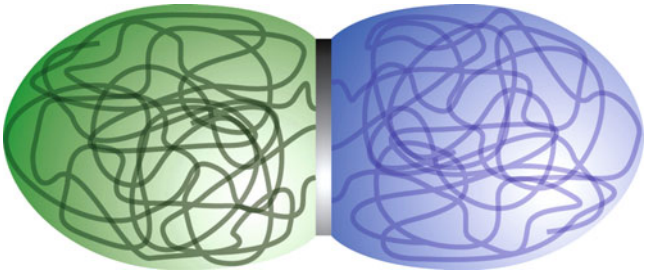

Fig. 1 Representation of a prolate ellipsoidal (cigar-like) Janus micelle with an oblate ellipsoidal (disc-like) core. The complex coacervate core is depicted in *grey*, while the corona is depicted in *blue* (ethylene oxide monomers) and *green* (acryl amide monomers)

have a tendency to demix. For sufficiently long chains and high volume fractions, φ, this will result in a macroscopic phase separation, as described by the equation:

$$\varphi\chi N \geq 2 \tag{2}$$

where χ is the Flory–Huggins interaction parameter between the segments of the two polymers, each with chain length N. Here it is understood that the equality sign is valid at the critical point and that this equation holds for a symmetric system of two homopolymers of equal length in a monomeric non-selective solvent. An extension of this formula to include nanoscale chain segregation, such as a mixing/demixing transition within a micellar corona, has yet to be developed. Hence, we have investigated a number of different sets of hydrophilic polymers, both experimentally and theoretically, in terms of their tendency towards local chain segregation.

3.1 Reversible Janus Micelles

Complex coacervate core micelles of poly(*N*-methyl-2-vinyl pyridinium iodide)-*block*-poly(ethylene oxide), P2MVP$_{42}$-*b*-PEO$_{446}$, and poly(acrylic acid)-*block*-poly(acryl amide), PAA$_{42}$-*b*-PAAm$_{417}$, were prepared by mixing aqueous solutions under charge stoichiometric conditions ($f_+ = 0.5$, pH 7.7, 1 mM $NaNO_3$). The resultant mixed micelles have a molar mass of about 500 kg mol^{-1} and both a hydrodynamic radius and radius of gyration of about 18 nm. Each micelle consists of about 16–18 diblock copolymers in total, 8–9 of each. Although the characteristics of these micelles are dependent on f_+, pH and ionic strength, they are independent of the preparation pathway, which indicates that these C3Ms may be formed in full thermodynamic equilibrium.

In the absence of PAAm, we observed a spherical morphology for C3Ms of identical composition (P2MVP, PAA, PEO) [59, 60], but depolarised dynamic light scattering (DDLS), cryogenic transmission electron microscopy (cryo-TEM), and small angle X-ray and neutron scattering (SAXS, SANS) experiments all indicated a non-spherical particle shape for C3Ms of P2MVP$_{42}$-*b*-PEO$_{446}$ and PAA$_{42}$-*b*-PAAm$_{417}$ (Figs. 2 and 3) [15, 16, 61]. To be more precise, although the DDLS experiments were consistent with a prolate ellipsoidal shape (cigar-like), all others were consistent with an oblate ellipsoidal shape (disc-like). This apparent inconsistency can be related to the part of the micelle probed: DDLS experiments are sensitive to the overall hydrodynamic volume of the particle, whereas all other experiments are sensitive only to regions of sufficient contrast between particle and solvent, i.e. beyond a certain threshold polymer fraction. Hence, DDLS experiments provide information on the overall particle shape, whereas the cryo-TEM and SAXS/SANS experiments describe the dimensions of the core of the particle (the polymer volume fraction in the micellar corona is too low to contribute significantly). We note the striking similarity between the value obtained for the long axis

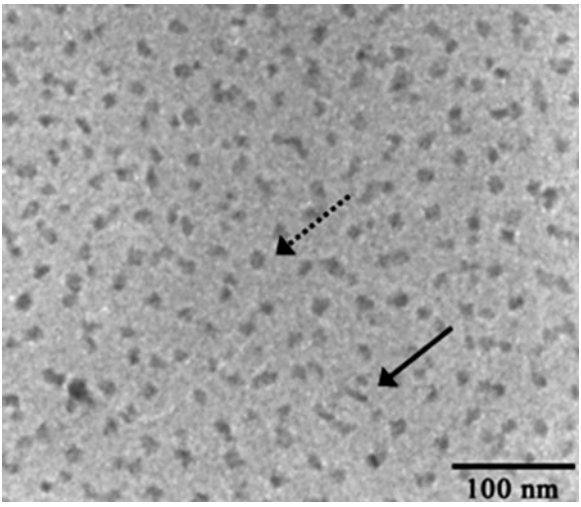

Fig. 2 Cryo-TEM images of a 1:1 mixture of PAA_{42}-*b*-$PAAm_{417}$ and $P2MVP_{42}$-*b*-PEO_{446} in H_2O (concentration $0.97\,g\,L^{-1}$, $f_+ = 0.53$). The *arrows* indicate head-on and side-on projections of the ellipsoidal 3D objects onto the 2D image

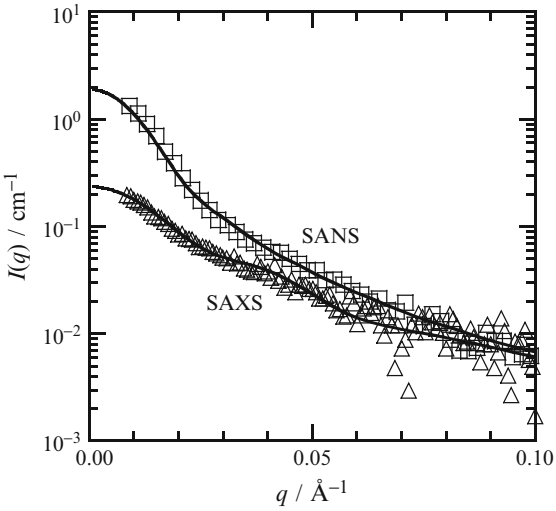

Fig. 3 Small angle neutron (*squares*) and X-ray (*triangles*) scattering curves given as $I(q)/\mathrm{cm}^{-1}$ versus $q/^{-1}$. The *symbols* correspond to the experimental data and the *solid lines* represent fits with a form factor model for monodisperse oblate ellipsoids

of the oblate ellipsoid ($\sim$20 nm) and the short axis of the prolate ellipsoid ($\sim$21 nm). If one were to rotate the oblate ellipsoid by 90° with respect to the prolate ellipsoid, and place the oblate ellipsoid in its centre, it would divide the prolate ellipsoid (and therefore the micellar shell) into two distinct domains, as schematically depicted

in Fig. 1. To the best of our knowledge, such a peculiar topology has not yet been reported for another polymeric micelle. One may anticipate that such a rare morphology is related to and even induced by the delicate balance between the two opposing forces at play in the current system: attraction between the core-forming monomers, forcing PAAm and PEO chains within the same entity, and repulsion between the corona-forming monomers PAAm and PEO, pushing them to be as far apart as possible.

Indeed, based on (2) and PAAm/PEO compatibility studies reported in the literature [62–64], we obtain a rough estimate for the Flory–Huggins interaction parameter χ of 0.05, indicating that PAAm and PEO are indeed fairly incompatible and should tend to avoid each other in the micellar corona. As an independent measurement of chain mixing within the micellar corona, we performed two-dimensional nuclear Overhauser-effect magnetic resonance spectroscopy experiments (2D ^{1}H NOESY NMR). The technique probes intermolecular through-space proximity (distances < 0.5 nm) by means of the nuclear Overhauser effect (NOE) which is extremely sensitive to the internuclear distance r (NOE $\propto r^{-6}$). The results are typically represented in a so-called contour plot with the one-dimensional ^{1}H NMR spectra on both axes and cross-peaks due to NOEs on the intersection of two straight lines at the chemical shifts of the corresponding protons. For example, the contour plot of C3Ms of poly[2-(dimethylamino)-ethyl methacrylate]-*block*-poly(glyceryl methacrylate), PDMAEMA$_{45}$-*b*-PGMA$_{90}$, and poly(acrylic acid)-*block*-poly(acryl amide), PAA$_{42}$-*b*-PAAm$_{417}$ showed off-diagonal cross-peaks between both core- and corona-forming blocks, indicating that PAA/PDMAEMA chains in the core and PGMA/PAAm chains in the corona are (randomly) mixed (Fig. 5) [65]. Conversely, no cross-peaks could be observed between PAAm and PEO protons in the contour plot of C3Ms of PAA$_{42}$-*b*-PAAm$_{417}$ and P2MVP$_{42}$-*b*-PEO$_{446}$, indicating that PAAm and PEO reside in different domains within the micellar corona (Fig. 6) [15, 16, 61]. Hence, from a combination of many different experimental techniques, we arrive at the conclusion that the reversible Janus micelles formed in aqueous solutions of PAA$_{42}$-*b*-PAAm$_{417}$ and P2MVP$_{42}$-*b*-PEO$_{446}$ can schematically be depicted as shown in Fig. 1. Furthermore, the Janus character of these C3Ms seems to be rather robust as we did not observe a transition towards a heterogeneous corona upon systematic variation of several important factors, such as the ionic strength and the PEO/PAAm mixing fraction, anticipated to decrease the tendency towards phase separation [61].

3.2 Radial Chain Segregation

Hence, we have investigated two different experimental systems and found two different coronal structures: chain mixing was observed in C3Ms of PAA$_{42}$-*b*-PAAm$_{417}$ and PDMAEMA$_{45}$-*b*-PGMA$_{90}$ (Figs. 4a and 5) [65], and lateral chain segregation was observed in C3Ms of PAA$_{42}$-*b*-PAAm$_{417}$ and P2MVP$_{42}$-*b*-PEO$_{446}$

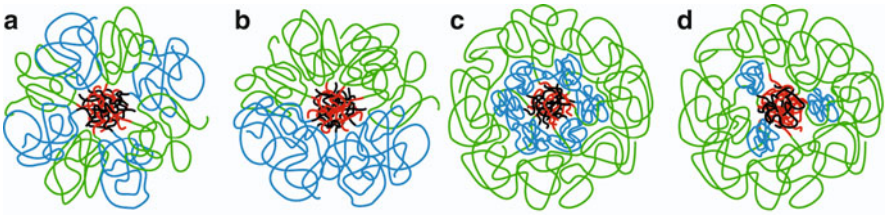

Fig. 4 Representation of the various types of internal organisation that may occur in micelles formed through co-assembly of charged block copolymers. Depicted are micelles with a corona consisting of two different neutral monomers (shown in *blue* and *green*) that are (**a**) mixed, (**b**) laterally segregated, (**c**) radially segregated, and (**d**) laterally and radially segregated. Both centrosymmetric micelles (**a, c**) and non-centrosymmetric micelles (**b, d**) are depicted. The micelle with a laterally segregated corona is generally referred to as a Janus micelle (**b**). The micelle depicted in (**c**) is most commonly known as onion-like or core–shell–corona micelle. The micelle with a laterally and radially segregated corona (**d**) is usually called a "patched" micelle. Note that in the case of (**c**) and (**d**) the *blue* and the *red/black* chains may also switch position

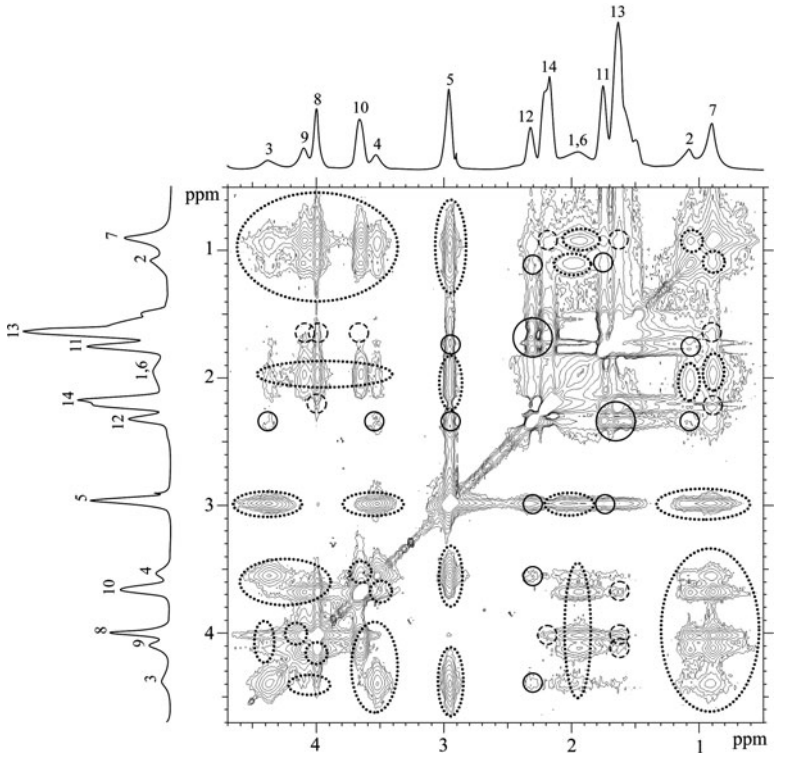

Fig. 5 2D ^{1}H NMR NOESY contour plot of a 1:1 mixture of PDMAEMA$_{45}$-*b*-PGMA$_{90}$ and PAA$_{42}$-*b*-PAAm$_{417}$ in D_2O at 1 mM $NaNO_3$ ($f_+ = 0.5$). *Circles* indicate intramolecular cross-peaks within PAA$_{42}$-*b*-PAAm$_{417}$ (*large circles, solid lines*) and PDMAEMA$_{45}$-*b*-PGMA$_{90}$ (*large circles, dotted lines*), as well as intermolecular cross-peaks between core blocks PAA$_{42}$ and PDMAEMA$_{45}$ (*small circles, solid lines*) and corona blocks PAAm$_{417}$ and PGMA$_{90}$ (*small circles, dotted lines*). Adapted from [65]

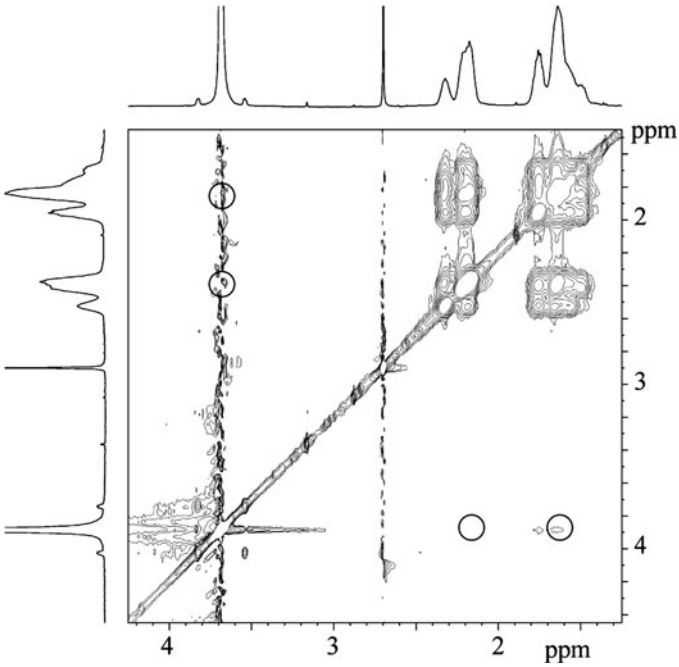

Fig. 6 2D ^{1}H NMR NOESY contour plot of a 1:1 mixture of PAA_{42}-*b*-$PAAm_{417}$ and $P2MVP_{42}$-*b*-PEO_{446} in D_2O at 1 mM $NaNO_3$ ($f_+ = 0.50$). The circles indicate where cross-peaks would appear in case of close contact between PAAm and PEO chains. Adapted from [16]

(Figs. 4b and 6) [15, 16, 61]. We then extended our experimental studies with two additional pairs of neutral polymers, to assess whether other types of chain segregation may also be observed experimentally.

Poly(*N*-methyl-2-vinyl pyridinium iodide)-*block*-poly(ethylene oxide), $P2MVP_{38}$-*b*-PEO_{211} and poly(acrylic acid)-*block*-poly(isopropyl acrylamide), PAA_{55}-*b*-$PNIPAAm_{88}$, were mixed under stoichiometric conditions ($f_+ = 0.5$, pH 7.7, 1 mM $NaNO_3$) at room temperature [17]. Spherical micelles were obtained with a hydrodynamic radius of about 14 nm and a micellar mass of roughly 380 kg mol^{-1}, i.e. each micelle contains ~16 $P2MVP_{38}$-*b*-PEO_{211} and ~11 PAA_{55}-*b*-$PNIPAAm_{88}$ copolymers. The micelles consist of a mixed PAA/P2MVP core and PEO/PNIPAAm corona, as deduced from the presence of cross-peaks between PEO and PNIPAAm protons in the NOESY contour plots (Fig. 4a). Interestingly, we are able to tune the solvency of the PNIPAAm chains with temperature: the polymer has a lower critical solution temperature (LCST) of about 32°C. Hence, at room temperature, the present experimental system corresponds to an A–B/C–D mixture with two charged monomers A and C, and two neutral hydrophilic monomers B and D (denoted system II in Sect. 1), and conversely, to an A–B/C–D mixture with two charged monomers A and C, one neutral hydrophobic monomer B, and one neutral hydrophilic monomer D (denoted system III). Hence, at elevated temperatures, i.e. above the LCST, we expect a structural rearrangement into a three-layered

core–shell–corona micelle (B–A/C–D) as discussed in Sect. 1. Indeed, based on light-scattering titration experiments, we found that the C3Ms completely and reversibly rearrange upon a temperature increase, changing the internal structure from mixed core/mixed corona (as depicted in Fig. 4a) to core/mixed shell/corona (as depicted in Fig. 4c) [17]. Hence, yet another type of nanoscale chain segregation has been obtained through co-assembly of charged copolymers: radial chain segregation.

Mixing of poly(*N*-methyl-2-vinyl pyridinium iodide)-*block*-poly(ethylene oxide), P2MVP-*b*-PEO, and poly(acrylic acid)-*block*-poly(vinyl alcohol), PAA_{305}-*b*-$PVOH_{184}$, also gives rise to the formation of complex coacervate micelles under charge neutral conditions (pH 8, 1 mM $NaNO_3$, $f_+ = 0.4$) [66]. Note that the large asymmetry between the PAA and P2MVP block lengths ($N_{PAA} = 305$; $N_{P2MVP} = 38$, 42 and 71) results in a corona that contains $\leq$15% vinyl alcohol monomers. Spherical micelles with a hydrodynamic radius of 14–20 nm and a micellar mass of 800–1400 g mol^{-1} were obtained for $P2MVP_{38}$-*b*-PEO_{211}, $P2MVP_{42}$-*b*-PEO_{446} and $P2MVP_{71}$-*b*-PEO_{454}, respectively. 2D ^{1}H NOESY NMR experiments did not show any cross-correlations between PEO and PVOH protons, again indicating their segregation in the micellar corona. Because the large difference between the amount of ethylene oxide and vinyl alcohol monomers in the micellar corona renders a Janus-type segregation improbable, and under the experimental conditions water is only a marginal solvent for PVOH and a good solvent for PEO, a "patchy" corona wherein PEO and PVOH chains are both laterally and radially segregated seems to be more plausible (Fig. 4d). Self-consistent field (SCF) calculations support this reasoning [66]. We note, however, that no direct experimental evidence has been provided.

In conclusion, we have investigated four different types of complex coacervate core micelles formed through co-assembly of two double hydrophilic block copolymers. In two of these systems at room temperature, $PDMAEMA_{45}$-*b*-$PGMA_{90}$/PAA_{42}-*b*-$PAAm_{417}$ and $P2MVP_{38}$-*b*-PEO_{211}/PAA_{55}-*b*-$PNIPAAm_{88}$, the neutral blocks in the micellar corona were found to mix (Fig. 4a) [17, 65]. Co-assembly of PAA_{42}-*b*-$PAAm_{417}$ and $P2MVP_{42}$-*b*-PEO_{446} gave rise to reversible Janus micelles (Fig. 4b) [15, 16, 61], whereas radial chain segregation was observed when the temperature of a solution containing C3Ms of $P2MVP_{38}$-*b*-PEO_{211} and PAA_{55}-*b*-$PNIPAAm_{88}$ was raised above the LCST of PNIPAAm (Fig. 4c) [17]. Finally, the PVOH and PEO chains in co-micelles of PAA_{305}-*b*-$PVOH_{184}$ and $P2MVP_{38}$-*b*-PEO_{211}, $P2MVP_{42}$-*b*-PEO_{446} or $P2MVP_{71}$-*b*-PEO_{454} were found to probably be both laterally and radially segregated (Fig. 4d) [66].

Let us now turn our attention to SCF calculations in order to gain a better understanding of the various parameters governing the (internal) micellar structure.

4 Theory and Modelling

Compared to surfactant self-assembling systems, the parameter space for polymer co-assembly is notably larger, and guidance of some sort (e.g. to assist interpretation of experiments, as discussed above) is timely. From previous work, we know

that it is feasible to present models for polymer assemblies using numerical SCF approaches. It is important to mention that for a successful analysis it is not necessary to go into all the molecular details. In fact, it is reasonable to design coarse-grained models, provided that the relevant molecular structures (i.e. the sequence of the segments in the chains, as well as the inter- and intramolecular interactions) are accurately accounted for. To explore the complete phase behaviour of A–B/C–D polymer assemblies is a formidable task and currently the work is far from finished. In particular, many open questions exist, not only for, e.g., kinetic effects, but also for various structural and equilibrium aspects.

From a philosophical point of view, we may argue that even when large scale simulations can precisely reproduce experimental observations, we still may not understand the detailed principles at work. For this we need more deep and systematic insights in sub-problems that present themselves, e.g. with respect to the segregation of chains in the core or in the corona. For this reason, it is of considerable interest to focus here on the phase behaviour of a mixed spherical polymer brush, which mimics the behaviour of chains in a spherical corona.

In a recent two-gradient SCF analysis, some of us have shown that Janus micelles can be analysed in depth [67]. In this work, the focus was on the fully symmetric case, where the complexity was reduced to the micellisation of triblock copolymers (terpolymers) with a core forming middle block. Both the micellar structure and its thermodynamic stability were considered. The two chains in the corona were equally long, had perfectly symmetric interactions with the core and the solvent, and only the interaction parameter between the segments of the two types of chains varied. In experiments, there is virtually always a chain length disparity, and the solvent strength cannot be the same for both polymer chains. Moreover, the number of corona chains and, hence, the average grafting density of the two chains is probably different for the two chains in the corona. Finally, there may be a difference in adsorption energy of the chains to the core. With this in mind, it is reasonable to collect systematic information on the importance of the various disparities for the structural features in the corona. We note that preliminary calculations of a mixed polymer brush in a flat geometry have been presented before to explain some of the experimental observed phenomena [66]. The goal here is to put these preliminary calculations in a somewhat broader perspective.

While focussing on phenomena that occur in the corona, it makes sense to simplify the problem right from the beginning. We therefore focus on systems that cannot adjust the aggregation number nor the geometry of the micelle by simplifying the system such that each (corona) chain is grafted with one of its ends onto the surface of a spherical core of given size (in 1G calculations). In line with experimental counterparts, we allow for the lateral mobility of the two chains, so that (in two-gradient calculations) lateral segregation is possible.

Let us further restrict our task to two types of chains, with chain lengths N_B and N_D, each with (spherical, flexible) segments with length b, grafted onto a (small) spherical particle with radius $R = 5b$. The two chains have grafting densities σ_B and σ_D, respectively. Instead of the grafting density, we prefer the use of the number of chains per particle, which is given by $n = 4\pi R^2\sigma$, for both chains. Interactions

are taken into account using the well-known Flory–Huggins interaction parameters within a Bragg–Williams approximation [68]. There will be a monomeric solvent, and the solvent qualities for the two chains are denoted by χ_B and χ_D. The θ value $\chi = 0.5$ separates the regimes where long polymer chains collapse ($\chi > 0.5$) or are swollen ($\chi < 0.5$). The pair interaction χ_{BD} controls the miscibility of the two chains. By convention, when this value is positive, the segments repel each other. For reasons of simplicity, we take the core surface to be ideal such that the core-chain interactions are equally strong as the chain-solvent interactions.

The SCF model takes the geometry of the system as an input. When our interest is in a Janus configuration of the chains, a two-gradient (2G) cylindrical coordinate system is appropriate, but in many other situations we may obtain first insights from a one-gradient (1G) spherical geometry, e.g. when the structure is onion-like. Because the 1G calculations are computationally less demanding than the 2G calculations, it is reasonable to explore the possible scenarios with the simplest geometry first. We will see, however, that one has to be cautious about direct interpretation of 1G results in this type of problem. This is illustrated by presenting the corresponding 2G results.

4.1 1G SCF Results

To solve the SCF equations, we make use of the discretisation scheme of Scheutjens and Fleer [69]. It is understood that here we cannot give full details on the SCF machinery. For this we refer to the literature [67, 70–72]. However, pertinent issues and approximations will be mentioned in passing. The radial coordinate system is implemented using spherical lattice layers $r = 1, \ldots, r_M$, where layers $r = 1, \ldots, 5$ are reserved for the solid particle. The number of sites per layer is a quadratic function of the layer number, $L(r) \propto\sim r^2$. The mean-field approximation is applied within each layer, which means that we only collect the fraction of lattice sites occupied by segments. These dimensionless concentrations are referred to as volume fraction $\varphi(r)$. We assume that the system is fully incompressible, which means that in each layer the volume fraction of solvent $\varphi_s = 1 - \varphi_B(r) - \varphi_D(r)$. Conjugated to the volume fractions are the segment potentials $u(r)$. The segment potentials can be computed from the volume fractions as briefly mentioned below.

The first SCF result that we discuss here is shown in Fig. 7. In this case, χ_{BD} has been varied from 0 to 1.5, with steps of 0.5, for the case that the lengths of the two chains is varied under the constraint that the sum of the two is fixed to 200. The most simple system is found for $N_B = N_D = 100$ and $\chi_{BD} = 0$. In this case, we have a spherical homodisperse, athermal brush. For this situation, the (dimensionless) segment potential is simply given by $u(r) = \ln[1 - \varphi_S(r)]$ [73]. In short, within a freely jointed chain model, we generate all possible conformations of the polymer chains with the constraint that the first segment is positioned at $r = 6$ (next to the surface). Depending on the positions visited by, e.g. a conformation c, we can exactly enumerate the potential felt by this conformation u_c. The statistical weight of

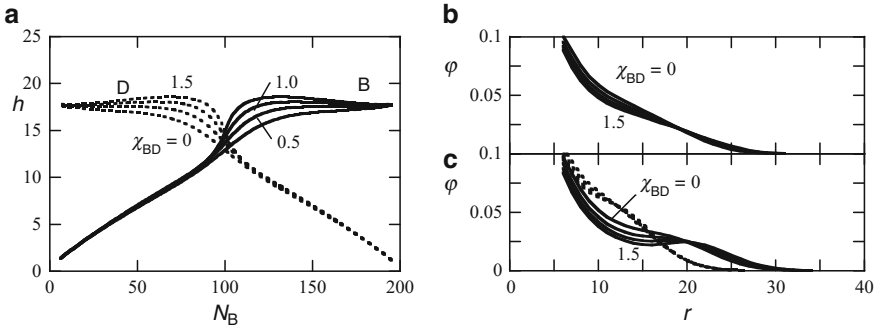

Fig. 7 (**a**) The height of the corona layer h in units of the segment size b as a function of the length of the B chain for four values of the pair interaction χ_{BD} as indicated. In all systems, $N_B + N_D = 200$ and the number of chains per particle $n_B = n_D = 15$. The *dashed lines* give the height (and profile) of the D chain and the *solid lines* those of the B chain. (**b**) The radial volume fraction profiles for $N_B = N_D = 100$ for four values of $\chi_{BD} = 0, 0.5, 1.0, 1.5$ (only the extremes are indicated). (**c**) The same as for (**b**), but with $N_B = 120$ and $N_D = 80$

this conformation is then given by the Boltzmann law: $G_c = \exp(-u_c)$. Knowing the statistical weights of all conformations gives, after normalisation, the volume fraction distribution of the polymer chains (and using the compressibility relation also for the solvent). Numerically, we (iteratively) search for the distribution of the brush segments for which the potentials are consistent with the volume fractions [70].

Once the self-consistent distributions are known, we can compute measurable quantities. In Fig. 7a we present the average position of the end-segment of both chains (for which we use the parameter h) above the core surface. This value is computed by the first moment:

$$h_X = \frac{\sum_r (r-5) L(r) \varphi_X(r,N)}{\sum_r L(r) \varphi_X(r,N)} \tag{3}$$

where $\varphi_X(r,N)$ is the radial distribution of segment $s = N$ of chain type X. This value is a measure for how far the chain extends from the core. Inspection of Fig. 7a shows that the longer chain extends further from the core. It is seen that the end-point of the longest chain is relatively independent of the length N_B, whereas the extension of the shortest chain is proportional to its length. As expected, the switching of positions occurs for $N_B = N_D = 100$, and the switching is more cooperative when the two chains repel each other stronger. In passing, we note that now the system is not athermal; in this case the segment potential for B is given by:

$$u_B(r) = -\ln[1 - \varphi_S(r)] - 2\chi_B \langle \varphi_B(r) \rangle + (\chi_{BD} - \chi_D - \chi_B) \langle \varphi_D(r) \rangle \tag{4}$$

and that of D is found by exchanging D for B and vice versa. In (4), the angular brackets give a three-layer average, properly weighted and adjusted to the geometry [74]. Interestingly, the height of the longest chain (cf Fig. 7a) passes through a weak maximum around the situation that the longest chain is about 50% larger than the smallest one.

In Fig. 7b, c we give the radial volume fraction distributions for the symmetric chain length case and for a slightly asymmetric length distribution (near the maximum in height difference). Much is known about the conformation of a spherical brush, even though a strong analytical theory is not available. In the case of a polymer star, there are two regions. In a proximal (inner) region the density profile falls off as a power-law, exactly in the region where the chain ends are depleted (dead zone). At larger distances from the centre, where the curvature is less strong, the profile is "quasi" parabolic [75]. In this example (Fig. 7b, $\chi_{BD} = 0$), the dead zone is mostly masked by the solid core and primarily the profile is parabolic-like (visible for $r > 10$).

Focussing on the case that the two chains are equally long, we can see from Fig. 7b that the profile extends slightly when the repulsion between the two chains increases. When solvent molecules enter the brush (and thus swell the brush), the number of unfavourable interactions between polymer segments is reduced. This has the same effect as improving the solvent quality slightly [67]: the height of a homopolymer brush increases with improving solvent quality. A systematic analysis of Fig. 7c proves that the smaller chain is somewhat compressed (as compared to a homodisperse brush) and that the longest one is pushed to the periphery and assumes an inhomogeneous conformation known as the flower [76]: a strongly stretched stem is formed in the region of the small chain and a coiled crown (much less stretched) is formed on the outside.

Even though we know that this system can, particularly for the higher values of χ_{BD} (e.g. when $\chi_{BD} = 1$), maintain a Janus-type distribution of its chains (see also Sect. 4.2), we find that the stratified structure (forced in a 1G calculations), as shown in Fig. 7c, is formed smoothly, i.e. without a jump. Although we do not exclude the possibility that jump-like changes may occur for very large values of χ_{BD}, space does not allow us to elaborate on this. Let us proceed to other scenarios for which similar transitions are (at least on the SCF level) expected.

Figure 8 gives information on what happens to the binary spherical brush when the solvent quality for the longest chain (here we choose the B chain) worsens. In a flat geometry, this is a scenario in which a jump-like transition was observed [66]. Basically, when χ_B increases, there is a tendency that the chain collapses. Quite obviously, the height of the B chain should then dramatically decrease. Inspection of Fig. 8a proves that this is indeed the case. The point at which the chain retracts to the surface depends also on the affinity of the B chain for the core. The stronger the chain is attracted to the surface (negative value of χ_{coreB}), the easier it is for the chain to collapse on the core. In these calculations we retained the repulsion between the B and D chains to a reasonably strong value of $\chi_{BD} = 1$. For this reason, the transition occurs in a rather abrupt manner. A strong affinity for the surface makes the collapse transition of the B chains also less abrupt. Exactly in the transition region it is found that the D chain is pushed slightly outward and the height passes through a small maximum. Again, this behaviour is more gradual when the transition is smooth, as is the case when $\chi_{BD} = 0$ (results not shown).

We may learn more about the collapse transition by inspection of the radial volume fraction and end-point distribution. In Fig. 8b, c we give an example for the

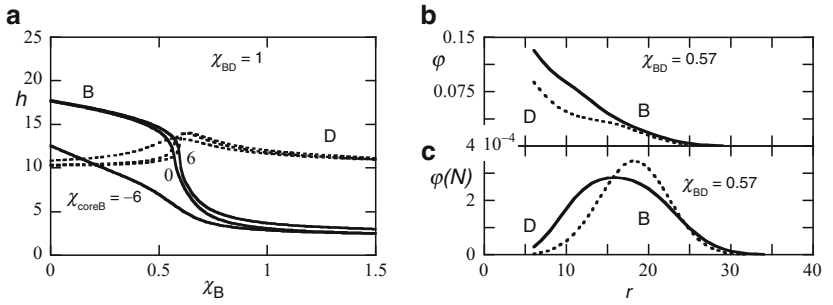

Fig. 8 (**a**) The height of the corona layer h in units of the segment size b as a function of the solvent quality for the B chain χ_B for three values of affinity of the B chain for the core χ_{coreB} as indicated. (**b**) The radial volume fraction profiles and (**c**) the corresponding radial end-point distribution for the case that $\chi_B = 0.57$ and $\chi_{coreB} = 0$. $N_B = 120$, $N_D = 80$, number of chains per particle $n_B = n_D = 15$, and $\chi_{BD} = 1$. The *dashed* lines give the height (and profiles) of the D chain, and the *solid lines* those of the B chain

case that the B chain is half-way in its transition, for $\chi_{coreB} = 0$. Discussing the end-point distribution first (Fig. 8c) we see that the ends of B are more widely distributed than those of D (which are more confined to the periphery). This wider distribution is characteristic for a chain that fluctuates more in terms of its conformations. Some chains have already contracted and are near the core, while other chains are still on the outside. The increased level of end-point fluctuations is characteristic for a chain that suffers a conformational transition. In line with this, the overall volume fraction profiles shown in Fig. 8b prove that the B chains near the surface are in the process of collapsing. The density at the core has increased already by about 50% compared to the case of the brush in good solvent. With decreasing solvent quality, this condensation process becomes more pronounced. Hence, if the solvent quality decreases further, the end points of the B chains go to smaller r-values and the D chains remain on the outside. Hence, these distributions become separated from each other more than is the case in Fig. 8c. Eventually an interface, including an interfacial tension between D and B, develops.

4.2 2G SCF Results

Above we have shown that the chain lengths, solvent qualities and adsorption energies are all relevant for how a bidisperse spherical brush is structured. In addition, the grafting densities of the chains are another factor. Depending on conditions, we can have a stratified configuration and the segregation/overlap of segment types remains significant even when the polymer segments of the two corona chains repel each other. One can wonder how realistic this scenario is. The weak point of the 1G calculations is that we do not allow for structures that reduce their symmetry, e.g. the Janus configuration.

There exists a threshold χ_{BD}^{cr} below which the two corona chains mix, and above which the Janus configuration becomes stable. For the symmetric system it was found [67] that this threshold interaction obeys the relationship $\chi_{BD}^{cr} N \varphi^{m} \approx 2$, where N is the length of the corona chains and φ^{m} the maximum density of chains in the corona (somewhere close to the core). In general, this value should (slightly) depend on chain lengths and chain length differences, solvent quality of the corona chains, etc. Up to now, we have chosen a relatively high χ_{BD} that is significantly larger than the threshold value mentioned above. We will now limit ourselves to the strong segregation case, mainly for illustration purposes.

Let us therefore move to the 2G SCF computations and focus on micellar objects with two sides. Again, it is obvious that we need repulsion between the two types of segments (as in Fig. 7), or poor solvent conditions for one of the chains (as in Fig. 8) for this to occur. The exact structures that are formed may be further influenced by the adsorption strength, the chain length differences and/or the grafting density disparities. We cannot deal here with all these degrees of freedom and therefore we choose to take the system of Fig. 8 and consider how this system behaves in a 2G analysis.

When the corona is laterally segregated and, hence, when there is an interface running in the radial direction between the two species of the corona, one should expect a non-trivial shape of the core. To investigate such phenomena, it is not appropriate to take an inert core (as described above). We thus extend the molecular model with a core-forming block. As in previous studies [67], we use triblock copolymers with a central block that (strongly) segregates from the monomeric solvent, i.e. $(B)_{N_B} - (C)_{N_C} - (D)_{N_D}$. The length of the central block is chosen such that the core has a radius $R = 5$ when it is spherical. Again we focus on micelles with aggregation numbers $n = 15$. In the first example, we wish to remain close to the system discussed in Fig. 8 and therefore we choose a strong segregation of C with the solvent such that $\chi_C = 2$. This leads to a high interfacial tension between core and corona and, for this reason, minimal deviations of the core shape from the sphere are expected. The SCF machinery for the 2G cylindrical coordinate system is not much more complex than the 1G spherical ones. All quantities now are function of two coordinates, where z runs along the axis of the cylinder and the r-coordinate goes in the radial direction.

Figures 9–11 give volume fraction contour plots in the (z, r) plane that cuts through the centre of the micelle. As above, the B chain is represented by solid lines and the D chain by dashed ones. For these graphs, we only varied the solvent quality of the longer B chain, ranging from a good solvent (Fig. 9) to a theta solvent (Fig. 10) to a poor solvent (Fig. 11). The shorter D chain is in good solvent conditions in all cases. As expected, we see a Janus structure in all three graphs. The micelle is oriented such that the B chain is situated at lower z-values and the D chain at higher z-values. The interface between the two types of chains is, at least qualitatively, seen from the figures. When the solvent quality decreases for the B chain, the volume occupied by B chains diminishes and the interface goes away from the equatorial plane, to close to an angle of 45° in the poor solvent case.

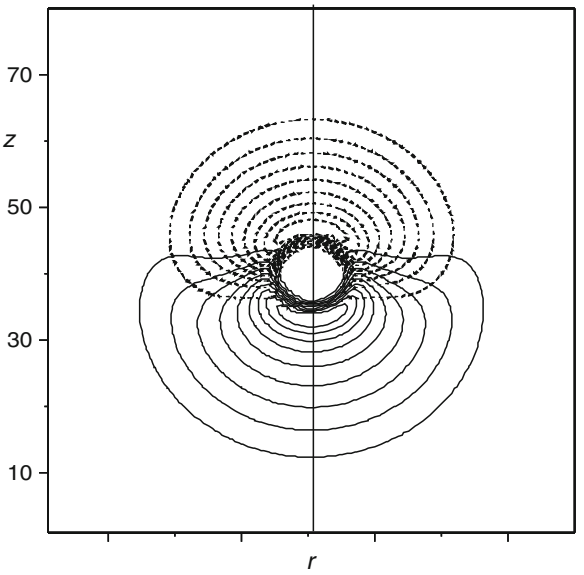

Fig. 9 Volume fraction contour plots for a cross-section through a Janus micelle composed of two types of chains $N_B = 120$ (*solid lines*), $N_D = 80$ (*dashed lines*), with $n_B = n_D = 15$. The *dashed lines* gives the height (and profiles) of the D chain, and the *solid lines* those of the B chain. $\chi_B = \chi_D = 0$, $\chi_{CB} = \chi_{CD} = \chi_C = 2$, and $\chi_{BD} = 1$. The rotational symmetry-axis around $r = 0$ (C_1 symmetry) is indicated by a *vertical solid line*. As indicated on the z-axis, the distance between two ticks is 10b

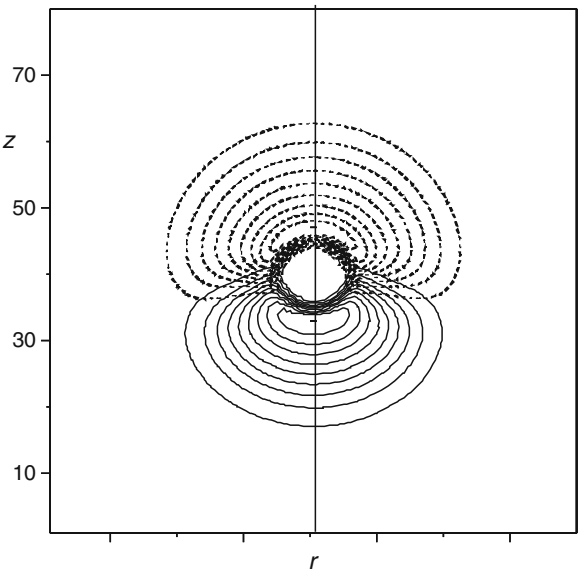

Fig. 10 Volume fraction contour plots as in Fig. 9, with $\chi_B = 0.5$

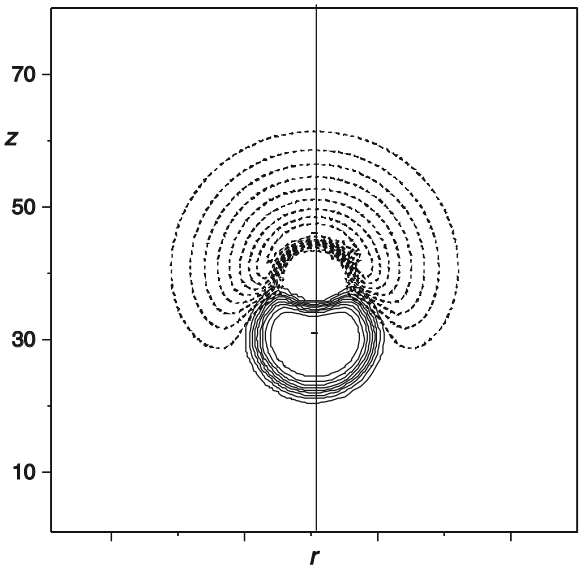

Fig. 11 Volume fraction contour plots as in Fig. 9, with $\chi_B = 1.0$

A more detailed investigation of the collapse transition of the B chains reveals that this process occurs smoothly, i.e. without a jump. This is consistent with the known behaviour of the collapse of a polymer brush upon a worsening of the solvent quality. In these calculations, the B and D chains have the same affinity for the core and thus the condensed B chains do not wet the core completely. Instead, a microscopic contact angle of approximately 90° is observed. Hence, the core and the collapsed B chain sit side-by-side, as can be seen from Fig. 11. The D chains remain on the side with high z-values, basically because these chains emanate from the core from that side. Only when the D chains are extremely long might we expect that they lean over to the side where the B chains have collapsed. Configurations such as those shown in Fig. 11 can thus be seen as super-amphiphiles, and these structures will aggregate with others such that the B core reduces contacts with the solvent. Anisometric Janus micelles have recently been reported, which subsequently were able to aggregate into supermicelles [77].

Figures 9–11 show that the 1G SCF predictions can only qualitatively be used to analyse binary spherical brushes. By the same token, we might expect that a 3G SCF analysis may give a binary spherical brush even more degrees of freedom to form structures with even lower symmetries, for example by splitting up the compact B regions over several subregions. So-called raspberry-like multicompartment micelles have indeed been reported recently [14, 18, 78, 79].

We conclude the results section by illustrating how the shape of the core can be influenced by the demixing that takes place in the corona. Close inspection of Figs. 9–11 shows that the perfect spherical shape of the core is not found, even with the high interfacial tension between core and solvent. Figure 12 shows a Janus

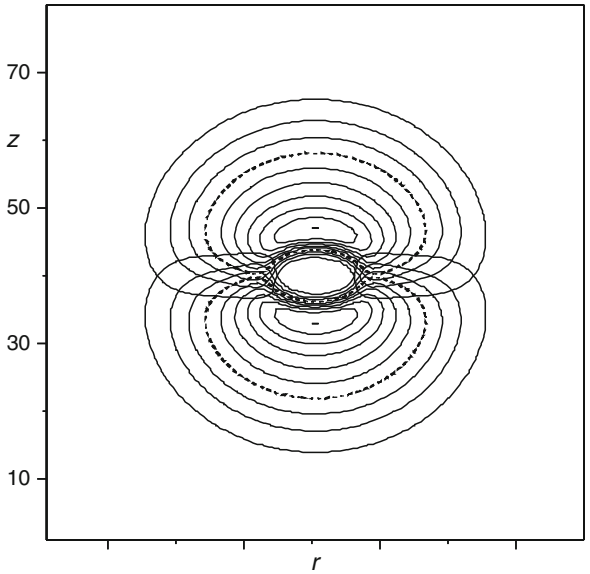

Fig. 12 Volume fraction contour plots for a cross-section through a Janus micelle composed of two types of corona chains $N_B = N_D = 100$, with $n_B = n_D = 15$, and $\chi_{BD} = 1$. The core-forming block has a length $N_C = 33$. $\chi_B = \chi_D = 0$, $\chi_{CB} = \chi_{CD} = \chi_C = 1.3$, and $\chi_{BD} = 1$. As indicated on the z-axis, the distance between two ticks is 10b. The *dashed contour line*, representing a volume fraction of approximately $\varphi = 4 \times 10^{-3}$, indicates the density "seen" hydrodynamically

micelle composed of symmetric triblocks $(B)_{100}(C)_{33}(D)_{100}$. As can be seen from Fig. 12, the interface between B and D is exactly in the equatorial plane. The interaction parameters of the core-forming block with B, D and the solvent are now reduced to a value 1.3. Comparison of the shapes of the core of, e.g., Fig. 10 with Fig. 12 shows that in the latter case the core is indeed wider in the equatorial plane than in the z-direction and the ratio of these dimensions is approximately 1.9. To estimate the asymmetry seen in a hydrodynamic experiment, we envision that the very dilute extremities of the micelle will not be seen, but rather that there exists a threshold density that resists the flow of solvent. In Fig. 12 we have chosen (quite arbitrarily) a contour line representing a volume fraction $\varphi = 4 \times 10^{-3}$. Using this contour line (dashed line in Fig. 12), we estimated that the width in the equatorial direction over that in the z-direction is approximately 0.875. These trends are consistent with the results of the experiments discussed above.

From the modelling, we may conclude that it is possible to have mixed micelles with a segregated corona. Qualitatively, the information that can be extracted for these micelles is consistent with experimental findings. Moreover, this gives support for the interpretation of experiments and strengthens the hopes that we can use SCF modelling to learn about complex forms of self-assembly. Even though the models that were used in the calculations were inspired by the experimental counterparts, we hasten to mention that we did not try to match the models and the experimental

results. For this we first need to account more fundamentally for the electrostatic driving forces that keep the binary copolymers together. A very primitive approach to try to capture the complex coacervate core properties was recently attempted by some of us [80], but we feel that much more work in this direction is necessary before a true comparison between theory and experiment is realistic.

5 Conclusion

We have shown that a combination of four simple building blocks (i.e. monomers) and exclusively non-covalent interaction forces, achieved via the co-assembly of fully water-soluble double hydrophilic block copolymers, results in mixed micelles in aqueous solutions. The chemically unlike polymer chains in the micellar corona may give rise to various coronal microstructures, ranging from mixed to segregated, in either the radial or lateral direction, or in both. Hence, co-assembly of charged block copolymers can result in the spontaneous formation of reversible Janus micelles.

Various aspects of the molecular modelling of Janus micelles are possible using suitable SCF theory. Modelling co-assembly and reversible micellisation is in principle possible but rather tedious. One way to use SCF models is to investigate scenarios. We have illustrated this by considering the binary spherical polymer brush both by 1G (spherical) and 2G (cylindrical) SCF models, focussing mainly on the structure of the corona. In 1G models, one can only consider the onion-like configuration in which the system is segregated radially. Even in the absence of repulsive interactions between the two polymer species, a gradual separation of segments may occur, e.g. due to disparities in chain length or solvent strength. Unless the solvent quality becomes poor, we are unlikely to find a true interface in the radial direction between repelling blocks. This rather occurs in the lateral direction, as shown in 2G calculations. When the interfacial tension between core and solvent is high, the deformation of the core away from the spherical shape may be small. However, when this interfacial tension is reduced, significant shape deviations of the core are predicted. The interface in the corona exerts a pulling force on the core such that the core flattens as a disk. At the same time, the corona elongates. Such trends were also seen in experiments on Janus micelles.

Acknowledgments We thank Gert Buurman for the creation of Fig. 1. This work is part of the research programme of the Stichting voor Fundamenteel Onderzoek der Materie (FOM), which is financially supported by the Nederlandse Organisatie voor Wetenschappelijk Onderzoek (NWO). It has been carried out in the framework of the EU Polyamphi/Marie Curie program (FP6–2002, proposal 505027). I.V. was financed by the SONS Eurocores program (Project JA016-SONS-AMPHI). Holger Schmalz is gratefully acknowledged for the synthesis of the P2MVP-*b*-PEO polymer, Rhodia (Aubervilliers, France) for providing us with a sample of PAA-*b*-PAAm, and C. Detrembleur, A. Aqil, and A. Debuigne for the synthesis of the PAA-*b*-PNIPAAm and PAA-*b*-PVOH polymers.

References

1. Zhang LF, Eisenberg A (1996) J Am Chem Soc 118:3168
2. Zhulina EB, Adam M, LaRue I, Sheiko SS, Rubinstein M (2005) Macromolecules 38:5330
3. Nagarajan R, Ruckenstein E (1991) Langmuir 7:2934
4. Missel PJ, Mazer NA, Benedek GB, Carey MC (1983) J Phys Chem 87:1264
5. Schlaad H, You LC, Sigel R, Smarsly B, Heydenreich M, Mantion A, Masic A (2009) Chem Commun:1478
6. Uchman M, Stepanek M, Prochazka K, Mountrichas G, Pispas S, Voets IK, Walther A (2009) Macromolecules 42:5605
7. Schmalz H, Schmelz J, Drechsler M, Yuan J, Walther A, Schweimer K, Mihut AM (2008) Macromolecules 41:3235
8. Li ZB, Hillmyer MA, Lodge TP (2006) Nano Lett 6:1245
9. Schacher F, Walther A, Ruppel M, Drechsler M, Mueller AHE (2009) Macromolecules 42:3540
10. Walther A, Drechsler M, Rosenfeldt S, Harnau L, Ballauff M, Abetz V, Muller AHE (2009) J Am Chem Soc 131:4720
11. Kriz J, Masar B, Plestil J, Tuzar Z, Pospisil H, Doskocilova D (1998) Macromolecules 31:41
12. Schrage S, Sigel R, Schlaad H (2003) Macromolecules 36:1417
13. Kim SH, Tan JPK, Nederberg F, Fukushima K, Yang YY, Waymouth RM, Hedrick JL (2009) Macromolecules 42:25
14. Kuo SW, Tung PH, Lai CL, Jeong KU, Chang FC (2008) Macromol Rapid Commun 29:229
15. Voets IK, de Keizer A, de Waard P, Frederik PM, Bomans PHH, Schmalz H, Walther A, King SM, Leermakers FAM, Cohen Stuart MA (2006) Angew Chem Int Ed Engl 45:6673
16. Voets IK, Fokkink R, Hellweg T, King SM, de Waard P, de Keizer A, Cohen Stuart MA (2009) Soft Matter 5:999
17. Voets IK, Moll PM, Aqil A, Jerome C, Detrembleur C, de Waard P, de Keizer A, Cohen Stuart MA (2008) J Phys Chem B 112:10833
18. Gohy JF, Khousakoun E, Willet N, Varshney SK, Jerome R (2004) Macromol Rapid Commun 25:1536
19. Luo LB, Eisenberg A (2002) Angew Chem Int Ed Engl 41:1001
20. Voets IK, de Keizer A, Cohen Stuart MA (2009) Adv Colloid Interface Sci 147–48:300
21. Plestil J, Konak C, Hu XS, Lal J (2006) Macromol Chem Physic 207:231
22. Prochazka K, Martin TJ, Webber SE, Munk P (1996) Macromolecules 29:6526
23. Talingting MR, Munk P, Webber SE, Tuzar Z (1999) Macromolecules 32:1593
24. Plestil J, Kriz J, Tuzar Z, Prochazka K, Melnichenko YB, Wignall GD, Talingting MR, Munk P, Webber SE (2001) Macromol Chem Phys 202:553
25. Zhang WQ, Shi LQ, Gao LC, An YL, Wu K (2005) Macromol Rapid Commun 26:1341
26. Harada A, Kataoka K (1995) Macromolecules 28:5294–5299.
27. Xie DH, Xu K, Bai RK, Zhang GZ (2007) J Phys Chem B 111:778
28. Xiong DA, Shi LQ, Jiang XW, An YL, Chen X, Lu JA (2007) Macromol Rapid Commun 28:194
29. Gohy JF, Varshney SK, Jerome R (2001) Macromolecules 34:3361
30. Park JS, Akiyama Y, Yamasaki Y, Kataoka K (2007) Langmuir 23:138
31. Chelushkin PS, Lysenko EA, Bronich TK, Eisenberg A, Kabanov VA, Kabanov AV (2007) J Phys Chem B 111:8419
32. Hofs B, Voets IK, de Keizer A, Cohen Stuart MA (2006) Phys Chem Chem Phys 8:4242
33. Lindhoud S, de Vries R, Norde W, Cohen Stuart MA (2007) Biomacromolecules 8:2219
34. Kabanov AV, Bronich TK, Kabanov VA, Yu K, Eisenberg A (1996) Macromolecules 29:6797
35. Burkhardt M, Ruppel M, Tea S, Drechsler M, Schweins R, Pergushov DV, Gradzielski M, Zezin AB, Muller AHE (2008) Langmuir 24:1769
36. Groger S, Geschke D, Karger J, Stallmach F, Konak C (2004) Macromol Rapid Commun 25:1015
37. Gohy JF, Varshney SK, Antoun S, Jerome R (2000) Macromolecules 33:9298

38. Pergushov DV, Remizova EV, Gradzielski M, Lindner P, Feldthusen J, Zezin AB, Müller AHE, Kabanov VA (2004) Polymer 45:367
39. Podhajecka K, Stepanek M, Prochazka K, Brown W (2001) Langmuir 17:4245
40. Cohen Stuart MA, Hofs B, Voets IK, de Keizer A (2005) Curr Opin Colloid Interface Sci 10:30
41. van der Burgh S, de Keizer A, Cohen Stuart MA (2004) Langmuir 20:1073
42. Harada A, Kataoka K (1999) Science 283:65
43. Stepanek M, Podhajecka K, Tesarova E, Prochazka K, Tuzar Z, Brown W (2001) Langmuir 17:4240
44. Yan XH, Liu GJ, Hu JW, Willson CG (2006) Macromolecules 39:1906
45. Bronich TK, Cherry T, Vinogradov SV, Eisenberg A, Kabanov VA, Kabanov AV (1998) Langmuir 14:6101
46. Bronich TK, Kabanov AV, Kabanov VA, Yu K, Eisenberg A (1997) Macromolecules 30:3519
47. Vinogradov SV, Bronich TK, Kabanov AV (1998) Bioconjugate Chem 9:805
48. Harada A, Kataoka K (1999) J Am Chem Soc 121:9241
49. Voets IK, de Keizer A, Cohen Stuart MA, Justynska J, Schlaad H (2007) Macromolecules 40:2158
50. Hofs B, Brzozowska A, de Keizer A, Norde W, Cohen Stuart MA (2008) J Colloid Interface Sci 325:309
51. Jaturanpinyo M, Harada A, Yuan XF, Kataoka K (2004) Bioconjugate Chem 15:344
52. Kakizawa Y, Harada A, Kataoka K (2001) Biomacromolecules 2:491
53. Kawarmura A, Harada A, Kono K, Kataoka K (2007) Bioconjugate Chem 18:1555
54. Yuan XF, Yamasaki Y, Harada A, Kataoka K (2005) Polymer 46:7749
55. Voets IK, de Keizer A, Cohen Stuart MA (2009) Adv Colloid Interface Sci 147–148:300
56. Kabanov AV, Kabanov VA (1998) Adv Drug Deliver Rev 30:49
57. Kataoka K, Harada A, Nagasaki Y (2001) Adv Drug Deliver Rev 47:113
58. Scott RL (1949) J Chem Phys 17:279
59. Voets IK, de Vries R, Fokkink R, Sprakel J, May R, de Keizer A, Cohen Stuart MA (2009) Eur Phys J E 30:351
60. Voets IK, van der Burgh S, Farago B, Fokkink R, Kovacevic D, Hellweg T, de Keizer A, Cohen Stuart MA (2007) Macromolecules 40:8476
61. Voets IK, Fokkink R, de Keizer A, May RP, de Waard P, Cohen Stuart MA (2008) Langmuir 24:12221
62. Silva M, Machado JC, Mano V, Silva GG (2003) J Polym Sci B Polym Phys 41:1493
63. Hefford RJ (1984) Polymer 25:979
64. Perrau MB, Iliopoulos I, Audebert R (1989) Polymer 30:2112
65. Voets IK, de Keizer A, Cohen Stuart MA, de Waard P (2006) Macromolecules 39:5952
66. Voets IK, Debuigne A, Detrembleur C, Jérôme R, de Keizer A, Cohen Stuart MA (2009) Eur Polym J 45:2913
67. Charlaganov M, Borisov OV, Leermakers FAM (2008) Macromolecules 41:3668
68. Flory PJ (1953) Principles of polymer chemistry. Cornell University Press, Ithaca
69. Fleer GJ, Cohen Stuart MA, Scheutjens JMHM, Cosgrove T, Vincent B (1993) Polymers at interfaces. Chapman and Hall, London
70. Evers OA, Scheutjens J, Fleer GJ (1990) Macromolecules 23:5221
71. Leermakers FAM, Eriksson JC, Lyklema J (2005) Association colloids and their equilibrium modelling. In: Lyklema J (ed) Soft colloids. Fundamentals of interface and colloid science, vol V. Elsevier, Amsterdam, p 4.1
72. Leermakers FAM, Wijmans CM, Fleer GJ (1995) Macromolecules 28:3434
73. Scheutjens J, Fleer GJ (1979) J Phys Chem 83:1619
74. Leermakers FAM, Scheutjens J (1990) J Colloid Interface Sci 136:231
75. Wijmans CM, Zhulina EB (1993) Macromolecules 26:7214
76. Skvortsov AM, Klushin LI, Leermakers FAM (2002) Europhys Lett 58:292
77. Erhardt R, Boker A, Zettl H, Kaya H, Pyckhout-Hintzen W, Krausch G, Abetz V, Müller AHE (2001) Macromolecules 34:1069
78. von Berlepsch H, Boettcher C, Skrabania K, Laschewsky A (2009) Chem Commun:2290
79. Hoppenbrouwers E, Li Z, Liu GJ (2003) Macromolecules 36:876
80. Voets IK, Leermakers FAM (2008) Phys Rev E 78:061801

Adv Polym Sci (2011) 241: 187–249
DOI:10.1007/12_2010_56

Published online: 20 April 2010

Fluorescence Spectroscopy as a Tool for Investigating the Self-Organized Polyelectrolyte Systems

Karel Procházka, Zuzana Limpouchová, Filip Uhlík, Peter Košovan, Pavel Matějíček, Miroslav Štěpánek, Mariusz Uchman, Jitka Kuldová, Radek Šachl, Jana Humpolíčková, and Martin Hof

Abstract In this article, we outline the principles and application of several time-resolved fluorescence techniques for studying the behavior of stimuli-responsive self-assembled polymer systems. We demonstrate the high research potential of fluorescence using results of several published studies performed by the research team at the Charles University in Prague in the framework of the Marie Curie Research Training Network "Self-Organized Nanostructures of Amphiphilic Copolymers" (MRTN-CT-2003-505027). We have chosen several interesting examples of complex self-assembling systems, the behavior of which could not have been understood without the help of targeted fluorescence studies. We have chosen four different techniques, two of them relatively popular (fluorescence anisotropy and nonradiative excitation energy transfer) and two only little used in polymer science (the solvent relaxation method and fluorescence correlation spectroscopy). The last part of the article is devoted to computer simulations (Monte Carlo and molecular dynamics) aimed at the interpretation of fluorescence data.

Keywords Block copolymer micelles · Fluorescence anisotropy · Fluorescence correlation spectroscopy · Molecular dynamics simulations · Monte Carlo simulations · Solvent relaxation method · Time-resolved fluorescence

K. Procházka (✉), Z. Limpouchová, F. Uhlík, P. Košovan, P. Matějíček, M. Štěpánek, M. Uchman, and J. Kuldová
Department of Physical and Macromolecular Chemistry, Faculty of Science, Charles University in Prague, Albertov 6, 12843 Prague 2, Czech Republic
e-mail: prochaz@vivien.natur.cuni.cz; zl@vivien.natur.cuni.cz; uhlik@sals.natur.cuni.cz; kosovan@vivien.natur.cuni.cz; matej@vivien.natur.cuni.cz; stepanek@natur.cuni.cz; mariuszuchman@o2.pl; jh@vivien.natur.cuni.cz

R. Šachl, J. Humpolíčková, and M. Hof
The Jaroslav Heyrovsky Institute of Physical Chemistry, Czech Academy of Sciences, Dolejškova 5, Prague 8, Czech Republic
e-mail: radek.sachl@jh-inst.cas.cz; jana.humpolickova@jh-inst.cas.cz; martin.hof@jh-inst.cas.cz

Contents

Abbreviations

An	Anthracene
c.m.c.	Critical micelle concentration
DLS	Dynamic light scattering
FCS	Fluorescence correlation spectroscopy
fwhm	Full width in half-maximum
IC	Internal conversion
ISC	Intersystem crossing, intersystem conversion
LCST	Lower critical solution temperature
LS	Light scattering
MC	Monte Carlo
MD	Molecular dynamics
M_n	Number-average molar mass
M_w	Weight-average molar mass
NMR	Nuclear magnetic resonance spectroscopy
Np	Naphthalene
NRET	Nonradiative excitation energy transfer
ORB	Octadecyl rhodamine B
PAA	Poly(acrylic acid)

PE	Polyelectrolyte
PEO	Poly(ethylene oxide)
PMA	Poly(methacrylic acid)
PS	Polystyrene
PVP	Poly(2-vinylpyridine)
rhs	Right hand side
SLS	Static light scattering
SRM	Solvent relaxation method
TCSPC	Time-correlated single photon counting
TRES	Time-resolved emission spectra
TRFS	Time-resolved fluorescence spectroscopy

1 Introduction

For several decades, fluorescence spectroscopy has been one of the most frequently used techniques for studying the conformations and dynamics of synthetic and natural macromolecules. The versatility and broad applicability of fluorescence techniques for investigation of both static and dynamic properties of different systems stems from two grounds:

1. Fluorescence, i.e., the emission of a photon due to a spontaneous spin-allowed transition from the excited to the ground state, is a phenomenon concerning an energetically rich species (excited fluorophore) that strongly interacts with surrounding molecules. Hence, this phenomenon is influenced by interactions of the fluorophore with its microenvironment and yields indirect information on properties of the host system in which the fluorophore is embedded. Because the fluorophore "feels" the effect only of neighboring molecules, fluorescence techniques can be used for probing very small spatial regions. This offers the possibility to investigate small domains in nano-to-meso-heterogeneous systems, where most of common macroscopic techniques fail. Some fluorescence characteristics (e.g., the excitation and emission wavelength) depend both on interactions of the fluorophore in the ground and excited state, and others (e.g., the fluorescence lifetime) on interactions in the excited state only. This generates certain diversity in the dependence of individual fluorescence characteristics on the properties of the host system and broadens the research potential.
2. The second fact that enables monitoring fast dynamic processes is that the excitation (absorption of a photon) and the "red-shifted" fluorescence emission are two events separated by a time-window ranging from units to hundreds of nanoseconds (depending on the fluorophore and the surrounding medium). On this timescale, a number of molecular processes proceed, e.g., translational and rotational diffusion of the fluorophore in a small volume comparable with the range of interactions, reorientation of molecules in the solvate shell, segmental dynamics of

flexible polymer chains, and nonradiative energy transfer due to dipole–dipole interactions. All those processes affect the fluorescence characteristics. The advanced fluorescence measurements introduced about 40 years ago with a time resolution corresponding to the rate of these processes (i.e., nanosecond and subnanosecond time-resolved fluorescence measurements) almost immediately opened a new field of study of fast processes at the molecular level.

As a result of enormous development in the technology and production of pulse lasers, laser diodes, detector systems, and powerful computers in recent decades, steady-state and time-resolved fluorometers now belong to the standard equipment of biochemical and macromolecular laboratories. For example, there are apparatuses combined with microscopes that are suitable for time-resolved fluorescence measurements of individual organelles in living cells. However, the widespread use of fluorescence techniques generates certain danger, which is connected with their routine use. We would like to point out that the fluorescence spectroscopy is an indirect technique and that the interpretation of results needs great care and precaution. It almost always requires additional information on the system.

When designing a fluorescence experiment and interpreting data, one more possible complication has to be kept in mind: Only a limited number of systems involve intrinsic fluorophores and are inherently luminescent. Such systems (e.g., proteins containing tryptophan) are very suitable for fluorescence studies and reliable information on the location, mobility, and accessibility of tryptophane residues can be obtained in a relatively straightforward way. In other cases, an extrinsic fluorescence probe has to be added to the system. Its addition modifies the system, which can be a problem (more or less severe) depending on the system studied and on the fluorescence technique used. Because the fluorescence reports on the behavior of the microenvironment of the probe, it does not yield information on the original system, but only on its small perturbed part, even though the overwhelming part of the system has not been altered at all and behaves as the system without added fluorophore. It is obvious that an attempt to reduce the probe content in the host system could partially suppress this problem, but would not eliminate it entirely.

The aim of this feature article is to outline our application of fluorescence techniques to polymer self-assembly studies. We do not intend to give a complete survey of the use of fluorescence in polymer chemistry. We focus only on techniques that we have been using within the POLYAMPHI network. We start with a description of the principles of fluorescence phenomena and an explanation of the role of processes that influence the rates of transition and the spectroscopic characteristics. Then we discuss several examples of our experimental studies, in which we applied different variants of time-resolved measurements. Finally, we show how computer modeling can be used to support the interpretation of data on complex systems.

2 Principles of the Fluorescence Techniques Used

2.1 State Diagram and the Characteristics of Time-Dependent Fluorescence

The most comprehensive description and explanation of all processes that affect the fluorescence and the role of additional external factors is provided by the Jablonski diagram (Fig. 1), which represents the scheme of energy levels of electronic and vibrational states of a molecule and the possible transitions [1].

The vertical axis indicates increasing energy of different quantum states in vacuo or the Gibbs free energy of the fluorophore in condensed systems (e.g., in solutions). Individual states corresponding to the optimum molecular geometry are depicted by horizontal lines. The arrows indicate possible transitions between different states. Typical values of rate constants of all processes have been also included.

Prior to excitation, the molecule is in the lowest vibrational state of the lowest electronic state (ground state), S_0. The absorption of a photon is governed by optical selection rules [2]. Its probability is proportional to the square of the transition dipole moment. The most severe restriction concerns the spin conservation. Further restrictions reflect the symmetry and overlap of corresponding wave functions. Regardless of the probability (reflected by the molar absorption coefficient), the single act of transition to a higher excited state due to absorption of a photon belongs to the fastest processes that occur in nature (except nuclear processes) and proceeds on timescales shorter than 10^{-15} s [3]. In this short time, neither the position of

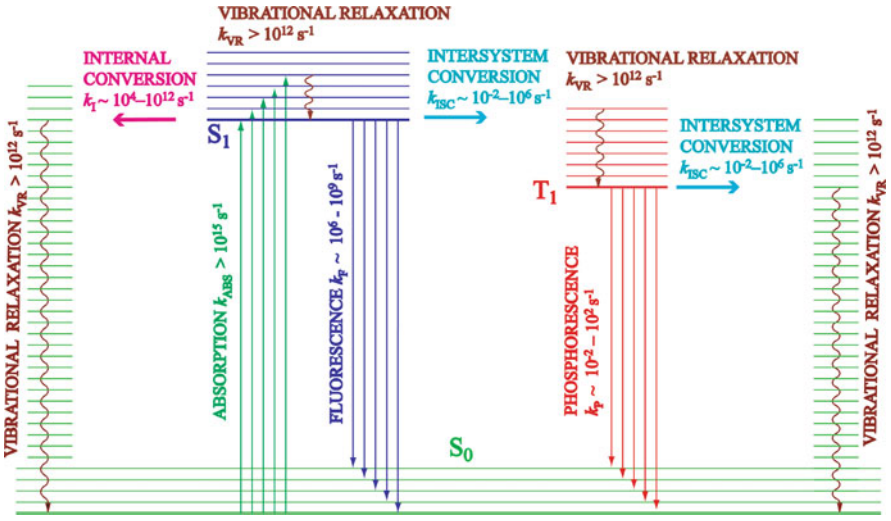

Fig. 1 The Jablonski diagram: the energies of the ground electronic singlet state S_0, excited singlet S_1, and triplet T_1 are depicted by *bold horizontal lines*; vibrational states by *narrow lines*; the most important transitions are depicted by *arrows* and *wavy lines*; the typical values (in orders of magnitudes) of rate constants of the processes have been also included

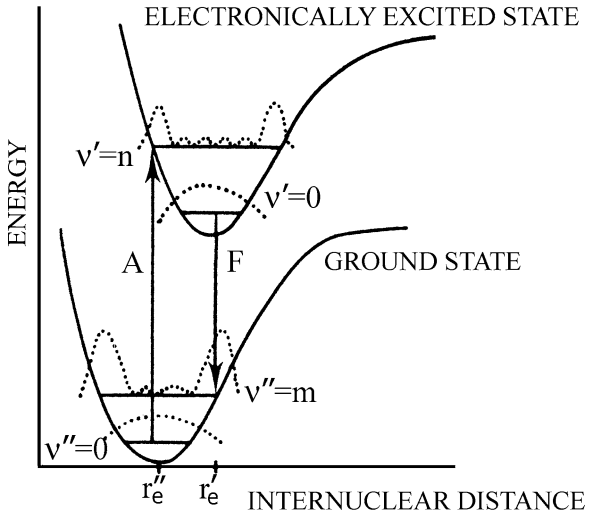

Fig. 2 The Franck–Condon principle: the energies of the ground and the first excited singlet states, S_0 (*lower curve*) and S_1 (*upper curve*), respectively, of a diatomic molecule are presented as functions of the distance between atoms, *r*. The probabilities of distances, *r*, are depicted by *dotted curves*; the *vertical arrows A* and *F* stand for absorption and emission, respectively

nuclei nor of surrounding molecules change and the excitation proceeds adiabatically without interaction with the environment. Immediately upon excitation, the molecule still keeps its ground state geometry (the Franck–Condon principle) [4, 5]. The excitation of a diatomic molecule is depicted in more detail in Fig. 2. Here, the energies of the ground and excited states (together with several vibrational levels) are drawn as functions of the distance between the atoms. The scheme is supplemented by several vibration wave functions to see the spatial overlap. The spatial overlap of wave functions shows that the absorption generates both the electronic and vibration excited state.

The vibration relaxation proceeds in most nonviscous solutions at timescales of 10^{-14}–10^{-12} s [6]. The excess energy is transferred to the surrounding medium during collisions of vibrating molecules with solvent molecules efficiently and quickly, because the collisions proceed roughly at the same frequency as vibrations (i.e., 10^{12}–10^{14} collisions s^{-1}) and the masses of colliding species are comparable. The series of nonradiative relaxation processes in the excited state involves one more process – the relaxation of the microenvironment that proceeds only in condensed polar systems. This process will be discussed in detail below (see Sect. 2.3).

So far, we have considered only the excitation to S_1. If the molecule is excited to a higher electronic state (S_2, S_3, etc.), in the overwhelming majority of cases, it reaches the lowest excited singlet state S_1 on the picosecond timescale by a cascade of nonradiative (vibration relaxation) processes and only then can the emission of a photon occur. There exist only a few exceptions from this rule, e.g., azulene [7], which exhibits fluorescence from S_2.

When describing the fluorescence as an observable spectroscopic phenomenon, we have to discuss the depletion of the excited state in a large ensemble of molecules. Even though the concentration of fluorophores and the fraction of excited molecules in fluorescence measurements are low (typically 10^{-6}–10^{-5} mol L^{-1} and less than 10^{-6}, respectively), the common steady-state irradiation generates about 10^9 excited molecules per milliliter. The depletion of the excited state is a stochastic process that involves a number of independent competing contributions, both radiative (fluorescence) and nonradiative (internal conversion or intersystem crossing to the triplet state T_1, both followed by the vibration relaxation). The probabilities (and rate constants) of individual contributing processes depend on the chemical nature of the molecule (on its spectroscopic properties) and on interactions with surrounding molecules.

The process that we are interested in, is the spin-allowed $S_1 \rightarrow S_0$ emission of a photon (fluorescence). Analogously to the absorption, its probability depends on the change of the dipole moment during the transition. It also depends on the energy difference between S_0 and S_1 [3]. For a fully allowed (spin, symmetry, overlap allowed) spontaneous emission, the quantum mechanics calculations predict a rate constant of about 10^9 s^{-1}. This means that the natural lifetime of the excited state of most molecules are in nanoseconds and that the depletion rate, measured as the number of excited photons per time unit (light intensity), after a short excitation pulse decays (in a simple case exponentially) on the nanosecond timescale. The observed lifetimes are often much shorter because different nonradiative processes contribute significantly to the depletion of the excited state. In some cases, they can be longer (10^1–10^2 ns) if the transition is not fully allowed, e.g., (a) the symmetry rule is not obeyed, but antisymmetric vibrations relax the selection rules or (b) the spatial overlap of the ground and excited state wave functions is small.

Because the probabilities of absorption and emission depend on dipole moments in the same states, there exists a straightforward (linear) relationship between the molar absorption coefficient and the rate constant of the spontaneous emission (the higher the probability of absorption, the higher the emission) [7]. However, the observed fluorescence intensity is often much weaker than that expected, because the competitive nonradiative processes can deplete the excited state much faster than fluorescence. Hence, according to the Franck–Condon principle, the molecule finishes in a higher vibrational level of the ground state S_0. Then, a fast vibrational relaxation takes place that causes the intrinsic Stokes shift (the red shift of fluorescence with respect to absorption) [8]. One more fact is important and should be kept in mind for further discussion: the absorption and emission of a photon by a particular molecule are two almost infinitely fast events, but they are separated by a time window of nanoseconds.

There exist a number of competing nonradiative processes that deplete the excited state and quench the fluorescence. The first one is the internal conversion, IC. Its rate varies over a wide range of orders of magnitudes. Its probability (efficiency) depends on the structure and properties of the molecule and on interaction with surrounding molecules. It can be affected experimentally, e.g., by the choice of solvent. For flexible and strongly interacting molecules, the process can proceed on

the picosecond timescale and can deplete the excited state before the considerably slower emission occurs. This explains why most molecules do not exhibit any fluorescence at all and only fairly rigid molecules are strongly emitting fluorophores, and why the fluorescence intensity increases in viscous solvents, at low temperatures (when the mobility of molecules and both the frequency and energy of collisions decreases), and in nonpolar solvents (where the interactions with solvent molecules are relatively weak).

Another important nonradiative process is the $S_1 \rightarrow T_1$ intersystem crossing, ISC. This transition is strictly forbidden by the spin-selection rule [2], but the selection rule is in reality relaxed by spin–orbital interaction in many systems that contain heavy atoms in the molecule (in this respect, the adjective "heavy" is relative: even carbon is heavy enough to break the rule). The probability (rate) of ICS depends on the energy difference between S_1 and T_1. For molecules with energetically close S_1 and T_1 states, the process can be very efficient (k_{ISC} ca. 10^{12} s^{-1}) due to the resonance effect and intermixing of S_1 and T_1 states. For other molecules with a large energy difference between the excited singlet and triplet state, the role of ISC is negligible.

After the $S_1 \rightarrow T_1$ transition, the molecule finishes in a dangerous situation. It contains a lot of excess energy and is therefore more reactive than in the ground state. The probability of photon emission and its return to the ground state S_0 (phosphorescence) is low because it represents the spin-forbidden transition and, in this case, the difference between T_1 and S_0 energies is large. The danger derives from a high probability of collisions with other molecules, which can cause a photochemical reaction and creation of a new chemical species (i.e., destruction of the original one). Indeed, most photochemical reactions involve molecules in T_1 state (as reactants, photosensitizers, etc.) [3]. It follows from the above outline that the phosphorescence is red-shifted with respect to fluorescence and that its intensity is usually very low due, in part, to its low natural rate (rate constants k_P ca. 10^{-3}–10^3 s^{-1}) and to efficient competitive nonradiative depletion of the T_1 state (mostly by vibrational relaxation, collision energy transfer, etc.). In some cases (if S_1 and T_1 states are energetically close), the molecule can gain enough energy either during collision with non-reactive solvent molecules or as a result of triplet–triplet annihilation and return to S_1. In this case, delayed fluorescence can be observed [3], but we will not discuss this process in detail.

Before we finish the general outline, a few characteristics have to be defined. The total rate constant of the depletion of the excited state S_1 is the sum of rate constants of all monomolecular depletion processes, $k_{tot} = \sum k_i$. If some bimolecular processes such as collision quenching contribute, then the corresponding terms would be the products of the pertinent bimolecular rate constants and quencher concentrations. The fluorescence quantum yield is the ratio of photons emitted per given number of absorbed photons, $q_F = N_{em}/N_{abs}$. It is (in contrast to the quantum yield of chemical reactions) always lower than 1 and it can be expressed as the ratio of time constant of fluorescence and the total rate constant, $q_F = k_F/k_{tot}$. Analogously the quantum yields of other processes can be defined.

In an ensemble of equivalent fluorophores (which concerns both their chemical structure and environment), e.g., in a dilute solution, the fluorescence intensity

after excitation with an ultrashort pulse decays exponentially. The experimental fluorescence lifetime (time in which fluorescence decays to 1/e of the initial value), τ_F, is the reciprocal value of k_{tot} ($\tau_F = 1/k_{tot}$). If individual fluorophores experience different microenvironments (in heterogeneous systems), their emission wavelengths and decay times differ and therefore the emission band is fairly broad, sometimes bimodal or multimodal and the decay is no longer single-exponential.

In the time window between the absorption and emission of a photon, a number of molecular processes can occur. They concern either (a) the fluorophore itself (its rotational and translational diffusion, conformational changes, transition between electronic states differing in dipole moment) or (b) molecules in its immediate vicinity (reorganization of the solvent shell, diffusion of quenchers, etc.). All these processes influence the fluorescence properties (position and shape of the emission band, quantum yield, decay time, etc.). In most cases, both the fluorophore and the surrounding molecules participate in the process and fluorescence characteristics are in fact influenced by their mutual interactions. Figure 3 shows a survey of important

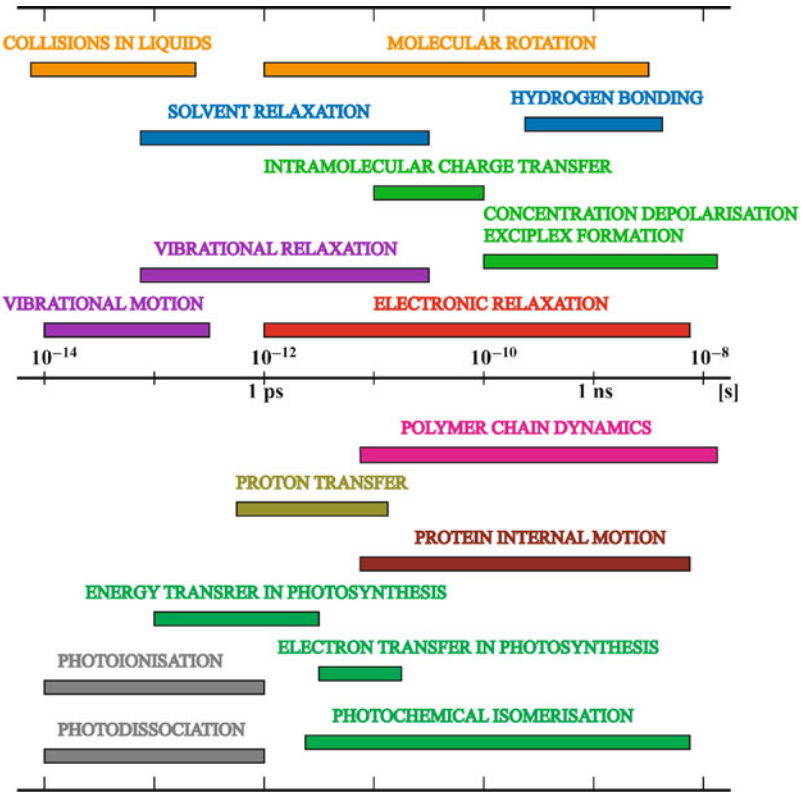

Fig. 3 The outline of fast dynamic processes: the rate of the polymer chain dynamics (vibrational motion and relaxation) strongly overlaps that of electronic relaxation and can be studied by the time-resolved fluorescence

dynamic processes that proceed at comparable velocities with the depletion of the S_1 state and can be studied by time-resolved fluorescence spectroscopy (TRFS). Some of them will be addressed in more detail in Sect. 2.2.

2.2 Time-Resolved Fluorescence Anisotropy

The photon absorption probability by a given molecule depends on a magnitude of the absorption dipole moment, $\boldsymbol{\mu}_A$, and on its orientation with respect to the excitation polarization described by the angle ϕ. The molecules with their transition dipole moment parallel to the excitation polarization are excited preferentially, while those oriented perpendicular are not excited at all. For a general orientation, the dipole moment can be decomposed into parallel and perpendicular components, $\boldsymbol{\mu}_A \cos\phi$ and $\boldsymbol{\mu}_A \sin\phi$, respectively, and the excitation probability is simply proportional to $(\cos\phi)$. The absorption and emission transition dipole moments, $\boldsymbol{\mu}_A$ and $\boldsymbol{\mu}_E$, can form any angle, ω; however, they are usually parallel in fluorophores containing symmetry planes.

Although the fluorophores are usually oriented randomly before the excitation (e.g., in solutions), the population of excited molecules with $\boldsymbol{\mu}_A$ parallel with respect to excitation polarization dominates immediately after the short polarized excitation pulse. The anisotropic orientation of excited molecules starts to relax due to the rotational Brownian motion of fluorophores and the excitation energy migration among fluorophores. The rate of the latter process depends strongly on the distance between fluorophores, and an appropriate dilution suppresses its effect considerably. The relaxation can be monitored by measuring the time-resolved fluorescence anisotropy, which is defined as $r(t) = [I_{II}(t) - I_{\perp}(t)] / [I_{II}(t) + 2I_{\perp}(t)]$, where $I_{II}(t)$ is the parallely polarized and $I_{\perp}(t)$ is the perpendicularly polarized fluorescence intensity with respect to the excitation pulse.

The theory shows that the time-resolved fluorescence anisotropy $r(t)$ is the autocorrelation function of orientations of the absorption dipole moment at the instant of excitation of a molecule, $\boldsymbol{\mu}_A(t=0)$, and that of emission at the time t, $\boldsymbol{\mu}_E(t) : r(t) = 2/5 \langle P_2(\boldsymbol{\mu}_A(t=0)\boldsymbol{\mu}_E(t))\rangle$, where P_2 stands for the Legendre polynomial of the second order and brackets $\langle\rangle$ denote the ensemble averaging. The initial anisotropy, $r(t=0) = r_0 = 0.6\cos\omega - 0.2$ depends on the angle ω between $\boldsymbol{\mu}_A$ and $\boldsymbol{\mu}_E$ and varies between limiting values -0.2 and 0.4, for perpendicular and parallel orientation of $\boldsymbol{\mu}_A$ and $\boldsymbol{\mu}_E$, respectively.

In many fluid systems, the rotational diffusion proceeds at the timescales comparable with the fluorescence decay and can be used for studying the viscosity of the microenvironment, local geometrical constraints, segmental motion of polymer chains, etc. In non-viscous solvents, it decays usually faster than fluorescence, but in very viscous systems a full randomization occurs at times much longer than the fluorescence lifetime. The extrapolation to $t \to \infty$ yields the residual anisotropy, r_∞. In the case of some polymer systems with entrapped fluorophores, only a partial

(i.e., locally anisotropic) orientation reorganization of the fluorophore proceeds and therefore r_∞ can give a non-zero value.

There exist a number of models predicting the time evolution of $r(t)$ for small fluorophores in the solution. They differ in accuracy and detail of physical description and in mathematical approximations. The simplest rotational model is based on the Debye hydrodynamic theory [9]. It assumes that the rotational diffusion proceeds in small steps between collisions of the fluorophore with surrounding molecules. An analytical expression for $r(t)$ as a sum of several exponentials was first derived by Favro [10]:

$$r(t) = \sum_i A_i \exp\left(-\frac{t}{\tau_{c,i}}\right). \tag{1}$$

The number of terms (up to five, but only three of them independent) and values of pre-exponential factor A_i depend on the fluorophore symmetry and on the orientations of $\boldsymbol{\mu}_A$ and $\boldsymbol{\mu}_E$ in the molecule. The rotation correlation times, $\tau_{c,i}$, reflect the main components of the gyration tensor only. For the parallel orientation of both dipole moments, the initial anisotropy in a fluid system has the highest possible value, $r_0 = \sum_i A_i = 0.4$. In the case of a spherical rotor, fluorescence anisotropy reduces to a single exponential function. For a symmetric rotor, $r(t)$ is either single- or double-exponential, depending on the orientation of dipole moments with respect to the long axis.

A typical time evolution of fluorescence anisotropy is a monotonously decreasing function. However, the sum of several exponentials with both positive and negative prefactors derived on the basis of a rigid rotor model does not preclude increasing or even a non-monotonous time evolution. The non-monotonous time evolution has been observed for perylene excited to S_2 quite far in the "blue region" with respect to the emission [11]. It starts, as predicted for the perpendicular orientation of dipole moments, at $r_0 = -0.2$, but increases rapidly to a slightly positive transient value and then decreases more slowly to $r_\infty = 0$. The non-monotonous $r(t)$ decay can be rationalized by the solvent effect on the rotation of the flat disc-like perylene around three different axes.

If the fluorophore contains several energetically close excited states differing in the polarization direction [12, 13], the excitation to higher states is usually followed by a few vibrational relaxations routs. In this case, the emission is strongly depolarized from the very beginning and the anisotropy measurement is useless. However, a similar depolarization occurs if the angle ω (quite common for low-symmetry fluorophores) is close to the magic angle, $\gamma = 54.7^\circ$. In this case, $\cos\gamma = 1/3$ and the fluorescence is depolarized at $t = 0$.

The rigid rotor model has been currently used for small fluorophores, but it is not suitable for tagged or labeled polymers. In this case, $r(t)$ monitors a combination of a fast rotation of the fluorophore around one or several single bonds attaching it to the polymer backbone, and a slower complex motion of a part of the chain together with the fluorophore. The relatively slow rotation of the whole polymer coil proceeds on a longer timescale than the fluorescence decay and is "invisible" in the time-resolved fluorescence measurement. It can be detected as a

significant residual anisotropy. Therefore, the anisotropy decay is often fitted to a double-exponential function with a constant term r_∞. There exist several models describing the behavior of labeled polymers with fluorophores embedded in the main chain. A convenient formula has been derived by Valeur and Monnerie [14] in the form: $r(t) = r_0 \exp(-t/\tau) \exp(-t/\rho) \operatorname{erfc}\sqrt{t/\rho}$, where r_0 is the initial anisotropy, and τ and ρ are two rotation correlation times describing a perturbed "crankshaft motion" of several successive polymer segments. This model reflects the facts that (a) fast local motion of segments resembles the rotation of a crankshaft, and (b) simultaneous distortion of several successive dihedral angles lowers the corresponding rotational barrier considerably.

For successful monitoring of the microviscosity, one aspect is very important: the emission wavelength of the probe should not be polarity-dependent. In many systems, the solvent relaxation proceeds at a comparable timescale with the rotational diffusion of the probe (see Sect. 2.3), the shape of fluorophore with its solvate shell continuously changes, and the emission maximum shifts with time. In such a case, the anisotropy measurements at different wavelengths yield different rotation correlation times, because the red-shifted decay reflects the behavior of a more relaxed state than that measured in the blue part of the emission band [15].

Some information on the microviscosity can also be obtained by steady-state anisotropy measurements. A comparison of results for different media (e.g., for a series of mixed solvents differing in composition) is tricky and requires the measurement of fluorescence lifetimes. The steady-state anisotropy, $\langle r \rangle$, is a time-average weighted by the fluorescence intensity decay, $I(t)$:

$$\langle r \rangle = \frac{\int_0^\infty r(t) I(t) \mathrm{d}t}{\int_0^\infty I(t) \mathrm{d}t}. \tag{2}$$

From (2), it is evident that the average value depends on the fluorescence lifetime and that the long-living probes always yield low $\langle r \rangle$. The best probe for anisotropy measurement should have a little faster $r(t)$ than $I(t)$ decay. The same condition applies for the time-resolved studies. If $I(t)$ decays much faster than $r(t)$, only a small portion of $r(t)$ is accessible. In the opposite case, the decay curves have to be measured with high statistics in a broad time range, but only small initial parts of $I_{\mathrm{II}}(t)$ and $I_\perp(t)$ curves are exploited for the evaluation of $r(t)$ decays. This prolongs needlessly the time-correlated single photon counting (TCSPC) time.

Fluorescence anisotropy studies are popular in biological and biochemical research of lipid membranes [16–18], proteins [19–22], etc. and also in polymer science. They have been performed for monitoring the conformations and flexibility of polymer chains in dilute, semidilute and concentrated solutions [23–27], in polymer melts and blends [28–31], and also for studying polymer self-assembly [32–34]. Nowadays, steady-state and time-resolved fluorescence anisotropy are currently used methods in polymer chemistry.

2.3 Solvent Relaxation

2.3.1 Theoretical Background

The solvent relaxation method (SRM) is a technique that provides unique information on the polarity and viscosity (more precisely on mobility) of the fluorophore solvate shell. Suitable probes should exhibit a large shift of their emission maxima to longer wavelengths in media with increasing polarity, but their photophysics should not be too complicated; that is, neither the position nor the shape of the emission band should be significantly affected by specific effects like hydrogen bonding, promoted dissociation in the excited state, charge transfer, structural changes, etc. Measurements with specifically interacting probes are possible and they have been applied in a number of studies, because such probes exhibit large changes in dipole moment upon excitation and sometimes offer additional advantageous properties. However, the interpretation of their behavior is not universal and needs very detailed knowledge of the probe photophysics [35]. Hence, we will confine the discussion to relatively simple probes and describe the technique that was originally developed and first applied for monitoring the relaxation behavior of the solvate shell in simple liquids. Popular probes for this purpose are coumarin dyes [36–38] or prodan [39–41], which undergo large dipole moment changes upon excitation and show quite regular polarity shifts. Now, we will explain the solvent relaxation for the case of a regular fluorophore dissolved in a simple liquid.

As already mentioned, the necessary condition for any radiative electronic transition (both for absorption and emission) is the change of the dipole moment of the molecule. The solvent relaxation process is depicted in Fig. 4 for a fluorophore that is immersed in a polar solvent and has the excited state dipole moment, $\boldsymbol{\mu}^*$, higher than that in the ground state, $\boldsymbol{\mu}$. The vertical axis shows the Gibbs free energy of the solvated fluorophore. Prior to excitation, the optimum arrangement and orientation of polar solvent molecules in the solvation shell of the fluorophore (with respect to its dipole) minimizes the Gibbs free energy of the system. Solvent molecules are usually small as compared with the fluorophore and they catch up both with its translational and rotational diffusion.

The absorption of a photon occurs in less than 10^{-15} s and the "electron cloud" redistribution and the consequent change of the dipole moment, $\Delta\boldsymbol{\mu} = \boldsymbol{\mu}^* - \boldsymbol{\mu}$, of the fluorophore (precisely of its electronic part) are almost immediate processes as compared with the rates of motions of nuclei within the fluorophore and surrounding molecules. This means that immediately upon excitation, the geometry of the fluorophore and the arrangement of molecules in the solvate shell correspond to the ground state. The solvation is not the optimum one and the Gibbs free energy of the solvated fluorophore at early times after excitation is higher than that in the equilibrium state.

The orientation polarization motions of solvent molecules necessary for optimum reorganization of the solvent shell are slower than the vibrational relaxation of the fluorophore, and the free energy after the vibrational relaxation is therefore higher than that in the equilibrium state. Although the vibrational relaxation is a process

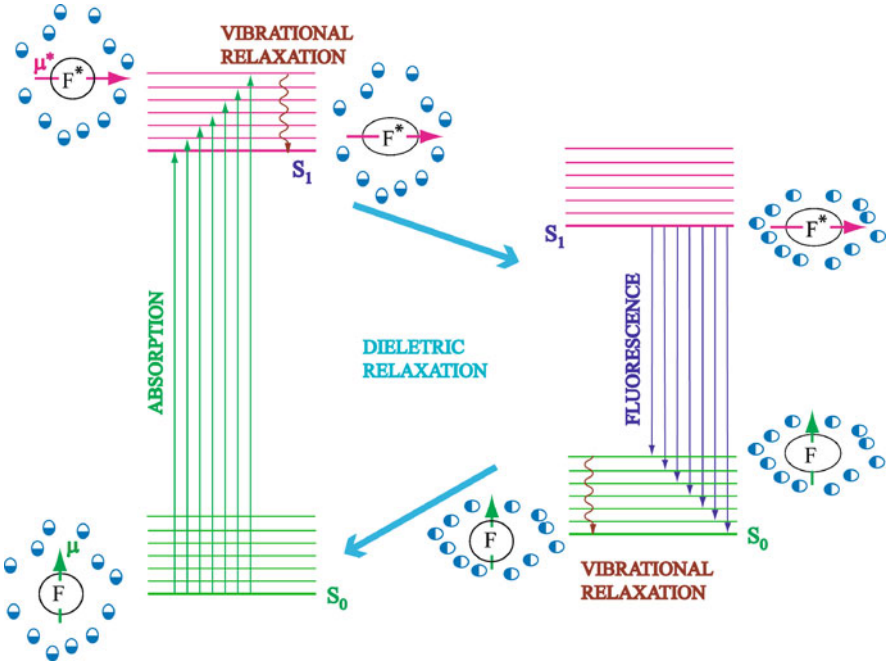

Fig. 4 Solvent relaxation: energies of the electronic states of a solvated fluorophore are depicted by *bold lines*, vibrational states by *thin lines*; the long arrows and *wavy lines* show individual processes; the changes of the dipole moment and geometry of the fluorophore upon excitation and emission are depicted by different orientations of the *short arrow* and the ellipsoidal prolongation. The changes in the arrangement and orientation of polar solvent molecules are also indicated

that occurs independently of the solvent polarity, the solvent relaxation proceeds only in polar solvents. Its extent is given by the strength of the dipole–dipole interaction between the fluorophore and the molecules in the solvate shell (local polarity of the nanoenvironment), while its rate reflects the mobility of the solvate shell (local viscosity of the nanoenvironment). In non-viscous solvents, the solvent relaxation can be quite fast and may partially overlap with the vibrational relaxation.

The next process is the emission of a photon. As already mentioned, the emission of photons in a macroscopic system of fluorophores proceeds on the nanosecond timescale. This means that most photons are usually emitted and detected from excited states with fully relaxed solvate shell. Because the excited state population decays exponentially, fast measurements enable detection of "hot" photons from non-relaxed states at early times. When discussing the relaxation at the level of a single molecule, we have to consider different timescales. An isolated single emission event is as fast as the absorption, and the electronic transition takes less than 10^{-15} s. It is evident that the fluorophore does not reach the relaxed ground state immediately after the emission of a photon. What follows, is a cascade of processes that resemble the mirror image of the above-described relaxations. Firstly, the vibrational relaxation occurs and, finally, the solvent equilibrates corresponding to

the ground state dipole. The above description explains the red-shift of the emission of common fluorophores in polar solvent, which is an experimentally recognized phenomenon known as the Stokes shift.

The simplest quantitative treatment of the solvent relaxation assumes that the fluorophore is placed in the cavity of radius a in the medium characterized by the relative dielectric permittivity ε and the refractive index n. It yields the Lippert equation [42] for the wavenumber shift between absorption and emission maxima of the fully relaxed host system:

$$\Delta\nu = \frac{2\left(\mu^* - \mu\right)^2}{hca^3}\left(\frac{\varepsilon - 1}{2\varepsilon + 1} - \frac{n^2 - 1}{2n^2 + 1}\right), \tag{3}$$

where h is the Planck constant and c is the light speed in vacuum. This equation offers the possibility to probe local polarity in heterogeneous systems (providing that the partitioning of the fluorophore between different domains is known).

2.3.2 Specific Features of Solvent Relaxation in Heterogeneous Systems

The majority of experimental works have addressed solvent relaxation in biological systems such as lipid membranes [43–45], proteins [46, 47], or nucleic acids [48], although a number of low-molar-mass systems have also been investigated [49–51]. Recently, very interesting relaxation processes on a relatively slow (nanosecond) timescale have been discovered in low-molar-mass solvent mixtures, reflecting the redistribution of solvent components in the solvate shell [52–54]. A couple of research groups have turned their attention to surfactants and polymeric nanoparticles (Pluronics micelles, etc.) [55, 56]. In the following discussion, we will focus on systems containing water-soluble nanoparticles with preferentially adsorbed probes that we studied experimentally. We will outline the strategy and goals of our studies and describe the methodology that we developed.

The studied aqueous system contains (a) relatively large polymeric nanoparticles, either simple spherical core–shell micelles or multilayer (onion skin) micelles, the hydrodynamic radius of which ranges from a few tens to one hundred nanometers; (b) much smaller fluorescence probes (units of nanometers), which have high affinity to the nanoparticle (otherwise they would escape in bulk solvent and would not report on the nanoparticle); and (c) even smaller solvent molecules. The fluorescent molecules are either hydrophobic or amphiphilic (fluorescent surfactants with a long hydrophobic tail and a water-soluble, often electrically charged fluorescent head group) and they bind in specific nanodomains in the core or close to the core–shell interface. The system is dilute, but the probes are localized either inside the nanoparticle or in the vicinity of its surface, where the concentration of polymer units is high. The discussion will be confined to fluorescent surfactants that physically bind in the inner part of the water-soluble shell of micelles formed by hydrophobic–hydrophilic copolymers. In contrast to the low-molar-mass solutions studied by SRM, the system is locally concentrated and strongly anisotropic.

The properties of the shell [density of polymer units, ionization degree (in weak polyelectrolyte shells), ratio of free-to-bound (solvating) water molecules, effective dielectric permittivity, etc.] change in the radial direction from the core–shell interface. In dense parts of the shell, the fluorophore often competes for water molecules with water-soluble polymer units. The relaxation of the solvate shell is very complicated compared with isotropic systems of small molecules and contains several contributions that differ significantly in relaxation rates. The complexity (when understood) offers an opportunity for detailed analysis, but a reliable knowledge of the behavior obtained by an independent method is indispensable. The time-resolved Stokes shift provides indirect information both on the solvation (hydration) of water-soluble polymer chains and on the segmental dynamics, because water molecules are engaged in the solvation of polymer segments, their motion is slowed down and coupled with segmental dynamics of polymer chains. If the affinity of the fluorophore to the nanoparticle is not high enough, the fluorescent part can move after excitation in the radial direction with respect to the nanoparticle and can experience higher microenvironment polarity during the lifetime of the excited state. This applies, e.g., to fluorescent surfactants with a short aliphatic tail that are not strongly anchored to the hydrophobic core. It is thus obvious that it is impossible to offer a universal scheme for the interpretation of solvent relaxation curves for systems containing fluorophores bound to nanoparticles. In Sect. 3.3, we will demonstrate that a careful analysis of data obtained by a combination of fluorescence SRM measurements with other experimental techniques provides details that are otherwise inaccessible, and that such an analysis helps to formulate reliable conclusions on the system behavior. As already mentioned, SRM has been very little used in polymer research so far. The main goal of pertinent parts of the paper is to "advertise" this technique and show its scientific potential.

2.4 Fluorescence Quenching and Nonradiative Excitation Energy Transfer

2.4.1 Fluorescence Quenching

In the preceding sections, it was shown that all nonradiative processes that compete with fluorescence shorten the fluorescence lifetime and weaken the emission intensity. Some of them, such as vibrational relaxation, depend on the fluorophore, solvent, and temperature. They predetermine the natural fluorescence lifetime, τ_{F0}, which is defined as the lifetime in the absence of any additional factors that can specifically quench the fluorescence. The molecules that strongly interact with the excited fluorophore are therefore called quenchers.

Fluorescence quenching requires a close approach of the quencher to the fluorophore and hence it can be used for studying various structural problems and dynamic processes. When both the fluorophore and quencher are dissolved in a solution, the time-resolved data report on the rate of diffusion. When the

fluorophore is covalently attached to a polymer that segregates in aqueous media into hydrophobic and hydrophilic domains, study with a water-soluble quencher can answer the question of whether the labeled part of a polymer chain is accessible to water or not. Fluorescence quenching experiments are easy to perform and they have been used in biochemistry and in polymer science since the early 1950s [57].

One can distinguish two types of quenching processes: (a) dynamic (collision) and (b) static quenching. In the first case, the quencher (usually a transition or heavy metal ion, a complex containing a metal ion, a molecule containing a heavy atom, or oxygen) collides with excited fluorophore. During the contact, the excitation energy is transferred to the quencher and dissipates into the surrounding medium. This quenching affects the lifetime and consequently the emission intensity. Both fluorescence characteristics fulfill the well-known Stern–Volmer equation [58]:

$$\frac{F_0}{F} = \frac{\tau_{F,0}}{\tau_F} = 1 + K_{SV} c_Q, \tag{4}$$

where F_0 and F, and $\tau_{F,0}$ and τ_F are the steady-state fluorescence intensities and fluorescence lifetimes in the absence and presence of the quencher, respectively. K_{SV} is the dynamic Stern–Volmer constant, which is a product of the dynamic quenching rate constant k_q and the fluorescence lifetime in the absence of the quencher, $K_{SV} = k_q \tau_{F,0}$, and c_Q is the concentration of the quencher. If the motion of the fluorophore and quencher is a free diffusion, the dynamic quenching constant, k_q, is a product of the quenching efficiency, γ, and the diffusion-limited bimolecular rate constant for collision, k, which can be calculated from the Smoluchovski equation:

$$k = 4\pi D R_{mol} N_A, \tag{5}$$

where D and R_{mol} are the sum of diffusion coefficients and molecular radii, respectively, and N_A is the Avogadro number.

Quenching may also occur by a static process, which does not involve diffusion, due to a reversible formation of a nonfluorescent fluorophore–quencher complex in the ground state. In this case, part of fluorophore is incorporated into the complex and does not contribute to the fluorescence at all, and another part of the fluorophore exhibits the unaffected fluorescence with the natural fluorescence lifetime, $\tau_{F,0}$. The intensity of the fluorescence in the presence of the quencher is weaker, but the lifetime is unaffected. The Stern–Volmer plot is again linear and reads:

$$\frac{F_0}{F} = 1 + K_A c_Q, \tag{6}$$

where K_A is the association constant for the fluorophore–quencher complex. It is evident that a combination of steady-state and time-resolved measurements allows an unambiguous discrimination between pure static and dynamic quenching. An independent test can be based on measurements at different temperatures. Increasing temperature accelerates the rate of diffusion and generally promotes the dissociation of the complex. Hence, the slope increases with temperature for dynamic quenching and decreases for static quenching.

In many real systems, the Stern–Volmer plots are not linear due to various transient effects, which might lead to an up-curvature of the plot. On the other hand, an uneven accessibility of fluorophores in heterogeneous systems causes down-curvature and the leveling of the plot. Quite a number of models for analyzing fluorescence decays in specific systems have been proposed in the literature [8].

2.4.2 Nonradiative Excitation Energy Transfer

The nonradiative excitation energy transfer, NRET (called also the resonance or direct energy transfer), belongs to processes that quench the fluorescence of the excited fluorophore (donor) by transferring the excitation energy to another fluorophore (acceptor) over nanometer distances. Its mechanism was first elucidated by Förster about 60 years ago. In contrast to collision quenching, which requires a close approach of interacting species, Förster quenching assumes a "long range" electrostatic interaction of the dipole moment of the excited donor and acceptor in the ground state. The theory predicts that the interaction strength decays with r^{-6}, which limits the NRET effect for most practically important donor–acceptor couples to the nanometer range. The transfer concerns the short-living and only weakly interacting excited states of both fluorophores and proceeds under the condition of the conservation of total energy as a resonant process. The energy conservation requires that the excited electronic state of the acceptor is either the same or slightly less than that of the donor, because some excess energy can be dissipated in the vibrational energy. From the spectroscopic point of view, it means that the emission band of the donor has to overlap with the absorption band of the acceptor. If the interaction is purely dipolar and weak, and if the rate of transfer is proportional to the square of vibronic interaction energy, then the Förster formula holds for the transfer rate constant [59–61]:

$$k_{\mathrm{T}} = \left(\frac{1}{\tau_{\mathrm{d}}}\right)\left(\frac{R_0}{R}\right)^6, \tag{7}$$

where τ_{d} the fluorescence lifetime of the donor in the absence of the acceptor, R is the distance between donor and acceptor, and R_0 is the Förster radius, which is defined as the critical distance for which the rate of energy transfer is the same as that of fluorescence:

$$R_0 = \frac{9(\ln 10)\kappa^2 Q_{\mathrm{d}} J}{128\pi^5 n^4 N_{\mathrm{A}}}, \tag{8}$$

where κ^2 is the orientation factor for the dipole–dipole interaction (depending on the angle between the involved dipole moments), Q_{d} is the quantum yield of the donor emission in the absence of the acceptor, n is the refractive index, N_{A} the Avogadro number, and J is the normalized spectral overlap integral given by:

$$J = \frac{\int F_{\mathrm{d}}(\lambda)\varepsilon_{\mathrm{a}}(\lambda)\lambda^4 \mathrm{d}\lambda}{\int F_{\mathrm{d}}(\lambda)\mathrm{d}\lambda}, \tag{9}$$

where $F_d(\lambda)$ is the emission spectrum of the donor (i.e., the fluorescence intensity of the donor in the absence of the acceptor at a given wavelength λ) and $\varepsilon_a(\lambda)$ is the molar absorption coefficient at the wavelength λ. The energy transfer efficiency ξ_T is equal to $k_T/(k_T + k_F + k')$, where k_T and k_F are the rate constant of the energy transfer and fluorescence decay, respectively, and k' is the sum of rate constants of all nonradiative de-excitation processes. ξ_T depends on the distance between the fluorophores, on the spectra overlap, and on the orientation factor κ^2 [62, 63]. This factor ranges from 0 to 4 depending on the orientation of fluorophores. It reaches the minimum value for the perpendicular orientation and the maximum value for the parallel and aligned orientation. Its evaluation causes some problems in experimental studies. For a random orientation of fast-rotating fluorophores, the averaging gives its "random dynamic" limit, $\kappa^2 = 2/3$.

Fluorescence quenching and NRET belong to popular fluorescence variants that have been exploited in a number of fields, including polymer and biopolymer research. NRET has been used in studies of polymer chain conformations [64–68], polymer miscibility [69–71], etc. Collision quenching, which reflects the accessibility of different quenchers, has been applied for testing the environment of pendant quenchers in polymer and biopolymer structures and associates [72–74]. Because the measurement is relatively simple, both techniques are "benchmark" fluorescence techniques in polymer science. Therefore, we could not avoid their use and, in spite of a number of review articles on that subject, we will briefly outline our results aimed at polymer self-assembly.

2.5 *Fluorescence Correlation Spectroscopy*

Fluorescence correlation spectroscopy (FCS) [75] is an optical method for studying dynamic processes, particularly the diffusion of intrinsically fluorescent or fluorescently labeled species, ranging from small molecules to nanoparticles. It has been widely used in biochemistry and biology [76–80], but its applications in polymer science [81, 82] are rather limited. In a typical experimental setup, the excitation beam passes through a very dilute (typically 10^{-9} M) solution of fluorescent particles and is focused in a very narrow region of roughly ellipsoidal shape. A small active (effective) volume, from which the signal (fluorescence emission) is detected, contains only a few fluorescent particles. The spatial profile of the excitation irradiation, $E(\boldsymbol{r})$, can be reasonably approximated by the Gaussian function:

$$E(\mathbf{r}) = E_0 \exp\left(-\frac{x^2+y^2}{2\omega_1^2} - \frac{z^2}{2\omega_2^2}\right), \tag{10}$$

where E_0 is the maximum intensity, $\boldsymbol{r} = (x, y, z)$ is the position with respect to the maximum irradiated center of the active volume and ω_1 and ω_2 are the half-axes of the ellipsoid and depend on the experimental setup. The fluorescent molecules undergo a translational diffusion motion, i.e., they enter and leave the active volume

and visit places irradiated with different intensity of the excitation beam. This affects the probability of excitation and causes non-negligible fluctuations in the fluorescence intensity.

The time-resolved monitoring and evaluation of the autocorrelation function of the emission intensity fluctuations yield information on the diffusion rate of fluorescent species. However, the experimental measurement is affected by a number of parasite side effects. First, the intensity of the focused beam is very high, which promotes photobleaching (mainly the transition to the triplet state). Hence, only a few very stable and resistant fluorophores (rhodamine dyes or BODIPY) can be employed and still an appropriate correction has to be used when evaluating the diffusion coefficients. Second, the multiple labeling of particles of finite size can generate additional problems. We will focus on some of these complications in Sects. 3.5 and 4.3.

The quantity measured in FCS experiments is the autocorrelation function of the fluorescence intensity fluctuations, $G(\tau)$, defined as:

$$G(\tau) = \frac{\langle F(t)F(t+\tau)\rangle}{\langle F(t)\rangle^2}, \tag{11}$$

where $F(t)$ is the emission intensity at time t and τ is the lag time. When it is assumed that the motion of photophysically and photochemically stable point-like particles is strictly diffusive, and the excitation intensity profile is exactly Gaussian, an analytical expression for the autocorrelation function can be derived in the form [83]:

$$G(\tau) = 1 + \frac{1}{V_{\mathrm{eff}} c_{\mathrm{F}}} \left(1 + \frac{\tau}{\tau_{\mathrm{D}}}\right)^{-1} \left[1 + \left(\frac{\omega_1}{\omega_2}\right)^2 \frac{\tau}{\tau_{\mathrm{D}}}\right]^{-1/2}, \tag{12}$$

where τ_{D} is the characteristic diffusion time and c_{F} is the average concentration of fluorescent particles in the active (effective) volume, i.e., their macroscopic concentration if we neglect the potential "optical tweezer" effect of the strong electric field. The illuminated effective volume V_{eff} is defined as:

$$V_{\mathrm{eff}} = \frac{\left[\int_V E(\mathbf{r})\mathrm{d}^3\mathbf{r}\right]^2}{\int_V E^2(\mathbf{r})\mathrm{d}^3\mathbf{r}}. \tag{13}$$

The characteristic diffusion time, τ_{D}, is the typical time within which a particle diffuses over the diameter of the active volume. It is related to the translational diffusion coefficient $D = \omega_1^2/4\tau_{\mathrm{D}}$. Of the parameters of (12), only three are independent. The parameters of the optical setup, V_{eff} and ω_1/ω_2 ratio, can be determined beforehand from an independent measurement using a small fluorophore with known diffusion coefficient (e.g., rhodamine B). Thus, only two unknown parameters, c_{F} and τ_{D}, remain to be obtained from the experimental data fit.

When discussing the application of FCS in polymer science, it is instructive to compare its advantages and disadvantages with the dynamic light scattering

(DLS) method, which serves as a "benchmark" technique for measuring diffusion coefficients of polymers. For sufficiently large, strongly scattering polymers and polymeric nanoparticles, DLS is a generally applicable technique and yields more precise data because it is less affected by parasite side effects and requires the evaluation of a lower number of unknown parameters from the fit than does FCS. A further advantage of DLS in comparison with FCS consists in the exponential form of individual contributions to autocorrelation functions, which facilitates the treatment of polydisperse systems and/or separation of translational diffusion of the particles from their internal motions by means of inverse Laplace transformation. Last, but not least, the possibility of performing angular measurements provides an additional piece of information on the character of processes that generate fluctuations in the scattered light intensity.

In contrast to light scattering (LS) techniques, FCS can be used for a wider range of particle sizes, but it requires strong fluorescence of the studied species. This apparent drawback is often advantageous and FCS can be used for studying relatively small fluorescent particles in an excess of strongly scattering large particles. Careful design of the FCS experiment (proper choice of the extrinsic probe, exploitation of the dependence of the quantum yield on experimental conditions, etc.) can add other advantages. For example, fluorescent surfactants with a long aliphatic tail are hardly soluble in water and form self-quenched dimers and trimers at concentrations well below the critical micelle concentration (c.m.c.). They bind strongly to polymeric nanoparticles in the form of monomers and the emission increases after binding. Hence, the partitioning of probes between nanoparticles and the bulk aqueous phase, and the potential presence of a fraction of free and fast-moving probes in the solution does not perturb the study of large labeled nanoparticles [84].

There is one more difference between DLS and FCS results. DLS provides the z-average D, which is strongly affected by the presence of small amounts of large and strongly scattering species such as microgels, micellar aggregates, etc. In some cases, the scattering can be dominated by traces of such strong scatters, and information on 90–95 wt% of the polymer material of interest is lost. In contrast to DLS, FCS yields the number average characteristics, which are equally affected by particles of all sizes and reflect their number fractions.

In our recent studies, we focused on several complicating factors arising in studies of nanoparticles of a non-negligible size (e.g., polymeric micelles, vesicles) that can carry several fluorescent labels. When the dimensions of such particles become comparable to the typical dimensions of the effective volume (ω_1, ω_2), the correlated motion of the fluorophores located on a single particle affects the shape of the autocorrelation function. Recently, an approximate expression for the FCS autocorrelation function of diffusing particles of finite size has been derived by Wu et al. [85]. They have shown that the autocorrelation function of uniformly labeled spherical particles can be expressed in a form similar to (12) where the diffusion time, concentration, and dimensions of the active volume are replaced by corresponding apparent quantities that depend on the particle size. Qualitatively, the same results were obtained in our computer simulations, which are discussed later (see Sect. 4.3).

Another contribution to the correlation function, which cannot be neglected for large particles, is their rotational motion. This problem has not been treated theoretically so far but intuitively one can expect that when a large particle rotates, the mean-square displacement of embedded flurophores would be larger than that without rotation. Hence, a higher apparent diffusion coefficient than that for a pure translational diffusion should be observed. Recently, we also addressed this problem in our computer simulations. Because the use of FCS in polymer science is very limited, we will describe its advantageous features in Sect. 3.5.

3 Fluorescence Studies of Self-Organizing Polymer Systems

3.1 Brief Introductory Remarks

In this section, we will outline our work [84, 86–98] performed either within (or strongly related to) the POLYAMPHI network. We selected four typical examples that show (a) application of different variants of TRFS and (b) their high research potential. We describe the motivation and strategy of each study, summarize the most important observations obtained by a combination of several experimental techniques underlining the results of fluorescence methods, and discuss their specific advantages. Finally, computer simulations aimed at the support and elucidation of the complex behavior are outlined (Sect. 4).

The first study [86] concerns the conformational transition of polyelectrolyte (PE) chains in aqueous solutions with pH. The only used experimental technique was time-resolved fluorescence anisotropy. The experimental work suggesting the formation of "supercoiled" globular structures within poly(methacrylic acid) (PMA) chains with decreasing degree of ionization was done before the publication of the highly recognized paper by Dobrynin, Rubinstein and Obukhov [99] and before our participation in POLYAMPHI. However, thanks to the advances in computer technology and the methodology of computer simulations, we were recently able to support our earlier conclusions, made on the basis of fluorescence study, by molecular dynamics (MD) simulations [87] (described in Sect. 4).

The second example concerns the multidisciplinary study of the micellizing block copolymer polystyrene-*b*-poly(2-vinylpyridine)-*b*-poly(ethylene oxide) (PS–PVP–PEO), which shows a high tendency to aggregation and the formation of micellar clusters [88, 89]. It shows the application of SRM for studying the mobility and structural details of different domains in micelle-like polymeric nanoparticles. The fluorescence technique reveals interesting features of studied systems that are hardly accessible by other techniques. Section 3.3 is devoted to the development of the methodology of the solvent relaxation technique for studying nanostructured self-assembling systems.

The third example concerns a series of our LS and fluorescence studies on the structure and dynamics of micellar shells formed by weak PEs [90, 91] and the effects caused by the hydrophobic modification of shell-forming blocks [92–96].

The knowledge of changes in the shell structure due to hydrophobic modification of micelles is very important for their application as vessels in targeted drug delivery systems. In commonly designed systems, a small number of targeting groups are attached at the ends of shell-forming chains. The targeting groups are usually quite large and complex structures and may have an amphiphilic character due to the presence of one or more hydrophobic domains. When attached to micelles, they could try to avoid the polar aqueous medium and bury partially in the shell, which would decrease the targeting efficiency. To address this problem, we performed studies of model micellar systems tagged by small, but strongly hydrophobic, fluorophores. The experimental study employed a combination of time-resolved fluorescence measurement of the nonradiative energy transfer with LS techniques and the data were interpreted with help of Monte Carlo (MC) computer simulations.

The last example is meant as a sort of advertisement of FCS in polymer research [84, 90, 97, 98]. This experimental technique is very popular in biochemical and biological research, but is only little used in polymer science.

3.2 Conformational Transition in Weak Polyelectrolyte Systems Studied by Fluorescence Anisotropy

3.2.1 Motivation

Weak PEs contain ionizable groups in their chains that can dissociate in polar solvents, leaving electric charges on the chain and producing small mobile counterions that can escape into the bulk solvent. In contrast to strong PEs, where the positions and the number of the charged groups on the chain is determined by the synthesis and are independent of external conditions (pH, ionic strength, etc.), the dissociation of weak PEs depends on pH, ionic strength and other parameters of the system. Under equilibrium conditions, the charges appear and disappear at different positions on the chain via reversible dissociation/association processes with a fairly high frequency. Hence, the distribution of charges is an "annealed variable" in contrast to strong PEs, where it is "quenched". This is why strong and weak PEs are also called "quenched" and "annealed" polyelectrolytes, respectively. Due to the high importance of PEs, their solutions and melts have been studied for a long time by a number of teams of experimentalists and theoreticians, and also by computer simulations [100]. The number of published studies is so vast that it is futile to give all relevant references. In the following text, we include only references to recent review articles and to the most important seminal studies relevant for the studied topic.

Because the understanding of the behavior of quenched PEs in solutions is much better than that of annealed PEs, first we will briefly summarize the most important conclusions concerning quenched PEs to show common features and then extend the discussion to weak PEs. It was realized relatively early that a sparsely ionized PE chain forms a compact globular conformation in a poor solvent whereas the

conformation of the chemically similar, but highly ionized polymer is much more expanded. Hence, the solvent quality for a PE not only depends on the polymer, solvent, and temperature but also on the degree of ionization. A poor solvent for a neutral chain can be a good solvent for the same polymer when it is charged. The first theoretical attempt to treat the quenched PE chain in poor solvent was made by Khokhlov [101]. He showed that a spherically symmetrical globular globular conformation deforms in a prolate ellipsoid (almost a cylinder) with increasing charge. More detailed (nowadays generally accepted) description is provided by the paper by Rubinstein, and Obukhov [99]. The article predicts the formation of "pearl necklace" structures as a series of collapsed parts of the chain (globules, pearls) interconnected by stretched parts of the chain (strings). This inspired by earlier theoretical works by Kantor and Kardar [102], who explained the pearl necklace formation by physical arguments as used by Rayleigh in 1882 when he explained the instability of charged oil droplets [103]. The repulsion of electric charges tends to expand the droplet, but the interfacial energy tries to contract it. When a critical charge is reached, the droplet becomes unstable and splits in two smaller droplets, which move away from each other, thus minimizing the Gibbs energy. Analogous arguments explain the formation of "pearls" on the chain. In poor solvents, an attempt to minimize the number of unfavorable interactions between the polymer segments and solvent molecules leads to a compact globular conformation with minimum surface area. When the charge in the globule is such that the Rayleigh instability condition is fulfilled, it splits in two smaller globules. Because of chain connectivity, the daughter globules (pearls) are kept at a certain distance by a stretched part of the chain and cannot separate from each other. The above hypothesis was confirmed both by MC and MD simulations [104, 105] and at present, it is a generally accepted scheme of behavior of quenched PE chains.

In annealed PE chains, the situation is more complex. The probability of dissociation of a particular ionizable group depends, among other factors, on its distance from the nearest already ionized group. Hence, the distribution of charges may change in a cooperative manner with changing conformation. Therefore, it is not surprising that both theoretical and computer studies predict behavior that differs from that of quenched PEs. It was theoretically predicted by Raphael and Joanny [106] that an annealed PE in poor solvent should undergo the first-order transition from a highly charged expanded conformation to a collapsed conformation with very low ionization degree with a change in pH. Recently, it was shown by MC simulations in a semi-grand canonical ensemble [107, 108] that this behavior occurs deep in the poor solvent regime. However, in a mild poor solvent (close to θ-conditions), the transition proceeds via the necklace of pearls. A number of theoretical studies and MC simulations that have appeared recently support the above scheme. Most of these studies confirmed the possibility of the cascade transition via the pearl necklace structure only under conditions close to the θ-state. However, some controversy still exists because, e.g., Ulrich et al. [109, 110] found the necklace of pearl structure in very bad solvents at high degrees of ionization, and other authors, e.g., Borukhov et al. argued that the plateau on the titration curve does not have to be related to the sharp conformational transition [111].

PMA belongs to the most common and most important weak PEs. The behavior of its aqueous solutions has been a subject of numerous studies [112–118], which started in early 1950s with the paper by Katchalski [112]. The most important achievements were made by Strauss et al. [113–116], Morawetz et al. [117], and by Ghiggino et al. [118]. It was soon recognized that PMA differs from other PEs, e.g., from chemically similar poly(acrylic acid). In 1985, Ghiggino and Phillips [118] were the first to propose the "necklace of pearls" model specifically for PMA on the basis of indirect fluorescence studies, i.e., more than 10 years before a similar model by Dobrynin became popular and generally recognized (however, their paper is almost unknown).

3.2.2 Outline of Experimental Study and the Most Important Observations

As already mentioned, our experimental study [86] was inspired by the Ghiggino work [118] and by papers published by the Morawetz group [117]. The study was performed several years before the the Dobrynin paper [99] and was aimed at better understanding the conformational transition at that time called "hypercoiling" or "supercoiling". We wanted to find our whether the transition proceeds as a cooperative sharp transition or as a progressive smooth process.

The strategy of the study was straightforward. A series of linear PMA samples differing in molar mass (M_w ca. 300,000) were synthesized and randomly tagged by pendant dansyl probes with degree of tagging below 1 mol%. Fluorescence lifetime and anisotropy measurements were performed in solutions differing in pH, ionic strength, and polymer concentration. The results were analyzed according to the model of Ghiggino and Phillips, and the working hypothesis that the supercoiling is a progressive process was tested. A dansyl moiety attached to the chain by a short flexible spacer (Fig. 5) is a suitable probe for this type of study. The position of the emission band does not depend on microenvironment polarity, but its quantum yield

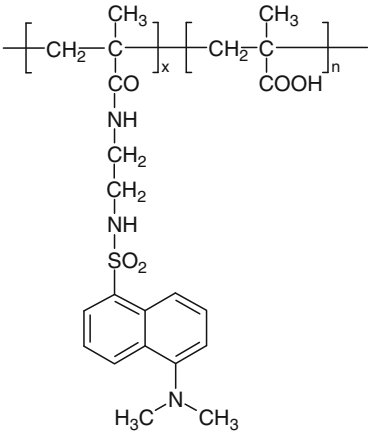

Fig. 5 The structure of dansyl-labeled PMA

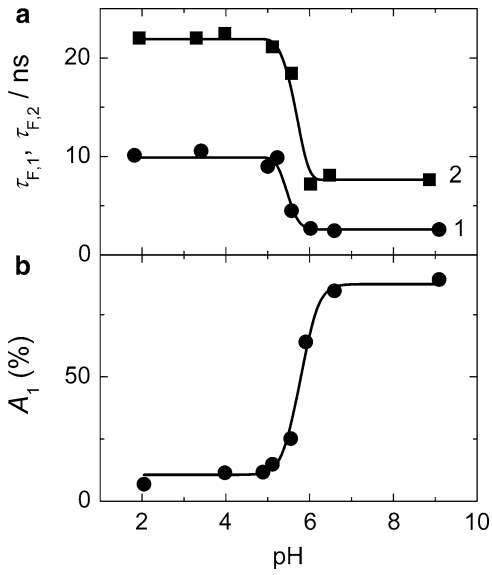

Fig. 6 Typical dependence of (**a**) the fluorescence lifetimes $\tau_{F,1}$ and $\tau_{F,2}$ (*1* fast process, *2* slow process) and (**b**) relative amplitude of the fast process A_1 of the dansyl-labeled PMA on pH

and fluorescence lifetime do. It is also a good probe for anisotropy measurements. The probes covalently attached to stretched parts of the chain (Fig. 5) are exposed to polar water molecules and can rotate fast, but those entrapped in nonpolar collapsed domains are considerably immobilized. It is evident that both the fluorescence and anisotropy decays monitor changes in chain conformation.

The most important results can be summarized as follows: The time-resolved fluorescence intensity decays measured in solutions of several PMA samples in a wide range of pH and ionic strength were always double-exponential. Both the short (units of nanosecond) and the long (tens of nanoseconds) fluorescence lifetimes increase with decreasing pH. Typical data are shown in Fig. 6a. The $\tau_{F,1}$ and $\tau_{F,2}$ dependences vs. pH (curves 1 and 2, respectively) exhibit a pronounced sigmoid shape, with the inflection point close to pH 5.5. The relative pre-exponential factor of the short-living fluorescence component, A_1, increases with increasing pH. The A_1 dependence on pH is depicted in Fig. 6b.

The obtained results can be explained as follows. In the pH region where the necklace of pearls structure exists, a fraction of probes are entrapped in compact globules and experience the nonpolar medium. The other probes attached to the stretched parts of the chains are exposed to polar water molecules. The probes are thus effectively distributed in two different microenvironments. The short lifetime corresponds to the water-exposed and the long one to the globule-embedded probes. The pre-exponential factors, when corrected by corresponding quantum yields, give the number fractions of both types of probes in the macroscopic ensemble. In the first approximation, the factors reflect the average numbers of monomer units in stretched and collapsed parts of the chain.

As the probe is more hydrophobic than the PMA monomer unit, we expect it induces a preferential collapse of the PMA chain in its vicinity. Nevertheless, the

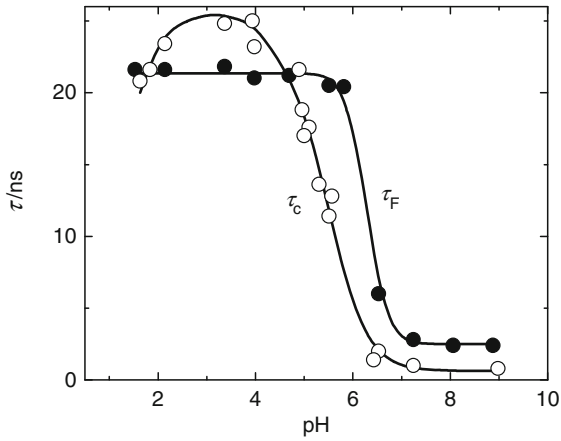

Fig. 7 Typical dependence of the mean rotation correlation time τ_c and the mean fluorescence lifetime τ_F of dansyl-labeled PMA on pH

measurements indicate that significant numbers of probes are exposed to water, even at low pH. A steep increase of fluorescence lifetimes and pre-exponential factor at around pH 5.5 suggests a sudden change in the microenvironment polarity of a considerable fraction of probes in a very narrow pH region.

Because of the complexity of the reorientation motion, we will discuss only the mean rotation correlation times, τ_c, even though the anisotropy decays indicate the presence of fast- and slowly rotating pendant probes. At high pH, the rotation correlation times are short (units of nanoseconds and less), but the residual anisotropy is non-negligible. It means that the rotation around single bonds of the spacer is fast, but reorientation does not proceed in all dimensions in the nanosecond time window. The τ_c dependence on pH is shown in Fig. 7. It is evident, that the reorientation slows down considerably with decreasing pH, but the change is quite gradual as compared with changes in mean fluorescence lifetime τ_F. The increasing values of the rotation correlation time reflect both (a) the locally restricted motion of the probe embedded in a collapsing part of the chain, and (b) rotation of the collapsed part of the chain around the axis defined by stretched parts connecting it with other globules (tens of nanoseconds are reasonable values for such a rotation). This type of "pseudo-one-dimensional" rotation of globules is supported by high residual anisotropy obtained at low pH.

A comparison of τ_F and τ_c vs. pH curves reveals interesting details: (a) curves in Fig. 7 differ in the steepness of the region close to their inflection points, and (b) onset of rising parts is shifted. Analysis of the above differences offers a deeper insight into behavior at the molecular level. The fluorescence lifetimes are sensitive to the polarity of the immediate microenvironment of the probe: when the chain starts to collapse at a certain pH, a small part of it reorganizes around the probe. Decreasing polarity hinders the dissociation of carboxylic groups in this domain and the interactions of the fluorophore with the microenvironment change suddenly (non-dissociated polymer units induce changes in the structure of water). The fluorescence lifetime is affected immediately and increases steeply with decreasing pH.

In contrast, the average rotation correlation time changes more slowly and we suppose that it better monitors the conformational behavior of PMA and shows gradual changes of chain conformations. A slow growth of τ_c is a result of a compromise between two effects: (a) the gradual increase in the mass of collapsing and fusing globules and (b) their increasing compactness. We believe that the comparison of τ_F and τ_c versus pH dependences supports the hypothesis that the conformational change is a gradual transition via the pearl necklace structures with pH. In the intermediate pH region, small globules grow and fuse with decreasing pH and simultaneously their density increases. At low pH, when only one compact globular conformation has been created, further decrease in pH promotes its compactness, which translates in its decreasing size and faster rotation. Hence the curve, which first rises with decreasing pH, drops appreciably in the low pH region.

The conclusions that we formulated in early 1990s are, in principle, in agreement with up-to-date knowledge. Water is a poor (but not too bad) solvent for non-ionized PMA and, hence, the conformational transition is expected to proceed not as a sharp transition, but via a cascade of pearl necklace structures. In Sect. 4.1, we will show that our recent MD simulations support the above description of the behavior. We included this almost-forgotten experimental study in the present feature article mainly because we returned to this problem and studied it theoretically within the POLYAMPHI network.

3.3 Solvent Relaxation Study of Self-Assembled Systems

3.3.1 Reversible Aggregation of Block Copolymer Micelles with PVP–PEO Shells in Acid Aqueous Solutions

Motivation

In a series of recent papers, we studied the copolymers containing PEO blocks [119–121]. PEO is biocompatible and easily soluble in aqueous media, and therefore it has been used as a shell of self-assembled biocompatible nanoparticles designed for targeted drug delivery [122]. The behavior of concentrated aqueous PEO solutions is fairly complex. It is influenced by the presence of a strongly hydrophobic ($-CH_2CH_2-$) group and hydrophilic (hydrogen-bonding) oxygen atom in its monomer unit. The amphiphilic character of PEO results in a strong aggregation tendency in some solvents. The presence of aggregated PEO chains in solutions has been proven by different experimental techniques, including light [123–127] and small-angle neutron scattering [128] and pulsed-field-gradient nuclear magnetic resonance (NMR) spectroscopy [125]. Even though various explanations of the aggregation mechanism (crystallization [123], inter-chain hydrogen bonding or the chain-ends effect [128], and subtle phase separation [129]) have been proposed, the exact origin of PEO aggregation under different conditions (PEO concentration, temperature, and also specific interactions with solvent molecules and other components) remains uncertain.

Some time ago, we investigated the behavior PEO-containing PE terpolymer PS–PVP–PEO in aqueous solutions [88, 89]. The micellization of this copolymer is strongly pH-dependent because PVP is protonized and therefore soluble in acidic solutions at pH lower than 4.8, but is deprotonized and therefore water-insoluble at higher pH. The PS–PVP–PEO micelle is a three-layer nanoparticle in which the PVP blocks form a middle layer between the rigid PS core and the PEO shell. The PVP layer is either collapsed at high pH, so that PS–PVP–PEO micelles resemble onion micelles formed in mixtures of PS–PVP and PVP–PEO diblock copolymers, or it is partially protonized, swollen, and flexible in acid aqueous media, so that the PVP layer becomes a soluble inner shell between the core and the outer PEO shell.

We found that the studied micelles containing long PEO chains, which should assure their solubility and thermodynamic stability, are surprisingly apt to a secondary aggregation and formation of micellar clusters. We suspected that the secondary aggregation of the PEO shell is caused by a hindered and incomplete solvation. Therefore, we supplemented the LS study of micellar solutions by SRM, with the aim of obtaining detailed information on the solvation of micellar shells.

Outline of Experimental Study and the Most Important Observations

The studied triblock copolymer PS–PVP–PEO was purchased from Polymer Source (Dorval, Canada). The number-average molar masses of PS, PVP, and PEO blocks were 2.1×10^4, 1.2×10^4, and 3.5×10^4 g mol^{-1}, respectively, and the polydispersity index of the sample was 1.10. The copolymer is insoluble in aqueous media, but the micelles can be prepared indirectly both in acidic and alkaline aqueous solutions by dialysis from 1,4-dioxane–methanol mixtures [88]. The micelles can be transferred from acidic to alkaline alkaline solutions and vice versa, but the addition of a base together with intense stirring promotes aggregation. Two factors contribute to the destabilization of micelles after the pH increase: (a) In alkaline media, the PVP blocks become insoluble, collapse and form an upper layer of the core. Since the cores of micelles are kinetically frozen, the association number does not change. The mass of insoluble cores increases, while the length of soluble shell-forming chains decreases, which results in a deteriorated thermodynamic stability of micellar solutions. (b) The PVP middle layer shrinks and PEO chains come close to each other, which worsens the solubility due to insufficient solvation of PEO blocks.

The most surprising feature of the behavior of PS–PVP–PEO micelles with water-soluble PVP (protonized) and PEO blocks in acidic media is their aggregation in the region of low pH. Because it is a rather unexpected phenomenon, we studied it in more detail. The distributions of relaxation times obtained by DLS are bimodal (Fig. 8). Angular dependences (not shown) prove that both fast and slow relaxation modes correspond to diffusive processes. The intensity of the slow mode decreases with increasing pH and decreasing copolymer concentration. At very low copolymer and HCl concentrations, the slow mode disappears completely. The DLS measurements thus show that PS–PVP–PEO solutions contain two types

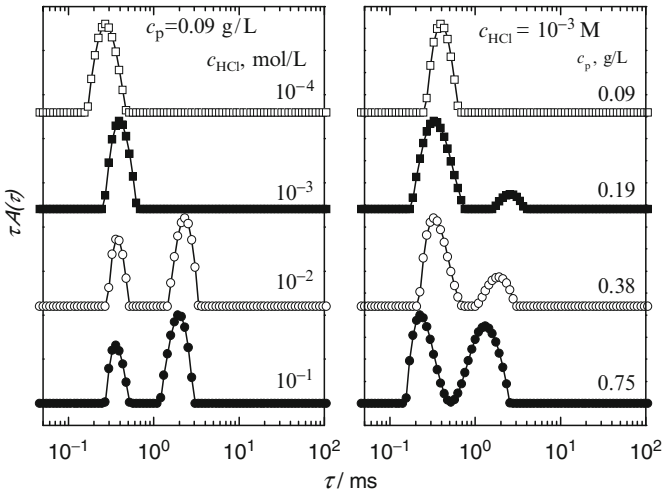

Fig. 8 Relaxation time distributions for PS–PVP–PEO solutions in HCl aqueous solutions, measured (*left*) at the copolymer concentration, c_p, of 0.09 g L^{-1} and HCl concentrations of 10^{-4}, 10^{-3}, 10^{-2} and 10^{-1} mol L^{-1}; and (*right*) in 10^{-3} M HCl, with copolymer concentrations of 0.09, 0.19, 0.38, and 0.75 g L^{-1}

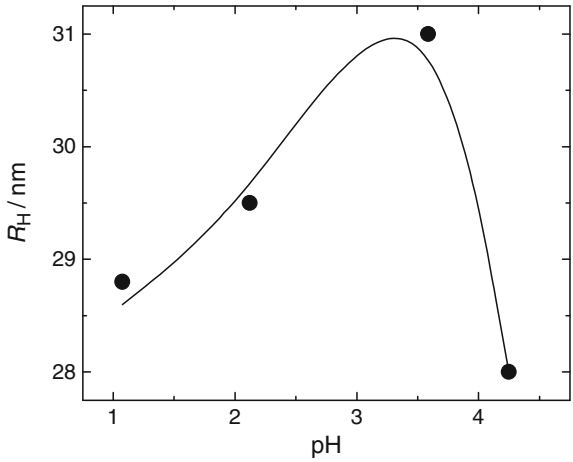

Fig. 9 Hydrodynamic radius, R_H, of PS–PVP–PEO micelles in acidic aqueous solutions, as a function of pH

of particles and the balance between individual micelles and aggregates shifts in favor of aggregates with (a) increasing concentration of HCl and (b) increasing copolymer concentration.

A strong effect of electrostatic screening is evident from the dependence of the size of micelles on pH (Fig. 9). In the pH range above 3, the concentration of ions and the screening are negligible and R_H increases with decreasing pH due to substantial protonization of PVP blocks. The maximum R_H is reached at around pH 3. Below this pH value, a decrease in R_H is observed due to electrostatic screening by an increasing concentration of small ions.

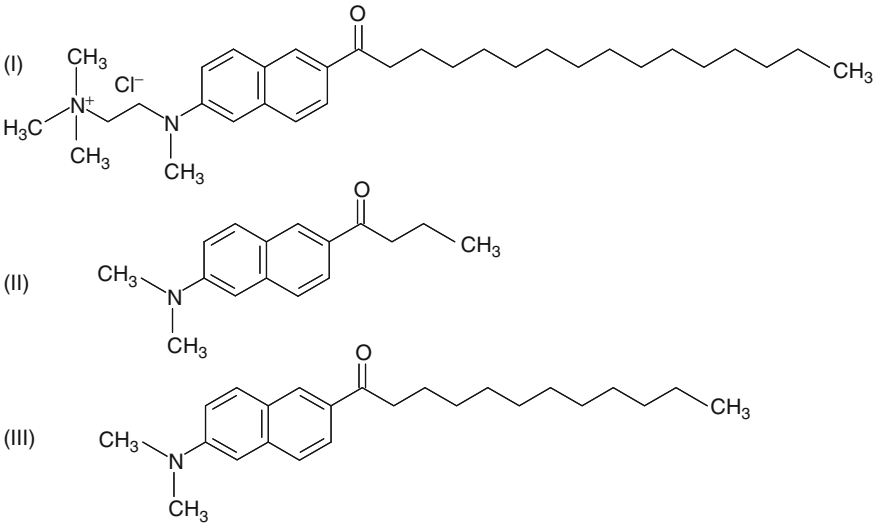

Fig. 10 Structures of (I) patman, (II) prodan, and (III) laurdan

Even though the aggregation of evenly charged micelles is a slightly surprising phenomenon, the effect of pH is an understandable result of electrostatic interactions. The addition of HCl supports the protonization of PVP blocks, but the H_3O^+ and Cl^- ions efficiently screen the electrostatic forces, which promotes the aggregation.

We performed the solvent relaxation study of acidic PS–PVP–PEO solutions with the aim of (a) proving the assumption that the formation of micellar clusters is a result of an insufficient solvation of PEO units, and (b) understandinghow the solvation is affected by pH and ionic strength.

First, we studied the solvent relaxation in solutions of diblock copolymer micelles. A commercially available polarity-sensitive probe, patman (Fig. 10, structure I), frequently used in phospolipid bilayer studies [123], was added to aqueous solutions of PS–PEO micelles. The probe binds strongly to micelles because its hydrophobic aliphatic chain has a strong affinity to the nonpolar PS core. The positively charged fluorescent headgroup is supposed to be located in the PEO shell close to the core–shell interface. The assumed localization has been supported by time-resolved anisotropy measurements.

The time-resolved emission spectra (TRES), $F_{TR}(\nu,t)$, were reconstructed using the steady-state emission spectrum, $F(\nu)$, and the fluorescence decays, $I(\nu,t)$, measured at different wave numbers ν, according to the formula [130]:

$$F_{TR}(\nu,t) = \frac{I(\nu,t)F(\nu)}{\int_0^\infty I(\nu,t)\mathrm{d}t}. \tag{14}$$

For monitoring the relaxation process, we used two parameters of the time-resolved emission spectrum: (a) the full width in the half-maximum (fwhm) at the time t after excitation, $\delta(t)$, and (b) the correlation function, $C(t)$, corresponding to the normalized time-dependent Stokes shift [130]:

$$C(t) = \frac{\nu_{\max}(t) - \nu_{\max}(\infty)}{\nu_{\max}(0) - \nu_{\max}(\infty)}, \tag{15}$$

where $\nu_{\max}$(t) the wave number of the emission maximum at the time t after excitation. The value,$\nu_{\max}(0)$, corresponding to the energy level of the maximum disturbed system immediately upon excitation is not experimentally available but can be estimated by assuming that the initial Stokes shift corresponds to the difference of the absorption maxima between the studied polar solvent and a nonpolar reference solvent (hexane, etc.) [131]. For patman, which is charged and insoluble in nonpolar nonpolar solvents, we used spectra of an analogous compound, prodan (Fig. 10, structure II), because their spectra are almost identical in a large series of common solvents.

The comparison of the span of measured values with that based on the "time zero" estimation suggests that at least 70% of the reorientation motion has been displayed by monitoring the fluorescence behavior of micelle-embedded patman with our instrumental setup (time resolution). Figure 11 (curve 1) depicts the relaxation correlation function monitored by patman bound to diblock PS–PEO micelles.

Furthermore, we measured the time-dependent halfwidth of the emission spectra, which provides useful information on the extent of the studied process. It has been shown that the halfwidth should be constant in continuously relaxing homogeneous systems. In spatially inhomogeneous systems, the relaxation behavior proceeds differently. Because the properties of the system vary in space, individual fluorophores distributed in the system are nonequivalent and their solvent shells respond with different rates to the local electric field. This inhomogeneity gives rise to a new phenomenon that reflects the time distribution of phases of

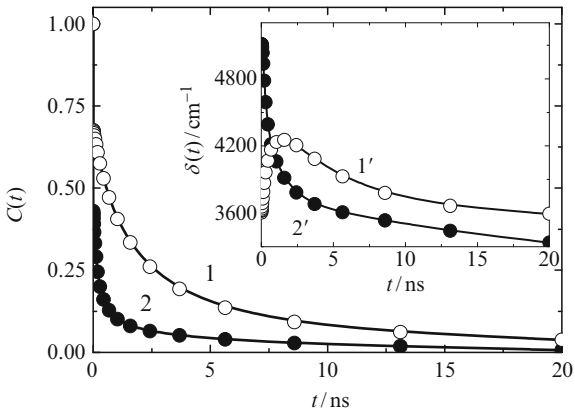

Fig. 11 Time-resolved Stokes shift, *C(t)*, of patman in PS–PEO micelles (*curve 1*) and PS–PVP micelles (*curve 2*). Inset: Time-dependent halfwidth of the time-resolved emission spectra of patman in PS–PEO micelles (*curve 1′*) and in PS–PVP micelles (*curve 2′*)

relaxations of individual solvation shells during the relaxation. The observed transient inhomogeneity increases significantly and the time-dependence of the observed halfwidth passes a pronounced maximum.

The time evolution of the halfwidth of the emission spectra provides information on whether the entire response, or just a part of it, was captured within the time-window of the experiment. If only a decrease is observed, the early part of the relaxation process is beyond the time resolution of the TCSPC equipment. By contrast, if only an increase is observed, the process is slow and the lifetime of the used fluorophore is not long enough for monitoring the overall relaxation process. The time evolution of the halfwidth is depicted in the inset in Fig. 11 (curve 1′). The curve with a well-pronounced maximum supports the conclusion that the experimental setup detects ca. 70% of the total response, which we have drawn from the "time zero" frequency estimate. Therefore, we assume that a major part of the relaxation dynamics of bound water molecules engaged in the solvation sphere of PEO units occurs in the nanosecond time-range and can be monitored by time-resolved fluorescence measurement.

In order to get an idea of where the dye is located in the micelle, we performed time-resolved anisotropy measurements. The anisotropy of polarity-sensitive probes is not a good tool for monitoring the microviscosity because both the reorientation time and the residual anisotropy are influenced by solvent relaxation, and are thus wavelength-dependent [15]. Nevertheless, the measurements provides rough information on the viscosity of the microenvironment of the probe. The measurement of decay curves was performed at different wavelengths. All decays clearly showed high residual anisotropy (Fig. 12), indicating that the dye is localized in a constrained and considerably rigid domain close to the core–shell interface.

To support the conclusion on the patman location, the PS–PEO micelles were also labeled by laurdan, which has a shorter aliphatic chain and almost the same fluorescent headgroup, but it misses the permanent charge at the nitrogen atom. The measurement shows that the entire Stokes shift is small and the microenvironment relaxation is very slow, without any fast process beyond

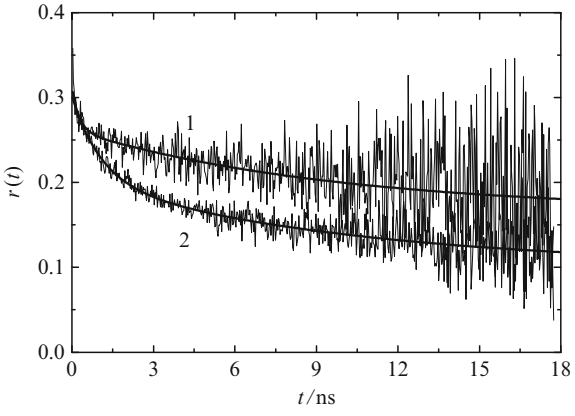

Fig. 12 Time-resolved anisotropy (experimental data and double exponential fits), *r(t)*, of patman in the PS–PEO micelles at emission wavelengths of 430 nm (*curve 1*) and 510 nm (*curve 2*)

experimental resolution. This indicates that the laurdan fluorescent headgroup is embedded in the PS core and that the aliphatic chain serves as an efficient anchor.

As we intended to study the pH-dependent hydration of PEO in triblock copolymer micelles, we measured the solvent relaxation for patman embedded in PS–PEO micelles both in acidic (0.01 M HCl) and alkaline (0.01 M NaOH) solutions for comparison. Because we found only marginal differences in the relaxation behavior, we can conclude that the dye itself does not exhibit any pH-dependent changes after binding to micelles and that the solvation of short PEO does not change much with pH (it is very important to emphasis that the PEO blocks are significantly shorter than those in the studied PS–PVP–PEO copolymer).

Consequently, the solvent relaxation was studied in PS–PVP micelles in 0.01 M HCl solution. The micelles are stable in acidic solution, where they are positively charged. Nevertheless, our earlier studies suggest that the PVP layer partially collapses around the core because PVP is only slightly protonized close to the nonpolar PS core [132]. A fairly high value of the residual anisotropy (around 0.2) measured at the maximum emission intensity (467 nm) suggests that patman is embedded in considerably rigid and little protonized domains close to the PS–PVP interface, which means that its location in PS–PVP micelles is similar to that in PS–PEO micelles.

The solvent relaxation in patman-labeled PS–PVP micelles is significantly faster than that in PS–PEO micelles. The shell-forming PVP chains are electrically charged and stretched at pH 2. A relatively open structure and low density of PVP shells assumes a considerable content of water and, therefore, an appreciable fraction of water molecules is not engaged in the solvation of PVP units. The fluorophore does not compete with PVP units for water molecules and the solvent reorganization is only weakly coupled with PVP segmental dynamics. The "time zero" estimation suggests that ca 60% of relaxation processes are beyond the experimental resolution. This conclusion is also supported by monitoring the fwhm that shows only the decrease (inset in Fig. 11, curve 2).

One can conclude that in both PS–PEO and PS–PVP micellar systems, the fluorescent surfactant patman is embedded in PEO-rich parts of the shell where the mobility of chains is strongly restricted. The differences in rates of the relaxation processes are mostly due to different solvation of the shell-forming chains and the different structure of water in the two types of shells. From the geometrical point of view, PEO chains are easily incorporated in the ice-like structure and the presence of both the hydrogen-bonding oxygen atom and the hydrophobic $–CH_2–$ group promotes the structure formation. The water-structure-supporting character of PEO is generally recognized and was confirmed by different experiments [133, 134]. The ice-like-structured water molecules bound to the concentrated and geometrically constrained (and hence only slightly mobile) PEO chains in the inner part of micellar shells are responsible for the slow relaxations in PS–PEO micelles.

After the study of reference diblock systems, the behavior of PS–PVP–PEO triblock was investigated in detail. For a correct interpretation of the pH effect on relaxation rates, the localization of the patman headgroup has to be known.

The following arguments support the assumption that it resides at the PVP–PEO interface and that pH changes do not cause hardly any displacements in the radial direction:

1. The hydrophobic chain tends to be buried in nonpolar parts of micellar structures (PS or non-protonized PVP), whereas the charged fluorophore headgroup prefers a polar environment.
2. At low pH, the swollen shell-forming PVP chains are partially protonized and we assume that the aliphatic chain of patman, which prefers the PS core to the partially protonized PVP, tries to pull the fluorophore closer to the core. However, the headgroup, which bears the same positive charge as the protonized PVP units, prefers the location in the PEO outer shell to the PVP middle shell due to electrostatic repulsion. Therefore, both effects roughly compensate each other and the location of patman hardly varies with pH. This assumption is supported by the experimental observation that in low pH solutions (below pH 4), both $C(t)$ and $\delta(t)$ show similar relaxation behavior as in PS–PEO micelles, which indicates the same microenvironment and supports the location of the headgroup in the PEO layer.
3. The time-resolved anisotropy measurements performed for pH 2 and 4 revealed fairly high values of the residual anisotropy (0.2 and 0.3, respectively), which indicates high rigidity of the microenvironment.
4. Fluorescence intensity measurements suggests that patman does not come to the immediate proximity of PVP segments: The patman fluorescence is quenched by deprotonized PVP chains. This was observed either in dioxane solution or in the alkaline solution of patman-labeled PVP–PEO micelles [89]. Becuase there is no observable decrease in fluorescence intensity for triblock copolymer micelles, it can be concluded that patman is not in direct contact with deprotonized PVP units.
5. Last, but not least, the measurements with increasing ionic strength of the solution at pH 2 did not show any effect on the solvent relaxation, which precludes significant displacement of patman in the radial direction from the interfacial region, either due to increasing protonization or to screening of electrostatic repulsion (at higher salt concentrations).

The correlation curves, as well as the shape of the time-dependent halfwidth, clearly suggest that the average mobility of the solvent molecules around patman decreases with increasing pH (Fig. 13). Although for pH 2–3, the limiting factor is the time-resolution of the instrumental setup, at pH 4, the relaxation processes is slow and its study is limited by the lifetime of the dye. We observe that the fast (experimentally unresolved) contribution decreases with increasing pH and that the nanosecond process, which is considered to be caused by the reorganization of bound water molecules engaged in the solvation sphere of PEO, prevails in the region of higher pH. At pH 4, we cannot monitor the end of the relaxation because the second contribution is too slow. The segmental motion and reorganization of the dehydrated polymer chains are assumed to be responsible for the slow relaxation, which exceeds the patman fluorescence lifetime.

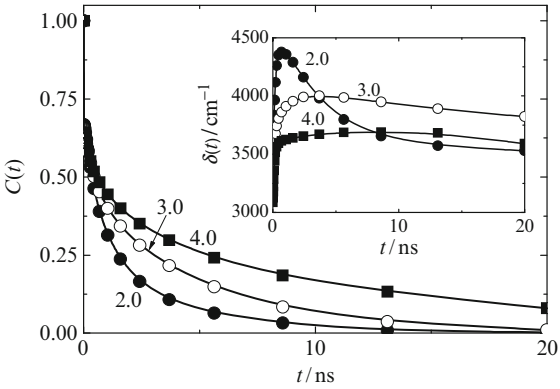

Fig. 13 Time-resolved Stokes shift, $C(t)$, of patman in PS–PVP–PEO micelles at pH values of 2, 3, and 4, as indicated on the corresponding curves. *Inset*: Time-dependent halfwidth, $\delta(t)$, of the time-resolved emission spectra of patman in PS–PVP–PEO micelles at different pH values, as indicated

The pH dependence of the solvent relaxation rate offers an explanation of the observed instability of micellar solutions at low pH and formation of a fraction of micellar clusters. The stability of micellar solutions assumes a proper solvation of PEO chains. However, PEO solvation promotes the ice-like structure and reduces entropy, which may cause solubility problems in systems with crowded PEO chains such as micellar shells formed by long PEO blocks. The addition of HCl (or other small ions) breaks the water structure, increasing the fraction of free and mobile water molecules, and reduces the fraction of PEO solvation-capable structured water molecules. Regarding the enthalpy-to-entropy interplay, the effect of increasing acidity resembles the effect of increasing temperature in the lower critical solution temperature (LCST) region. In both cases, the mobile solvent molecules would have to "condense" at the chain to assure its solubility and sacrifice considerable translational entropy. Regarding the LCST, the unfavorable entropy contribution increases with increasing temperature and at LCST, the phase separation occurs. In the studied case, the entropy contribution increases with the concentration of HCl: the mobile water molecules "liberated" due to the breakdown of the ice-like structure after the addition of small ions would have to form the structured solvation shell of PEO monomer units to provide sufficient thermodynamic stability of micelles in the solution. The complex entropy-to-enthalpy balance shifts towards free water molecules with decreasing pH, which promotes the formation of micellar clusters and minimizes the fraction of water molecules engaged in solvation shells.

The relaxation behavior at pH 1 is very interesting, but we could not analyze it because the time-resolved emission bands were bimodal. We studied the possibility of analyzing complex time-resolved spectra and in our recent paper [135] we describe a successful method of decomposition and treatment of bimodal time-resolved spectra. We used two probes with the same fluorescent headgroup differing in the length of the aliphatic tail. They have different affinity to micelles that allows study of their partitioning between micelles and bulk solvent. A detailed description and extended discussion exceeds, unfortunately, the scope of this paper, but we not only succeeded in treating the two time-resolved contributions (from free and micelle-solubilized probes) separately, but we also identified a slow contribution due to the

motion of the probe with respect to micelle upon excitation. Because the solvent relaxation processes are very specific and complex, we have not yet attempted to perform the corresponding computer simulations.

3.4 Study of Shell-Forming Chain Conformations by Nonradiative Energy Transfer

3.4.1 Studies of Reference Systems of Nonmodified Weak Polyelectrolyte Shells in Solutions with Low Ionic Strength

Motivation

The properties of PE micelles in aqueous solutions are determined by the behavior of micellar shells, which can be regarded as convex PE brushes. Depending on the degree of charging and ionic strength, the PE brush can undergo several patterns of behavior. In systems where the density of charge on the PE chains is high, the electrostatic force acting on counterions is strong and prevents their escape in bulk solvent, which means that the brush remains electrically neutral. At low ionic strength, the osmotic pressure is high and individual brush-forming chains are strongly stretched. The brush is swollen and obeys the osmotic regime. In solutions with high ionic strength, the excess of small ions screens electrostatic interactions and the brush collapses, obeying the salted brush regime. We have been systematically studying the behavior of both hydrophobically modified and unmodified PE shells by a combination of several experimental techniques. Even though we have been interested mainly in modified systems, which we studied using fluorescence techniques, first we had to study the corresponding unmodified micelles as reference systems for comparison.

Outline of Experimental Studies and the Most Important Observations

The micelles were prepared by stepwise dialysis of diblock copolymer PS–PMA from mixed solvents to pure water. The copolymer contains one PS and one PMA block with an almost identical number of monomeric units (about 200). Further experimental details and copolymer characterization are given in [90]. Micelles were characterized by static light scattering (SLS) and DLS. The Zimm plot of experimental data in a borate buffer is regular and we used it for the evaluation of the weight average molar mass (M_w) of micelles and their radius of gyration. The scattering functions depend almost linearly on q^2 (scattering vector), which indicates that the micelles interact weakly with each other and that their interaction can be described by the excluded volume effect only. The monodisperse spherical micelles were further visualized by atomic force microscopy after their deposition on a fresh mica surface [90].

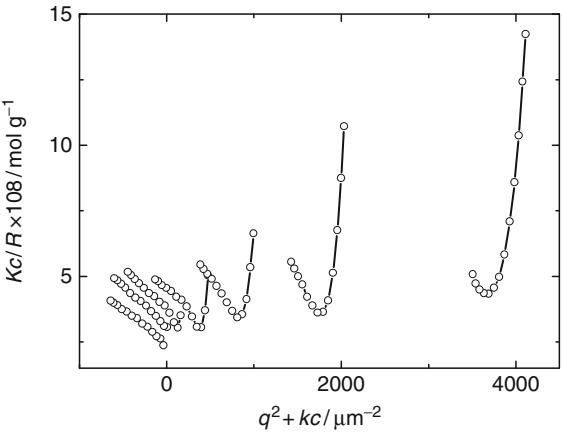

Fig. 14 Zimm plot of PS–PMA micelles in pure water (concentration range: 2.5×10^{-3} to 2.0 g L^{-1})

The Zimm plot of micelles in a solution with extremely low ionic strength, which was prepared by repeated dialysis against an excess of deionized water in plastic flasks to prevent an alkaline ions release from glass, is shown in Fig. 14. At medium concentrations, one can observe an enormous deviation from the regular (linear) behavior. The dependences exhibit minima at q values that change with concentration. Such type of behavior is due to spatial correlations between individual micelles and is typical for strongly interacting systems. Because the irregular shape is observed at concentrations at which the average distances between micelles exceed 10–20 times their diameter, it suggests that structural correlations of scatters and the observed destructive interference of the scattered light at non-zero angles is due to long range electrostatic forces between significantly charged micelles.

We can conclude that that the "charged osmotic brush" regime, in which counterions escape into bulk solvent, can be observed when the experiments are performed in solutions with pH close to pK_A at very low ionic strength. Because our study provided the very first indirect evidence of behavior of PE micelles that, at that time, was only hypothetical and highly doubted by recognized theoreticians, we were looking for independent support and performed an MC study (see Sect. 4.2).

3.4.2 Nonradiative Energy Transfer Study of Conformations of Hydrophobically Modified Shell-Forming PMA Chains

Motivation

Many systems based on water-soluble block copolymer micelles have been developed and studied as vehicles for targeted drug delivery [122, 136, 137]. A typical copolymer suitable for such applications should fulfill several conditions: biocompatibility, biodegradability, and the ability to form hydrophobic domains that are capable of solubilizing and delivering hydrophobic drugs. The nanoparticles for an efficient targeted delivery have to bear targeting (recognition) groups at

their periphery. They are usually chemically attached to the shell-forming blocks [138–142]. The targeting groups are chemically complex structures and may have an amphiphilic or partially hydrophobic character that could influence the targeting effect. In other worlds, their interaction with water does not have to be favorable and they could try to escape from the energetically unfavorable aqueous surrounding at the micellar periphery and bury deep within the shell close to the hydrophobic core. When this happens, their disappearance from the uppermost part of the shell negatively affects the drug delivery efficiency.

We addressed the above problem by studying a system of modified PS–PMA micelles with long PMA blocks end-tagged by a strongly hydrophobic molecule in mixtures of water with organic solvents and in purely aqueous media where electrostatic effects dominate the behavior [93–96]. We used anthracene (An) as the end-attached hydrophobic group, which allowed for fluorescence study. When we started the study, it was not a priori clear what would happen when such slightly modified micelles were dispersed in aqueous media.

Outline of Experimental Study and the Most Important Observations

For the experimental study, we used two almost identical PS–PMA samples, very similar to those studied in the above-described study. The first sample contained one pendant naphthalene group (Np) in between PS and PMA blocks. The second sample was tagged by Np in the same way as the previous one, but also by one An at the end of the PMA block. The two fluorophores, Np and An, were chosen because they represent a suitable pair for NRET studies and they can be chemically attached to specific sites of the studied system [143].

Experimental results were obtained by two experimental techniques, LS and TRFS. When the micelles are formed, all attached Np molecules (potential excitation energy donors) are localized at the core–shell interface. The Np fluorescence quenching due to NRET is expected if some energy traps (An) come relatively close to Np, i.e., to distances shorter or comparable with the Förster radius, R_0 (for the Np–An pair, ca. 2.1 nm [144]). Hence, the NRET study should prove whether a fraction fraction of shell-embedded An could closely approach the core.

The time-resolved quenching of the Np emission due to Np-to-An energy transfer is shown in Fig. 15. Three transfer-affected fluorescence decays (measured in the double-tagged system) normalized by decays in the absence of traps (measured in the single-tagged system under identical conditions) are plotted as functions of time in solvents differing in polarity (1,4-dioxane/water mixtures). The broken-like curve obtained in water-rich media, consisting of a steeply decreasing part and a constant part with almost no smoothly curved part in between, can be neither explained nor fitted by assuming any type of a continuous monomodal distribution of Np–An distances [92, 95]. It suggests the existence of two types of Np donors, which are either very strongly affected by NRET, or fully unaffected. In a spherically symmetrical system in which all Np are uniformly distributed in a narrow spherical layer at the core–shell interface, the concept of two types of Np molecules looks strange.

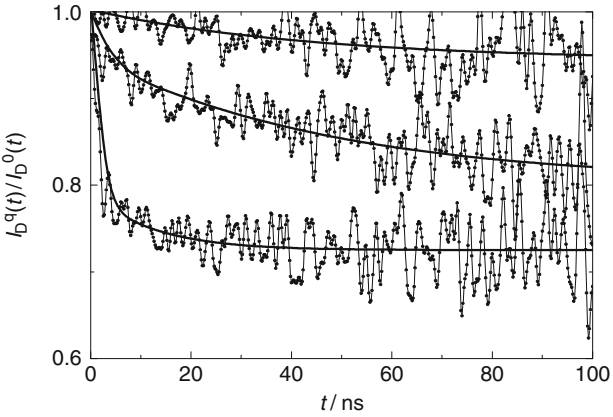

Fig. 15 Experimental kinetic NRET curves (Np-to-An energy transfer) of fluorescently labeled PS–PMA micelles in 5% water, 95% 1,4-dioxane (*top*); in 20% water, 80% 1,4-dioxane (*center*); and in water (*bottom*). Experimental data fitted by multiexponential functions

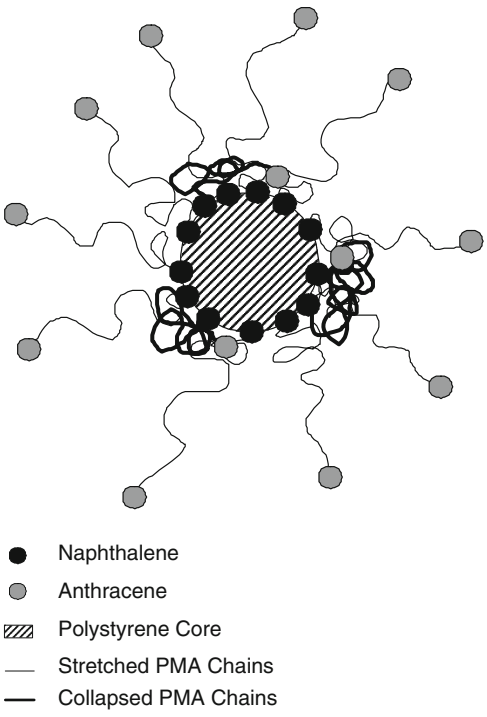

Fig. 16 Hydrophobically modified PS–PMA micelles with attached Np and An probes

However, it can be rationalized when we postulate a rather specific conformational behavior of An-tagged shell-forming chains, which is depicted in Fig. 16.

The model assumes the coexistence of two distinctly different conformations created by identical shell-forming chains in each micelle under equilibrium

conditions. The coexisting forms are (a) strongly collapsed and (b) stretched chains (see Fig. 16). Accepting the above scheme, it is obvious that some Np donors are affected by pendant An traps, which return in their immediate vicinity, while the other Np donors remain unaffected. Because in a typical fluorescence measurement, the fraction of excited fluorophores is less than 10^{-6}, a maximum of one Np per micelle is excited in the experimental study. Hence, the fluorescence decay from some micelles is very strongly quenched and that from others is unaffected by NRET, which leads to the "broken-like" time-resolved fluorescence response.

A pronounced bimodal distribution of chain conformations in a micelle that contains about 10^2 chains is something that one would hardly expect in an equilibrium system, even though bimodal distributions have been tentatively proposed for some other equilibrium polymer systems [145]. To elucidate the studied problem, we performed a series of simulations for modified micellar shells using the MC technique for neutral systems and the combined MC-mean field simulation. The simulations are described later (see Sect. 4.2).

3.5 Comparative Experimental FCS and DLS Study of Polymeric Nanoparticles

3.5.1 Motivation

For almost a decade, we have been using both DLS and FCS for studying various self-assembling polymer systems. We have developed a simple titration method for the evaluation of the number-average molar mass, M_n, of amphiphilic water-soluble nanoparticles. This method is very useful because the M_n of large particles is not easy accessible by common techniques such as osmotic pressure measurements, which lose precision for masses exceeding 10^5 g mol^{-1}. In the developed FCS method, an aqueous solution of the fluorescent surfactant with a strong affinity for polymeric nanoparticles and the self-quenched fluorescence (due to the formation of associates) is continuously added to the aqueous solution of nanoparticles. At relatively low fluorophore-to-nanoparticle ratios, ξ, single fluorophore molecules (which are no longer self-quenched) bind to different nanoparticles and the fraction of labeled fluorescent particles increases, which means that the particle number, $\langle N \rangle$, measured as the frequency of fluctuations, grows. When $\xi = 1$, each nanoparticle is on average labeled by one fluorescent probe (in reality, there is a Poisson distribution of the number of probes per one micelle) and the added probes start to bind to the already labeled polymer particles. If the size of nanoparticles is small enough, the frequency of fluctuations stops increasing and levels off, because the detector registers the double-labeled (or multiply-labeled) particle as one "point". The only difference is that some fluctuations are larger that the other. The experimental frequency as a function of the added amount of the probe consists of a linearly increasing and a constant part. The crossing point yields the number concentration of nanoparticles and the M_n. Very soon, we observed that the method gives

good results for small nanoparticles (R_H ca. 10–30 nm, M_n ca. 10^5–10^7 g mol^{-1}), but it strongly underestimates molar masses of large nanoparticles (R_H higher than 50 nm). Because the M_n evaluation is very simple and does not require fitting the correlation curve, the analysis of discrepancies is straightforward and shows that the multiple labeling of large particles causes a higher frequency of fluctuations than that corresponding to the correct particle number. A careful comparison of results of both methods (based on autocorrelation functions) shows that they agree reasonably well for small and monodisperse particles, whereas for large particles, FCS yields very low values for $\langle R_H^{-1}\rangle_n^{-1}$ in comparison with the LS data and that the different polydispersity-affected averaging procedures cannot explain the observed differences. Therefore, we decided to perform a systematic comparative study devoted to the solution of the above open questions. In Sect. 3.5.2, we present some unpublished preliminary data on that topic.

3.5.2 Outline of Experimental Studies

In several of our papers [84, 90, 97, 98], we describe the characterization of various amphiphilic block copolymer micelles by FCS. The amphiphilic fluorophore octadecyl rhodamine B (ORB, Fig. 17) was used as a fluorescent marker for the micelles. ORB is suitable for labeling the micelles because it has a very low intersystem-crossing rate, which makes it highly resistant to photobleaching. Moreover, the contribution of the free probe emission to the signal is typically lower than 10% under the used experimental conditions because (a) free ORB in aqueous solutions forms self-quenched aggregates with a low fluorescence quantum yield, and (b) ORB is sparingly soluble in water and has a high binding affinity to amphiphilic block copolymer micelles in aqueous media. Using time-resolved fluorescence measurements, the partition coefficient, K, between PS–PMA micelles and bulk aqueous solution was found to be 1.5×10^5 [84].

In the experiments described below, FCS measurements were performed for varying concentrations of ORB added to the studied solution of micelles. The obtained autocorrelation curves were fitted to the function, assuming the presence of two types of fluorescent particles (free probe and labeled micelles) characterized

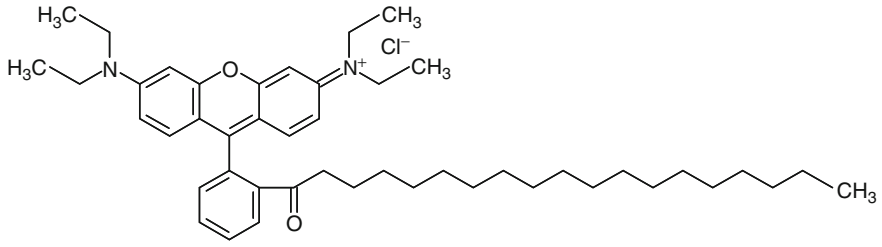

Fig. 17 Octadecyl rhodamine B

by diffusion times $\tau_{D,1}$ and $\tau_{D,2}$, absorption cross-sections σ_1 and σ_2, and fluorescence quantum yields q_1 and q_2:

$$G(\tau) = 1 + \frac{1 - \Phi(1 - e^{-\tau/\tau_C})}{\langle N \rangle (1 - \Phi)} \sum_{=1}^{2} Y_i \sigma_i^2 q_i^2 \left(1 + \frac{\tau}{\tau_{D,i}}\right)^{-1} \left[1 + \left(\frac{\omega_1}{\omega_2}\right)^2 \frac{\tau}{\tau_{D,i}}\right]^{-1/2}, \tag{16}$$

where $\langle N \rangle$ is the particle number, Φ is the fraction of molecules converted to the triplet state and τ_C is the characteristic time for the transition (τ_C^{-1} is the transition rate), Y_1 and Y_2 are the molar fractions of the two types of particles, and ω_1/ω_2 has the same meaning as in (12). It is necessary to point out that the simple model assumes only diffusive motions of point-like particles and does not account for photon correlations caused by rotational motion of the micelles or by multiple labeling, which will strongly affect the behavior of large particles (R_H exceeding 50 nm) in the FCS experiment.

Figure 18 shows a typical dependence of the particle number on the ORB concentration, c_{ORB} (the inset in Fig. 18 shows a typical FCS autocorrelation function). As explained in the previous section, the curve reaches the limiting value, $\langle N_{sat} \rangle$, at the ORB concentrations at which virtually all micelles bear at least one ORB label. Provided that the effective volume, V_{eff}, is known from an independent calibration measurement based on the acquisition of $\langle N \rangle$ for a fluorescent dye solution of a known concentration, the M_n of micelles can be calculated using a simple relationship:

$$\langle M \rangle_n^{FCS} = \frac{cN_A}{\langle N_{sat} \rangle V_{eff}}, \tag{17}$$

where c is the weight concentration of the copolymer and N_A is the Avogadro constant. The diffusion time of the labeled micelles, yields the number-average translational diffusion coefficient of the micelles, $\langle D \rangle_n = \omega_1^2/4\tau_{D,2}$, from which the hydrodynamic radius, $\langle R_H^{-1} \rangle_n^{-1}$, can be calculated using the Stokes–Einstein formula.

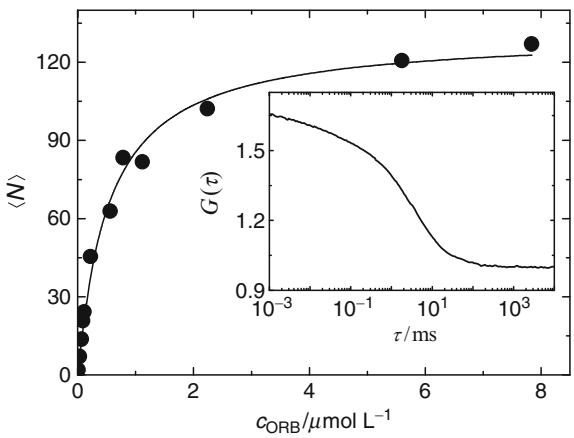

Fig. 18 Particle number, $\langle N \rangle$, as a function of the fluorescent probe concentration, c_{ORB}, for PS–PVP–PEO micelles in 0.01 M HCl. *Inset*: Typical correlation curve for an FCS measurement of ORB-labeled PS–PVP–PEO micelles 0.01M HCl

Table 1 Molar masses and hydrodynamic radii of several micellar systems, measured by light scattering and by FCS

Copolymer[a]	Solvent	$M_w \times 10^{-6}$ (g mol^{-1})[b]	$M_n \times 10^{-6}$ (g mol^{-1})[c]	$\langle R_H^{-1}\rangle_z^{-1}$ (nm)[b]	$\langle R_H^{-1}\rangle_n^{-1}$ (nm)[c]	Ref.
PS_{198}–PMA_{221}	0.05 M $Na_2B_4O_7$	8.0	4.7	54	42	[84]
PS_{136}–PVP_{117}–PEO_{795}	0.01 M HCl	2.7	0.5	37	28	[97]
PS_{136}–PVP_{117}–PEO_{795}	0.01 M NaOH	5.4	1.1	35	22	[97]
PS_{272}–PMA_{155}	0.01 M $Na_2B_4O_7$	3.0	2.3	30	–	[90]
PS_{29}/PVP_{217}^{d}	0.1 M HCl	0.8	0.5	32	28	[98]

[a]Subscripts denote degrees of polymerization of the blocks
[b]Measured by LS
[c]Measured by FCS
[d]Multiarm star copolymer with 20 PS_{29} and 20 PVP_{217} arms

Table 1 summarizes the molar masses and hydrodynamic radii of several amphiphilic block copolymer micelles obtained by FCS and LS measurements. Not surprisingly, values found by LS are larger due to the very high sensitivity of LS to larger particles (LS provides M_w and z-average provides the diffusion coefficients). A closer inspection of data and of experimental conditions is interesting, e.g., for PS–PVP–PEO micelles, the differences are very pronounced. One source of discrepancy is the different concentration ranges used in FCS and LS. As the FCS measurements were performed at lower concentrations, the differences reflect the secondary aggregation of PS–PVP–PEO micelles at higher concentrations, i.e., in the concentration range of LS measurements (units of g L^{-1}). Under experimental conditions of FCS measurements (polymer concentrations about 10^{-2} g L^{-1}), only individual micelles are present in the solution. Table 1 includes data for relatively small nanoparticles only. The effect of the size of studied nanoparticles has already been described in Sect. 3.5.1. To get better understanding of the effects caused by multiple labeling, etc., we performed a series of MC simulations (see Sect. 4.3).

4 Interpretations of Fluorescence Data with the Help of Computer Simulation

4.1 Interpretation of Time-Resolved Fluorescence Anisotropy Data by Molecular Dynamics Simulations

In a series of simulation papers, we used MD for studying the conformational behavior of linear and branched PEs. In one study, we addressed the time-resolved fluorescence anisotropy decays from fluorescently tagged weak PE chains in aqueous media, which we had experimentally studied earlier (see Sect. 3.2). We wanted to investigate and explore the relationship between the conformational behavior of the PE and the experimentally observable fluorescence anisotropy decays.

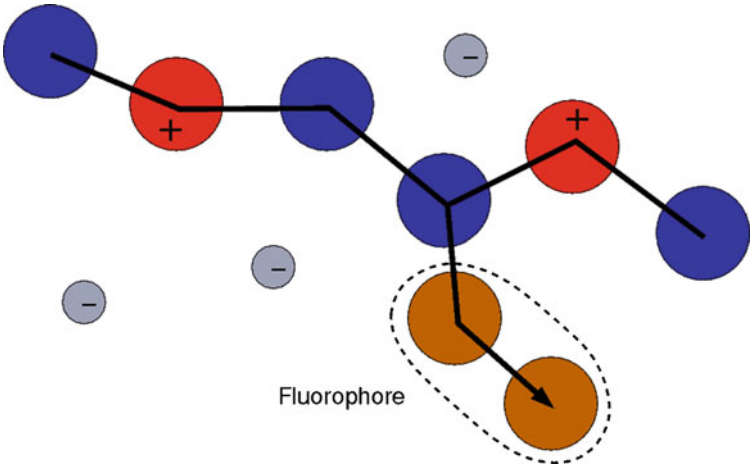

Fig. 19 Polymer model used in the simulations. *Red* uncharged monomer units, *blue* charged monomer units, *grey* counterions, *brown* fluorophore

4.1.1 The Model

In the simulation study of fluorescence anisotropy decay, a generic bead-spring model of the polymer was used. It is schematically shown in Fig. 19. Each bead can represent one or several monomer units in a real polymer. The degree of dissociation, α, is defined as the fraction of monomer units carrying electric charges. The interaction between monomer units of the polymer is modeled by the Lennard–Jones potential and the solvent quality is controlled by the depth of this potential, ε. As shown by Micka, Holm and Kremer, $\varepsilon \approx 0.34$ corresponds to the theta state [146]. The simulation study was performed for several values of $\varepsilon > 0.33$, i.e., under poor solvent conditions. The simulation technique used was MD coupled to a Langevin thermostat, i.e., the polymer was simulated in an implicit solvent. The counterions were simulated explicitly. A more detailed description of the polymer model can be found in the original paper [87].

The fluorophore was modeled by two beads that are attached as a short pendant side-chain (tag). Both the absorption and emission dipole moments of the fluorophore are defined by the direction of the tag (parallel), as indicated by the vector in Fig. 19, and the fluorescence anisotropy was calculated from its orientation autocorrelation function. For simplicity, we assumed that the reorientaional motion of the fluorophore is the only source of fluorescence depolarization. We neglected energy transfer and other processes that might occur in real systems. The fluorescence anisotropy decays were interpreted using the mean relaxation time, defined as:

$$\tau_{\text{mean}} = \frac{\sum_i A_i \tau_i}{\sum_i A_i} = \int_0^\infty r(t)\mathrm{d}t. \tag{18}$$

There were two reasons for using the mean correlation time, τ_{mean}, rather than relaxation times of individual modes, τ_i: (a) experimental data were analyzed in the same way, (b) individual components, τ_i, reflect different types of the real motion, but they have no clear physical meaning in the coarse-grained model.

4.1.2 Conformational Behavior

Here, we summarize the patterns of conformational behavior that obviously affect the fluorescence anisotropy decay. For a detailed discussion we refer the reader to the original paper and references therein [87]. The conformational behavior of the polymer reproduced by simulations is in line with theoretical predictions [99] as well as other simulation works [104, 105]. The basic trends are depicted by a few snapshots in Fig. 20. With increasing degree of charging, the polymer undergoes the following conformations: a collapsed spherical conformation (Fig. 20a) deforms first in a prolate ellipsoid (Fig. 20b). At higher degrees of charging, it goes through a series of pearl-necklace structures with gradually increasing number of pearls (Fig. 20c). At high degrees of ionization, it ends up in an expanded conformation (Fig. 20d).

4.1.3 Comparison of Simulated and Experimental Data

The simulation study was aimed at the question of whether our intuitive interpretation of experimental fluorescence anisotropy data on PMA solutions was correct

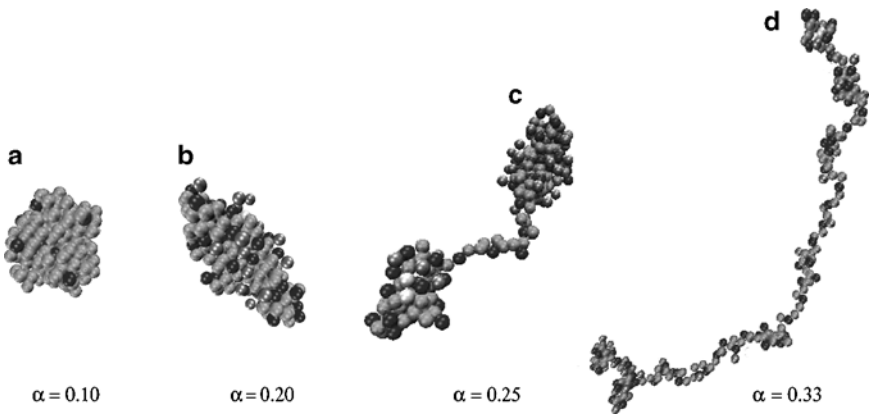

Fig. 20 Polyelectrolyte conformation as a function of the degree of dissociation (α). Simulation snapshots of the polymer with $\varepsilon = 1.3$, for several degrees of ionization: $\alpha = 0.06$ (**a**), $\alpha = 0.20$ (**b**), $\alpha = 0.25$ (**c**), and $\alpha = 0.33$ (**d**). Counterions not shown. For better visibility the snapshots differ in magnification; the real sizes of the monomer units are the same in all cases

or whether it needed revision. At the time our experimental study was performed, the nature of the PMA supercoiling process was not understood. A vivid discussion was focused on the question of whether the conformational change with pH is a cooperative (i.e., almost discontinuous) or progressive (continuous) process. It is fair to say that the present knowledge is still limited and there survives certain controversy concerning the interpretation by different research groups. Despite a number of later experimental and theoretical studies [104, 105, 107, 108, 147], the above question has not been unambiguously resolved until now. As mentioned above, theoretical studies by Raphael and Joanny [106] and recent MC simulations by Uyaver and Seidel [107, 108] indicate that a sudden sharp transition from a very compact globule to an almost fully stretched chain conformation occurs in really bad solvents, while in solvents of medium quality a gradual transition via the "necklace of pearls" takes place. Concerning PMA, water is a bad but certainly not too bad a solvent because the non-dissociated (i.e., uncharged) COOH is a hydrophilic group and almost neutral PMA is still reasonably soluble at low pH.

The comparison of simulation data with experimental data is shown in Fig. 21. It has to be noted that a strongly simplified polymer model was used and therefore only semiquantitative agreement was expected and achieved. The problem of mapping the simulation model onto a real polymer has been extensively discussed in the original paper [87]. The simulated and experimental orientational correlation times exhibit the same type of behavior, i.e., they progressively decrease with increasing degree of dissociation. The results of MD simulations thus support our intuitive interpretation of fluorescence experiments on PMA performed about two decades earlier.

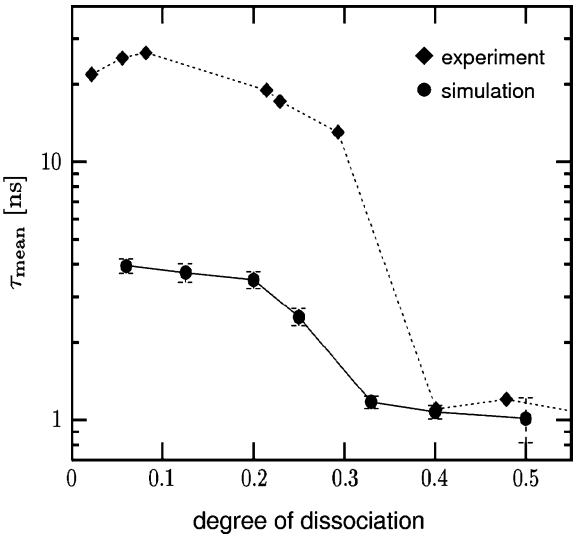

Fig. 21 Comparison of the experimental data (*diamonds*) and simulation (*circles*) of the mean characteristic decay time of the fluorescence anisotropy

4.1.4 Molecular Dynamics Simulations of Annealed Polyelectrolyte Chains

The main simplification of the above study can be summarized as follows: although the simulation was performed for a polymer with a fixed distribution of charges, it was compared to an experiment when the real PE was annealed, i.e. the charges on the polymer were not fixed but mobile. Therefore, we wanted to see to what extent the assumption of fixed charges affects the simulation. For this purpose, we simulated a polymer with mobile charges using essentially the same model as before [148]. The employed model for the mobile charges was simple, yet it captured certain essential features of the weak (annealed) PEs. The dissociation of the weak PE groups was modeled using a MC procedure. At a predetermined rate, the MD simulation was stopped, a random charged group on the chain was selected, and the charge was moved to a new position on the chain. The move was accepted using the standard Metropolis criterion [149]. In this way, the overall degree of charging of the polymer was kept constant while the distribution of charges along the polymer chain was allowed to vary.

The main result of the simulations was that the conformation of the polymer and distribution of charges along the chain are correlated. When the solvent for the polymer is not too poor, the charges are almost homogeneously distributed along the chain [148] and the probability of charging slightly increases close to the ends of the polymer. The inhomogeneity close to the ends is a consequence of lower charge density around the ends of the polymer. This intuitive result is in agreement with the simulation study of Limbach and Holm on end-effects on strong PEs [150].

A similar behavior was observed for PEs in poorer solvents when their degree of charging was high, as shown in Fig. 22. The simulation snapshot shows that

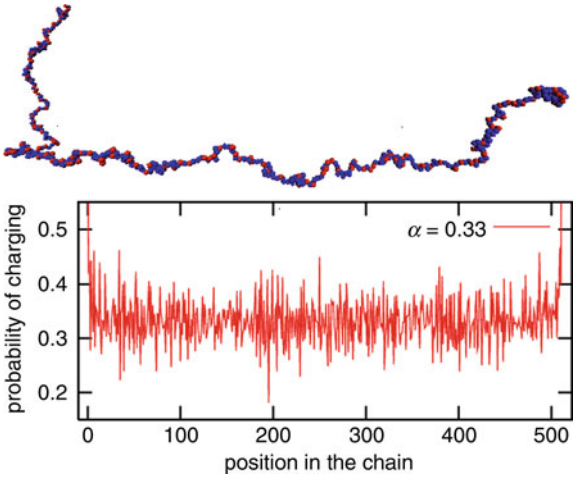

Fig. 22 The probability of charging of individual monomer units as a function of their position in the chain, in poor solvent for $\alpha = 0.33$ and $\varepsilon = m1.0$

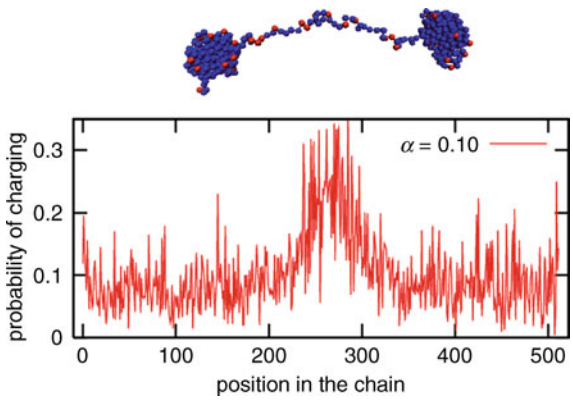

Fig. 23 The probability of charging of individual monomer units as a function of their position in the chain, in poor solvent for $\alpha = 0.1$ and $\varepsilon = 1.0$

the polymer conformation is expanded and that the plot of probability of charging of individual monomers as a function of their position in the backbone is homogeneous except for the ends, in accordance with the results for polymers in better solvents. However, when the degree of charging of such polymer is decreased so that the pearl-necklace conformation is formed, the situation changes dramatically. Figure 23 shows a simulation snapshot of such polymer and the plot of the probability of charging has a clear maximum in the central part that corresponds to the string connecting the pearls. This behavior can be understood when it is compared to the case of a polymer with fixed distribution of charges. In the latter case, when the pearl-necklaces are formed, there is a high density of charge inside pearls whereas the charge density in the strings is much lower. The strong (quenched) PE may respond by adopting the internal structure of the pearl so that the charged groups concentrate at its periphery, which has been observed in our simulation work on fluorescence anisotropy decays [87]. Besides this possibility, the weak PE has an option to transfer some portion of the charge from the pearls to the string and in this way to reduce the charge density in the pearls. This is exactly what is shown in the plot in Fig. 23. Hence, it could be concluded that the mobility of charges can serve as an additional mechanism for stabilizing the pearl-necklace structures in weak PEs as compared to the strong ones. Again, these results support the arguments for the formation of pearl-necklaces in weak PE systems. Yet, it has to be kept in mind that it is not the end of the puzzle. Some theoretical studies [106] predict a stepwise transition of weak PEs from a high degree of charging directly to a low degree of charging. In other words, they predict a forbidden range of degrees of ionization of a weak PE. In the light of these arguments, it would be desirable to work out a model in which the dissociation is explicit, i.e. the degree of dissociation is not fixed but comes out as a result of the simulation. This is the subject of currently running research projects and results may be expected in near future.

4.2 Monte Carlo Simulation of Shell-Forming Chain Conformations

4.2.1 Models and Simulation Techniques

In our computer studies of the conformational behavior of the shell-forming chains, we used MC simulations [91, 95] on a simple cubic lattice and studied the shell behavior of a single micelle only. Because we modeled the behavior of shells of kinetically frozen micelles, we simulated a spherical polymer brush tethered to the surface of a hydrophobic spherical core. The association number was taken from the experiment. The size of the core, lattice constant (i.e., the size of the "lattice Kuhn segment") and the effective chain length were recalculated from experimental values on the basis of the coarse graining parameterization [95].

The interactions are described by contact energies and the electrostatic energy. For contact energies we used the common matrix of interaction parameters in which the "reference interactions"(i.e., those where solvent is involved) are zero. The optimized parameters in units of kT are $\varepsilon_{\text{S-S}} = 0$, $\varepsilon_{\text{PMA-S}} = 0$, $\varepsilon_{\text{C-S}} = 0$, $\varepsilon_{\text{PMA-PMA}} = -0.27$, $\varepsilon_{\text{PMA-C}} = 0.8$, and $\varepsilon_{\text{C-C}} = 0.8$, where S, C and PMA stand for solvent (i.e., empty lattice site, occupied implicitly by solvent), C core (lattice point at the surface of the core or an attached hydrophobic pendant group), and the PMA bead (i.e., the Kuhn lattice segment, irrespectively of the ionization).

The electrostatic interactions (in aqueous solutions of annealed PEs, such as PMA, where the potentially ionizable groups get charged) are treated indirectly by solving the spherically symmetrical Poisson–Boltzmann equation (PBE) for the electrostatic potential $\varphi(r)$ [95]:

$$\frac{1}{r^2}\frac{\mathrm{d}}{\mathrm{d}r}\left[r^2\frac{\mathrm{d}\phi(r)}{\mathrm{d}r}\right] = -\frac{\rho(r)}{\varepsilon_0\varepsilon_\mathrm{r}}, \tag{19}$$

where ε_0 and ε_r are the dielectric vacuum permittivity and the relative (position dependent) permittivity of the dielectric medium, and the charge density $\rho(r)$ includes both the charge of the micelle (in the mean-field approximation) and of all small ions.

We consider the following components: –COOH, $–COO^-$, H_3O^+, OH^-, Na^+, and Cl^-, but not all are independent since they have to fulfill the relations, $K_\mathrm{w} = a_{H_3O^+} \cdot a_{OH^-}$ and $K_\mathrm{A} = \left(a_{H_3O^+} \cdot a_{A^-}\right)/a_{\text{COOH}}$, where K_w and K_A are the ionization product of water and the effective dissociation constant describing the dissociation of carboxylic groups in PMA, respectively. The effective dissociation constant for PMA in solutions as a function of ionic strength and degree of ionization was measured by Morcellet et al. [151] and by Porasso et al. [152]. Nevertheless, we use the constant value $\mathrm{p}K_\mathrm{A} = 4.69$ for the monomeric methacrylic acid as a reasonable first approximation [153] because most theoretical calculations for PEs employs $\mathrm{p}K_\mathrm{A}$ for the monomeric unit, which facilitates the comparison with data of other authors on similar systems. The activities of components a_i are calculated using

the Debye–Hückel limiting law [91]. The only independent parameters used in our simulations are pH and ionic strength, $I = (1/2)\ \Sigma c_i {z_i}^2$. The position-dependent concentrations of small ions are expressed according to the Boltzmann theorem as $c_i(r) = c_{i,\infty} \exp(-q_i z_i \varphi(r)/kT)$.

In summary, the computer simulation of micelles with shells formed by an annealed PE is a combination of MC with the self-consistent field treatment of electrostatic forces. However, it goes beyond the mean-field approximation. It is also evident from simulation snapshots (see below) that the a priori assumption of the spherical symmetry of the electrostatic field (which is an inherent feature of studied micelles) does not impose a strong constraint on instantaneous chain conformations.

4.2.2 Results and Discussion: Shell-Forming Chains at Low Ionic Strengths

We performed a series of coarse-grained lattice MC simulations for PE brushes tethered to spherical cores that mimic the studied micelles as close as possible. Details on the coarse-graining procedure can be found in [95]. MC simulations yield (a) snapshots of micellar structures and (b) a number of ensemble average characteristics, such as radius of gyration, R_G (as a function of pH and I) and its distribution, segment density profiles of the shell-forming blocks, ionization profiles, radial dependences of the electrostatic potential, etc. To give an idea of simulated structures, we show two snapshots that depict typical micelles at different pHs (pH 4 and 6, Figs. 24 and 25, respectively). A comparison of both snapshots shows increasing swelling of micellar shells with pH due to the well-known effect of ionization. The dependences of gyration radii on pH are shown in Fig. 26. The snapshots and rather trivial dependences of radii of gyration on pH have been included in order

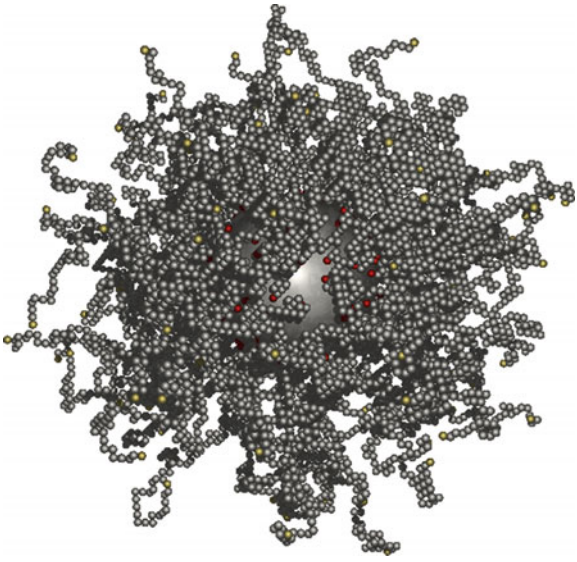

Fig. 24 Snapshot pf PS–PMA micelle at pH 4 and I 0.01

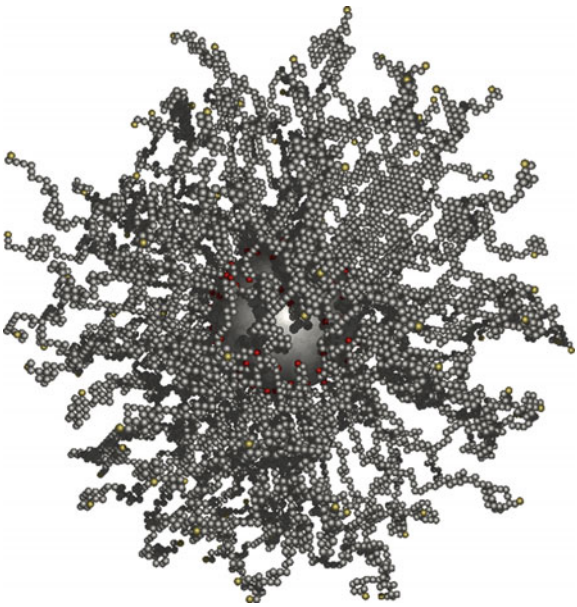

Fig. 25 Snapshot pf PS–PMA micelle at pH 6 and *I* 0.01

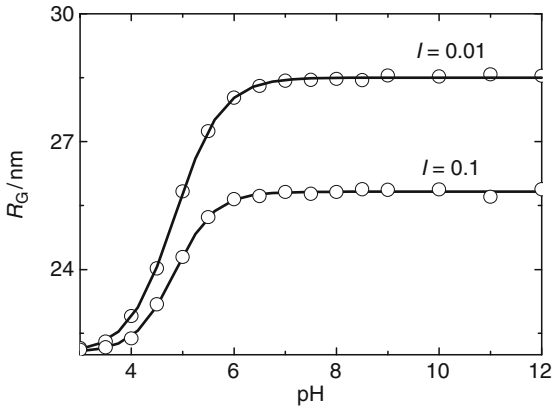

Fig. 26 Simulated dependence of R_G of PS–PMA micelles on pH for ionic strengths, *I*, of 0.01 and 0.01

to document the basic correctness of the model and the simulation procedure used. We would like to point out that the pronounced coiling of the shell-forming chains at the micellar periphery, where the degree of dissociation and electrostatic interactions are important, demonstrates that the constraint imposed by the a priori assumed spherical symmetry of the electrostatic field is weak and does not artificially restrict the conformational behavior of individual chains.

Furthermore, we discuss data that are directly related to the PE behavior at low close to pK_A. Figure 27 shows the electrostatic potential as a function of the distance from the micellar center, *r* (the function related to the vertical scale on the right) and the *r*-dependent concentration profiles of the positive and negative charge

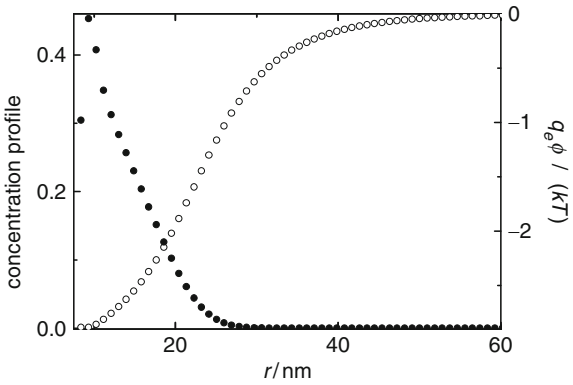

Fig. 27 Simulated concentration profile (*black circles* correspond to *left* axis) and electrostatic potential (*white circles* correspond to *right* axis) in PS–PMA micelles as a function of the distance from the micellar center for pH 5 and ionic strength 0.001

(corresponding to the vertical scale on the left) for the same condition, i.e., pH 5 and $I = 0.001$. It is evident that the electrostatic potential at the periphery of micelles is significantly negative and that there exists an excess of negative charge in the shell and an excess of positive charge around micelles.

4.2.3 Interpretation of NRET Data: Conformations of Hydrophobically Modified Chains

A pronounced bimodal distribution of chain conformations in a micelle that contains about 10^2 chains is something that one would hardly expect in an equilibrium system, even though bimodal distributions were earlier tentatively proposed for some other equilibrium polymer systems [145]. To elucidate the studied problem, we performed a series of simulations for modified micellar shells using the MC technique for neutral systems and the combined MC-mean field simulation technique for charged aqueous systems. Figure 28 compares the distributions of radial distances of end segments from the core (i.e., distances of An), $\rho_T(r)$, in the modified and unmodified systems. Similar information can be obtained from the distribution function of random Np–An pair distances, $P_{NA}(r_{NA})$, i.e., the distribution of distances of An traps around a randomly excited Np donor, averaged over all donors in the modified micellar system, which allows for the calculation of fluorescence decays. Both functions are bimodal in the modified system (with a narrow peak in the region of small distances), which confirms our working hypothesis used for the above-outlined tentative interpretation of NRET results. The Np fluorescence decay can be calculated using the $P_{NA}(r_{NA})$ function; however, the MC method offers a more direct evaluation of its shape. The simulation yields a number of independent micelles and, for each equilibrated micelle, it is possible to solve numerically the master equation [92] describing the probability $p(t)$ that the excitation is located at time t at the fluorophore that was excited at time $t = 0$:

$$\frac{\mathrm{d}p(t)}{\mathrm{d}t} = -\left[\frac{1}{\tau_\mathrm{d}} + \sum_{i=1}^{n} k_\mathrm{T}(r_i)\right] p(t), \tag{20}$$

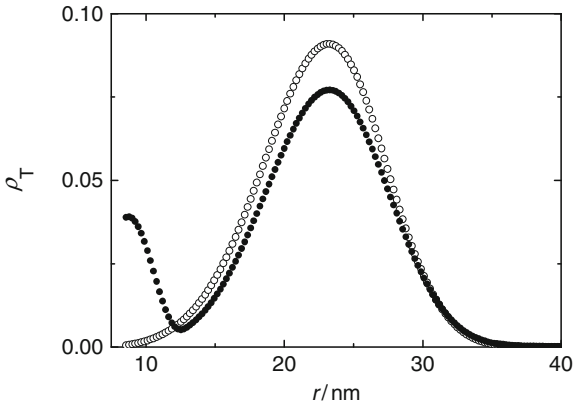

Fig. 28 Simulated distributions of radial distances of end segments from the core in hydrophobically modified (*black circles*) and unmodified (*white circles*) PS–PMA micelles

where τ_d is the natural (unaffected) fluorescence lifetime of the donor (Np) and $k_T(r_i)$ are the position-dependent rate transfer constants:

$$k_T(r_i) = \left(\frac{1}{\tau_d}\right)\left(\frac{R_0}{r_i}\right)^6, \tag{21}$$

describing the rate of NRET for individual pairs, i, formed by the randomly excited Np and all fixed An traps in one micelle. The first term of the right hand side (rhs) of (20) describes the depletion rate of the excited state by fluorescence, and the sum of $k_T(r_i)$ multiplied by p describes the net effect of NRET in system with a fixed position of all An. The averaging over different arrangements of traps around the excited donor (i.e., over all possible conformations of the shell-forming chains in the micellar system) yields the following formula for the enumeration of the experimentally accessible fluorescence decay:

$$I_d^q(t) = I_d^0(t)\left\langle \exp\left[-\sum_{i=1}^{n}\left(\frac{R_0}{r_i}\right)^6\left(\frac{t}{\tau_d}\right)\right]\right\rangle. \tag{22}$$

The comparison of experimental and calculated decays that is depicted in Fig. 29 shows a good quantitative agreement of both dependences.

To summarize the results of MC simulations, we can say that the computer study confirmed our hypothesis on the bimodal distribution of conformations of the modified shell-forming chains. The results are interesting both from the theoretical and practical points of view. Concerning the practical design of micelle-based systems with the end-attached targeting groups, the study indicates that the choice of a suitable group requires great care.

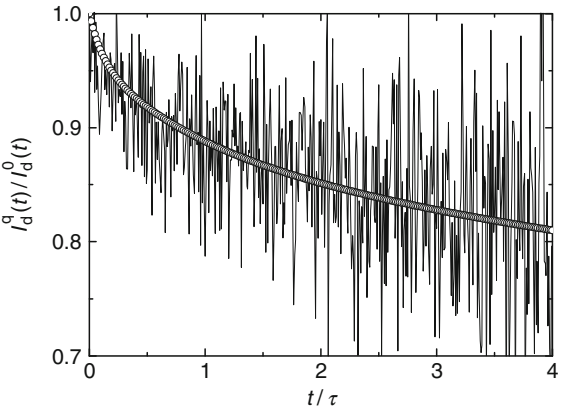

Fig. 29 Comparison of experimental curve (*noisy*) and simulated data (*circles*) describing the NRET kinetics of fluorescently labeled PS–PMA micelles

4.3 Monte Carlo Simulation of FCS Data

As mentioned in Sect. 2.5, we used computer simulations to address some problems that arise when FCS is used to study the diffusion of larger particles. In particular, we simulated how the FCS results are affected when large particles carry multiple labels and looked at how important is the effect of the rotational diffusion of such particles.

We used a simple simulation program that was developed in our laboratory. The program simulates an FCS experiment, i.e., it emulates the behavior of an ensemble of particles diffusing in a volume irradiated by a laser beam with a defined spatial intensity profile. The particles can be either point-like or finite-sized and they perform both translational and rotational diffusive motion. The probability of displacement in time Δt is drawn from the known probability distribution:

$$P(x,\Delta t) = \frac{1}{2}\sqrt{\pi D\Delta t}\exp\left(-\frac{x^2}{4D\Delta t}\right), \tag{23}$$

where x is the position of the particle, Δt is the time interval and D is the translational diffusion coefficient. Besides translational diffusive motion, the finite-sized objects can optionally perform rotational diffusion. Because the probability distribution for the rotational diffusion cannot be expressed in an analytical form, the rotational diffusion is simulated "by definition", i.e., in the time interval Δt, each object is rotated n_{rot} times around random axes by an angle φ given by the expression:

$$\phi = \sqrt{\frac{6\Theta\Delta t}{n_{\mathrm{rot}}}}, \tag{24}$$

where Θ is the rotational diffusion coefficient, which is related to the translational diffusion coefficient, D, as:

$$\Theta = \frac{kT}{8\pi\eta R^3} = \frac{3D}{4R^2}, \tag{25}$$

where R is the radius of the particles, k is the Boltzmann constant, T is the temperature and η is the viscosity of the solvent. Each of the diffusing particles can carry several fluorescent labels distributed over its volume or on the surface. The number of emitted photons in the interval Δt is given by the Poisson distribution:

$$P_\nu(n) = \nu^n \frac{\mathrm{e}^{-\nu}}{n!}, \tag{26}$$

where ν is the expected mean number of successful results (number of photon emissions in our case). For a particle in position (x,y,z) we obtain ν as:

$$\nu = Q \Delta t \, E(x,y,z), \tag{27}$$

where $E(x,y,z)$ is the excitation profile defined by (10) and Q is the instrument constant. In a real system, Q comprises a number of factors such as detection efficiency and quantum yield. In the simulation, it is an adjustable parameter that influences the computational efficiency but has no effect on the results. The simulated system is in spherical boundary conditions so that when a particle diffuses out of the simulation cell, it is deleted and a new particle is generated at a random position on the surface of the cell. The boundary conditions perturb the correlations at longer times that may potentially cause problems. However, for a given size of the simulation cell, as well as other parameters of the simulated system, analytical expressions can be derived that estimate the expected systematic error. Moreover, this error can be made arbitrarily small by choosing a large enough system and simulating for long enough. On the other hand, a natural limitation is the acceptable computer time for one simulation. For practical purposes, we accept an error of up to 5% in the obtained diffusion coefficient and concentration, which is still better than can be obtained from experiments.

4.3.1 Simulation Results

We used the computer simulations to study the effect of the size of diffusing particles on the results obtained from the FCS measurements. The simulated particles were spheres that could carry one of more particles on their surface. The translational diffusion coefficient of the particles was calculated from (25) and was used as an input parameter. The obtained fluorescence intensity trace of the simulated system was processed to calculate the autocorrelation function $G(\tau)$ (11), which was then fitted using the analytical expression for point-like particles (12).

When the diffusing particles carry only one fluorescent label, the statistical characteristics of the diffusion of the labels exactly corresponds to that of point-like particles. Data points in Fig. 30 show the simulation data for particles carrying one label. The data are plotted using relative units: On the vertical axis, we plot the ratio of the apparent diffusion time (i.e., that obtained from the fit of the autocorrelation function) to the true diffusion time (i.e., that which was an input parameter of the simulation). On the horizontal axis, we plot the ratio of the particle radius, R, and

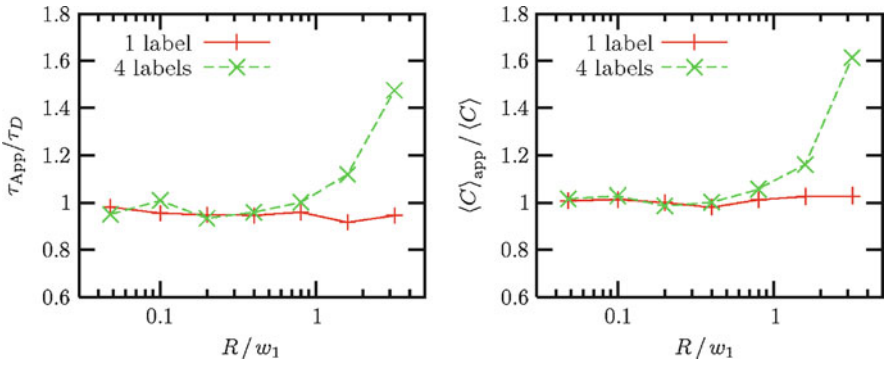

Fig. 30 Effect of multiple labeling on the apparent diffusion times τ_{App}, (*left*) and on the apparent concentration, $\langle C\rangle_{App}$ (*right*)

the typical dimension of the active volume, ω_1. Since the particles carrying one single label behave in the same way as point-like particles, in our set of units, we should obtain that the ratio $\tau_{App}/\tau_D = 1.0$. The deviations from this value characterize the intrinsic error of the simulation. As mentioned in previous paragraphs, we set up the simulated system so that the error should be up to 5%. Since these simulation data agree well with the theory, we used them as a reference set of data to which other results are compared. In the case of particles, which carry more fluorescent labels, there is an additional correlation between the motion of labels attached to the same particle, which is reflected in the autocorrelation function. When data from such simulation are fitted using (23), an apparent diffusion time is obtained, which should be significantly different from the translational diffusion time used as an input for the simulation. Figure 30 also shows the simulation results for particles carrying four labels. The data in the left graph of Fig. 30 show that when $R \ll \omega_1$, the apparent diffusion time does not significantly differ from the true value. On the other hand, when $R \approx \omega_1$, the apparent diffusion time significantly differs from the real value. This is in agreement with the theoretical predictions of Wu et al. [85]. A similar plot for the apparent concentration is shown is shown in the right graph of Fig. 30. Again, for point-like particles the single-label data points are very close to unity for any particle size while the four-label data points significantly deviate from the real values when $R \approx \omega_1$.

Another, yet unexplored, problem is the extent to which the autocorrelation function and the obtained diffusion characteristics are affected by the rotational diffusion of the particles. Intuitively, one can expect that the rotational diffusion effectively speeds up the decay of the autocorrelation function and hence shorter diffusion times should be observed. This is shown in Fig. 31. The one-label, no rotation data points are the same as in Fig. 30 and serve as a reference. The other data points show the same system in which the rotation of the diffusing particle is switched on. As could be expected, when the relative size of the particle is small as compared to the dimensions of the active volume, the rotation has little effect. However, when the particle dimensions are comparable to those of the active volume, the apparent diffusion time

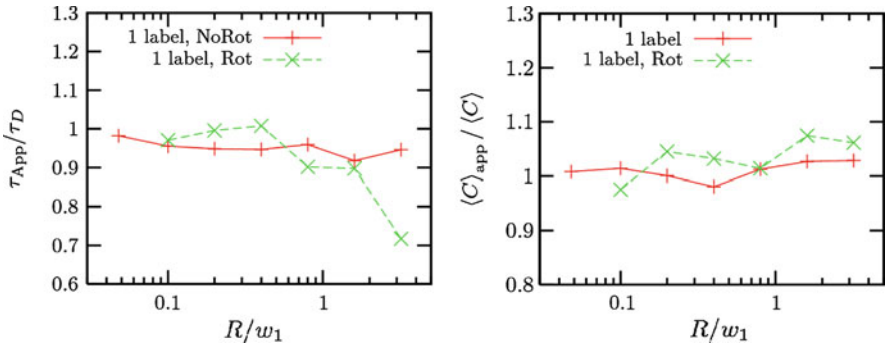

Fig. 31 Effect of rotation on the apparent diffusion time, τ_{App}, (*left*) on the apparent concentration, $\langle C \rangle_{App}$ (*right*)

is significantly lower than the real one. When the rotational diffusion is switched on for particles that have more than one label (data not shown), the effect of rotation is much weaker. It can be understood by analyzing the extreme case: for a very high number of labels, the large particle is uniformly covered with fluorophores and it does not matter at all if it is rotating or not. Hence, with increasing number of fluorophores on the diffusing particle, the effect of rotation is gradually suppressed. Figure 31 shows that the effect of rotation on the apparent concentration is close to the intrinsic error of the method and hence can be considered as negligible.

To summarize the results of the MC simulations, we may say that when the diffusing particles have dimensions comparable to the dimensions of the effective illuminated volume, their size (and shape) strongly affects the autocorrelation function. If such system is treated using the standard model for point-like particles, the obtained apparent diffusion coefficients may significantly differ from the real ones. On the other hand, when the large particles also perform rotational diffusive motions, then the apparent diffusion times are affected in the opposite direction, as in the case of multiple labeling. The effect of rotational diffusion is important when there is only one label per particle, and with increasing number of fluorophores it diminishes. Both these effects should be taken into account when FCS is applied to study the diffusion of particles that have dimensions comparable to the dimensions of the illuminated volume. On a semi-quantitative basis, the simulation results explain the discrepancy between the diffusion coefficients (hydrodynamic radii) of large particles when measured by FCS and DLS.

5 Concluding Remarks

In this article, we have selected and reviewed several studies performed during (or closely connected to) our participation in the POLYAMPHI network with the aim of showing the high research potential of fluorescence techniques for investigating self-assembled stimuli-responsive polymer systems. The selection was based on three criteria.

First, we wanted to show interesting associative and conformational behavior of amphiphilic copolymer systems in aqueous media containing both neutral water-soluble (e.g., PEO) and weak PE blocks (e.g., PMA, PVP). On purpose, we omitted common types of straightforward studies that are currently performed by a number of groups (and also in our laboratory) and chose to focus on the specific features of their behavior and on their detailed investigation that could not have been done without specialized fluorescence techniques. One of goals was the demonstration that the structure of water and its changes due to the solvation of water-soluble chains plays an important role in self-assembling processes. In our studies, we often observe fairly unexpected behavior and witness how the intricate entropy-to-enthalpy balance influences the behavior of aqueous nanoparticle systems. In contrast to biochemists and biologists, who take great care over the role of water and talk about "hydrophobic effect" or "biological water", polymer scientists usually prefer universal scaling laws, etc. and forget that the tiny solvent molecules represent an important component of the system.

The second criterion was the choice of fluorescence techniques itself. We wanted to include examples of both relatively widely used techniques like NRET or fluorescence anisotropy and show their specific application, and also give some examples of techniques little used in polymer research, like SRM or FCS. One of goals was the "advertisement" of SRM because, in contrast to FCS that is finding supporters among other POLYAMPHI members [152, 155], SRM is a "Cinderella" in polymer science.

The third criterion of the selection derives directly from the main goals of the paper. We wanted to show how computer modeling could help in the interpretation of fluorescence data on complex systems. As already mentioned, fluorescence is an indirect technique and an unambiguous interpretation needs pieces of independent information. In our studies, we combined fluorescence with a number of experimental techniques and computer simulations. We hope that we have persuaded readers that computer modeling offers a deep insight into the behavior of studied systems and, besides being a semi-quantitative reproduction of observed trends, can yield new hints for experimental research.

Acknowledgments The authors would like to acknowledge the EU support (Marie Curie MRTN-CT-2003-505027, "POLYAMPHI"), the support of the Ministry of Education, Youths and Sports of the Czech Republic (Research Plan MSM0021620857), the Grant Agency of the Czech Republic (203/07/0659), the Grant Agency of the Academy of Sciences of the Czech Republic (IAA400400621, IAA401110702, and KJB401110701) and the Grant Agency of Charles University (43-257269).

References

1. Jablonski A (1935) Z Phys 94:38
2. Levine IN (1975) Molecular spectroscopy. Wiley, London

3. Turro NJ (1991) Modern molecular photochemistry. University Science Books, Sausalito, California
4. Franck J (1926) Trans Faraday Soc 21:536
5. Condon E (1926) Phys Rev 28:1182
6. Fleming GR (1986) Chemical applications of ultrafast spectroscopy. Oxford University Press, New York
7. Beer M, Longuet-Higgins HC (1955) J Chem Phys 23:1390
8. Lakowicz JR (1983) Principles of fluorescence spectroscopy. Plenum, New York
9. Debye P (1945) Polar molecules. Dover, New York
10. Favro LD (1960) Phys Rew 119:53
11. Michl J, Thulstrup EW (1986) Spectroscopy with polarized light. VCH, New York
12. Procházka K, Medhage B, Mukhtar E, Almgren M, Svoboda P, Trnìná J, Bednář B (1993) Polymer 34:103
13. Birks JB (1970) Photophysics of aromatic molecules. Wiley, London
14. Valeur B, Monnerie L (1976) J Polym Sci Pt B-Polym Phys 14:11
15. Stubbs CD, Williams BW (1992) In: Lakowicz JR (ed) Topics in fluorescence spectroscopy: biochemical applications. Plenum, New York, p 231
16. Lentz BR (1993) Chem Phys Lipids 64:99
17. Gidwani A, Holowka D, Baird B (2001) Biochemistry 40:12422
18. Klymchenko AS, Duportail G, Demchenko AP, Mely Y (2004) Biophys J 86:2929
19. Ha TJ, Ting AY, Liang J, Caldwell WB, Deniz AA, Chemla DS, Schultz PG, Weiss S (1999) Proc Natl Acad Sci USA 96:893
20. Swaminathan R, Hoang CP, Verkman AS (1997) Biophys J 72:1900
21. Heikal AA, Hess ST, Baird GS, Tsien RY, Webb WW (2000) Proc Natl Acad Sci USA 97:11996
22. Volkmer A, Subramaniam V, Birch DJS, Jovin TM (2000) Biophys J 78:1589
23. Birch DJS, Geddes CD (2000) Phys Rev E 62:2977
24. Kujawa P, Aseyev V, Tenhu H, Winnik FM (2006) Macromolecules 39:7686
25. Katsumoto Y, Tsunomori F, Ushiki H, Letamendia L, Rouch J (2001) Eur Polym J 37:475
26. Wang B, Liu MZ, Chen Y, Liang R, Chen SL, Jin SP (2007) J Appl Polym Sci 104:1714
27. Pistolis G, Andreopoulou AK, Malliaris A, Kallitsis JK (2005) J Phys Chem B 109:11538
28. Viovy JL, Monnerie L, Merola F (1985) Macromolecules 18:1130
29. Viovy JL, Frank CW, Monnerie L (1985) Macromolecules 18:2606
30. Monnerie L (1991) J Non-Cryst Solids 131:755
31. Adams S, Adolf DB (1999) Macromolecules 32:3136
32. Kiserow D, Procházka K, Ramireddy C, Tuzar Z, Munk P, Webber SE (1992) Macromolecules 25:461
33. Sen S, Sukul D, Dutta P, Bhattacharyya K (2001) J Phys Chem A 105:7495
34. Kim C, Lee SC, Shin JH, Kwon IC, Jeong SY (2000) Macromolecules 33:7448
35. Sýkora J, Slavíček P, Jungwirth P, Barucha J, Hof M (2007) J Phys Chem B 111:5869
36. Chakrabarty A, Chakraborty D, Seth D, Hazra P, Sarkar N (2005) Chem Phys Lett 412:255
37. Sen P, Roy D, Mondal SK, Sahu K, Ghosh S, Bhattacharyya K (2005) J Phys Chem A 109:9716
38. Lang B, Angulo G, Vauthey E (2006) J Phys Chem A 110:7028
39. Hutterer R, Schneider FW, Sprinz H, Hof M (1996) Biophys Chem 61:151
40. Moyano F, Biasutti MA, Silber JJ, Correa NM (2006) J Phys Chem B 110:11838
41. Rowe BA, Neal SL (2006) J Phys Chem B (2006) 110:15021
42. Lippert E (1957) Z Elektrochem 61:962
43. Badea MG, DeToma RP, Brand L (1978) Biophys J 24:197
44. Chattopadhyay A, Mukherjee S (1993) Biochemistry 32:3804
45. Hutterer R, Schneider FW, Lanig H, Hof M (1997) Biochim Biophys Acta – Biomembranes 1323:195
46. Gafni A, DeToma RP, Manrow RE, Brand L (1977) Biophys J 17:155
47. Toptygin D, Gronenborn AM, Brand L (2006) J Phys Chem B 10:26292

48. Brauns, EB, Madaras ML, Coleman, RS, Murphy CJ, Berg MA (1999) J Am Chem Soc 121:11644
49. Middelhoek ER, Vandermeulen P, Verhoeven JW, Glasbeek M (1995) Chem Phys 198:373
50. Gulbinas V, Markovitsi D, Gustavsson T, Karpicz R, Veber M (2000) J Phys Chem A 104:5181
51. Chakrabarty D, Charkraborty A, Seth D, Sarkar N (2005) J Phys Chem A 109:1764
52. Cichos F, Willert A, Rempel U, von Borczykowski C (1997) J Phys Chem A 101:8179
53. Molotsky T, Huppert D (2003) J Phys Chem A 107:8449
54. Mukherjee S, Sahu K, Roy D, Mondal SK, Bhattacharyya K (2004) Chem Phys Lett 384:128
55. Sen P, Ghosh S, Sahu K, Mondal SK, Roy D, Bhattacharyya K (2006) J Chem Phys 124:204905
56. Adikhari A, Dey S, Das DK, Mandal U, Ghosh S, Bhattacharyya K (2008) J Phys Chem B 112:6350
57. Kasha M (1952) J Chem Phys 20:71
58. Stern O, Volmer M (1919) Phys Z 20:183
59. Förster T (1949) Z Naturforsch 4A:321
60. Förster T (1959) Discuss Faraday Soc 7:27
61. Van Der Meer WB, Coker G, Chen SS-Y (1991) Resonance energy transfer. Wiley, New York
62. Dale RE, Eisinger J, Blumberg WE (1979) Biophys J 26:161
63. Eisinger J, Blumberg WE, Dale RE (1981) Biophys J 33:155
64. Chee CK, Rimmer S, Soutar I, Swanson L (2001) Polymer 42:5079
65. Kuzmenkina EV, Heyes CD, Nienhaus GU (2005) Proc Natl Acad Sci USA 102:15471
66. Suwa M, Hashidzume A, Morishima Y, Nakato T, Tomida M (2000) Macromolecules 33:7884
67. Holappa S, Kantonen L, Winnik FM, Tenhu H (2004) Macromolecules 37:7008
68. Dias FB, Knaapila M, Monkman AP, Burrows HD (2006) Macromolecules 39:1598
69. Pham HH, Farinha JPS, Winnik MA (2000) Macromolecules 33:5850
70. Xiang ML, Jiang M, Zhang YB, Wu C, Feng LX (1997) Macromolecules 30:2313
71. Feng JR, Yekta A, Winnik MA (1996) Chem Phys Lett 260:296
72. Torchilin VP, Levchenko TS, Whiteman KR, Yaroslavov AA, Tsatsakis AM, Rizos AK, Michailova EV, Shtilman MI (2001) Biomaterials 22:3035
73. Mizusaki M, Morishima Y, Winnik FM (1999) Macromolecules 32:4317
74. Barros TC, Adronov A, Winnik FM, Bohne C (1997) Langmuir 13:6089
75. Magde D, Elson EL, Webb WW (1974) Biopolymers 13:29
76. Schwille P, Bieschke J, Oehlenschlager F (1997) Biophys Chem 66:211
77. Schwille P (2001) Cell Biochem Biophys 34:383
78. Sanchez SA, Gratton E (2005) Acc Chem Res 38:469
79. Remaut K, Lucas B, Raemdonck K, Beckmans K, Demeester J, De Smedt SC (2007) J Controlled Release 121:49
80. Humpolíčková J, Beranová L, Štěpánek M, Benda A, Procházka K, Hof M (2008) J Phys Chem B 112:16823
81. Zettl H, Hafner W, Boker A, Schmalz H, Lanzendorfer M, Müller AHE, Krausch G (2004) Macromolecules 37:1917
82. Bonne TB, Papadakis CM, Ludtke K, Jordan R (2006) Colloid Polym Sci 285:491
83. Pecora BJ, Pecora R (2000) Dynamic light scattering. Wiley, New York
84. Humpolíčková J, Procházka K, Hof M, Tuzar Z, Špírková M (2003) Langmuir 19:4119
85. Wu B, Chen Y, Muller JD (2008) Biophys J 94:2800
86. Bednář B, Trnĭná J, Svoboda P, Vajda S, Fidler V, Procházka K (1991) Macromolecules 24:2054
87. Košovan P, Limpouchová Z, Procházka K (2006) Macromolecules 39:3458
88. Štěpánek M, Matějíček P, Humpolíčková J, Procházka K (2005) Langmuir 21:10783
89. Humpolíčková J, Štěpánek M, Procházka K, Hof M (2005) J Phys Chem A 109:10803
90. Matějíček P, Podhájecká K, Humpolíčková J, Uhlík F, Jelínek K, Limpouchová Z, Procházka K, Špírková M (2004) Macromolecules 37:10141
91. Uhlík F, Limpouchová Z., Jelínek K, Procházka K (2004) J Phys Chem 121:2367

92. Uhlík F, Limpouchová Z, Matějíček P, Procházka K, Tuzar Z, Webber SE (2002) Macromolecules 35:9497
93. Matějíček P, Uhlík F, Limpouchová Z, Procházka K, Tuzar Z, Webber SE (2002) Macromolecules 35:9487
94. Matějíček P, Humpolíčková J, Procházka K, Tuzar Z, Špírková M, Hof M, Webber SE (2003) J Phys Chem B 107:8232
95. Uhlík F, Limpouchová Z, Jelínek K, Procházka K (2003) J Phys Chem 118:11258
96. Matějíček P, Uhlík F, Limpouchová Z, Procházka K, Tuzar Z, Webber SE (2002) Collect Czech Chem Commun 67:531
97. Štěpánek M, Humpolíčková J, Procházka K, Hof M, Tuzar Z, Špírková M, Wolff T (2003) Collect Czech Chem Commun 68:2120
98. Štěpánek M, Matějíček P, Humpolíčková J, Havránková J, Podhajecká K, Špírková M, Tuzar Z, Tsitsilianis C, Procházka K (2005) Polymer 46:10493
99. Dobrynin AV, Rubinstein M, Obukhov SP (1996) Macromolecules 29:2974
100. Dautzenberg H, Jaeger W, Kotz BPJ, Seidel C, Stscherbina D (1994) Polyelectrolytes: formation, characterization and applications. Hanser, Munich
101. Khokhlov AR (1980) J Phys Chem A 13:979
102. Kantor Y, Kardar M (1995) Phys Rev E 51:1299
103. Lord Rayleigh (1882) Philos Mag 14:184
104. Limbach HJ, Holm C (2003) J Phys Chem. B 32:8041
105. Limbach HJ, Holm C, Kremer K (2004) Macromol Symp 211:43
106. Raphael E, Joanny JF (1990) Europhys Lett 13:623
107. Uyaver S, Seidel C (2003) Europhys Lett 64:536
108. Uyaver S, Seidel C (2004) J Phys Chem B 180:18804
109. Ulrich S, Laguecir A, Stoll S (2005) J Chem Phys 122:094911
110. Laguecir A, Ulrich S, Labille J, Fatin-Rouge N, Stoll S, Buffle J (2006) Eur Polym J 42:1135
111. Borukhov I, Andelman D, Borrega R, Cloitre M, Leibler L, Orland H (2000) J Phys Chem B 104:11027
112. Katchalski A (1951) J Polym Sci 7:393
113. Strauss UP, Schlesinger MS (1978) J Phys Chem 82:571
114. Strauss UP, Schlesinger MS (1978) J Phys Chem 82:1627
115. Strauss UP, Vesnaver G (1975) J Phys Chem 79:1558
116. Strauss UP, Vesnaver G (1975) J Phys Chem 79:2426
117. Wang Y, Morawetz H (1986) Macromolecules 19:1925
118. Ghiggino KP, Tan KL (1985) In: Phillips D (ed) Polymer photophysics. Chapman and Hall, London
119. Popelka S, Machová LK, Rypáček F, Špírková M, Štěpánek M, Matějíček P, Procházka K (2005) Collect Czech Chem Commun 70:1811
120. Matějíček P, Štěpánek M, Uchman M, Procházka K, Špírková M (2006) Collect Czech Chem Commun 71:723
121. Šachl R, Uchman M, Matějíček P, Procházka K, Štěpánek M, Špírková M (2007) Langmuir 23:3395
122. Harada A, Kataoka K (2006) Prog Polym Sci 31:949
123. Polik WF, Burchard W (1983) Macromolecules 16:978
124. Zhou P, Brown W (1990) Macromolecules 23:1131
125. Kinugasa S, Nakahara H, Fudagawa N, Koga Y (1994) Macromolecules 27:6889
126. Polverari M, van de Ven TGM (1996) J Phys Chem 100:13687
127. Duval M. (2000) Macromolecules 33:7862
128. Hammouda B, Ho DL, Kline S (2004) Macromolecules 37:6932
129. De Gennes, PG (1991) C R Acad Sci, Ser II 313:1117
130. Horng ML, Gardecki JA, Papazyan A, Maroncelli M (1995) J Phys Chem 99:17311
131. Fee RS, Maroncelli M (1994) Chem Phys 183:235
132. Martin TJ, Procházka K, Munk P, Webber SE (1996) Macromolecules 29:6071
133. Bieze TWN, Barnes AC, Huige CJM, Enderby JE, Leyte JC (1994) J Phys Chem 98:6568
134. Blandamer MJ, Fox MF, Powell E, Stafford JW (1967) Makromol Chem 124:222

135. Šachl R, Štěpánek M, Procházka K, Humpolíčková J, Hof M (2008) Langmuir 24:288
136. Bonacucina G, Cespi M, Misici-Falzi M, Palmieri GF (2009) J Pharm Sci 98:1
137. Zhao Q, Ni PH (2006) Prog Chem 18:768
138. Yasugi K, Nakamura T, Nagasaki Y, Kato M, Kataoka K (1999) Macromolecules 32:8024
139. Otsuka H, Nagasaki Y, Kataoka K (2001) Curr Opin Colloid Interface Sci 6:3
140. Dufresne MH, Gauthier MA, Leroux JC (2005) Bioconjugate Chem 16:1027
141. Rieger J, Stoffelbach F, Cui D, Imberty A, Lameignere E, Putaux JL, Jerôme R, Auzely-Velty R (2007) Biomacromolecules 8:2717
142. Hu ZY, Luo F, Pan YF, Hou C, Ren LF, Chen JJ, Wang JW, Zhang YD (2008) J Biomed Mater Res A 85A:797
143. Martin TJ, Webber SE (1995) Macromolecules 28:8845
144. Berlman IB (1973) Energy transfer parameters of aromatic compounds. Academic, New York
145. Shusharina NP, Linse P (2001) Eur Phys J 4:399
146. Micka U, Holm C, Kremer K (1999) Langmuir 15:4033
147. Heitz C, Rawiso M, Francois J (1999) 40:1637
148. Košovan P, Limpouchová Z, Procházka K (2008) Collect Czech Chem Commun 73:439
149. Allen DJ, Tildesley MP (1987) Computer simulation of liquids. Clarendon, Oxford
150. Limbach HJ, Holm C (2001) J Chem Phys 114:9674
151. Morcellet M, Wozniak M (1991) Macromolecules 24:745
152. Porasso RD, Benegas JC, van den Hoop MAGT (1999) J Phys Chem B 103:2361
153. Lide DR, Frederikse HPR (1995) Handbook of chemistry and physics, 76th edn. CRC, Boca Raton, FL
154. Zettl H, Häfner W, Böker A, Schmalz H, Lanzendörfer M, Müller AHE, Krausch G (2004) Macromolecules 37:1917
155. Zettl H, Zettl U, Krausch G, Enderlein J, Ballauff M (2007) Phys Rev E 75:061804

Index